DEPARTMENT OF MECHANICAL
AND MANUFACTURING ENGINEERING

GROWTH BY PULSED LASER DEPOSITION AND CHARACTERIZATION OF TRANSITION METAL OXIDE THIN FILMS FOR POTENTIAL USE IN NOVEL APPLICATIONS

DOCTOR OF PHILOSOPHY DISSERTATION

EFTHYMIOS CH. SVOUKIS

2015

EFTHYMIOS CH. SVOUKIS

University of Cyprus

DEPARTMENT OF MECHANICAL
AND MANUFACTURING ENGINEERING

GROWTH BY PULSED LASER DEPOSITION AND CHARACTERIZATION OF TRANSITION METAL OXIDE THIN FILMS FOR POTENTIAL USE IN NOVEL APPLICATIONS

EFTHYMIOS CH. SVOUKIS

A dissertation submitted to the University of Cyprus in partial fulfillment of the requirements for the degree of Doctor of Philosophy

April 2015

EFTHYMIOS CH. SVOUKIS

EFTHYMIOS CH. SVOUKIS

© Svoukis Efthymios

April 2015

Thesis at University of Cyprus.

Validation Page

Efthymios Ch. Svoukis

Growth by Pulsed Laser Deposition and Characterization of Transition Metal Oxide Thin Films for Potential Use in Novel Applications

The present Doctoral Dissertation was submitted in partial fulfilment of the requirements for the degree of Doctor of Philosophy at the Department of Mechanical and Manufacturing Engineering and approved on the April 20, 2015 by the members of the Examination Committee.

Research Supervisor

____
Professor
John Giapintzakis

Other Members

____
Professor
Valentin Craciun

____
Professor
Charis Theocharis

____
Associate Professor
Claus Rebholz

____
Associate Professor
Theodora Kyratsi

EFTHYMIOS CH. SVOUKIS

Declaration

The present doctoral dissertation was submitted in partial fulfillment of the requirements for the degree of Doctor of Philosophy of the University of Cyprus. It is a product of original work of my own, unless otherwise mentioned through references, notes, or any other statement.

Doctoral Candidate

Efthymios Ch. Svoukis

Copyright Statement

Copyright in text of this thesis rests with the author. Copies (by any process) either in full, or of extracts, may be made only in accordance with instructions given by the author.

The ownership of any intellectual property rights which may be described in the thesis is vested by the author, subject to any prior agreement to the contrary, and may not be made available for use by third parties without the written permission of the author.

EFTHYMIOS CH. SVOUKIS

Abstract

State – of – the – art technology demands new "*exotic*" materials that can be used in miniaturized circuits but also further increase their capabilities. Transition metal oxides have attracted great interest over the last decades, due to the rich spectrum of physical properties that they exhibit.

This thesis work presents a study for the growth and characterization of three different correlated oxides: $La_5Ca_9Cu_{24}O_{41}$, $LiCoO_2$ and VO_2. Each one of these materials has unique transport properties with a possible novel application in the IC industry.

Crystalline highly oriented and epitaxial thin films of all the above oxides have been produced using the Pulsed Laser Deposition technique. Structural, morphological and transport characteristics of the produced films have been examined with respect to deposition conditions.

In the case of $La_5Ca_9Cu_{24}O_{41}$ the goal was the stoichiometric transfer of the complex structure to thin films for exploitation of a new highly efficient magnetic mode of thermal conduction. This magnetic mode of conduction could be used for thermal management in ICs.

$LiCoO_2$ has widely been used in the past as a cathode material in lithium ion rechargeable batteries. In this study, this material was investigated for resistive switching phenomena for possible further exploitation in the IC industry. $LiCoO_2$, compared to other materials proposed for scanning probe mediated approaches in nanoscale patterning, is highly stable as an oxide compound, exhibiting reversible electrochemical surface modifications. Growth of epitaxial $LiCoO_2$ thin films is important for usage in data storage applications.

VO_2 was selected for the final part of this thesis work. Epitaxial growth of VO_2 thin films is important for the investigation of the first order semiconductor – metal transition and also as a first step for the experimental investigation of TiO_2 / VO_2 heterostructures with sharp interface, for which theoretically predicted quantum phenomena similar to those observed in graphene have been proposed.

EFTHYMIOS CH. SVOUKIS

Περίληψη

Η τεχνολογία αιχμής χρειάζεται νέα «*εξωτικά*» υλικά που θα μπορούσαν να χρησιμοποιηθούν στην περαιτέρω σμίκρυνση των ηλεκτρονικών κυκλωμάτων καθώς και την αύξηση των λειτουργιών τους. Τα οξείδια μετάλλων μετάπτωσης απέκτησαν μεγάλο ενδιαφέρον στα τελευταία χρόνια, λόγω του μεγάλου φάσματος φυσικών ιδιοτήτων που παρουσιάζουν.

Στην παρούσα ερευνητική εργασία, παρουσιάζεται η ανάπτυξη και ο χαρακτηρισμός τριών οξειδίων: $La_5Ca_9Cu_{24}O_{41}$, $LiCoO_2$ και VO_2. Το κάθε ένα από αυτά παρουσιάζει μοναδικές ιδιότητες που σχετίζονται με μία πιθανή καινοτόμα εφαρμογή στη βιομηχανία ολοκληρωμένων κυκλωμάτων.

Κρυσταλλικά – υμένια με υψηλόβαθμο προσανατολισμό και επιταξίας από τα παραπάνω υλικά παραχθήκαν με τη μέθοδο εναπόθεσης με παλμικό λέιζερ. Περαιτέρω τα υμένια μελετηθήκαν όσον αναφορά στις δομικές, μορφολογικές και φυσικές τους ιδιότητες.

Στην περίπτωση του $La_5Ca_9Cu_{24}O_{41}$ στόχος ήταν η στοιχειομετρική μεταφορά της δομής και στη συνέχεια η μελέτη της μεταφοράς θερμότητας με μαγνητικές διεγέρσεις. Αυτός ο νέος τρόπος μεταφοράς θερμότητας θα μπορούσε να χρησιμοποιηθεί για την απαγωγή θερμότητας από ενεργοβόρες συσκευές με ηλεκτρονικά κυκλώματα..

Το $LiCoO_2$ έχει χρησιμοποιηθεί στο παρελθόν σε επαναφορτιζόμενες μπαταρίες ιόντων λιθίου. Το συγκεκριμένο υλικό μελετήθηκε στη παρούσα διατριβή ως πιθανό μέσο αποθήκευσης δεδομένων. Σε σύγκριση με άλλα υλικά το $LiCoO_2$ παρουσιάζει αυξημένη χημική σταθερότητα και αναστρεψιμότητα σε επιφανειακές ηλεκτροχημικές αλλαγές. Η ανάπτυξη επιταξιακών υμενίων είναι απαραίτητη ώστε να χρησιμοποιηθεί ως μέσο αποθήκευσης δεδομένων.

Το VO_2 επιλέχτηκε ως το τελευταίο κομμάτι στην παρούσα εργασία. Η επιταξιακή ανάπτυξή του είναι σημαντική για τη μελέτη της μετάβασης ημιαγωγού – μετάλλου που παρατηρείται σε αυτό. Περαιτέρω αποτελεί το πρώτο βήμα για την πειραματική μελέτη ετεροδομών TiO_2 / VO_2, με οξεία διεπιφάνεια, για τις οποίες προβλέφθηκαν θεωρητικά κβαντικά φαινόμενα παρόμοια με αυτά που εμφανίζονται στο γραφένιο.

EFTHYMIOS CH. SVOUKIS

Acknowledgements

First of all, I would like to thank my supervisor and mentor Professor John Giapintzakis for his help, support and guidance for all these years.

I would like also to thank the members of committee, Dr. Valentin Cracium, Dr. Charis Theocharis, Dr. Claus Rebholz and Dr. Threodora Kyratsi for their helpful advices and suggestions.

I consider myself blessed working with scientists that through the years became friends. I am indebted to Dr. Zacharias Viskadourakis for helping me in the early steps in the laboratory. I thank Dr. Georgios Athanasopoulos for his help and guidance in and out of the lab. Dr. Cristian Mihailescu offered generously assistance and valuable suggestions. I would like also to thank Dr. Maria Pervolaraki. Dr. Chrysi Papageorgiou has been an excellent co – worker.

Finally, I am grateful to my parents Argyri and Christos, my sisters Aikaterini and Alexandra – Maria and especially to my lovely wife Helena and new born son Panagiotis.

April 20, 2015

Efthymios Ch. Svoukis

EFTHYMIOS CH. SVOUKIS

List of Publications

1. Mai V. H., Moradpour A., Senzier P., Pasquier C., Wang K., Rozenberg M., Giapintzakis J., Mihailescu C. N., Orfanidou C. M., **E. Svoukis**, E., Breza A,. Lioutas Ch. B., Franger S., Revcolevschi A., Maroutian T., Lecoeur P., Aubert P., Agnus G., Salot R., Albouy P. A., Weil R., Alamarguy D., March K., Jomard F., Chrétien P. and Schneegans O. Memristive and neuromorphic behavior in a Li_xCoO_2 nanobattery. *Sci. Rep.* **5,** (2015).

2. **Svoukis E.**, Athanasopoulos G. I., Moradpour A., Schneegans O., Revcolevschi A., and Giapintzakis J. Growth and transport properties of HT–Li_xCoO_2 thin films deposited by pulsed laser deposition. *Appl. Surf. Sci.* **258**, 9366–9369 (2012).

3. **Svoukis E.**, Athanasopoulos G. I., Altantzis Th., Lioutas Ch., Saint – Martin R, Revcolevschi A. and Giapintzakis J. Structural and thermal characterization of $La_5Ca_9Cu_{24}O_{41}$ thin films grown by pulsed laser deposition on (1 1 0) $SrTiO_3$ substrates. *Thin Solid Films* **520**, 4613–4616 (2012).

4. Moradpour A., Schneegans O., Franger S., Revcolevschi A., Salot R., Auban – Senzier P., Pasquier C., **Svoukis E**., Giapintzakis J., Dragos O., Ciomaga V. and Chrétien P. Resistive Switching Phenomena in Li_xCoO_2 Thin Films. *Adv. Mater.* **23**, 4141–4145 (2011).

5. Athanasopoulos G. I., Pervolaraki M., **Svoukis E.**, Androulakis J., Saint – Martin R, Revcolevschi A. and Giapintzakis J. Pulsed laser deposition and thermal characterization of Ni-doped $La_5Ca_9Cu_{24}O_{41}$ thin films. *Appl. Surf. Sci.* **257**, 5200–5203 (2011).

6. Athanasopoulos G. I., **Svoukis E.**, Pervolaraki M, Saint – Martin R, Revcolevschi A. and Giapintzakis J. Thermal conductivity of Ni, Co, and Fe-doped $La_5Ca_9Cu_{24}O_{41}$ thin films measured by the 3ω method. *Thin Solid Films* **518**, 4684–4687 (2010).

7. Athanasopoulos G. I., **Svoukis E.**, Viskadourakis Z., and Giapintzakis J. *"Thermal conductivity measurements of anisotropic samples using the 3-omega method".*

EFTHYMIOS CH. SVOUKIS

Thermal Conductivity 30 / Thermal Expansion 18, Eds. Daniela S. Gaal and Peter S. Gaal, ISBN: 978-1-60595-015-0, pp. 823-833.A, (2010)

EFTHYMIOS CH. SVOUKIS

List of Conference Participations

1. European Materials Research Society Spring Meeting, Strasbourg, France, May 28 – 30, 2013.
2. Nature Conference Frontiers in Electronic Materials, Aachen, Germany, June 17 – 20, 2012.
3. 11th International Conference on Nanosciences & Nanotechnologies, Thessaloniki, Greece, 2012.
4. European Materials Research Society Spring Meeting, Strasbourg, France, May 14-18, 2012.
5. XXVII Panhellenic Conference on Solid State Physics and Material Science, Lemesos, Cyprus, 2011.
6. European Materials Research Society Spring Meeting, Nice, France, May 9 – 13, 2011.
7. XXVI Panhellenic Conference on Solid State Physics and Material Science, Ioannina, Greece, 2010.
8. NOVMAG Workshop, Kolymbari, Greece, September 24 – 28, 2010.
9. European Materials Research Society Spring Meeting, Strasbourg, France, June 7 – 11, 2010.
10. 30th International Thermal Conductivity Conference and the 18th International Thermal Expansion, Pittsburgh, USA, August 29 – September 2, 2009.
11. European Materials Research Society Spring Meeting, Strasbourg, France, June 8 – 1 2, 2009.

Funding

This work was co – funded by:

- The European Regional Development Fund and the Republic of Cyprus through the Research Promotion Foundation (Project PENEK/0308/09).
- UCY Large Scale Research Program, Project Thermoelectric Nanosensor Networks.
- FP6 – IST, Project NOVMAG, Project reference: 032980.

EFTHYMIOS CH. SVOUKIS

Oh, wonder!

How many goodly creatures are down there!

How beauteous making is!

O brave new world…

Paraphrase: The Tempest Act 5, scene 1, 181–184

EFTHYMIOS CH. SVOUKIS

List of Contents

Validation Page i

Declaration ii

Copyright Statement ii

Abstract iii

Περίληψη iv

Acknowledgements v

List of Publications vi

List of Conference Participations viii

Funding viii

List of Contents x

List of Figures xvi

List of Tables xxvi

Abbreviations xxvii

1 Introduction **1**

1.1 Motivation: Technological & Scientific significance 1

1.2 Present work 2

1.3 Thesis structure 3

1.4 Novel results & main achievements 4

2 Physical Vapour Deposition Techniques **7**

2.1 Thermal evaporation and sputtering 7

2.2 Pulsed laser deposition 9

EFTHYMIOS CH. SVOUKIS

2.2.1 Introduction 9
2.2.2 Excimer laser technology 10
2.2.3 PLD a non – equilibrium process 11
2.2.4 Basic principles of PLD 12
2.2.5 PLD setup 12
2.2.6 Deposition parameters 15
2.2.7 Stages of PLD 18
2.2.7.1 Light interactions with the ceramic target 19
2.2.7.2 One – dimensional plume expansion 20
2.2.7.3 Three – dimension plume expansion 21
2.2.7.4 Thermalization of the plume 22
2.2.7.5 Thin film growth on the substrate 25
2.2.8 Advantages & disadvantages of PLD 26
2.3 Summary 27
3 Characterization Techniques 28
3.1 Structural characterization 28
3.1.1 X – ray diffraction of powders and thin films 28
3.1.1.1 Two circle diffraction, Bragg Brentano geometry 29
3.1.1.2 Four circle diffraction 30
3.1.1.3 X – ray reflectivity 32
3.1.2 Transmission electron microscopy 33
3.1.3 Reflection high energy electron diffraction 34
3.1.3.1 Geometry and basic principles 34
3.1.3.2 Kinematic theory approach 35
3.1.3.3 Utility of RHEED on growth characterization 36
3.2 Transport characterization 37
3.2.1 Thermal characterization: The 3ω method 37

EFTHYMIOS CH. SVOUKIS

3.2.1.1 Basics of the 3ω method 37
3.2.1.2 Instrumentation 38
3.2.1.3 Extension of the 3ω method for thin film characterization 39
3.2.2 Electrical characterization 41
3.2.2.1 Classical four – probe method 41
3.3 Morphology characterization 42
3.3.1 Atomic force microscopy 42
3.3.2 Scanning electron microscopy 43
4 Thin Film Growth 44
4.1 Epitaxy in thin films 44
4.2 Lattice parameter mismatching 44
4.3 Growth basic thermodynamics 45
4.3.1 Hetero – epitaxy 45
4.3.2 Growth modes 46
4.4 Microstructure 48
4.4.1 Strain – defects 48
4.4.2 Zone model of thin films 49
4.4.3 Columnar structure 50
5 Lanthanum Calcium Copper Oxide –$La_5Ca_9Cu_{24}O_{41}$ 51
5.1 Introduction 51
5.2 Crystal structure of LCCO 52
5.3 Thermal conductivity of LCCO 53
5.4 Thermal management 54
5.5 Synthesis of bulk LCCO and PLD target preparation 55
5.6 Towards c – axis LCCO Growth 56
5.7 Growth on $SrLaAlO_4$ (100) 56

5.8 Growth on $Gd_3Ga_5O_{12}$ (100) 61
5.9 Growth on α – SiO_2 and Al_2O_3 (0001) 64
5.10 Growth on LCCO (001) Single Crystal 65
5.11 Growth on STO 66
5.11.1 Grown on $SrTiO_3$ (001) 66
5.11.1.1 Termination control 66
5.11.1.2 Thin film growth and characterization 68
5.11.2 $SrTiO_3$ (110) 70
5.11.2.1 Preliminary experiments on STO (110) 70
5.11.2.2 Single crystal LCCO thin film 77
5.12 Conclusions 80
6 Lithium Cobalt Oxide – $LiCoO_2$ 81
6.1 Introduction 81
6.2 Data storage challenges 82
6.3 $LiCoO_2$ structure and properties 83
6.3.1 Structure of HT – LCO 83
6.3.2 Lithium intercalation / de – intercalation 84
6.3.3 Electronic transport properties of LxCO 85
6.4 Synthesis of LxCO and target preparation 86
6.5 Low pressure growth 86
6.6 Growth on c – cut Sapphire 87
6.6.1 Substrate preparation 88
6.6.2 Thin film deposition 88
6.6.3 X – ray diffraction characterization 89
6.6.3.1 Out – of – plane configuration 89
6.6.3.2 In – plane configuration 91
6.6.4 TEM growth investigation 92

EFTHYMIOS CH. SVOUKIS

6.6.5 Surface morphology investigation 94
6.6.6 CP – AFM surface resistive maps 96
6.6.7 CP – AFM surface resistance modifications 98
6.7 Growth on n++ Si (111) 100
6.7.1 Substrate preparation 100
6.7.2 Thin film deposition 100
6.7.3 Out of plane X – ray diffraction characterization 101
6.7.4 CP – AFM surface resistance mapping and modifications 102
6.7.5 TEM growth investigation on sample grown at 400°C 107
6.8 Mechanism of surface modification in LxCO thin films 108
6.9 Conclusions 109
7 Vanadium Dioxide – VO_2 110
7.1 Introduction 110
7.2 VO_2 structure and properties 111
7.2.1 Crystal structures of VO_2 112
7.2.2 Electronic properties of VO_2 phases 113
7.2.3 Phase transition mechanism 114
7.3 Selection of TiO_2 (001) for a substrate 114
7.3.1 TiO_2 (001) termination control 115
7.3.2 Growth of VO_2 thin films 117
7.3.1 RHEED in situ investigation 118
7.4 X – ray diffraction characterization 119
7.4.1 Out – of – plane configuration 119
7.4.2 In – plane configuration 123
7.4.3 XRR 125
7.5 Surface morphology investigation and elemental analysis 126
7.6 TEM growth investigation 127

EFTHYMIOS CH. SVOUKIS

7.7 Electrical characterization 129

7.8 Conclusions 132

8 Conclusions & Main Results 133

8.1 LCCO 133

8.2 LCO 134

8.3 VO_2 135

9 Appendix – A 136

10 Appendix – B 140

References 142

EFTHYMIOS CH. SVOUKIS

List of Figures

Figure 1.1: *Schematic diagram of the main core of the current thesis*......................................4

Figure 2.1: *History of maximum laser pulse intensity throughout the past 40 years* [38]. 9

Figure 2.2: *Simplified sequence of reactions evolved in the production a rare earth – halide (RH)* excimer and lasing.* 11

Figure 2.3: *Photo image of the PLD configuration used in the LAMP – lab of UCY. The laser beam enters in the deposition chamber through a periscopic path. Insert shows the substantial intensity variation of light across a cross section of the beam for a KrF excimer laser* [53]*. To achieve homogenization of the beam a mask is used.* 13

Figure 2.4: *Schematic diagram of the PLD deposition chamber configuration including the RHEED system located in the LAMP – lab of UCY.* 14

Figure 2.5: *Stages involved in the PLD process. Stage 1: Light interactions with the ceramic target, Stage 2: One – Dimension plume expansion, Stage 3: Three – Dimension plume expansion, Stage 4: Thermalization of the plume and Stage 5: Thin film growth.* 19

Figure 2.6: *Photo of the anisotropic plume expansion in HV. The laser Φ deposited on the LCO target was set to 1.3 Jcm^{-2}, with a laser spot of 10mm^2.* 21

Figure 2.7: *Photo of the plume expansion in the presence of a background gas. The propagating front between ablation plume and background gas is observed. The laser Φ deposited on the LCCO target was set to 2 J cm^{-2}, with a laser spot of 11mm^2.* 22

Figure 2.8: *ICDD emission images of neutral Mn – plume species as obtained by ablating $LiMn_2O_4$ in (a) HV and (b) at 0.2 mbar of oxygen* [75]*. The presence of oxygen as background gas, changes the shape, speed and angular distribution of the plume.* 24

Figure 2.9: *Possible processes that could take place during thin film growth on a substrate. Multi – cation thin films are grown stoichiometricaly only if atoms of all desired components are available in the precise ratio at specific positions.* 25

Figure 3.1: *Schematic of the Bragg's law.* 29

Figure 3.2: *The two – dimensional Bragg Brentano geometry used in this study. The circle centered on the sample represents the goniometer. The source has a fixed position and*

the sample and detector are rotated by θ and 2θ, respectively. A Ni filter is also included for the reduction of $K_β$ radiation. 30

Figure 3.3: *Schematic diagram of the four – circle geometry corresponding to the Rigaku Smartlab dirfractometer. All possible rotation axes of the sample and the detector, or the rotation axes of the goniometer, (2θ, ω, χ and φ) are clearly defined.* 31

Figure 3.4: *A schematic diagram of the RHEED geometry. $θ_{inc.}$ and $θ_{diff.}$ are the incident and diffracted angles and φ the azimuthal angle. On the phosphor screen diffracted streaks appear.* 34

Figure 3.5: *a) Interaction of the Ewald sphere, from the incident electron beam, with the reciprocal space rods. Reflections occur in directions defined by the interactions of the Ewald sphere with the reciprocal lattice rods. In the case of a perfect surface, reflections will appear as spots on the phosphor screen.b) Section of the Ewald sphere interaction with the reciprocal space rods (top view).* 35

Figure 3.6: *RHEED pattern from a commercial $SrTiO_3$ surface. Kikuchi (marked with arrows) lines are evidence of a flat, crystalline, free of defects surface. The 0th Laue circle is marked with a dotted circle and with asterisk is marked the direct beam.* 36

Figure 3.7: *Diagram of the mechanism for the low amplitude 3ω signal generation, due to Joule heating over the metal heater.* 38

Figure 3.8: a) *Circuit layout diagram for measuring the 3ω component of the voltage across the metal strip deposited on the sample. The ac current is provided by the Keithley 6221 current source and the 3ω signal is measured with the Stanford SR830 lock – in amplifier. Both instruments are controlled by a PC using LabVIEW software. b) Real image of a fabricated heater on a commercial substrate surface.* 39

Figure 3.9: *Schematic diagram of the heat flow from a metal strip with half – width b through a low thermal conductivity thin film of deposited material on a thermal anisotropic substrate.* 41

Figure 3.10: *Experimental setup for the electronic characterization of thin films by using the four – probe method. A photo of a sample mounted on the sample – holder (insert).* 42

Figure 3.11: *A schematic diagram of a CP – AFM system. By using a conductive tip, the electrical properties and topography of thin films can be simultaneously investigated.* . 43

EFTHYMIOS CH. SVOUKIS

Figure 4.1: *Schematic diagram of possible growth modes due to lattice matching: a) Homo – epitaxy, b.i) tensile hetero – epitaxy followed by relaxation, b.ii) compressive hetero – epitaxy followed by relaxation and b.iii) domain hetero – epitaxy.* 45

Figure 4.2: *Diagram of the atomistic processes taking place in hetero – epitaxial growth. Three surface energies γ are involved in the film growth.* 46

Figure 4.3: *Four basic thin film growth modes a) Frank-van der Merwe; b) Volmer – Weber; c) Stranski – Krastanov; d) Step flow.* 48

Figure 5.1: *a) Crystal structure representation of LCCO, along the c – axis. The structure consists of alternating layers of CuO_2, Cu_2O_3 and in between containing a layer of La / Ca – ions. b) Top view of CuO_2 planes containing chains. c) Top view of Cu_2O_3 planes containing ladders.* 52

Figure 5.2: *Thermal conductivity as a function of temperature for a LCCO single crystal, from reference 14. The c – axis is parallel to the ladders and contributions to κ from phonon and magnons are present. The a – and b – axis are perpendicular to the ladders, with phononic only contribution to κ, and have comparable values of thermal conductivity.* .53

Figure 5.3: *A device with conventional isotropic heat removal (a). A prototype device with LCCO, where heat is conducted primarily along one direction (b).* 54

Figure 5.4: *Rietveld refinement using PowderCell of LCCO powder. All XRD peaks can be indexed according to the LCCO structure with R_{exp}=2.30. Insert: EDX pattern of the same powder.* 55

Figure 5.5: *The a – axis of LCCO has only 0.33% lattice mismatch with three lattice spacings of [100] SLAO. The b – axis has –0.19% mismatch with the [001] lattice parameter of SLAO. The position of oxygen atoms of LCCO and SLAO are different.* 57

Figure 5.6: *XRD patterns of LCCO thin films grown on SLAO at different deposition temperatures. Only a small temperature regime (700–800°C) exists where the LCCO thin films are crystalline, free of secondary phases and (0k0) oriented. With asterisks are marked additional peaks, appearing on the film grown at 850°C. Films grown below 650°C, showed no evidence of crystallinity.* 58

Figure 5.7: *Rocking curve of the (040) LCCO peak of a film grown at 750°C. The Gaussian Fit results in a FWHM of 1.26 deg.* 59

Figure 5.8: *Azimuthal scans of a LCCO thin film grown on SLAO (100). Low intensity peaks (marked with red arrows) appear between the main peaks of LCCO.* 60

EFTHYMIOS CH. SVOUKIS

Figure 5.9: *Thermal conductivity as a function of temperature for a LCCO thin film grown on SLAO (top) and for a SLAO substrate (bottom). At room temperature the cross – plane thermal conductivity of the LCCO thin films is ~70% that of a LCCO single crystal [135].* 61

Figure 5.10: *The GGO cubic garnet crystal structure.* 61

Figure 5.11: *XRD pattern of a LCCO film grown on GGO at 700°C. Only (0k0) reflections are present, evidence of a b – axis oriented thin film. All films grown on GGO (100) substrates within the temperature region 700–800°C showed similar XRD patterns.* 62

Figure 5.12: *RHEED pattern after the growth of LCCO on GGO at room temperature in a UHV environment. The incident electron beam is accelerated with 30kV. A spotty pattern appears along specific azimuthal angles, indicative of Stranski – Krastanov growth.* 63

Figure 5.13: *SEM image of a LCCO thin film grown on GGO at 750°C. At large field of view, the surface is free of agglomeration particles. Magnified image of a small area revealed sub – micron cracks, attributed to thermal expansion coefficient difference (insert).* 63

Figure 5.14: *XRD patterns of LCCO thin films grown at 700°C on "no lattice matching" substrates a – SiO_2 (top) and Al_2O_3 (0001) (bottom). Films in both cases are b – axis oriented due to thermodynamic reasons. Post deposition RHEED pattern is presented as insert for each thin film.* 64

Figure 5.15: *XRD prior and post homoepitaxial growth of LCCO on a plane LCCO (001) single crystal. The (00l) peaks intensity is enhanced after the thin film growth.* 65

Figure 5.16: *8μm x 8μm AFM image of an as – received STO (001) substrate. Terraces, but not well defined, and impurities are present on the surface of the substrate.* 66

Figure 5.17: *2μm x 2μm AFM images of STO (001) samples after annealing at 900°C for 1 hour in oxygen atmosphere. The difference in the width of the terraces is due to difference in vicinal angles. The substrates surface morphology of large and small vicinal angle samples are presented in a and b, respectively. A RHEED pattern of a STO (001) substrate prior annealing is presented in image c.* 67

Figure 5.18: *XRD pattern of a LCCO thin film grown on a chemically and thermally treated STO (001) substrate at 700°C. All peaks are related to the (0k0) peaks of LCCO. Insert of EDX spectrum, where peak positions are only related to the atoms of the substrate and the thin film.* 68

EFTHYMIOS CHASVOUKIS

Figure 5.19: *Diffraction pattern of a LCCO film grown on a STO (001) substrate at 700°C. a) The existence of lighter intensity spots around the intensive spots in a diffraction image, is evidence of crystallites with small deviation angles. b) Conventional TEM of the same sample. Zone II type growth is present within the film structure, with average column width of 16.3nm. The thickness of the film was estimated to be 149 ± 8 nm.* 69

Figure 5.20: *Cross – section high resolution TEM image of a LCCO film grown on a STO (001) substrate at 700°C. The columns appear to be free of defects. A FFT transform of the selected area is presented as an inset.* 70

Figure 5.21: *Conventional planar view TEM image of the top surface of a LCCO thin film grown on a STO (001) substrate at 700°C.* 70

Figure 5.22: *Schematic representation of the non reconstructed surface of STO (110).* 71

Figure 5.23: *XRD patterns of LCCO thin films grown on STO (110) substrates at different deposition temperatures. Only a small temperature regime (650–700°C) exists where the LCCO thin films are crystalline, free of secondary phases, and (0k0) oriented (with all the (0k0) peaks present).* 72

Figure 5.24: *Selected area electron diffraction pattern of a cross – section TEM sample demonstrating the overlap of the individual patterns of the substrate and the film.* 74

Figure 5.25: *a) High – Resolution TEM micrograph. b) Presence of a non – uniform extrinsic layer at early stages of growth.* 74

Figure 5.26: *A planar – view TEM demonstrating that the majority of the grains are oriented along a preferential orientation ($[100]_{LCCO}//[1\text{-}10]_{STO}$).* 75

Figure 5.27: *Thermal conductivity as a function of temperature of two LCCO thin films grown on STO (110) substrates with 1500 and 500 pulses and keeping all the other deposition conditions the same. Film thickness affects the measured thermal conductivity. At room temperature the thermal conductivity of the thicker film is ~73% of the one reported for LCCO single crystals* 76

Figure 5.28: *Thermal conductivity as a function of temperature of a rectangular shape LCCO pellet, following sintering at 950°C for 5 and 72hours. The pellet was synthesized by solid state reaction method and measured using the conventional steady – state method. Sintering time affects the value of the measured thermal conductivity but doesn't change the qualitative behavior of the thermal conductivity over temperature.* 77

EFTHYMIOS CH. SVOUKIS

Figure 5.29: *XRD patterns of thin films grown with different* Φ *above* $\Phi_{thres.}$. *The* $\Phi_{thres.}$, *necessary for stoichiometric transfer and growth of crystalline thin films, was experimentally found to be* $0.6 Jcm^{-2}$. ... 78

Figure 5.30: *Cross section HR – TEM image of a b – axis LCCO single – crystal thin film grown on STO (110).* ... 79

Figure 5.31: *Optical probing of heat spreading over the surface of a LCCO single – crystal thin film. A spot size of* $0.5\mu m^2$ *with heating power 250μW was used. A small anisotropic spread, comparable to LCCO single crystal, is evident.* ... 80

Figure 6.1: *Crystal structure representation of LCO for hexagonal lattice structure. Consists of alternating* CoO_2 *and* Li^+ *ions layers stacked along the c – axis.* ... 83

Figure 6.2: *Phase diagram and c – axis lattice parameter distortion, at room temperature for LxCO, based on literature reports* [165,167]. ... 84

Figure 6.3: *Variation of electronic and transport properties related to the x value within the LxCO structure.* ... 85

Figure 6.4: *XRD patterns of a LCO thin film grown at* 275^oC *in low pressure conditions, prior and post annealing at* 650^oC *for 5h in air. CP – AFM investigation of the same film after annealing (inset) revealed a granular highly resistive structure.* ... 87

Figure 6.5: $0.1\mu m^2$ *AFM image and RHEED pattern of the same c – cut sapphire sample after annealing at* 1200^oC *for 5h. in air. Terraces are present in both cases.* ... 88

Figure 6.6: *XRD patterns of LCO thin films deposited on annealed c – cut sapphire substrates in the temperature range from room temperature to* 800^oC. ... 89

Figure 6.7: *HR XRD of the (0003) peak of a LCO thin film grown at* 600^oC. *Layer fringes appear, evidence of epitaxial growth.* ... 90

Figure 6.8: *The c – axis lattice parameter of the LCO thin films grown on c – cut sapphire, as a function of their deposition temperature.* ... 91

Figure 6.9: *Azimuthal scans of a LCO thin film grown on c – cut sapphire at* 600^oC. *The in – plane epitaxy is verified from the symmetry of both the peaks of the substrate and the thin film.* ... 92

Figure 6.10: *Conventional TEM images (a – e), high resolution TEM images (g, i and j) and diffraction patterns (h and insets in: f, g, i and j) of LCO thin films grown on c – cut sapphire at various deposition temperatures 200, 300, 400, 600 and* 700^oC. ... 93

EFTHYMIOS CH. SVOUKIS

Figures 6.11: *AFM images (10 x 10 μm^2) of LCO thin films deposited on c – cut sapphire at various deposition temperatures. The scale is the same for all images.* 94

Figure 6.12: *The average surface roughness of LCO thin films on c – cut sapphire as a function of the deposition temperature. The roughness of the films can be reduced by performing growth at higher temperatures.* 95

Figure 6.13: *SEM images of a LxCO thin film deposited on c – cut sapphire at 600°C with a large field of view. The film is free of cracks, holes and particulates.* 95

Figure 6.14: *CP – AFM surface resistance maps (10 x 10 μm^2) of LCO thin films deposited on c – cut sapphires at various deposition temperatures. The resistance scale is the same for all images.* 96

Figure 6.15: *The average logarithm of the surface resistance of the LCO thin films on c – cut sapphire as a function of the deposition temperature. The deposition temperature affects the surface electric properties of the thin films.* 97

Figure 6.16: *Surface resistance modifications in LCO thin films grown on c – cut sapphire substrates at various deposition temperatures, by applying a +/– 6V bias. The resistance scale is the same for all images. The reading bias was +1V.* 98

Figure 6.17: *Average logarithm of the surface resistance of the LCO films on c – cut sapphire as a function of the deposition temperature prior and post bias applications.* 99

Figure 6.18: *Line scan on a surface – resistance modified LCO thin film. 2.5 orders of magnitude difference exist between the areas modified with low (–6V) and high (+6V) bias.* 99

Figure 6.19: *Hexagonal – like symmetry of Si in plane (111).* 100

Figure 6.20: *XRD patterns of LCO thin films deposited on etched n++ Si (111) substrates in the temperature range of 300 to 600°C.* 101

Figures 6.21: *CP – AFM images (10 x 10 μm^2) of LCO thin films deposited on n++ Si (111) at various deposition temperatures. Roughness and resistance were investigated on each sample simultaneously.* 103

Figure 6.22: *The average surface roughness of the LCO thin films on n++ Si (111) as a function of the deposition temperature. At deposition temperatures above 400°C, rough films are grown* 104

EFTHYMIOS CH. SVOUKIS

Figure 6.23: *Surface resistance modifications in the LCO thin films grown on n++Si (111) at various deposition temperatures, by applying a +/– 8V bias. On the left and right are shown the surface resistance modifications prior and post annealing at 550°C for 1h in air, respectively.* 105

Figure 6.24: *Average logarithm of the surface resistance of L_xCO films on n++ Si (111) as a function of the deposition temperature prior and post bias application.* 106

Figure 6.25: *Formation of conducting and insulating regions, using opposite probe voltage polarities in concentric squares. The experiment was performed on a post annealed LxCO sample grown at 400°C on n++Si (111), using positive (+4V) and negative (-4V) bias and reading bias of +1V.* 106

Figure 6.26: *Conventional TEM images and diffraction patters of LxCO thin films grown on n++ Si (111) at 400°C prior and post annealing, top and bottom respectively.* 107

Figure 6.27: *Schematic diagram of the mechanism of electrochemical reactions occuring within the condensation H_2O capillary meniscus nanocell at the tip / film contact.* 108

Figure 7.1: *The oxygen – vanadium phase diagram. Within the dashed rectangle, stable V_xO_{2x-1} phases are present* [181]. 111

Figure 7.2: *Crystallographic structures of main VO_2 phases. a) R phase above T_{SM} and b) M_1 below T_{SM}. In the M_1 phase there is a pairing and tilting of the vanadium atoms along the a – axis. M_1 has double the volume of the R phase.* 112

Figure 7.3: *a) The d_{II} and π^* states, top and bottom respectively. The schematic electronic band diagrams of VO_2 for R and M_1 phases close to the Fermi level are presented in b) and c) respectively.* 113

Figure 7.4: *16 μm^2 AFM image (a) and RHEED pattern (b) of an as – received TiO_2 (001) substrate at room temperature.* 116

Figure 7.5: *16 μm^2 AFM image and RHEED pattern of a chemically and thermally treated at 800°C TiO_2 (001) substrate are presented in a) and b) respectively. Reconstruction of TiO_2 (001) surface observed after annealing in UHV conditions at 800°C, is shown in the 0.06 μm^2 AFM image in c). Inset in c): a real image showing color change of the substrate. A line scan of the reconstructed surface is presented in d).* 117

Figure 7.6: *Schematic diagram of the deposition conditions (temperature and pressure) over a typical deposition.* 118

EFTHYMIOS CHISVOUKIS

Figure 7.7: *Specular spot intensity oscillations of a VO_2 thin film grown on TiO_2 (001), at 400^oC in 0.017mbar, which are evidence of a layer – by – layer growth. A RHEED pattern of the bare substrate prior deposition is presented as an inset.* 119

Figure 7.8: *$2\theta - \omega$ XRD patterns of VO_2 thin films produced in various deposition temperatures.* 120

Figure 7.9: *High resolution $2\theta - \omega$ patterns of VO_2 thin films in small step scans close to (002) peaks of TiO_2 substrate and VO_2 thin film.* 121

Figure 7.10: *The c – axis lattice parameter of the VO_2 thin films grown on TiO_2 (001), as a function of their deposition temperature.* 122

Figure 7.11: *a) Rocking curve on the (002) VO_2 peak for a thin film grown at 400^oC. b) FWHM of the rocking curve of VO_2 thin films as a function of their deposition temperature.* 123

Figure 7.12: *Azimuthal scan of a VO_2 thin films grown on TiO_2 at 200, 400 and 600^oC. Film and substrate azimuths are in the same direction, showing a possible cube – on – cube epitaxy.* 124

Figure 7.13: *3D images of the reciprocal space mapping for VO_2 thin film grown at 400^oC and 500^oC, in a) and b), respectively.* 124

Figure 7.14: *XRR measurements on thin films grown at 200, 300, 350 and 400^oC.* 125

Figure 7.15: *a) Simulation of XRR data. b) Thickness of films as a function of the deposition temperature for specified number of pulses.* 125

Figure 7.16: *AFM images ($10 \times 10\ \mu m^2$) of VO_2 thin films deposited on TiO_2 (001) substrate at various temperatures. The scale is the same for all images.* 126

Figure 7.17: *EDX analysis spectrum (a) and a secondary electron SEM image (b) are shown, for a sample grown at 400^oC.* 126

Figures 7.18: *TEM images, SAED patterns and HR TEM images of VO_2 thin films grown on TiO_2 at 280, 300 and 400^oC. The deposition temperature affects the type of growth. At 400^oC the film is epitaxially grown, whereas below 400^oC, a columnar growth has been observed.* 127

Figures 7.19: *TEM images, SAED patterns and HR TEM images of VO_2 films grown at 500 and 600^oC.* 128

EFTHYMIOS CH. SVOUKIS

Figures 7.20: *TEM image of a VO_2 thin film grown at 400°C. Elemental distribution maps of Ti, V and O for the same specimen. No interdiffusion and a sharp interface between substrate and thin film was detected.* 129

Figure 7.21: *Resistance of VO_2 thin films grown at various deposition temperatures upon heating and cooling. An SMT is present in all samples, below the reported value for a VO_2 single crystal.* 130

Figure 7.22: *Electrical resistivity of the VO_2 thin film grown at 400^oC. With red and blue are shown the heating and cooling cycles, respectively. The SMT close to T_{SM} is presented as an inset.* 131

Figure 7.23: *Derivative of the electrical resistivity of a VO_2 thin film grown at 400^oC. With red and blue are shown the heating and cooling cycles, respectively. The transition temperatures for both cycles was calculated based on the Gaussian model.* 132

Figure 9.1: *A magnon in a perfectly ordered antiferromagnetic ladder, created from a flip of a single spin. The excitation can move along the ladder in two possible directions.* 139

Figure 10.1: *Third harmonic voltage as a function of frequency for a range of temperatures for a LCCO(001) single crystal. Inset: the sample placed on the sample holder.* 140

Figure 10.2: *Thermal conductivity of the LCCO single crystal as a function of temperature and comparison with typical literature values for micron – size crystals.* 141

EFTHYMIOS CH. SVOUKIS

List of Tables

Table 2.1: *Adjustable parameters in the conventional PLD and typical values used for the growth of oxide thin films.* 15

Table 2.2: *Typical oxide substrates, used in PLD. For each substrate, structure and transport properties are presented.* 17

Table 3.1: *Measurement techniques applicable in a four – circle diffractometer. Different crystallographic information of a thin film can be obtained by scanning a specified axis.* 32

Table 4.1: *Zone structures and typical characteristics of the produced thin films.* 50

Table 5.1: *Theoretical calculations for identifying suitable substrates for c – axis LCCO growth. The ratios of a and b LCCO lattice parameters over the lattice parameters of specifically oriented substrates at room temperature.* 56

Table 5.2: *Results of EDX analysis for the LCCO target and the three LCCO thin films with different number of pulses. Nearly perfect stoichiometric transfer is achieved, despite the complexity of the structure.* 73

Table 7.1: V_xO_{2x-1} *chemically stable phases exhibiting a SMT accompanied with the transition temperatures* [182,183]. 111

Table 7.2: *Lattice constant and mismatches of R structures of* VO_2 *and* TiO_2 *at room temperature* [184,185,187]. 115

EFTHYMIOS CH. SVOUKIS

Abbreviations

AFM	Atomic Force Microscopy
CP	Conductive Probe
D_R	Deposition Rate
$d_{T\text{-}S}$	Distance Target – Substrate
EDX	Energy Dispersive X – ray Spectrometer
HV	High Vacuum
HSTs	Heterostructures
IC	Integrated Circuit
ICDD	Intensified Charged Couple Device
LAMP-Lab	Laser Assisted Materials Processing Lab
LCCO	$La_5Ca_9Cu_{24}O_{41}$
LCO	$LiCoO_2$
LxCO	Li_xCoO_2
MBE	Molecular Beam Epitaxy
MME	Mechanical and Manufacturing Engineering
NOVMAG	NOVel MAGnetic – mode heat transport for thermal management in microelectronics
PLD	Pulsed Laser Deposition
PVD	Physical Vapour Deposition
RHEED	Reflection High – Energy Electron Diffraction
RR	Repetition Rate
TEM	Transmission Electron Microscopy
SEM	Scanning Electron Microscopy
SMT	Semiconductor Metal Transition
T_{SM}	Transition Temperature from Semiconductor to Metal
UHV	Ultra High Vacuum
UCY	University of Cyprus
UV	Ultra Violet
YBCO	$YBa_2Cu_3O_7$
κ	Thermal Conductivity
λ	Wavelength
τ	Pulse duration
Φ_e	Evaporation rate
Φ	Fluence – Energy density per area

EFTHYMIOS CH. SVOUKIS

Introduction

1.1 Motivation: Technological & Scientific significance

The need for new "*exotic*" materials to be used in the state – of – the – art technology is a strong request of the electronic industry, due to miniaturization of the circuits and the demand of higher speed computation devices [1].

Transition metal oxides have attracted great interest over the last decades, due to the rich spectrum of physical properties that they exhibit such as antiferro / ferro – magnetism [2,3], gigantic magnetoresistance [4], superconductivity [5] *etc*. Efforts have are made by the scientific community not only to understand the dependence of the properties on the preparation of the materials, but also upon their incorporation in working devices [6].

Physical properties (electrical, thermal, magnetic, optical *etc.*) of thin films are usually different from those of the bulk [7]. Understanding the relation between the physicochemical properties and the growth method of the thin films is crucial for optimization of these properties. Epitaxial thin films have attracted a lot of attention due to their superiority in their properties, compared to the polycrystalline ones.

Furthermore, at the interface of the thin films new "*tailored*" materials may appear with completely different properties from the "*parent*" thin films [8,9]. Only within the last 20 years it has been realized that the growth of thin films or heterostructures (HSTs) from strongly correlated oxides could possibly be more interesting than solely exploiting their bulk properties [10,11].

The major physical vapour deposition (PVD) techniques for the epitaxial growth of thin films and metastable HSTs are atomic layer deposition, sputtering, molecular beam epitaxy (MBE) and pulsed laser deposition (PLD) [12,13,14,15]. PLD technique has been improved in the last years in such a way that even complex structures, such as layered (*e.g.* perovskite structure) and artificially layered oxides can be fabricated [16,17]. The control of the

EFTHYMIOS CH. SVOUKIS

oxidation during growth resulting in the formation of stable phases can only be controlled via oxygen gas inside the deposition chamber.

The ability of using an *in situ* monitoring tool such as high – pressure reflection high energy electron diffraction (RHEED) during PLD growth for the determination of growth type is a key factor in the optimization of the growth conditions [18,19].

Defect – free thin films and HSTs can be obtained not only by optimization of the deposition parameters. Layer – by – layer growth requires a smooth, atomically flat and clean substrate. The termination layer(s) of the substrate can influence the properties of the thin films. Kawasaki *et al*. is the first one who proposed a two – step surface chemical treatment for $SrTiO_3$ (100), resulting in single TiO_2 termination with atomic steps [20]. Therefore, not only a good lattice matching is essential, but also a good initial surface of the substrate [21].

1.2 Present work

The focus of the study is on the growth and characterization of thin films of three different oxides: $La_5Ca_9Cu_{24}O_{41}$ (LCCO), $LiCoO_2$ (LCO) and VO_2. Each one of these materials has unique transport properties with a possible application in the IC industry. Crystalline highly oriented and epitaxial thin films of all the above oxides have been produced using the PLD method. Structural, morphological and transport characteristics of the produced films have been examined with respect to deposition conditions.

The work conducted on LCCO was externally financed from the European Commission under the 6th Framework Project within the "*Novel magnetic-mode heat transport for thermal management in microelectronics"* (NOVMAG) project [22]. LCCO exhibits a new highly efficient magnetic mode of thermal conduction. This magnetic mode of conduction could be used for thermal management in ICs. When compared to conventional materials with high thermal conductivity LCCO offers significant advantages: a) it is electrically insulating, b) heat is conducted primarily along one crystal axis and c) heat is carried by localised spins thus potentially allowing for tunable heat conductivity at room temperature by manipulation of the spins with magnetic fields or light. Primary objective of the thesis was the growth of high quality LCCO thin films.

Work performed on LCO was part of a collaboration with research groups started through the collaboration of the NOVMAG project and was driven by academic interest.

EFTHYMIOS CH. SVOUKIS

After restrictive switching phenomena were reported in the $NaCoO_2$ compound an investigation similar behaviour in LCO thin films was undertaken. LCO has widely been used as a cathode material, in lithium ion rechargeable batteries, and is more stable than $NaCoO_2$. Growth of epitaxial LCO thin films was important for possible further exploitation in the IC industry. LCO, compared to other materials proposed for scanning probe mediated approaches in nanoscale patterning, is highly stable as an oxide compound, exhibiting reversible electrochemical surface modifications.

VO_2 is a "*smart material*" that exhibits a first – order structural / electronic transition very close to room temperature. During the transition, VO_2 changes from a high – temperature semiconductor rutile phase to a low – temperature insulating monoclinic phase. The nature this transition has investigated for more than three decades, however, it is not resolved. Recent *state – of – the – art* experiments began revealing the hidden aspects of this issue. In 2009, $(TiO_2)_n/(VO_2)_m$ multilayer nanostructures were theoretically investigated and the appearance of quantum phenomena similar to those observed in graphene were predicted. This could open a new world of opportunities for spintronic technology. Exotic phenomena, theoretically predicted in nanostructures require a sharp interface between the VO_2 film and the substrate. Additionally, a high quality single crystal thin films are also necessary. The program "*Heterostructures*", funded by Research Promotion Foundation (ΠΕΝΕΚ / 609 / 65), had as an initial goal the growth and characterization of high quality VO_2 thin films as a "*precursor*" of the aforementioned HSTs.

1.3 Thesis structure

The thesis is subdivided in 8 chapters. It is written in a progression way and each chapter can be seen as unique and important pillar for the fulfilment of the work. Figure 1.1 is a schematic representation of the progression path used for chapters 5, 6 and 7.

Chapter 2: Physical deposition techniques used in the current study are presented. The full aspects of the PLD method are presented.

Chapter 3: Characterization techniques used through the study are presented. Structural (XRD, RHEED and TEM), transport (3ω and standard four – probe method) and morphological (AFM and SEM) are presented.

EFTHYMIOS CH. SVOUKIS

Chapter 4: Aspects of thin film growth are described. This theoretical background was used as a map for optimization of the thin films growth.

Chapters 5 - 7: Results and discussion for LCCO, LCO and VO_2 thin films are presented. These chapters are the main core of the thesis.

Chapter 8: General conclusions of the current work and ideas for future investigation are presented.

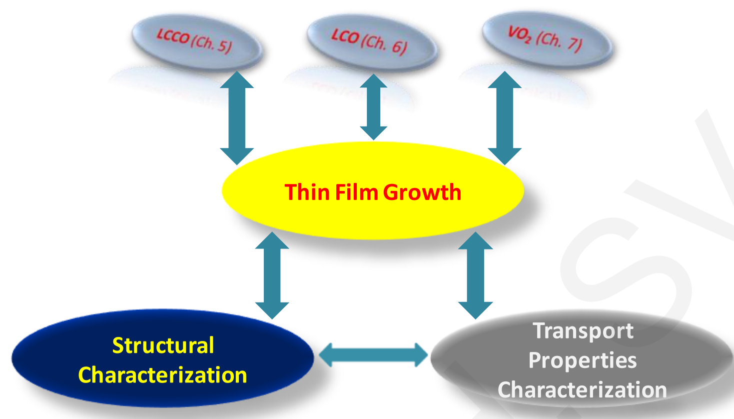

Figure 1.1: *Schematic diagram of the main core of the current thesis.*

1.4 Novel results & main achievements

This dissertation presents a study of the growth and characterization of three different correlated oxides: LCCO, LCO and VO_2.

In the case of LCCO the goal was the stoichiometric transfer of the complex structure to thin films for exploitation of a new highly efficient magnetic mode of thermal conduction. This magnetic mode of conduction could be used for thermal management in ICs.

LCO has been used widely in the past as a cathode material in lithium ion rechargeable batteries. In this study, this material was investigated for resistive switching phenomena for possible further exploitation in the IC industry. LCO, compared to other materials proposed for scanning probe mediated approaches in nanoscale patterning, is highly stable as an oxide compound, exhibiting reversible electrochemical surface modifications. Growth of epitaxial LCO thin films is important for usage in data storage applications.

Epitaxial growth of VO_2 thin films is important for the investigation of the first order semiconductor – metal transition and also as a first step for the experimental investigation of

EFTHYMIOS CHASVOUKIS

TiO_2 / VO_2 HSTs with sharp interface, for which theoretically predicted quantum phenomena similar to those observed in graphene have been proposed.

The originality of the work has been described in the previous paragraphs and below are given the main novel results and main achievements:

- Stoichiometric growth of LCCO thin films with preferential out – of – plane orientation on $SrLaAlO_4$ (100), $Gd_3Ga_5O_{12}$ (100), Al_2O_3 (0001) and $SrTiO_3$ (100) substrates has been achieved. For each type of substrate the optimum growth conditions have been identified.
- The cross - plane thermal conductivity of LCCO thin films grown on $SrLaAlO_4$ (100), $Gd_3Ga_5O_{12}$ (100), Al_2O_3 (0001) and $SrTiO_3$ (100) has been measured over a wide range of temperatures.
- *c* – axis oriented LCCO thin films have been successfully fabricated by homo-epitaxial growth on LCCO (001) single crystals.
- *b* – axis oriented single–crystal LCCO thin films have been successfully fabricated by hetero – epitaxial growth on $SrTiO_3$ (110) single crystals.
- Anisotropic heat conduction on a *b* – axis oriented single – crystal LCCO thin film has been observed for the first time.
- LCO has been found to exhibit reversible surface resistance modifications and is proposed to be suitable for data storage applications.
- High quality *c* – axis oriented LCO thin films have been grown successfully on Al_2O_3 (0001) substrates.
- *c* – axis oriented LCO thin films have been grown successfully on Si (111) substrates.
- A mechanism for the processes involved in the surface resistance modification of LCO films has been suggested.
- VO_2 thin films have been grown epitaxially on TiO_2 (001) substrates.
- The semiconductor-metal transition temperature of VO_2 thin films has been investigated as a function of deposition temperature.
- The diffusion phenomena involved in the early stages of VO_2 thin films growth have been studied and the optimum deposition temperature for the growth of VO_2 thin films free of diffusion phenomena has been identified.

EFTHYMIOS CH. SVOUKIS

- Incorporation of the 3ω method in a commercial physical property measurement system for measurement of the thermal conductivity of bulk samples and thin films has been achieved.
- Incorporation of the electrical transport methods, 4 – probe and Van der Pauw, in a commercial physical property measurement system for measurement of the electrical resistivity and Hall resistivity of bulk samples and thin films has been achieved.

EFTHYMIOS CH. SVOUKIS

Physical Vapour Deposition Techniques

Last decade, thin films were incorporated in daily devices, inducing new possibilities. Thin film deposition techniques used in the electronic industry include thermal evaporation, sputtering and MBE. PLD has been mainly used in academia but recently efforts are made to also be used in industry. All PVD techniques have objective the controllable transfer of atoms to a substrate and the formation of a thin film Understanding the theoretical background of each method, and stages – parameters involved can be further used for the production of high quality thin films.

2.1 Thermal evaporation and sputtering

Thermal evaporation and sputtering are the two most well – known techniques for the growth of thin films, widely used in the IC industry. Both can be described as PVD techniques. Experimentally both techniques appeared in the 19th century [23].

In thermal evaporation atoms are removed from the source by thermal means, where in sputtering they are dislodged from a solid target via bombardment by gaseous ions [24]. Both of them take place in high vacuum (HV) environment [25], with typical deposition rates, $D_R = 0.1 - 1\,\mathring{A}/\sec$ [26].

During thermal evaporation, atoms evaporate from the material that has been transformed to liquid after heating up. The evaporation rate (Φ_e) at a specific temperature reaches a maximum value that can expressed as:

$$\Phi_e = \frac{\alpha_e N_A \left(P_e - P_h\right)}{\sqrt{2\pi MRT}}, \qquad (2.1)$$

EFTHYMIOS CH. SVOUKIS

where α_e is the coefficient of evaporation, P_e the equilibrium pressure, P_h the hydrostatic pressure, M the molecular weight, R the gas constant and T the absolute temperature. Typical value for the evaporation rate is $\Phi_e \approx 1.3\times10^{17}\dfrac{\text{atoms}}{\text{cm}^2\,\text{sec}}$, with low kinetic energy for the evaporated atoms, $E\approx0.1eV$ [27].

Despite the simplicity of thermal evaporation, it cannot be used for the growth of multi – cation compounds, because individual cations have different evaporation properties. Consequently, the stoichiometry of the thin film will be different from a single initial material [28].

Thin film uniformity is desirable and necessary for microelectronic application. Kinetic theory predicts, that the angular distribution of the evaporated mass over area is cos(φ) – dependent. Careful experimental measurements showed that angular distribution is governed by:

$$\frac{d\bar{M}_s}{dA_s} \sim \cos^n(\varphi), \tag{2.2}$$

where $d\bar{M}_s$ small mass on the substrate, dA_s a small region on the substrate, φ the angle between the normal of the surface source and the substrate and n a parameter that describes the directionality of the vapour. When n is high the evaporation flux has high directionality [27].

In a typical sputtering setup, the material from which the thin film is grown is connected to a negative bias of a DC or RF power source [29]. The substrate is grounded opposite to the cathode. Typical pressures of 1–1000*mtorr* of Ar atmosphere produces positive Ar^+ ions. These ions eject neutral atoms from material due to momentum transfer. Furthermore, due to ion – matter interaction, radiation (X – rays, photons) and other particles (secondary and Auger electrons, negative ions *etc.*) are also emitted from the material [30].

The preparation of targets for various materials is made by thermo – mechanical pressing. Targets used in the sputtering technique have purities of >99.99% and densities lower than those of the theoretical values. This results on the production of particulates, release of trapped gasses or growth of inferior quality thin films. Typical value for the evaporation rate is $\Phi_e \approx 3\times10^{16}\dfrac{atoms}{cm^2\,\text{sec}}$ with low kinetic energy for the evaporated atoms, $E\approx2\text{–}30eV$ [27].

EFTHYMIOS CH. SVOUKIS

2.2 Pulsed laser deposition

2.2.1 Introduction

Following the production of the first functionalized laser (ruby, λ= 694.3*nm*) by T.H. Maiman [31], and the early ablation experiments performed by Smith and Turner [32], laser research has produced a variety of improved and specialized laser types, optimized for different performance goals, including: maximum pulse energy, minimum cost, *etc*. A brief history is presented in Fig. 2.1. Impressive amount of theoretical work accompanied by experimental work has been done in the last decades to understand laser – matter interactions from solid surfaces [33,34].

PLD is a PVD technique that has been popular within the scientific community [35]. The popularity of the technique compared to other PVD is based on its versatility, flexibility and applicability to almost *any* material [36]. In the late ’80*s*, it was found to be a suitable method for the successful growth of high temperature superconductor thin films such as $YBa_2Cu_3O_7$ (YBCO) [37]. YBCO is as a multi – cation oxide material in which individual cations have different evaporation properties and the superconductive properties of the produced thin films are highly affected by the stoichiometric transfer!

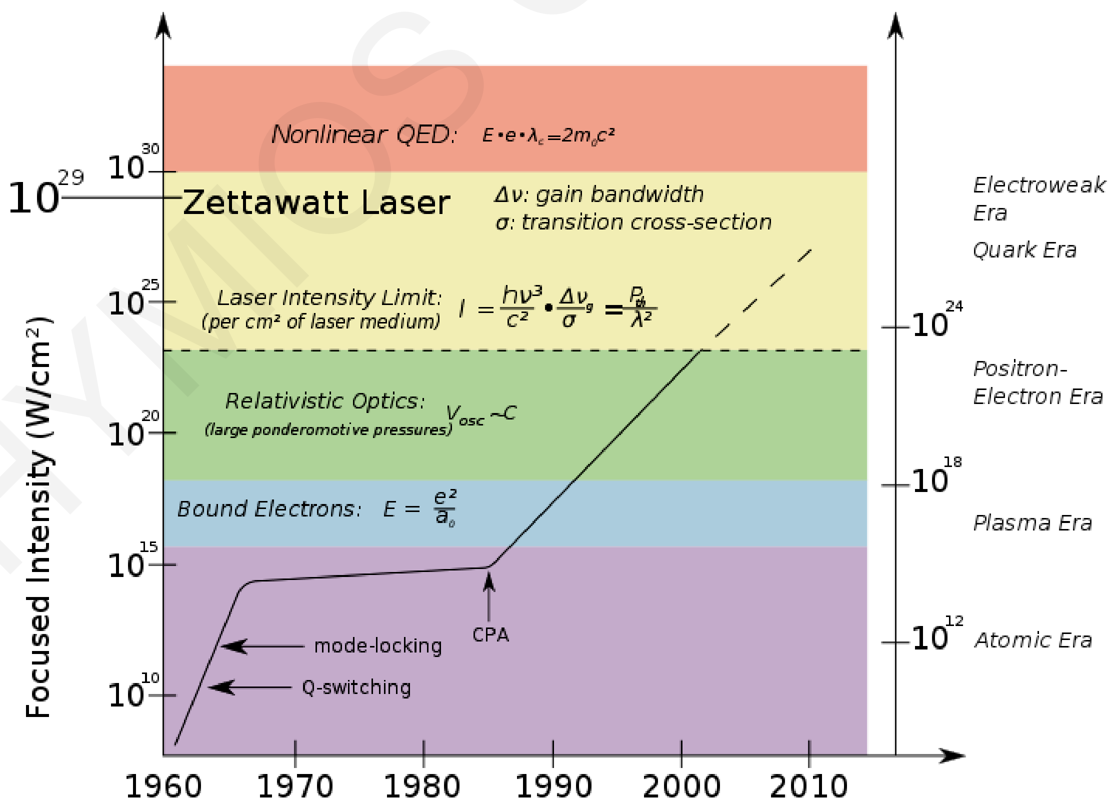

Figure 2.1: *History of maximum laser pulse intensity throughout the past 40 years [38].*

EFTHYMIOS CH. SVOUKIS

Since then, PLD has been established as an appropriate technique for the growth of metals, nitrides, carbides, nanowires, artificial HTSs, polymers and carbon – based composites [39]. PLD has evolved from an academic curiosity, to a deposition technique for scientific research [40].

2.2.2 Excimer laser technology

Excimer lasers are among the most powerful in the ultra – violet (UV) region of the electromagnetic spectrum. Commercial available systems can generate laser radiation wavelength (λ) in the range 126 – 600*nm*, depending on the active lasing medium. Among the commonly used excimers are krypton fluoride (KrF^*, λ=248*nm*)[1], argon fluoride (ArF, λ=193*nm*) xenon chloride (XeCl, λ=308*nm*) and argon (Ar_2, λ=126*nm*) lasers [41].

Rare – gas halide excited complexes are formed from combination of rare gasses (Kr, Ar, *etc.*) and halides (F, Cl, *etc.*). Production of **exci**ted di**mers** (excimers), molecules in the excited state via electrical discharge, is based on complex reaction processes. A simplified sequence for the production of a rare earth (*R*) – halide (*H*) excimer (RH^*) and production of a laser beam (lasing) is presented schematically in Fig. 2.2 [42].

Two reaction branches dominate the formation of the excimer, the neutral and the ion branch that take place in the n*s* time scale region. In the neutral branch, excited state *R* – atoms react with the *H* – molecules in the so called "*harpooning reactions*" [43]. Ion pair recombination of positive *R* – atoms and negative *H* – atoms take place in the presence of a buffer gas (Ne, He, *etc.*) in the ion branch. The excimer molecule RH^* is unstable and decays to *R* and *H* that form a covalent ground state through an emission of a photon. Components *R* and *H* are available for a new excitation cycle [44].

[1] This kind of excimer laser was used in the current PhD work.

EFTHYMIOS CH. SVOUKIS

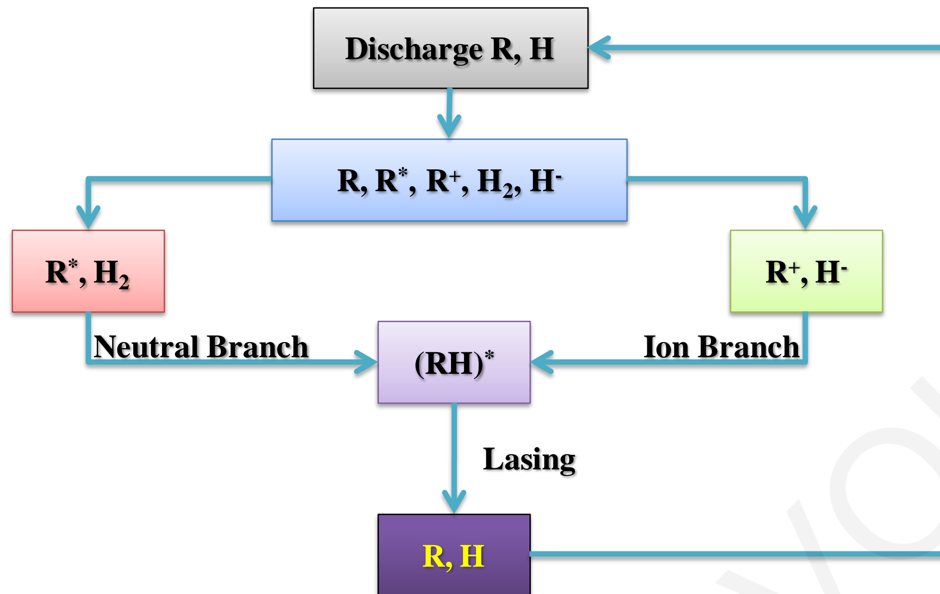

Figure 2.2: *Simplified sequence of reactions evolved in the production a rare earth – halide $(RH)^*$ excimer and lasing.*

2.2.3 PLD a non – equilibrium process

Within the first stages of the PLD process electromagnetic radiation (photons), excites electrons in the structure of the investigated material, via absorption. High energy laser intensity[2] vaporizes the surface layers of the material, within a finite volume, resulting to a luminous plasma plume enclosing kinetic and thermal energy. Particles in the plasma (ions, electrons, *etc.*) have temperatures of the order of several thousand Kelvins with a high degree of ionization while the deposition chamber remains at almost room temperature during the entire operation [40].

An advantage of PLD due to the complex processes involved is the possible usage of the technique for the stabilization of *new* or *no* thermodynamically stable structures. The non – equilibrium formation of the plasma, allows several degrees of freedom for the growth of the film (temperature, pressure, *etc.*). Optimization of the process via optimization of the deposition conditions can improve the quality of the films.

[2] Typical pulse durations (τ) are the *ns* region for conventional PLD.

EFTHYMIOS CH. SVOUKIS

2.2.4 Basic principles of PLD

In the conventional PLD technique, an energetic pulsed laser beam[3] is focused on the target of the material, resulting in ablation of the material and forward transfer of it to a desired substrate. At the early stages of the process, a dense vapor appears in front of the target. Due to absorption of a part of the laser pulse by the vapor, its temperature and pressure increase and the gas expands from the target to the substrate, the so called plasma – plume is created. The energy distribution of the ablated materials can be described with a Maxwell Boltzmann – Distribution [45,46]. The kinetic energy of the ablated material is attenuated due to collisions with the background pressure gas molecules resulting in a gradual thermalization when it arrives on the substrate. Features of the processes involved will be described extensively in following chapters, *vide infra*.

The plume can be described as being highly forward directed, resulting in a non – uniform thickness distribution on the substrate surface [47]. Similarly to thermal evaporation the angular distribution is ~$\cos^{n}(\varphi)$. The parameter n takes values varying from ~4–30, due to the directionality of the plasma [48].

Typical deposition rate for a film that is grown by PLD is in the range of $10^{-3} - 1\overset{o}{A}/\,pulse$, providing a laser shot – to – shot control of the deposition process, which is ideal where sub – monolayer control is needed. A typical deposition pulse duration[4] of ~500μs [26], corresponds to $D_R = 10^3 - 10^6\ \overset{o}{A}/\sec$ [49], orders of magnitude higher compared to the other PVD techniques described in Section 2.1. Each pulse can be seen as distinct, where deposited atoms rearrange on the substrate's surface by diffusion resulting in the nucleation and formation of a continuous thin film [26,50].

2.2.5 PLD setup

Figure 2.3 shows a photo of the deposition system located in the Laser Assisted Materials Processing Lab (LAMP – Lab) of UCY. The system is equipped with a high –

[3] Excimer lasers are usually used in conventional PLD.

[4] Deposition pulse duration is the inverse of the deposition frequency and different from τ.

EFTHYMIOS CH. SVOUKIS

pressure RHEED real time observation system. The system exceeds the limits of conventional PLD and can be described as a state – of – the – art deposition system.

All films studied in this work were grown using a KrF^* excimer laser (Coherent COMPex Pro 201 F, λ=248*nm*), with a maximum repetition rate of 10*Hz*. The maximum energy per pulse was 700*mJ* with a pulse duration of τ~25*ns* [51]. A metal rectangular mask has used for selecting the homogenous part of the laser beam (insert in Fig. 2.3). The rectangular beam is projected via a focusing lens (focal length ~500*mm*) on the target with an inclination of ~45° through a silica window. To ensure minimum losses during the entrance of the beam, the port is covered with antireflection coating of magnesium fluoride MgF_2, a proven material for high energy lasers operating in UV range. The *c* – axis of MgF_2 coating is parallel to the normal of optics surface, allowing transmittance up to ~99.5% [52]. The energy density per area, known as fluence (Φ), deposited on the target was controlled by the adjustment of the energy per pulse and the spot size on the target.

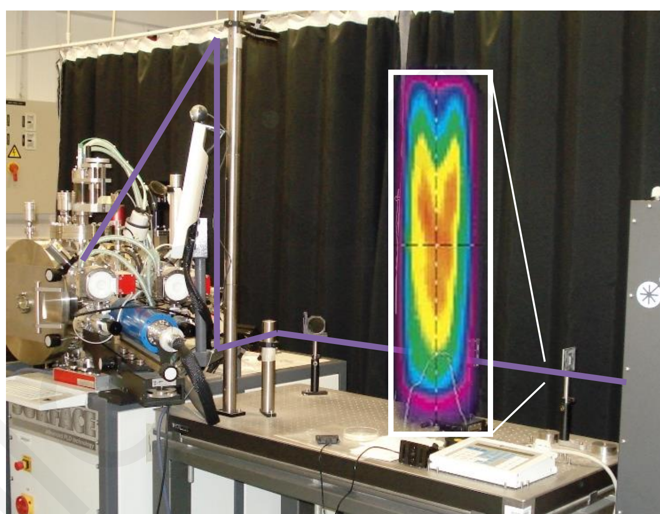

Figure 2.3: *Photo image of the PLD configuration used in the LAMP – lab of UCY. The laser beam enters in the deposition chamber through a periscopic path. Insert shows the substantial intensity variation of light across a cross section of the beam for a KrF excimer laser [53]. To achieve homogenization of the beam a mask is used.*

A commercial fully automated, HV deposition chamber (Surface GmbH) was utilized for the growth of thin films [54]. The deposition chamber can accommodate up to 4 different targets on the multi – target holder. Targets are continuously rotated and toggled to avoid the formation of anomalies (craters, dendrite form, *etc.*), ensuring a uniform ablation and hence, a not changing deposition. Selection of target, repetition rate, energy per pulse, number of pulses can be controlled during the deposition.

The substrate is mounted on a sample carrier with mechanical contact or with the use of colloidal adhesive silver paint and is placed on a specific position near the heater. The precise position of the substrate is crucial for the reproducibility of the experimental work. The temperature of the heater can be monitored and regulated via a PID controller. Temperature readings are recorded with an S – type thermocouple[5] placed inside the sample carrier, that allows accurate temperature control up to ~1000^oC under oxygen as well as HV conditions.

The pressure inside the deposition chamber is controlled with a turbo pump in combination with two mass flow controllers [55]. To ensure a clean atmosphere inside the deposition chamber, the chamber is always evacuated to a base pressure <$5\cdot10^{-6}mbar$. High purity (5.0) oxygen and nitrogen are used during the deposition and venting of the chamber, respectively. Usage of purity gasses was necessary to protect the thin films from contamination due to unwanted atoms.

The system is fully computer controlled and can be used in the recipe mode or in the manual mode depending on the experimentalist's desire. A schematic view of the deposition chamber used in the current study is presented in Fig. 2.4.

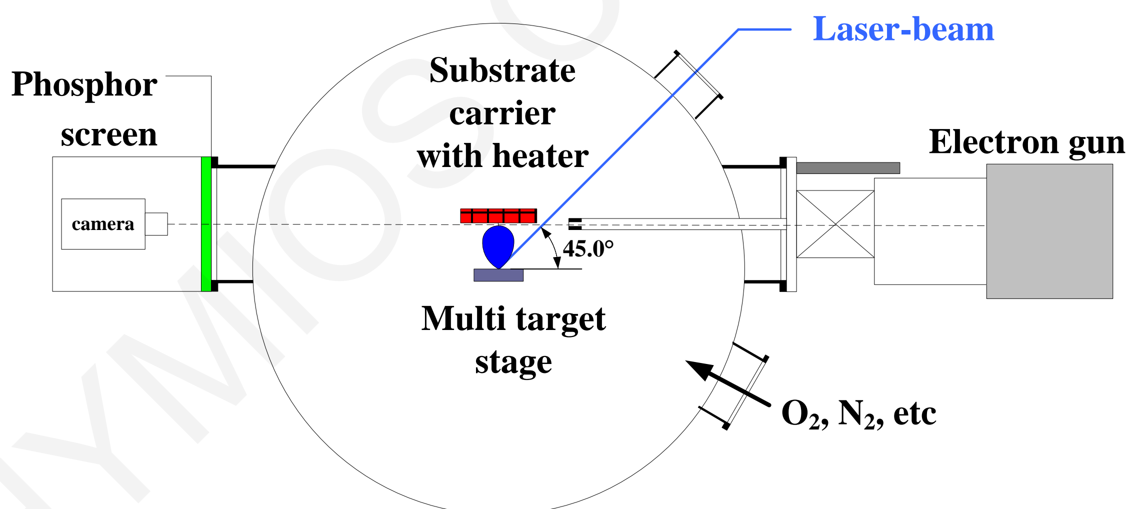

Figure 2.4: *Schematic diagram of the PLD deposition chamber configuration including the RHEED system located in the LAMP – lab of UCY.*

[5] Are constructed using one wire of 90% Pt and 10% Rh and a second wire of 100% Pt that serve as a positive and a negative lead, respectively.

EFTHYMIOS CH. SVOUKIS

2.2.6 Deposition parameters

For every material that is used as a target for the growth of a stoichiometric thin film, there is a set of optimal deposition parameters. Their optimization is a challenge, since they are highly correlated. Adjustable parameters in the conventional PLD and typical values used for the growth of oxide thin films, are presented in Table 2.1 [56]:

Table 2.1: *Adjustable parameters in the conventional PLD and typical values used for the growth of oxide thin films.*

Parameter	*Typical values for growth of oxide thin films*
Laser Specifications	UV range: $193nm \leq \lambda \leq 308nm$
Φ deposited on the target	E: $300 - 700mJ$, Φ:$0.6 - 5Jcm^{-2}$
Spot specifications	$S<1cm^2$, rectangular shape
Background gas composition	O_2, Ar / O_2 mixture, *etc.*
Background pressure	P: vacuum – $400mbar$
Target-substrate distance & relative orientation	d_{T-S}: $20 - 90mm$, substrate surface parallel to the target top surface
Target density / composition	Metallic or high density ceramic target, single or multi – composition target
Substrate Temperature	T: Room Temperature -1000^oC
Substrate	SiO_2, Si, Al_2O_3, MgO, $SrTiO_3$, *etc.*

The stoichiometric transfer of material and the growth of thin films, arises from the non – equilibrium nature of the ablation process due to absorption of high energy density by a small area of the target [57].

The ablation process is governed by variety of laser parameters that are used and also the transport properties of the target used. Laser parameters include: λ, τ, repetition rate (RR), Φ and spot size (S). The physical properties of the target material play an important role in the early stages of the ablation process: reflectance and absorption coefficients for the specific λ used, specific heat (C_p) and thermal conductivity (κ) [58]. For ceramic or metallic targets excimer lasers are used, which can provide pulse widths τ in the ns region and a laser pulse energy (E) of several hundred mJ. Shape and size of the focused spot will determine the Φ deposited on the target, therefore, well defined shapes and sizes are desired [59].

Preferred target materials are single crystals, due to their high density and homogenous composition. Single crystals cannot be always obtained, and ceramic targets are

EFTHYMIOS CH. SVOUKIS

alternatively used. Ceramic targets are widely used in PLD, due to ease of their fabrication for multi – cation compounds. For ceramic oxides, sintered pellets with densities close to the theoretical ones are used in order to reduce particulate formation during the ablation process [60].

The amount of energy deposited on the ceramic target is very important for PLD. Use of very low $\Phi \leq 0.04 Jcm^{-2}$, results in no damage of the surface. Small increase of Φ, results in changing the surface morphology, generation of defects and eventually, due to heating of the target, in thermal evaporation [61]. In this case, the irradiation of a multi – cation target (*e.g.,* YBCO) results in a flux whose composition is determined mainly by the vapor pressures of the constituents cations. The produced thin film doesn't have the same stoichiometry as the target. With further increase of the Φ, an ablation threshold is reached ($\Phi_{thres.}$), where laser energy absorption is higher than that needed for evaporation. Each target material has a different ($\Phi_{thres.}$) which is highly related to the material properties. At deposited fluencies higher than ($\Phi_{thres.}$), ablation occurs and flux is replaced with the formation of a plasma at the target surface [62]. For YBCO a value of $\Phi_{thres.}$=0.75Jcm^{-2} has been reported and similar values exist for other oxides also [63]. At high Φ, re – sputtering of the film will appear due to collisions with the plasma species [64]. In the case of a multi – cation target, the appropriate choice of Φ would result in a plasma formation with composition independent of the vapor pressures of the component cations, which is necessary for stoichiometric transfer. Φ is determined by the area, where the photonic energy is deposited. Small areas are needed to achieve higher Φ and well defined shapes are mandatory for reproducibility of the experimental work.

Each pulse provides enough material for a sub – monolayer of the desired material phase. D_R will depend on parameters including the target – substrate distance (d_{T-S}), background pressure (P) and Φ. Species inside the plasma can have kinetic energies up to 250eV [55]. Strong interactions and collisions take place between the ablated species and the background gas. Most of the energy is attenuated through collisions with the cold gas molecules. Background gas can be used to moderate the kinetic energies of the species inside the plasma to values ~1eV. The theoretical description of the kinetic energy of the plasma is complicated, due to its composition (atoms, ions, nanoparticles, *etc.*). Extensive pressure can also lead to preferential diffusion of light atoms in the plume; resulting to a non – stoichiometric transfer. Mainly for the growth of oxide thin films, the background gas provides the necessary oxygen species, required for the phase formation [62].

EFTHYMIOS CHISVOUKIS

The d_{T-S} has also to be taken under consideration. Typically, the substrate is placed at the end of the plasma, where little preferential diffusion appears and limited re – sputtering happens on the film [64]. Distance can be used as a parameter for the kinetic energy reduction of the plasma species. Variation of the d_{T-S} has a huge impact on the crystallinity and surface roughness of the thin films [65]. In the case of an optimized distance, species will land on the substrate and nucleate the forming layer, where for a smaller distance due to their high kinetic energy, they will sputter the top layers of the thin film or be implanted inside it, us increasing its roughness. Thin film thickness uniformity can also be improved by increasing the d_{T-S}.

In principle, thin film growth can be performed on all possible substrates, amorphous or crystalline. Factors such as: film – substrate lattice mismatch, thermal expansion matching and chemical compatibility are just a few of the many parameters that have to be considered [66]. For oxide compounds with cubic / tetragonal or trigonal / hexagonal crystal structure, oxide substrates with square planar surface or hexagonal symmetry are typical used, respectively. Commonly used oxide substrates and some of their properties are presented in Table 2.2. The thermal expansion mismatch between most of the oxides and Si can result to the appearance of defects or cracks attributed to strain effects. Oxide thin film growth on Si is a challenge. Possible solutions for the thermal expansion mismatch exist, such as the use of an intermediate buffer layer.

Table 2.2: *Typical oxide substrates, used in PLD. For each substrate, structure and transport properties are presented.*

Substrate	***Structure***	$a\left(\overset{o}{\mathrm{A}}\right)$	$b\left(\overset{o}{\mathrm{A}}\right)$	$c\left(\overset{o}{\mathrm{A}}\right)$	***BandGap*** (eV)	***Thermal expansion coefficient*** $\left(x10^{-6}/K\right)$
$\alpha-SiO_2$	Amorphous	–	–	–	9.00	–
TiO_2	Tetragonal	4.594	4.594	2.958	3.00	9
Al_2O_3	Trigonal	4.758	–	12.99	8.80	10
MgO	Cubic	4.212	4.212	4.212	7.80	12.3
$SrLaAlO_4$	Tetragonal	3.756	3.756	12.636	1.40	12
$SrTiO_3$	Cubic	3.905	3.905	3.905	3.25	10.4
Si	Cubic	5.431	5.431	5.431	1.11	2.56
$Gd_3Ga_5O_{12}$	Cubic	12.376	12.376	12.376	4.40	–

EFTHYMIOS CH. SVOUKIS

The temperature of the substrate is a crucial parameter for the crystallinity of the thin films. Energy is transferred to the deposited atoms, which diffuse on the surface of the substrate. The mean diffusion time (t_D) of the deposited atoms is given by:

$$t_D = v^{-1} \cdot e^{-\frac{E_A}{k_B T}}, \tag{2.3}$$

with v is the atomistic process frequency, E_A the activation energy for diffusion, k_B the Boltzmann's coefficient and T the substrate's temperature [26]. During this t_D, atoms migrate on the substrate, re – arrange and nucleate forming phases stable at the specific temperature. Extremely high temperatures on the substrate's surface will dramatically alter the conditions of the initial surface and possibly affect the thin film and assist the appearance of secondary phases.

Some of the adjustable parameters that can be manipulated during the deposition process have been discussed in detail. There is no global recipe for all possible materials for the growth of a defect – free, oriented thin film. For known materials, the existing bibliography is useful for the initialization of the deposition parameters, followed by their experimental optimization. In the case of new – exotic compounds, the deposition parameter optimization is far more challenging.

2.2.7 Stages of PLD

Processes involved in PLD can be separated in five stages and are graphically presented in Fig. 2.5:

1. Light interactions with the ceramic target
2. One – Dimension plume expansion
3. Three – Dimension plume expansion
4. Thermalization of the plume
5. Thin film growth

All five stages cannot be disconnected due to their overlap in time. Stage 4 can only be observed in the presence of a background gas. Despite the simplicity of the experimental setup, all physical processes involved in the above stages are highly complex. In a simplified form, all the processes can be seen as a fast boiling of material in a localized volume with the use of laser.

EFTHYMIOS CH. SVOUKIS

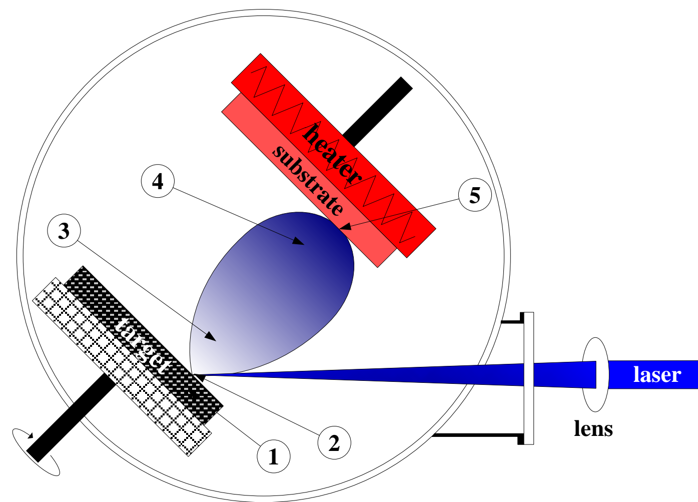

Figure 2.5: *Stages involved in the PLD process. Stage 1: Light interactions with the ceramic target, Stage 2: One – Dimension plume expansion, Stage 3: Three – Dimension plume expansion, Stage 4: Thermalization of the plume and Stage 5: Thin film growth.*

2.2.7.1 Light interactions with the ceramic target

For a full explanation of the effects that take place in the first stage of the PLD process, lattice and electronic dynamics have to be considered. For a typical laser λ used in PLD, photons are absorbed by the electrons of the material through band electron transitions. The laser beam disturbs the electron distribution that thermalizes via electron – electron and electron – phonon interactions. Especially in the case of metals, thermalization occurs in the femtosecond time regime and thus, it is extremely fast. For semiconductors and ceramic materials, thermalization is rather complex involving multiphoton processes as well as avalanche ionization and can be seen on a time scale that can be as long as nanoseconds [67]. Physical properties of the ceramic target, such as the dielectric constant, play a significant role in this step.

The amplitude of the electric field can be expressed as:

$$E = \sqrt{\frac{2\Phi}{n c \varepsilon_0}}, \tag{2.4}$$

with Φ is the power density, n the refractive index of the material, c the speed of light and ε_0 the electric permittivity of vacuum. Every material has a sufficient Φ that produces breakdown and hence, ionization.

EFTHYMIOS CH. SVOUKIS

Fast and strong deposition of energy on the surface results in a strong heating on the top of the surface, within nanoseconds. Depending on the properties of the ceramic target, according to the Fick's law, the heating energy travels inside the ceramic, to a heat diffusion length:

$$L_{th} = \sqrt{D_{th}\,\tau}\ , \tag{2.5}$$

where D_{th} is the thermal diffusivity[6] and τ the pulse duration. The electric field penetrates at a distance called absorption or optical penetration depth:

$$L_{abs} = a^{-1}, \tag{2.6}$$

where α is the absorption coefficient of the material.

In the case that $L_{th} >> L_{abs}$, the energy of the laser beam is absorbed in a thin layer close to the surface of the target, and this is valid for metallic targets with high α coefficient due to high electron density[7]. If $L_{th} << L_{abs}$, the absorption of the energy occurs in the bulk of the target. This is more preferable for the ablation of multi – cation targets with a low a coefficient [68].

As it has been described previously, low Φ may result in preferential evaporation of the most volatile material in the case of a multi – cation target. The same phenomenon can appear in areas of the spot with non – uniform energy, such as at the edge of the spot.

2.2.7.2 One – dimensional plume expansion

In the second stage, the initially formed plasma, absorbs electromagnetic energy from the laser beam. This further increase of the plasma energy, leads to indirect plasma production constituted from all the possible cations. All these multiple scattering processes tend to equilibrate the plasma and take place within a region known as the Knudsen layer [69]. The

[6] Thermal diffusivity depends on the thermal conductivity κ, specific heat C_p and density of the material ρ, as $D_{th} = \frac{\kappa}{C_p \rho}$.

[7] In the case of metallic targets and radiation bellow the plasma frequency, typical values for the optical penetration depth are $L_{abs} \approx 10 nm$.

EFTHYMIOS CH. SVOUKIS

Knudsen layer has a typical thickness of 30–100μm (few mean – free paths) and pressure of 5–10bar. Typical temperatures of the plume within the second stage are ~10^4K, well above the typical evaporation temperatures of most materials ≤3000K. This Knudsen layer modifies the initial velocity distribution to a shifted Maxwellian distribution. Velocities of the species span within the range $-\infty < u_x < +\infty$:

$$P(u_x) = A\left(\frac{m}{2\pi k_B}\right)^{\frac{3}{2}} v_x^n e^{\frac{-m(u_x-u)^2}{2k_BT}}, \tag{2.7}$$

where m is the mass of the species, k_B the Boltzmann constant, v_x the velocity along the propagation direction (in our case the x axis), u the flow velocity of the plasma, T the temperature of the plasma and n an integer describing the angular distribution of the plasma propagation with typical values in the range of $3 \le n \le 4$.

2.2.7.3 Three – dimension plume expansion

In the third stage of the process, the plume will expand highly anisotropic, typically peaked normal to the target surface as a result of the pressure gradients in the initial plume. A real image of a LCO plume in HV is presented in Fig. 2.6. The anisotropic expansion of the plume is evident.

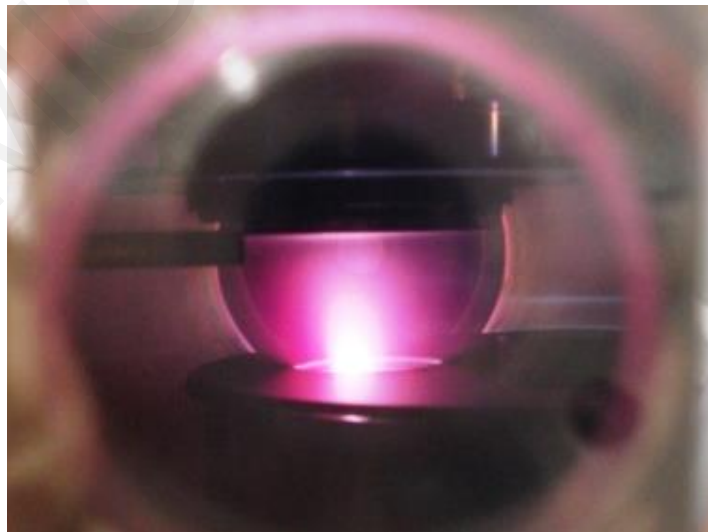

Figure 2.6: *Photo of the anisotropic plume expansion in HV. The laser Φ deposited on the LCO target was set to 1.3 Jcm^{-2}, with a laser spot of 10mm^2.*

EFTHYMIOS CH. SVOUKIS

In the adiabatic expansion model, presented by Singh and Narayan [70], the isothermal expanding plume is constantly augmented with species from the target. According to the model, exponential density gradients are assumed for the plasma and the initial velocities of its species vary linearly from the center of the plume. Consequently, the highest velocities are obtained in the direction normal to the target surface due to dependence of the expansion velocities on the initial velocities of the species. The Singh and Narayan model is in agreement with the one proposed by Anisimov *et al.* where the plume expansion can be characterized as ellipsoid [71].

During the expansion of the plume its composition is complex, and can also change during its expansion. Within the first millimeters of the expansion, Bremsstrahlung emission is observed due to deceleration of charged particles within the plume.

2.2.7.4 Thermalization of the plume

In the case of the existence of a background gas in the deposition chamber, there is a reduction in the kinetic energy of the plume species known as thermalization of the plume (forth stage of PLD). The thermalization is accompanied by an increase in the number of chemical reactions between plume constituents and background gas. A typical image of a plume at 1*mbar* where thermalization of the plume appears, is presented in Fig. 2.7.

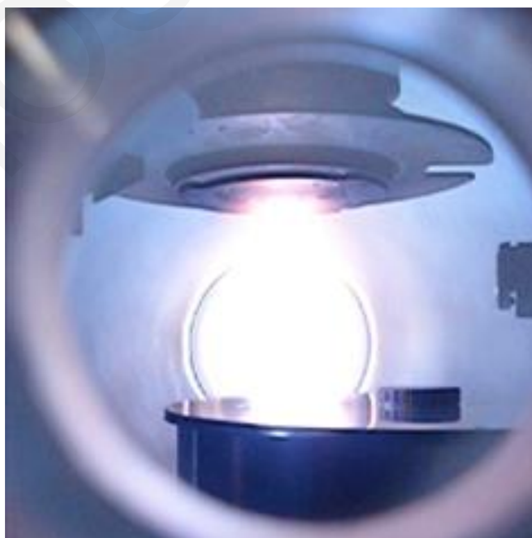

Figure 2.7: *Photo of the plume expansion in the presence of a background gas. The propagating front between ablation plume and background gas is observed. The laser Φ deposited on the LCCO target was set to 2 J cm^{-2}, with a laser spot of 11mm^{2}.*

EFTHYMIOS CH. SVOUKIS

The presence of the background gas is one of the main parameters in the PLD process that is highly correlated to the deposition rate of the thin film. The plume dynamics in the presence of a background gas is highly affected by the nature of the gas and the gas pressure. At background gas pressures below $10^{-2} mbar$ the plume expansion is similar to the one in HV. In contrary, at pressures above $10^{-1} mbar$ the background gas influences progressively the plume dynamics.

The initial high pressures formed in the previous stages, act like a piston towards the background gas. Within the microsecond time region, a hemispherical front is formed creating a shockwave at the interface between ablation plume and background gas, equalizing the pressures of the plume and the background gas.

Based on the shockwave model of Zeldovich *et al.* [72], the plume mass can be expressed as:

$$M_p \approx \frac{2}{3} \pi R_{SKW}^3 \rho_g , \tag{2.8}$$

where R_{SKW} is the distance at which the hemispherical shockwave starts and ρ_g is the average gas density. The total mass of the plume is crucial for propagation dynamics, but the individual masses from a multi – component plume influence the behavior of a part of the total plume.

The plume expansion within the background gas can be seen as it follows the standard diffusion law, where the current of the diffusion species (J_x) can be expressed as:

$$J_x = -D \frac{\partial n_A}{\partial x} , \tag{2.9}$$

where n_A is the concentration of A – atoms and D the diffusion constant:

$$D = \frac{1}{3} u_A \lambda_A . \tag{2.10}$$

Within Eq. (2.10), $u_A \sim m_A^{-0.5}$ is the velocity of the A – atoms and $\lambda_A \sim m_A^{-0.9}$ the mean free path between collisions of the gas atoms and the A – atoms with mass m_A. Thus, $D \sim m_A^{-1.4}$ which is strongly non stoichiometric, affected by the mass of the species within the plume.

Heavy ions in the plume, due to their inertia, have larger stopping distances. Strikovski and Miller, reported the dependence of the stopping distance on the atomic mass of the target [73]. Similar work for multi – cation targets with several atomic masses or with light

EFTHYMIOS CH. SVOUKIS

elements (*e.g.* Li) has not be published. Unquestionably, the stopping distance of the plume species is highly correlated with the optimization of d_{T-S} and D_R.

The mass density of the background gas, impacts the angular distribution of the plume. Gas atoms are responsible for the scattering processes that take place during the plume expansion. Light atoms in the plume are scattered much more than heavy atoms in a gas [74]. Taking under consideration the propagation dynamics, the angular distribution of $\sim \cos^n(\varphi)$ has to be reconsidered in the case $d_{T-S} / \lambda_A \geq 10$.

In the case of a multi – cation target, the plume dynamics is far more complex. Though nascent, plume has initially temperatures of the order of ~$10^4 K$ within the Knudsen layer and adiabatically cools to ~$10^3 K$ and plasma species (ions, neutrals and molecular species) can have energies close to 1–500eV, depending on material properties.

These conditions must be taken care of while studying plume dynamics and can only be analyzed with specialized equipment such as intensified charged couple devices (ICDD) [68]. A typical emission image of the plume in HV and in the presence of background gas is presented in Fig. 2.8 [75].

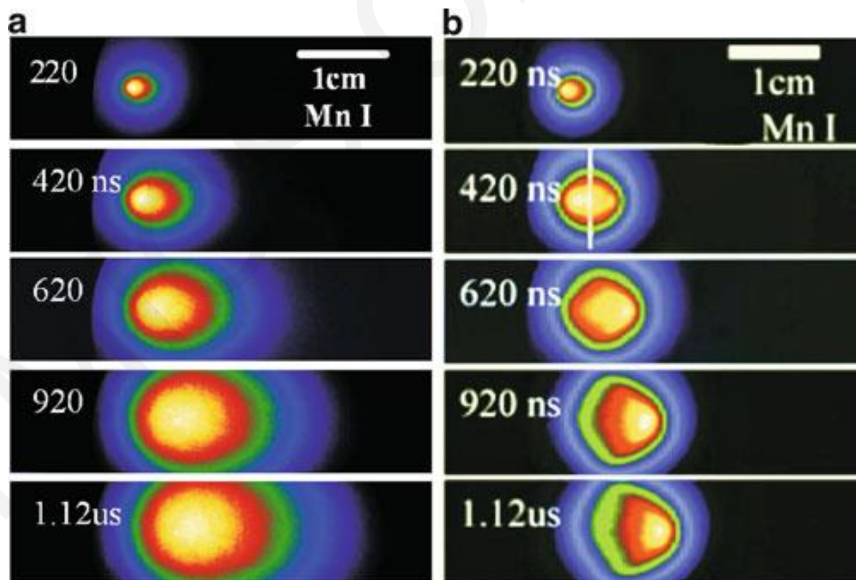

Figure 2.8: *ICDD emission images of neutral Mn – plume species as obtained by ablating $LiMn_2O_4$ in (a) HV and (b) at 0.2 mbar of oxygen [75]. The presence of oxygen as background gas, changes the shape, speed and angular distribution of the plume.*

2.2.7.5 Thin film growth on the substrate

Ablated material from the target arrives on the substrate. All the processes that take place during the growth are part of the fifth stage of the PLD. Growth of the film is by itself a complex procedure due to numerous processes that can take place between the deposited material and the substrate.

Plume constituted by atoms, molecules, ions and charges species, arrives on the surface of the heated substrate. Due to their possible high kinetic energy and / or elevated temperature of the substrate, species diffuse on the surface of the substrate creating energetically favorable bonds with the substrate or neighboring atoms. This way, atoms start to nucleate and form a continuous thin film [64].

The elevated kinetic energy of the plume species and high substrate temperature can also induce a microscopic scale process such as diffusion interactions within the thin film or implantation in the substrate under the thin film [57]. Such processes modify the thin film properties and composition. Re – sputtering of atoms and ions can also be observed, accompanied by surface morphology changes. A schematic diagram of all the microscopic processes that could take place in the fifth stage of PLD is presented in Fig. 2.9.

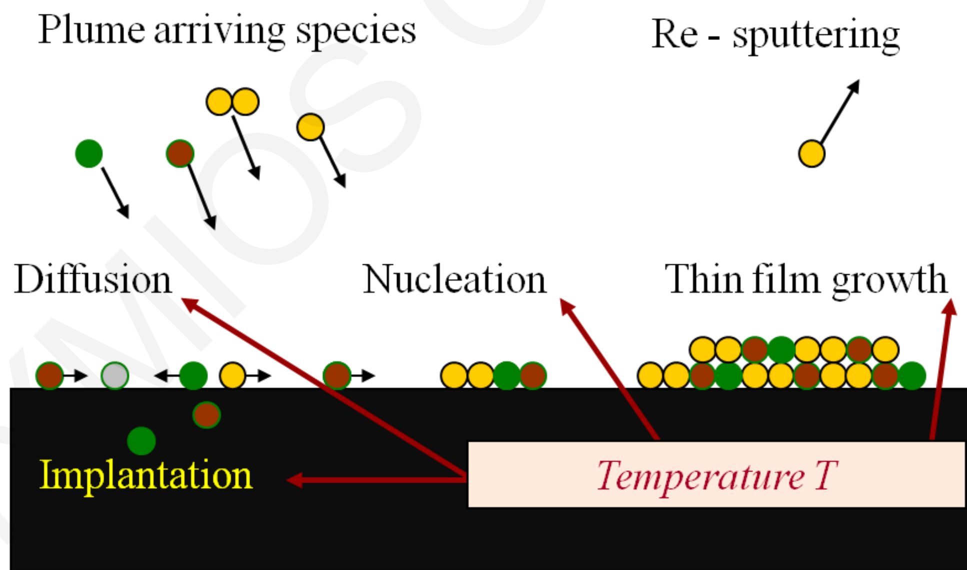

Figure 2.9: *Possible processes that could take place during thin film growth on a substrate. Multi – cation thin films are grown stoichiometricaly only if atoms of all desired components are available in the precise ratio at specific positions.*

EFTHYMIOS CH. SVOUKIS

Surface energy effect on the growth mode of a thin film will be discussed explicitly in Ch. 4, *vide infra*. Typical growth models for the nucleation and growth of thin films are:

1. Two – dimensional full monolayer (Frank – van der Merwe) growth.
2. Step flow growth.
3. Three dimensional island (Volmer – Weber) growth.
4. Initial few monolayer growth, followed by three dimensional island formation (Stranski – Krastanov) growth.

2.2.8 Advantages & disadvantages of PLD

PLD has a number of advantages compared to other PVD techniques.

1. Incongruent plume generation, which promotes the accurate control of the stoichiometric transfer.
2. Can be used to deposit any kind of materials, whereas other PVD techniques such as MBE cannot be used with volatile materials.
3. Laser is placed outside the deposition chamber:
   a. Offering flexibility on the geometrical arrangements of the PLD systems.
   b. Reduction of thin film contamination.
4. The pulse nature of the technique, allows for accurate control of film thickness.
5. Flexibility on the deposition parameters (Φ, d_{T-S}, T, λ, *etc.*) offers unlimited choices.
6. Can be used for the production of materials far from equilibrium.
7. Relatively high kinetic energy of the ablation plume species is responsible for the production of high quality thin films at relatively low deposition temperatures.

Whereas modified PLD techniques have been proposed for the reduction of PLD shortcomings, some of them still remain due to intrinsic processes of the technique [35].

1. Droplet formation on the top surface of the thin film is possible. Minimization of the droplet formation can be achieved by controlling the deposition conditions.
2. Impurities in the target or the vacuum chamber could be transferred to the thin film. High purity materials and gasses have to be used to avoid contamination.

EFTHYMIOS CH. SVOUKIS

3. Inhomogeneities in the energy distribution over the spot size will affect the angular distribution of the plume.
4. High kinetic energy species within the plume may cause re – sputtering resulting in the generation of defects within the thin film structure. Control of the deposition conditions can eliminate this phenomenon.
5. The major disadvantage of PLD is that it cannot be used for continuous thin film deposition over large surface areas, which is necessary for industrial use. Use of multiple laser beams is a possible solution.

2.3 Summary

PLD can be described as a simple experimental technique concerning the needed hardware. However, deposition processes and their theoretical understanding are rather complex due to their nature. High purity thin films can be obtained by optimization of the deposition condition parameters, which vary from one material to another and this makes it a challenging procedure. PLD is appropriate for the growth of multi – cation thin films, and also is comparable to other state – of – the – art PVD techniques.

EFTHYMIOS CH. SVOUKIS

Characterization Techniques

All films produced in the current work, were characterized with a variety of techniques. The structure quality of the thin films was investigated using techniques such as XRD, TEM and RHEED. Transport properties (thermal and electrical) were investigated using home – made developed techniques such as 3ω and 4 – probe. The surface morphology, a key – playing parameter was investigated with AFM and SEM techniques. The characterization techniques used in this work are briefly introduced.

3.1 Structural characterization

3.1.1 X – ray diffraction of powders and thin films

XRD is a common non – destructive technique used for powders and thin films. Due to the electromagnetic radiation used, with wavelengths comparable with the inter-atomic distances within the solid structures, the technique is applicable for the investigation of the crystal structure of crystalline bulk materials and thin films. Due to the high penetration depth of the X – rays, parameters of the crystalline structure such as: lattice parameters, crystallographic orientation, grain size *etc.* can be precisely determined.

The periodicity of the crystal structure creates geometrical arrangements on crystallographic planes, indexed with the so – called Miller indices (*hkl*). Incident electromagnetic waves interact with the periodicity of the structure and diffraction occurs. Maximum intensity in the diffraction happens when the Bragg law applies [76,77]:

$$2 d_{hkl} \sin(\vartheta_{in}) = n\lambda, \tag{3.1}$$

EFTHYMIOS CH. SVOUKIS

where d_{hkl} is the inter – planar spacing, ϑ_{in} the incident angle, n the order of the diffraction and λ the wavelength of the X – rays used in the experiment $K_{a1} = 1.540562\,\overset{o}{A}$. A diffraction diagram is acquired by defining the diffraction intensities as a function of the diffraction angles. The Bragg's law can be schematically visualized in Fig. 3.1.

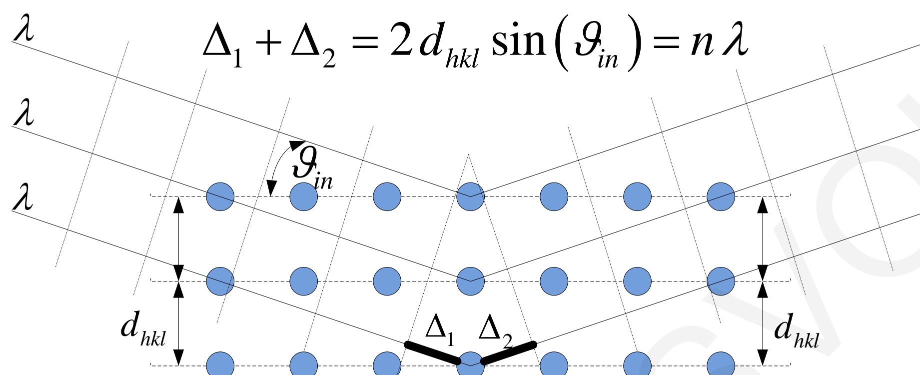

Figure 3.1: *Schematic of the Bragg's law.*

Structural characterization by XRD was achieved with the use of two diffrenr instruments. The Shimadzu XRD – 6000 (two circle geometry) of the Chemistry Department at UCY was initially used [78]. Subsequently all the structural characterization was carried out using the Rigaku Smartlab (four circle geometry) diffractometer of the LAMP – lab [79]. All diffractometers, regardless the circle geometry, include a few common key parts:

1. An X – ray source, where the X – rays are produced and collimated.
2. A sample holder, where the sample is attached in specific distance from the X – ray source.
3. A goniometer, for accurate measurement of angles.
4. A detector, which measures the diffraction intensity at specified angles.

3.1.1.1 Two circle diffraction, Bragg Brentano geometry

The two – circle diffraction is the most commonly used diffraction geometry, also called Bragg Brentano geometry. In this two – dimensional analysis arrangement, shown in Fig. 3.2, the X – ray source is at a fixed position, the sample rotates at an angle ϑ and the detector rotates at an angle 2ϑ. This kind of diffraction measurements are known as $\vartheta - 2\vartheta$ scans.

EFTHYMIOS CH. SIOUKIS

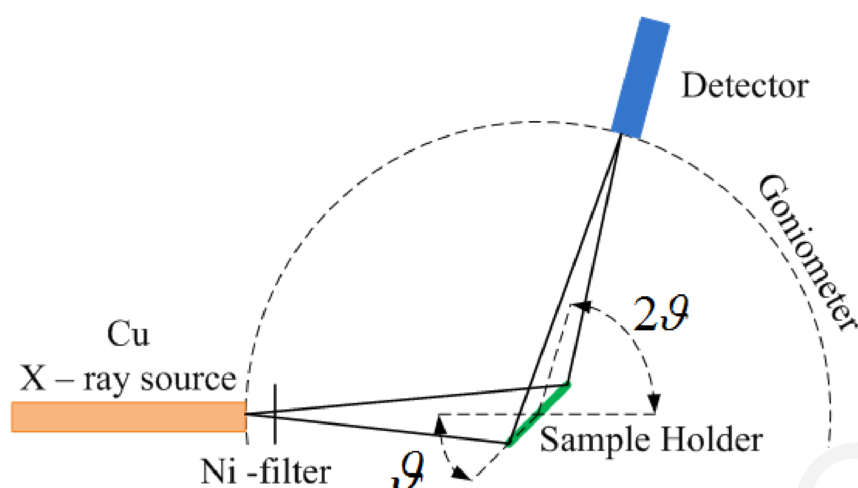

Figure 3.2: *The two – dimensional Bragg Brentano geometry used in this study. The circle centered on the sample represents the goniometer. The source has a fixed position and the sample and detector are rotated by θ and 2θ, respectively. A Ni filter is also included for the reduction of K_β radiation.*

Bragg Brentano geometry achieves a high diffracted intensity without sacrificing good resolution. Furthermore, it is a relatively straightforward method, based on the convenience of sample preparation. Due to the physics of the two circle diffraction, limited to the planes parallel to the top surface of the sample, only out – of – plane information appears in the diffraction pattern [80].

3.1.1.2 Four circle diffraction

Four circle diffraction geometries are used for the investigation and determination of in – plane epitaxial relations in single – crystal or highly – oriented thin films.

In addition to the rotational angle of the detector with respect to the incident beam, 2ϑ - axis, a four circle diffractometer provides further structural or epitaxial information about thin films growth with the usage of ω – axis, χ – axis and φ – axis. A schematic diagram of a four circle difractometer such as Rigaku Smartlab is shown in Fig. 3.3.

EFTHYMIOS CH. SVOUKIS

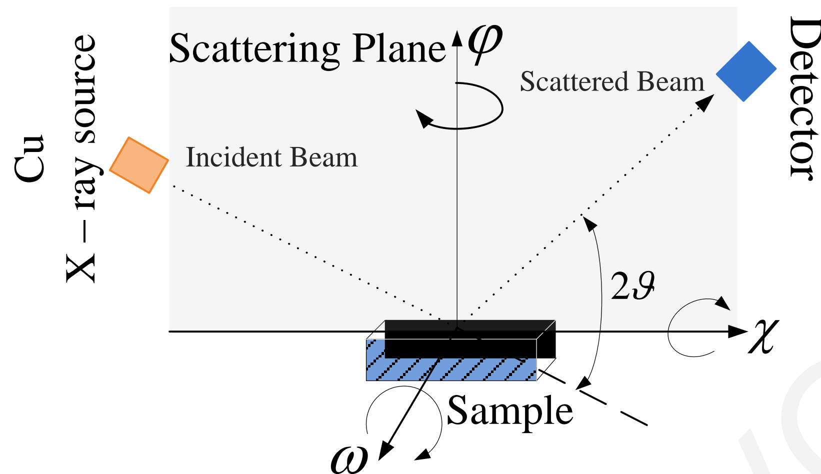

Figure 3.3: *Schematic diagram of the four – circle geometry corresponding to the Rigaku Smartlab dirfractometer. All possible rotation axes of the sample and the detector, or the rotation axes of the goniometer, (2θ, ω, χ and φ) are clearly defined.*

The ω rotation axis corresponds to the incident angle of the X – ray beam in the scattering plane. The rotation axis parallel to the scattering plane is called the χ – axis. The rotation axis for the in – plane rotation of the sample is called φ – axis. By rotating these three axes (ω, χ and φ), every crystallographic plane of the sample can be investigated [81].

In – plane measurement techniques vary in the relative positions of the incident X – ray beam, sample, and detector; scanning directions of the axes; and optical resolution. By rotating the axes in the direction corresponding to the change in the parameter to be measured, we can obtain the information needed.

The suitable measurement technique can provide a wide range of crystallographic information, including thin film structure, crystallinity, crystal orientation, and lattice constants [82]. Diffraction measurement techniques, classified based on the scanning method of the axis, are shown in Table 3.1.

EFTHYMIOS CH. SVOUKIS

Table 3.1: *Measurement techniques applicable in a four – circle diffractometer. Different crystallographic information of a thin film can be obtained by scanning a specified axis.*

Measurement technique	***Information obtained***	***Scan axis***
Out of plane measurement 1D – scan	Information on lattice planes parallel to sample surface. Qualitative analysis and crystal structure.	$2\vartheta/\omega$
In – plane measurement 1D – scan	Information on lattice planes near and parallel to sample surface. Qualitative analysis and crystal structure.	$2\vartheta\chi/\varphi$
Rocking curve measurement 1D – scan	Information on film crystallinity, thickness, and composition ratio	$2\vartheta/\omega$
Pole figure measurement 2D – scan	Information on distribution of specific crystal orientation.	$\chi(\alpha),\varphi(\beta)$
Reciprocal Space Mapping measurement 3D – scan	Information on three – dimensional components of preferred orientation, crystal orientation, and degree of preferred orientation.	$2\vartheta\omega/\omega$ $2\vartheta\chi/\varphi$

3.1.1.3 X – ray reflectivity

X – ray reflectivity (XRR) is a non – destructive measurement technique capable of evaluating a thin film thickness, density, and surface or interface roughness of the thin film and substrate. In XRR, the goniometer is used symmetrically, but with grazing angles with respect to sample surfaces [80]. The technique can be used for the following tasks [81,83]:

1. Measure film thickness from nanometers to microns.
2. Investigate the surface roughness and interface thickness (arising from roughness due to interdiffusion or existence of secondary phases in the early stages of growth).
3. Determine the density of a film of known composition.
4. Evaluate the structure of a multilayer or single layer film.
5. Perform tasks 1 – 4, with a wide range of materials, whether crystalline or amorphous.

EFTHYMIOS CH. SVOUKIS

3.1.2 Transmission electron microscopy

TEM has the same basic operation to as optical microscope but TEM resolution is in the order of $\sim 1\,\overset{o}{\mathrm{A}}$, by utilizing electrons instead of photons.

Taking under consideration relativistic effects, the relativistic wavelength can be expressed as:

$$\lambda_e \approx \frac{h}{\sqrt{2m_0E\left(1+\frac{E}{2m_0c^2}\right)}}, \tag{3.2}$$

where h is Plank's constant, m_o the rest mass of the electrons, c the speed of light, and E electrons kinetic energy [84]. For electrons with $E<50keV$[8], relativistic effects can be neglected. Much higher magnifications are possible compared to the optical microscope and TEM is used for a detailed characterization materials into the atomic level.

Nanometer – thin areas of a sample are transparent to highly energetic electrons. Electrons interact with the atomic planes of the sample. All interaction processes are highly depended on the nano – structural arrangement of the atoms in the planes and their characteristics. Therefore, TEM is the most powerful imaging technique in material science for the investigation in nano – scale. Basic modes of TEM are the imaging and the diffraction.

Imaging mode reveals information on crystal structure defects, grain boundaries and imperfections in the thin film growth. High – resolution TEM is an imaging mode that is being used for the formation of images from columns of atoms. Diffraction in a specified nano – area provides information for the in – plane crystallographic ordering and out – of plane growth orientation [85].

TEM technique can also be equipped with Energy Dispersive X – ray Spectrometer (EDX) for nano – analysis. This technique is appropriate for the determination of the concentrations of the different elements in the volume of a thin film.

[8] For electrons, $m_0c^2 \approx 500\,keV$

EFTHYMIOS CH. SVOUKIS

3.1.3 Reflection high energy electron diffraction

RHEED has become a *state – of – the – art* technique for surface characterization, due to its high sensitivity [86]. An electron beam is diffracted from the periodic arrangement of surface atoms. Initially the technique was used for *in situ* monitoring of growth in MBE setups [87,88]. A RHEED system attached to a PLD deposition chamber is shown in Fig. 2.4.

3.1.3.1 Geometry and basic principles

Mono – energetic electrons with kinetic energies, typically E~10–50keV, produced from an electron gun, approach the surface of the substrate at typical grazing angles $0.1-5^{o}$. The λ of the electrons can be calculated via Eq. (3.2). Typical electron λ are $\sim 0.05-0.1\overset{o}{\mathrm{A}}$, order of magnitude smaller than a typical d_{hkl}. Theoretically, based on their kinetic energy, electrons are able to penetrate a sample with few hundred of *nm* thickness [19]. Due to the grazing incidence angle, electrons interact electrostatically only with the top atomic layers (surface lattice) of the investigated sample. A phosphor screen acts as a detector of the diffracted electrons, where spots or streaks appear. A schematic diagram of the RHEED geometry is presented in Fig. 3.4.

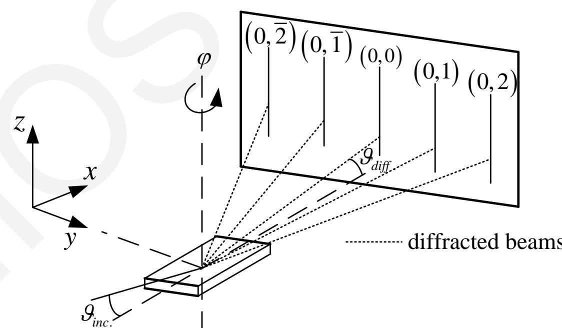

Figure 3.4: *A schematic diagram of the RHEED geometry. $\theta_{inc.}$ and $\theta_{diff.}$ are the incident and diffracted angles and φ the azimuthal angle. On the phosphor screen diffracted streaks appear.*

Surface characterization techniques (XRD, XRD, TEM, Probe Techniques *etc.*) can reveal information of the crystal structure or surface morphology. The strong advantages of RHEED compared to the other surface techniques are its compatibility with HV or UHV environments and the possibility of *in situ* monitoring of the thin film growth during the PLD process.

EFTHYMIOS CH. SVOUKIS

3.1.3.2 Kinematic theory approach

A kinematic theory approach can be used for understanding and qualitative description of RHEED patterns. It is a simplified theory, where only elastic electron scattering is assumed [26]. Based on the kinematic theory, spots appear in the phosphor screen, when the difference in the momentum of the diffracted beam $\left(\vec{k}_{diff.}\right)$ and incident $\left(\vec{k}_{inc.}\right)$ is a reciprocal space vector $\left(\vec{G}\right)$. Conservation of momentum and energy require:

$$\vec{k}_{diff.} - \vec{k}_{inc.} = \vec{G} \tag{3.3}$$

$$\left|\vec{k}_{diff.}\right| = \left|\vec{k}_{inc.}\right|. \tag{3.4}$$

In the case of two – dimensional surface lattice, the reciprocal lattice can be seen as a lattice of infinite, parallel, equally spaced thin rods perpendicular to the investigated sample surface. A surface lattice is presented in Fig. 3.5(a). The Ewald sphere is defined as a sphere with radius of $\left|k_{inc.}\right| = \frac{2\pi}{\lambda}$ [50].

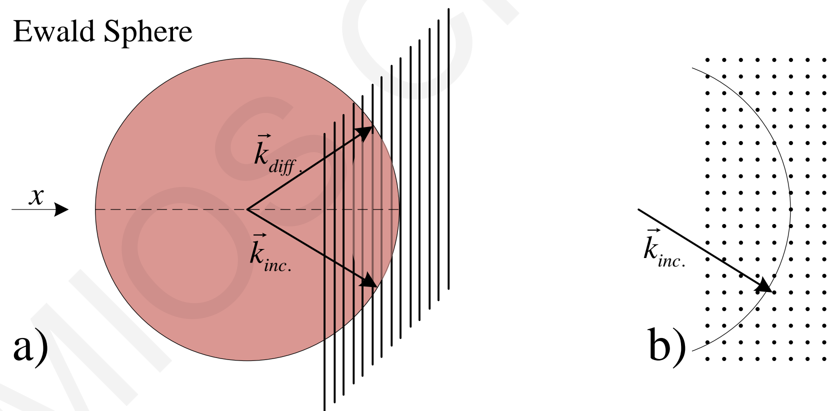

Figure 3.5: *a) Interaction of the Ewald sphere, from the incident electron beam, with the reciprocal space rods. Reflections occur in directions defined by the interactions of the Ewald sphere with the reciprocal lattice rods. In the case of a perfect surface, reflections will appear as spots on the phosphor screen.b) Section of the Ewald sphere interaction with the reciprocal space rods (top view).*

The Ewald sphere is very large compared to the reciprocal space of oxide materials. When the diffraction conditions are satisfied, diffraction spots appear on the phosphor screen in concentric circles called Laue – circles, Fig 3.5(b). RHEED is a diffraction technique, where inelastic scattering has to be taken under consideration for the full explanation of the

EFTHYMIOS CH. SVOUKIS

theory involved. Non – linear effects result in anomalies in the RHEED intensities, known as Kikuchi lines [88,90]. Appearance of Kikuchi lines is an indication of a very flat surface.

A real RHEED pattern from a perfect commercial $SrTiO_3$ (001) prior deposition is presented in Fig. 3.6. A spot pattern, with symmetrical Kikuchi lines is observed, evidence of a flat, crystalline, free of defects surface. In the patters, the 0th Laue circle is marked with a dotted circle, the specular spot is marked on the image with the $(0,0)$ diffraction and with asterisk a part of the direct beam.

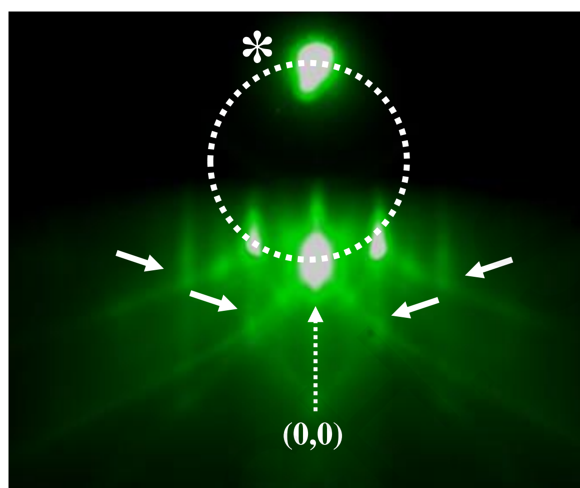

Figure 3.6: *RHEED pattern from a commercial $SrTiO_3$ surface. Kikuchi (marked with arrows) lines are evidence of a flat, crystalline, free of defects surface. The 0th Laue circle is marked with a dotted circle and with asterisk is marked the direct beam.*

3.1.3.3 Utility of RHEED on growth characterization

Static RHEED patterns can provide information such as lattice parameters, surface roughness, step of the vicinal surface, crystallographic order [86,88,91]. Real time intensity observation can provide sufficient information for the determination of the thin film growth. Specular spot intensity oscillations, correspond to periodicity of unit cells being completed during growth. Maximum intensities correspond to completed unit cell layers [92,93]. This kind of growth can only be observed in the Frank – van der Merwe mode.

EFTHYMIOS SVOUKIS

3.2 Transport characterization

Accurate measurements of physical properties, are very important, as they are crucial inputs to models for the development of novel devices. Transport characterization of thin films is a challenge due to their small thickness and extremely low mass. In this section, general experimental setups for the measurement of all relevant transport properties are presented.

3.2.1 Thermal characterization: The 3ω method

Thermal conductivity measurement methods can be divided in two groups: *steady state* and *dynamic* [94]. In 1987 Cahill proposed the 3ω method, a new ac dynamic method for the determination of the thermal conductivity of insulating bulk samples [95]. The method was further extended for thermal conductivity characterization of insulating thin films [96].

3.2.1.1 Basics of the 3ω method

The 3ω method is closely related to the hot – wire and hot – strip methods where a thin metal strip is fabricated on the top side of the sample [97]. It can be described as a 4 – probe ac measurement technique which is based on the principle of using a metal strip as both heater and thermometer. An ac current is driven through the current pads of the metal heater

$$I = I_0 \cos\left(\omega t\right). \tag{3.5}$$

The excitation current generates heat that consists of ac and dc components, the latter of angular frequency *2ω*

$$P = I^2 R_0 = I_0^2 R_0 \cos^2\left(\omega t\right) = \frac{I_0^2 R_0}{2}\left(1+\cos\left(2\omega t\right)\right). \tag{3.6}$$

Heat generation over the heater with resistance R_0 results to a temperature rise with dc – and ac – components, at angular frequency *2ω* with a phase shift *φ*.

$$T\left(t\right) = \Delta T_{dc} + \Delta T_{ac} \cos\left(2\omega t + \phi\right). \tag{3.7}$$

Within the temperature range, where the resistance of the heater is proportional to the temperature, that is given by

EFTHYMIOS CH. SVOUKIS

$$R(t) = R_0\left(1 + \alpha_R \Delta T_{DC} + \alpha_R \Delta T_{AC}\cos(2\omega t + \phi)\right), \tag{3.8}$$

where $\alpha_R = \frac{1}{R_0}\frac{dR}{dT}$ is the temperature coefficient of the resistance, with typical values for metals $\alpha_R \sim 3x10^{-3} K^{-1}$ [98]. The measured voltage across the voltage pads will be:

$$\begin{aligned} V(t) = I\,R(t) \approx I_0 \cdot R_0\left(1 + \alpha_R \Delta T_{dc}\right)\cos(\omega t) + \frac{I_0 R_0}{2}\alpha_R \Delta T_{ac}\cos(\omega t + \phi) + \\ + \frac{I_0 R_0}{2}\alpha_R \Delta T_{ac}\cos(3\omega t + \phi) \end{aligned} \tag{3.9}$$

Investigation of the ac temperature oscillations ΔT_{ac} can be used for the thermal characterization of the sample. A schematic diagram of the *3ω* harmonic signal generation is presented in Fig. 3.7.

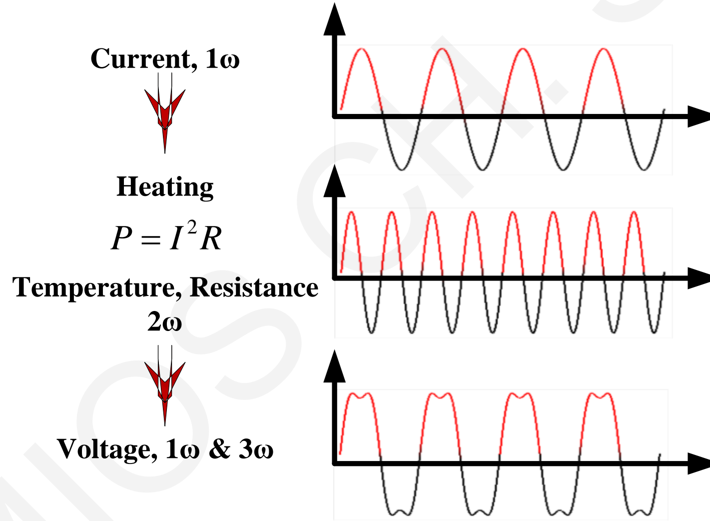

Figure 3.7: *Diagram of the mechanism for the low amplitude 3ω signal generation, due to Joule heating over the metal heater.*

3.2.1.2 *Instrumentation*

The amplitude of the *3ω* signal is ~30*db* less than the V_0 voltage. A lock – in amplifier was necessary for the detection of the 3ω signal. The Keithley 6221 ac current source provided the excitation current and the Stanford SR830 lock – in amplifier was used to filter out the *3ω* signal. All measurements were carried out inside a Quantum Design PPMS

cryostat. Fig. 3.8 shows the schematic of the experimental circuit used for measuring the *3ω* component of the voltage across the metal strip.

The metal strip was made out of aluminum which was deposited on the films by thermal evaporation through a nickel shadow mask. The heater / sensor metal pads were connected to the sample – holder pads using 25μm gold wires and low – temperature silver paint. The width *2b* of the metal line is 32μm and the length ℓ of the metal line between the voltage pads is 1mm.

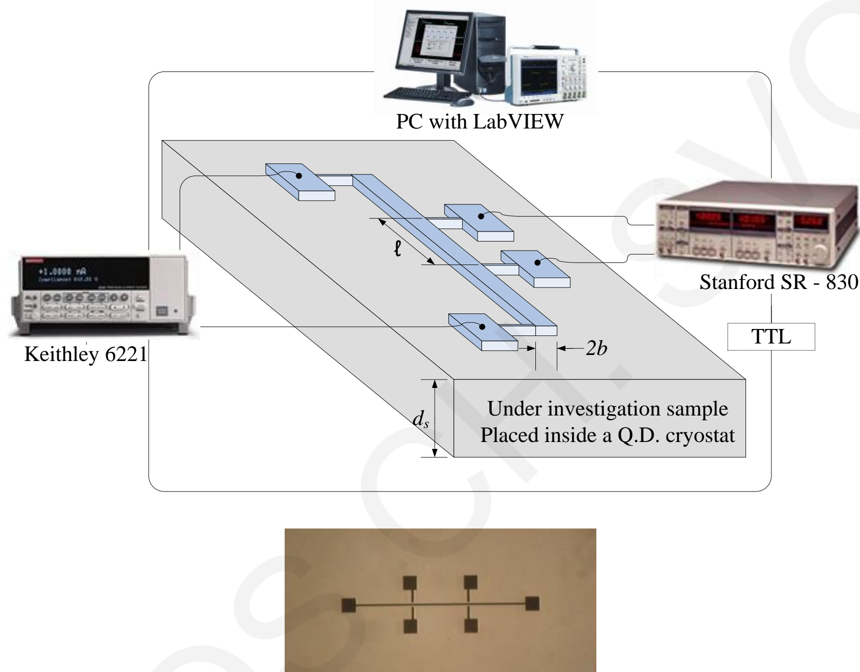

Figure 3.8: a) *Circuit layout diagram for measuring the 3ω component of the voltage across the metal strip deposited on the sample. The ac current is provided by the Keithley 6221 current source and the 3ω signal is measured with the Stanford SR830 lock – in amplifier. Both instruments are controlled by a PC using LabVIEW software. b) Real image of a fabricated heater on a commercial substrate surface.*

3.2.1.3 Extension of the 3ω method for thin film characterization

Borca – Tasciuc *et al.* found an expression for the temperature rise in the general case of planar multi – layered structures with arbitrary thickness and properties [99]. The derivation is based upon the use of a *2 – dimensional* heat conduction model and a uniform heat flux condition between the heater and the top surface. By neglecting the contributions of the thermal resistance and the mass of the heater and by using the integral Fourier transformation

EFTHYMIOS CH. SYVOUKIS

technique, the temperature oscillation ΔT_{AC} of a heater with width *2b* and length ℓ can be expressed as:

$$\Delta T_{AC} = -\frac{P}{\pi \ell \kappa_{y,1}} \int_0^\infty \frac{1}{A_1 B_1} \frac{\sin^2(bk)}{b^2 k^2} dk \, , \tag{3.10}$$

where,

$$A_{i-1} = \frac{A_i \dfrac{\kappa_{y,i} B_i}{\kappa_{y,i-1} B_{i-1}} - \tanh(\phi_{i-1})}{1 - A_i \dfrac{\kappa_{y,i} B_i}{\kappa_{y,i-1} B_{i-1}} - \tanh(\phi_{i-1})}, \quad i = 2,..n \tag{3.11}$$

$$B_i = \sqrt{\kappa_{xy,i} k^2 + i \frac{2\omega}{D_{y,i}}} \tag{3.12}$$

$$\phi_i = B_i d_i \quad \kappa_{xy} = \frac{\kappa_x}{\kappa_y} \, . \tag{3.13}$$

In Eq. (3.10) – (3.13), *n* is the total number of layers including the substrate, the subscript *i* corresponds to the ith layer starting from the top, the subscript *y* corresponds to the direction perpendicular to the layer's interface and *d* is the layer thickness. The effect of anisotropic thermal conductivity is introduced with the term κ_{xy}, which is the ratio of the in – plane (along *x* – axis) to cross – plane (along *y* – axis) thermal conductivity of the layer [100].

In the case that a thin long metal heater is fabricated on top of an insulating film deposited on an anisotropic, substrate, neglecting contribution from the mass of the heater and thermal boundary resistances, the thermal oscillation can be written as a summation of contributions from both the film and the substrate:

$$\Delta T_{s+f} = \Delta T_s + \Delta T_f \tag{3.14}$$

In the case of *1 – D* heat flow in the film, the thermal oscillation can be expressed as:

$$\Delta T_{s+f} = \frac{P d_f}{2bl\kappa_f} + \frac{P}{\pi l \kappa_y} \int_0^\infty \frac{1}{\tanh^p\left(\sqrt{\kappa_{xy} k^2 + i\dfrac{2\omega}{D}} d\right)\sqrt{\kappa_{xy} k^2 + i\dfrac{2\omega}{D}}} \frac{\sin^2(bk)}{b^2 k^2} dk \tag{3.15}$$

Parameter *p* depends on the boundary condition at the bottom surface of the substrate and takes the values *0*, *1*, *–1* in case of semi – infinite, adiabatic and isothermal boundary condition, respectively [101].

EFTHYMIOS CH. SVOUKIS

The aforementioned analytical approach is an approximation which is valid only when the thermal conductivity of the film is much lower than of the substrate, $\kappa_f / \kappa_s \ll 1$, and also when the heat flow is *1 – dimensional* in the film (no heat spread effects appear inside it), $d_f / 2b \ll 1$. A schematic representation of the heat dissipation inside the film / substrate system, according to the theoretical solution, is shown in Fig. 3.9.

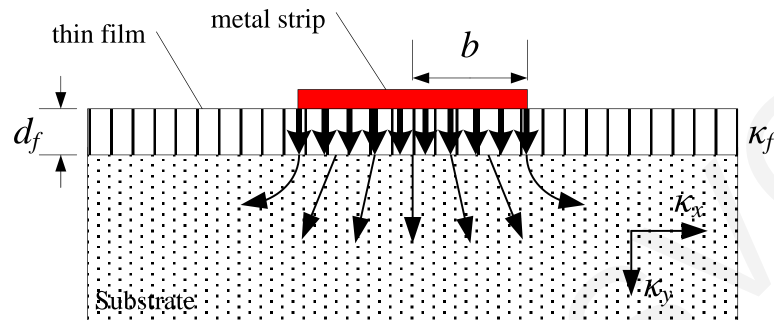

Figure 3.9: *Schematic diagram of the heat flow from a metal strip with half – width b through a low thermal conductivity thin film of deposited material on a thermal anisotropic substrate.*

3.2.2 Electrical characterization

3.2.2.1 Classical four – probe method

An experimental setup based on the four – probe method was created based on a fully automated LABView setup. A diagram of the setup is presented in Fig. 3.10.

- By using the configuration created, the resistance can be measured with high accuracy. The sample was placed inside a Quantum Design PPMS cryostat allowing measurement over the temperature range from 400 – 1.8*K*. Magnetic fields of ± 9*T* can be applied perpendicular to the sample surface. A photo of a mounted sample is presented in Fig. 3.10.
- To ensure a well – defined electric field, gold pads were created over the entire width of the sample with the use of a shadow mask.
- Gold has a poor adhesion on oxides. A few minutes annealing step at 400^oC in atmosphere was established to achieve diffusion of the gold atoms in the thin films and decrease of the contact resistance.

EFTHYMIOS CH. SVOUKIS

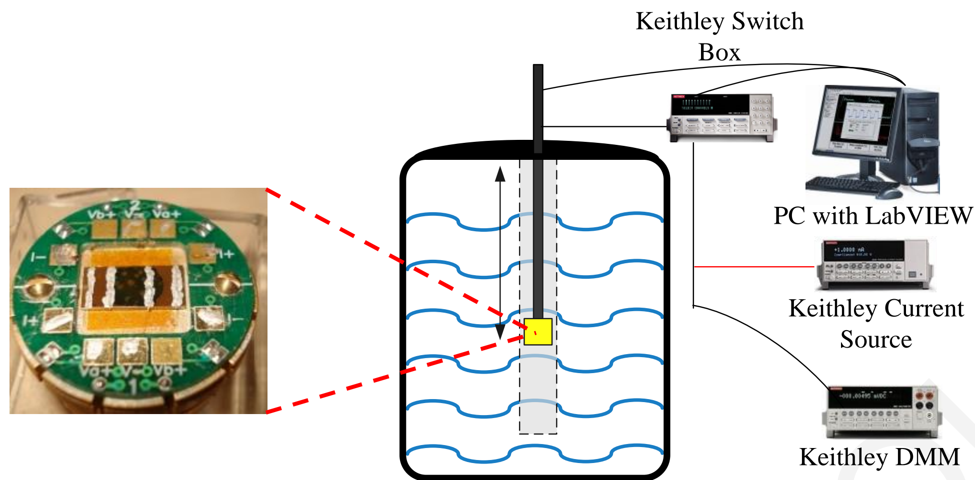

Figure 3.10: *Experimental setup for the electronic characterization of thin films by using the four – probe method. A photo of a sample mounted on the sample – holder (insert).*

The gold pads were deposited by sputtering on the thin films via a shadow mask and further thermally annealed at $400^{o}C$ for 5*min.* This technique leads to a well – defined ohmic contact, with low contact resistance [102].

3.3 Morphology characterization

3.3.1 Atomic force microscopy

AFM is a local surface technique for every type of surface: polymer, ceramics, oxide thin films, atomically stepped terraces *etc.* A scanning tip, fabricated by Si or Si_3N_4 is attached to a cantilever. A laser beam is deflected by the cantilever arm, a photodetector acquires the beam position, providing information for the surface. AFM resolution is correlated with the tip radius, therefore, it can reach few $\overset{o}{A}$ [103].

AFM can provide topographical images of a sample's surface roughness. In the present study AFM was used for determination of surface topology of substrates used for the deposition of thin films. Film nucleation and growth mechanisms are correlated with the surface topology. Furthermore, an AFM equipped with a conductive tip was used for the simultaneous investigation of the electrical properties and topography of thin films. Electrical

EFTHYMIOS CH. SVOUKIS

conductivity maps were produced with the usage of CP – AFM. A schematic CP – AFM diagram is presented in Fig. 3.11.

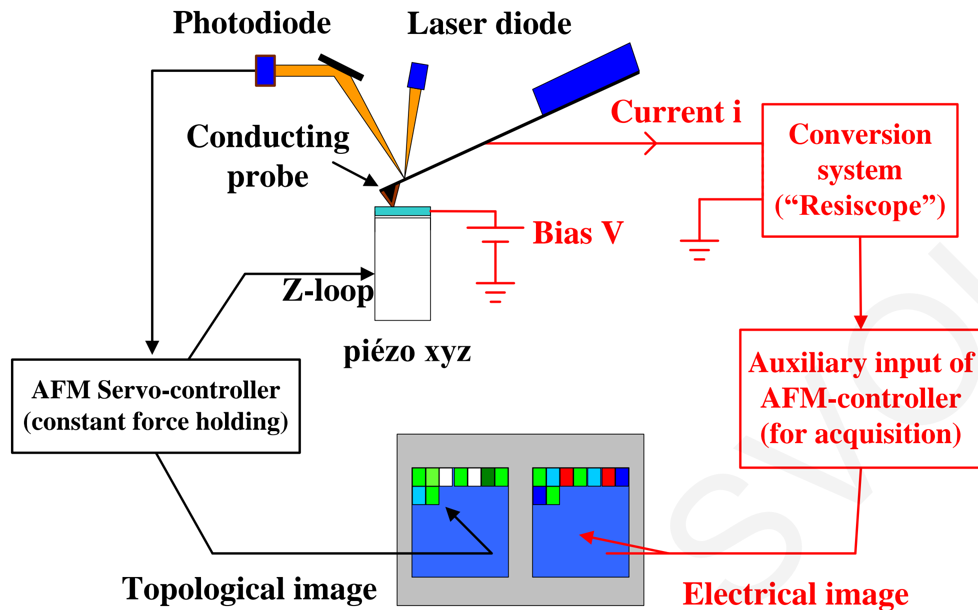

Figure 3.11: *A schematic diagram of a CP – AFM system. By using a conductive tip, the electrical properties and topography of thin films can be simultaneously investigated.*

3.3.2 Scanning electron microscopy

Large area surface morphology of thin films was investigated with SEM. The studies were performed with a Tescan Vega LSU, working in HV and employing an electron accelerating voltage of 20*kV*.

SEM can work in two basic imaging modes, the secondary and backscatter. Secondary electron imaging was used for the morphology investigation of the produced thin films over extended areas. Grains and cracks can be observed in cases of non – optimized deposition conditions. Backscattered electron imaging was used to detect the existence of impurity phases on the surface of the thin film. The SEM system is equipped with an EDX spectrometer, providing information on the atomic percentage of the constituent elements in the under investigation area of the thin film [104].

EFTHYMIOS CH. SVOUKIS

Thin Film Growth

Properties of thin films can be evaluated and understood only by their correlation with the growth processes that take place. It is the only way for optimizing the deposition conditions and achieving film engineering. Numerous parameters can determine the growth mode and structural characteristics of thin films. Chapter 4 will refer to the theory of thin film growth.

4.1 Epitaxy in thin films

Epitaxy can be defined as the growth of a high quality single crystal thin film on top of a single crystal substrate with specific crystallographic orientations. The roots of the word are Greek "*επί + τάξης*", meaning in order.

Epitaxy can be classified in two types: Homo – epitaxy and Hetero – epitaxy. Homo – epitaxy is the simplest form, where thin film and substrate are from the same material. Homo – epitaxy is widely being used in the IC industry by growing Si layers with different doping levels on Si wafers.

Hetero – epitaxy, is a more complicated process, where a crystalline thin film of a material is grown on a substrate with different chemical composition. In this case the thin film and the substrate could have different chemical and transport properties [105].

4.2 Lattice parameter mismatching

A key role in hetero – epitaxy plays the lattice parameter matching between the thin film and the substrate. The lattice mismatch (or misfit) can be expressed as the relative difference of the atoms spacing between the thin film and substrate:

EFTHYMIOS CH. SVOUKIS

$$m = \frac{a_{film} - a_{sub.}}{a_{sub.}} \cdot 100\% \,. \qquad (4.1)$$

Based on the lattice misfit, the thin film in the early stages can be strained or compressed. A critical thickness (d_c in Fig. 4.1) exists below which coherent growth appears. Dislocations formed during growth will result in the relaxation of the thin film [106]. Generally high quality hetero – epitaxial thin films can be obtained by choosing substrates with similar crystallographic space group and as small as possible lattice mismatch typically $m<7\%$. Lattice misfit can also be expressed as the relative difference of integer multiplicities of atoms spacing's, known as domain lattice matching [107]:

$$m = \frac{x \cdot a_{film} - y \cdot a_{sub.}}{y \cdot a_{sub.}} \cdot 100\%,\ x, y \in I^* \,. \qquad (4.2)$$

In Fig. 4.1, homo – epitaxy, tensile –, compressive – and domain – hetero – epitaxy is schematically presented.

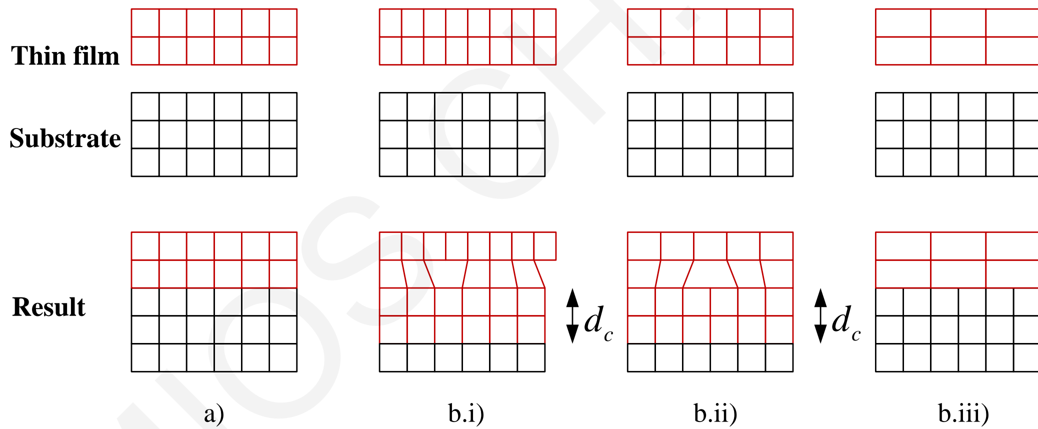

Figure 4.1: *Schematic diagram of possible growth modes due to lattice matching: a) Homo – epitaxy, b.i) tensile hetero – epitaxy followed by relaxation, b.ii) compressive hetero – epitaxy followed by relaxation and b.iii) domain hetero – epitaxy.*

4.3 Growth basic thermodynamics

4.3.1 Hetero – epitaxy

Plume species arrive on the substrate surface, diffuse on the surface resulting on the formation of aggregates. Aggregates tend to grow or shrink through the growth process. Schematic diagram of the atomistic processes that take place are presented in Fig. 4.2. Three

EFTHYMIOS CH. SVOUKIS

surface energies γ are involved, identified with the subscripts f, s and v representing the film, substrate and vapor respectively.

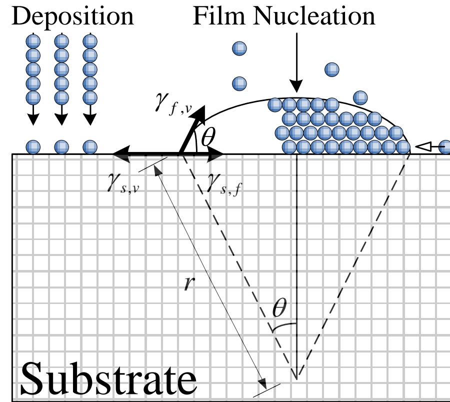

Figure 4.2: *Diagram of the atomistic processes taking place in hetero – epitaxial growth. Three surface energies γ are involved in the film growth.*

The balance between the growth or shrinkage of the aggregates is governed by the free energy change (ΔG) of the aggregate. Neglecting interfacial phenomena, ΔG can be expressed as:

$$\Delta G = 2\pi(1-\cos\theta) r^2 \gamma_{f,v} + \pi r^2 \sin^2\theta(\gamma_{s,f} - \gamma_{s,v}) + \pi \frac{2-3\cos\theta+\cos^3\theta}{3} \Delta G_V, \qquad (4.3)$$

where ΔG_V is the free energy change within the volume of the aggregate [24]. The condition for equilibrium known as Dupre – Young [108], an analogue to the case of a liquid droplet on a solid surface, where θ is the so called wetting angle can be expressed as:

$$\gamma_{s,v} = \gamma_{s,f} + \gamma_{f,v} \cos\theta \ . \qquad (4.4)$$

4.3.2 Growth modes

A thermodynamic approach to capillary theory can be used for the determination of the growth mode of a thin film. Thin film surface morphology, can be justified by using Eq. (4.4). The balance between the interfacial tensions γ can control the growth mode of a thin film close to equilibrium [36].

EFTHYMIOS CH. SVOUKIS

Layer – by – layer (Frank – van der Merwe) growth involves the coalescence of single monolayer agglomerates that spread over the substrate surface, forming a continuous thin film. This type of growth can be promoted in the cases of high substrate – thin film bonding, such as in the case of homo – epitaxy [109]. In this case the new monolayer "*wets*" the substrate ($\theta = 0$), therefore:

$$\gamma_{s,v} = \gamma_{s,f} + \gamma_{f,v} \quad . \tag{4.5}$$

In the case of a weak bonding between the thin film and substrate, the Wolmer – Weber growth is promoted [110]. Arriving atoms diffuse on the surface and attach to previously agglomerates. This happens when the atoms prefer to agglomerate, creating three dimension islands ($\theta > 0$), therefore:

$$\gamma_{s,v} < \gamma_{s,f} + \gamma_{f,v} \tag{4.6}$$

In hetero – epitaxial growth, the so called Stranski – Krastanov growth mode is the one mostly observed, that it can be seen as an intermediate state of the ones mentioned above. At the early stages (few monolayer), the thin film "*wets*" the substrate, but later islands are formed. This anomalous growth can be attributed to the biaxial strain that rises from the lattice mismatch between the thin film and the substrate. Within early mono – layers misfit dislocations are formed introducing the three dimensional growth [36]. Energetically it can be seen as:

$$\gamma_{s,v} > \gamma_{s,f} + \gamma_{f,v} \tag{4.7}$$

Step flow growth is present in the case of fast diffusion of deposited atoms on the substrate surface terraces and their nucleation on the step edges. All growth modes are schematically presented in Fig. 4.3. Due to the non – equilibrium processes involved during the growth of thin films by the PLD method, all the growth modes presented in the previous paragraph can be described only as limiting cases. Deposition conditions greatly affect the balance between the volume of the material deposited per pulse (supersaturation), the surface diffusion time for layer creation and substrate T that can alter the growth mode of a thin film [26].

Layer – by – layer growth, the "*holly grail*" of thin film growth, is more likely to happen in the case of small volume of material deposited per pulse, due to the smaller time needed for the deposited atoms to optimize their positions [24]. The volume of the deposited material can be controlled via Φ, background P and $d_{T\text{–}S}$. Surface mobility can be controlled by substrate T, background P, Φ and $d_{T\text{–}S}$. Increase of substrate temperature, increases the

EFTHYMIOS CH. SVOUKIS

surface diffusion rate. A detailed report of the influence of the deposition *T* on the structure of the thin film will be presented in section 4.4.2. Optimization of the deposition conditions is not only crucial for obtaining the desired phase in thin film form but also for achieving the preferred growth mode.

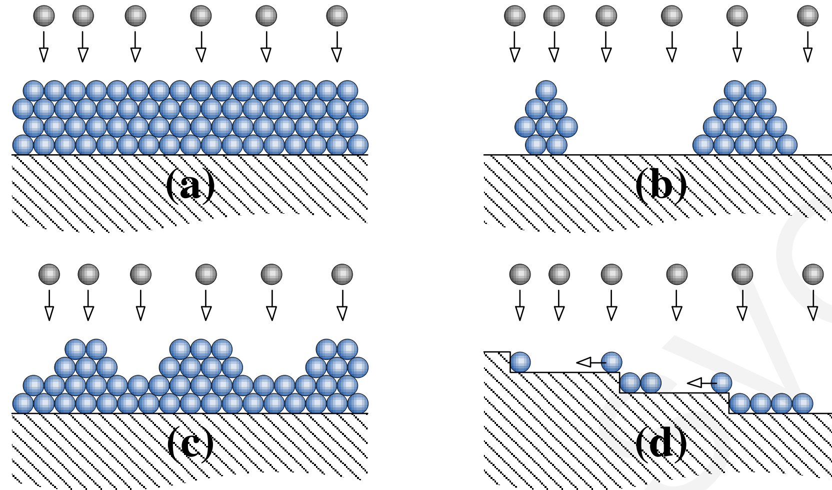

Figure 4.3: *Four basic thin film growth modes a) Frank-van der Merwe; b) Volmer – Weber; c) Stranski – Krastanov; d) Step flow.*

EFTHYMIOS CH. SVOUKIS

4.4 Microstructure

4.4.1 Strain – defects

Strain is being induced during the early stages of thin film growth. Due to lattice mismatching between thin film and substrate, tensile or compressing forces store elastic energy at their interface of the thin film. This energy is related to the mechanical properties of the thin film and the lattice mismatching.

At a specific thickness d_c (Fig. 4.1), the pseudomorphism limit, a maximum storage capacity of elastic energy is reached. Beyond that thickness, defects are created and / or transition to the Volmer – Weber growth mode occurs to relief the strain [111]. Typical defect formations are: stacking faults, low – angle grain boundaries, twining and misfit dislocations. Strain effects in the early stages greatly affect the transport properties of thin films, especially in the cases where d_c is comparable with the total thin film thickness [112]. Further increase of the thickness of the thin film above d_c, will introduce further defects until the misfit strain will

be minimized. The critical thickness, by assuming that no inter – diffusion appears at the interface, can be expressed as:

$$d_c = \frac{b}{8\pi m(1+v)} \ln\left(\frac{e}{r_0} d_c\right) \approx \frac{b}{9.9m} , \quad (4.8)$$

where, b is the magnitude of the Burger vector, m the lattice mismatch, v the Poisson ratio, e the base of the natural logarithm and r_0 the dislocation core [24].

The phenomenon of micro – crack formation appears in the case of thermal expansion coefficient difference between the thin film and the substrate. Defects due to strain effects exist in small thickness, whereas micro – cracking appears in order of magnitudes higher.

4.4.2 Zone model of thin films

Deposition T is a key player in hetero – epitaxial thin film growth. Layer – by – layer epitaxy can be triggered by lowering the supersaturation level and promoting one – dimension agglomeration. Further increase of T results in reducing the probability of impurity formation within the volume of the thin film [24].

An important parameter is the ratio of the substrate T to the melting temperature of the thin film T_m. Four main structural zones can be found for the growth of thick films as proposed by Thornton [113].

At Zone I $(T/T_m < 0.2)$, films consist of amorphous or poor crystallinity columns, typically 20*nm* in diameter, surrounded by smaller grains. A transition Zone T exists for $0.2 < T/T_m < 0.3$, where grains may expand to 50*nm*. Both Zones I and T exist due to Stranski – Krastanov growth mode. At Zone II $(0.3 < T/T_m < 0.5)$, surface diffusion appears. Grain and column boundaries become mobile. Further increase of temperature, Zone III $(T/T_m > 0.5)$, enhances surface diffusion, resulting in decrease of porosity and re – crystallization of the volume of the thin film [114]. Extensive temperature, close to T_m, can result in non – obtaining the desired phase due to possible phase transformation. In Table 4.1, the main characteristics of each zone are presented. Generally there is no universal deposition T for all the ceramic materials, but typical deposition temperatures are $0.4 < T/T_m < 0.8$.

EFTHYMIOS CH. SVOUKIS

Table 4.1: *Zone structures and typical characteristics of the produced thin films.*

Zone	T/T_m	*Structure Characteristics & Film Properties*
I	< 0.2	Voided boundaries, porous, poor crystallinity or amorphous
T	0.2 – 0.3	Similar to Zone 1, but free of voids
II	0.3 – 0.5	Columnar growth, plane boundaries
III	> 0.5	Large grains, low dislocation density, smooth surface

4.4.3 Columnar structure

Columnar grained structures is a typical behavior of thin films grown at Zones I and II [115]. Within the volume of the film, parallel rod – shaped columns appear. Generation of columns can be attributed to low diffusion mobility of the deposited atoms. Columnar structure has been observed especially on high melting materials and high energy bonding structures or after annealing procedures [116].

Columnar structure can induce a desired anisotropy such as in the case of waveguides. Generally, transport properties of thin films such as thermal conductivity are greatly affected by columnar structures [117,101,118].

Columns generally follow the so called "*tangent rule*". The angle between the columns and the substrate (β) is generally less than the angle of the spot centre and the substrate normal (α). Experimentally it is found that:

$$\tan\alpha = 2\tan\beta . \tag{4.9}$$

Shelf – shadowing effects generally reduce surface mobility [24].

EFTHYMIOS CH. SVOUKIS

Lanthanum Calcium Copper Oxide – $La_5Ca_9Cu_{24}O_{41}$

5.1 Introduction

Heat removal from electronic devices is crucial for their further miniaturization. In current typical Si – based devices, reduction of the working temperature, exponentially increases their robustness and life span [119]. Innovative microchips, hard drives, *etc.* consist of multilayer stacks. Each stack is constituted by a nano – scale thin film with independent transport and electronic properties. Uncontrollable temperature increases can activate diffusion reactions within the layers, change the properties in each layer and even melt the device. Considering Moore's law, prevention of overheating of novel devices becomes increasingly difficult [1]. Increase of the number of components per area increases self – heating problems within components as well as heating of neighbouring components.

Exploitation of novel materials and new device design approaches at a *nano* level has been identified as a research target within the scientific community. This was the scientific goal of the European program NOVMAG [22].

Classical thermal transport systems have limited use. In insulating materials heat is mainly carried by phonons, whereas in metals by electrons. Theoretical predictions by X. Zotos *et al.* showed that in the family of low – dimensional quantum magnet materials ballistic heat transport is expected [120]. The initial theoretical models have been experimentally verified in single crystals of prototype materials such as $SrCuO_2$, Sr_2CuO_3 and $(Sr,Ca,La)_{14}Cu_{24}O_{41}$ [121,122].

All aforementioned low – dimensional quantum magnet materials to be used in devices, they should be grown in thin film form and free of structural defect in order to maintain their properties.

EFTHYMIOS CH. SVOUKIS

5.2 Crystal structure of LCCO

The spin ladder family of compounds was discovered, as a research by – product, during the time of chasing new Cu – based high temperature superconductors [123]. The structure of LCCO, presented in Fig. 5.1.a, consists of three kind of layers stacked along the b axis:

- A CuO_2 layer – one dimensional spin chains (Fig.5.1.b.).
- A Cu_2O_3 layer – two leg Heisenberg spin ladders (Fig.5.1.c).
- A layer of La / Ca ions located between Cu_2O_3 – CuO_2 layers.

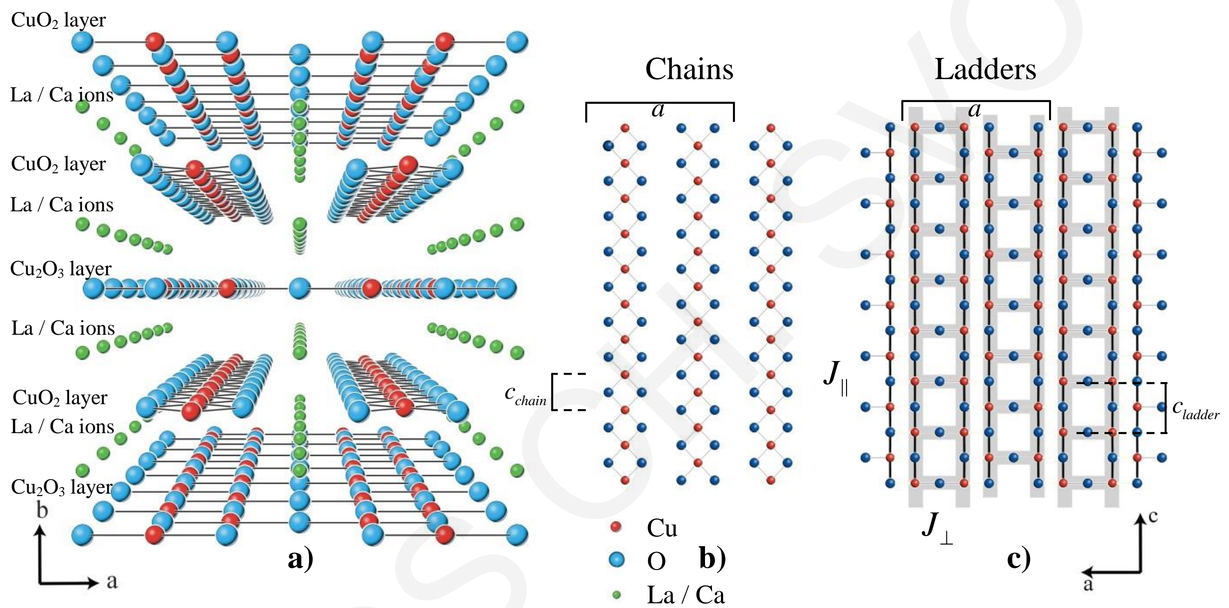

Figure 5.1: *a) Crystal structure representation of LCCO, along the c – axis. The structure consists of alternating layers of CuO_2, Cu_2O_3 and in between containing a layer of La / Ca – ions. b) Top view of CuO_2 planes containing chains. c) Top view of Cu_2O_3 planes containing ladders.*

Within ladder layers, Cu – ions form antiferromagnetic (180°) Cu – O – Cu bonds and are connected to adjacent ladders with (90°) Cu – O – Cu ferromagnetic bonds with exchange coupling along the legs of the ladders $(J_{\parallel})$ and along the rungs $(J_{\perp})$ [124,125]. In chains, Cu ions are ferromagnetically coupled [126].

Along the *a* – and *b* – axis, the ladders, chains and La layers have practically the same lattice parameters. Along the *c* – axis, the structure is incommensurable with $7\times c_{ladder} \approx 10\times c_{chain}$ (Fig. 5.1.b – c.) [127]. The super – cell has orthorhombic symmetry

EFTHYMIOS CHATZIOUKIS

$(CCCM)$, with bulk lattice parameters $a = 11.305\,\overset{o}{A}$, $b = 12.612\,\overset{o}{A}$ and $c = 27.608\,\overset{o}{A}$, total volume $V = 3935.69\,\overset{o}{A}^3$, and is constituted of 316 atoms [128].

5.3 Thermal conductivity of LCCO

The thermal conductivity of LCCO is highly anisotropic, with κ_a and κ_b (perpendicular to the ladders) following a typical phononic behavior with a low temperature maximum at ~25K followed by a monotonic decrease (T^{-1}). The thermal conductivity along the ladders (κ_c), exhibits two peaks. The first peak, appears at ~25K and is due to phonons. The second peak, appears at ~180K due to an increased magnetic conductivity contribution [122]. At room temperature, thermal conductivity has relatively high values $\kappa_c \geq 100\,Wm^{-1}K^{-1}$ with a very high anisotropy ratio $\kappa_c/\kappa_a \sim 50$.

The thermal conductivity, measured via a steady state method, of a LCCO micron – size single crystal as a function of temperature is presented in Fig. 5.2 [22]. Lower values of the thermal conductivity have been published in larger volume samples [129,130,131].

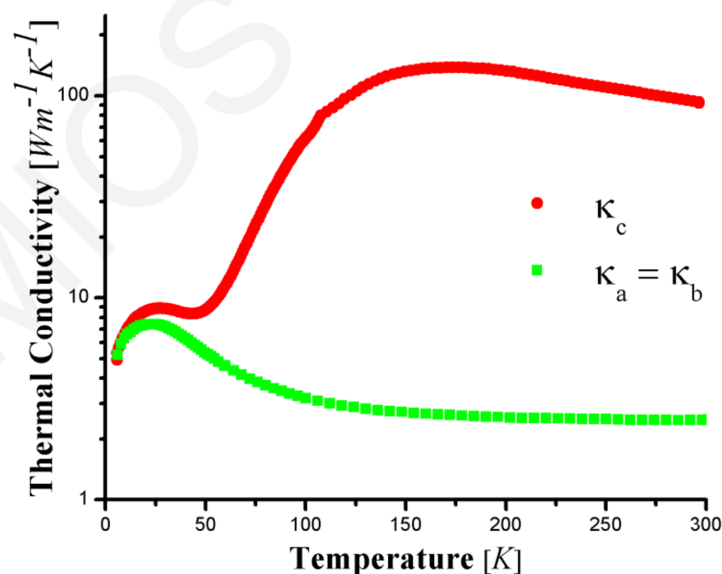

Figure 5.2: *Thermal conductivity as a function of temperature for a LCCO single crystal, from reference 14. The c – axis is parallel to the ladders and contributions to κ from phonon and magnons are present. The a – and b – axis are perpendicular to the ladders, with phononic only contribution to κ, and have comparable values of thermal conductivity.*

EFTHYMIOS CH. SVOUKIS

5.4 Thermal management

Thermal management refers to solutions for keeping the electronic elements at or below their maximum operating temperature. Solutions are more imperative when taking into account the increase in the number of electronic elements over area. Solutions such as: active cooling, heat piping, thermal interface materials, *etc*. have been proposed by the IC industries [132].

A possible strategy for thermal management is the use of novel materials with high and anisotropic thermal conductivity for the efficient channelling of unwanted heat, produced by the IC elements. This effective heat channelling can span the life of the heat – generating element. Further it can prevent failure of sensitive adjacent structures, permitting further miniaturization.

A possible material for use in such a device needs to have the following characteristics, and LCCO exhibits all of them:

- To be an electrical insulator.
- To have highly anisotropic κ.
- To exhibit high values of κ, $\kappa \geq 100 Wm^{-1}K^{-1}$.

Conventional heat conductors are usually isotropic e.g. an example where heat spreads isotropicaly is presented in Fig.3.a. A prototype device of effective heat channelling by using LCCO in vertical direction is presented in Fig. 5.3.b. Such advanced cooling devices can increase the number of adjacent components and decrease their distance.

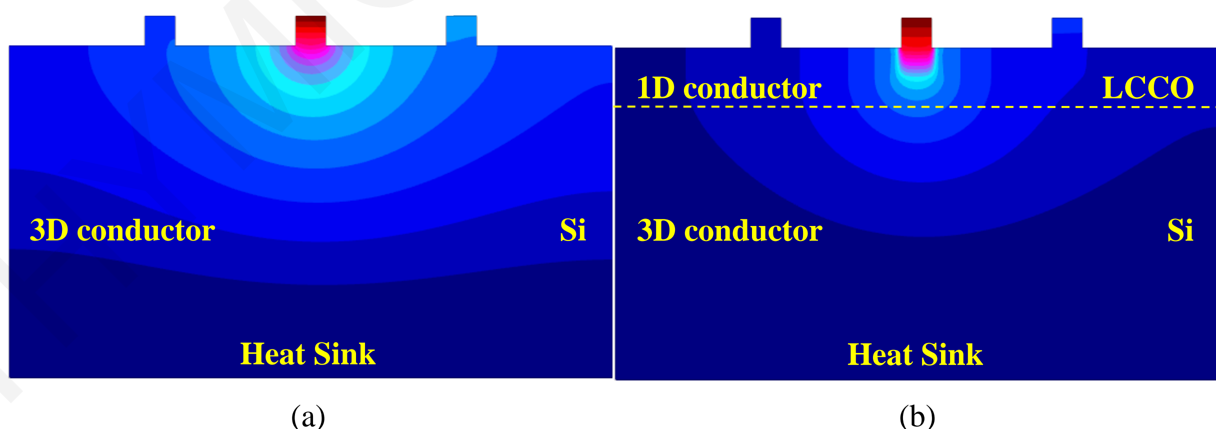

Figure 5.3: *A device with conventional isotropic heat removal (a). A prototype device with LCCO, where heat is conducted primarily along one direction (b).*

EFTHYMIOS CH. SVOUKIS

5.5 Synthesis of bulk LCCO and PLD target preparation

Bulk LCCO was initially synthesized by our collaborators at the Laboratoire de Physico – Chimie de l'Etat Solide in the Université Paris Sud. For the preparation of LCCO powders the solid state reaction was used.

Powders of La_2O_3, $CaCO_3$ and CuO with purity of 99.99% (Alfa Aesar), were mixed with the stoichiometric molar ratio of La:Ca:Cu = 5:9:24. They were grinded with an agate mortar and then pelletized. A sintering process at 900^oC for $12h$ took place in order to decarbonate the material. The resulting powder was reground and sintered again at 950^oC for $48h$ and at 970^oC for $48h$ in air, in order to complete the reaction and crystallisation of the desired material. The fine LCCO powder was cold pressed into a pellet that was then sintered at 970^oC for $48h$ in air in order to obtain a dense target, suitable for PLD. For all sintering procedures, heating / cooling rate of $5^oC\,/\,min$ was used [128].

The PLD target was characterized via XRD. The obtained pattern was refined via Rietveld analysis using PowderCell. All reflections were indexed and the lattice parameters of the structure were in good agreement with the literature values (section 5.2).

A refined XRD pattern is presented in Fig. 5.4. EDX investigations were also performed for elemental analysis of the final targets (La / Ca = 0.549 and (La+Ca)/Cu = 0.579). An EDX spectrum is shown as an insert in Fig. 5.4.

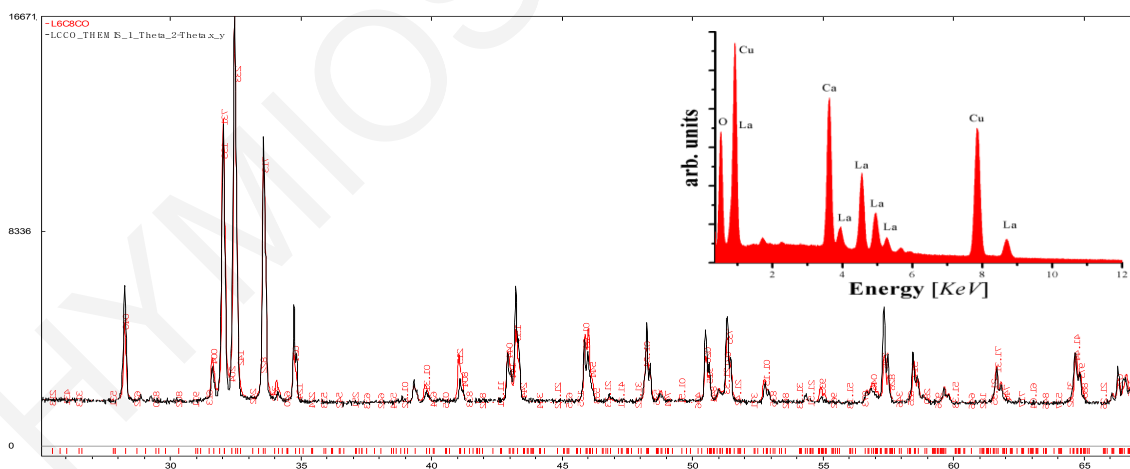

Figure 5.4: *Rietveld refinement using PowderCell of LCCO powder. All XRD peaks can be indexed according to the LCCO structure with R_{exp}=2.30. Insert: EDX pattern of the same powder.*

EFTHYMIOS CH. SVOUKIS

5.6 Towards c – axis LCCO Growth

LCCO can be used for heat channelling, when it is grown as highly oriented or epitaxial single crystalline thin films. Notably *c* – axis grown LCCO films would be optimum for thermal management in a columnar *c* – axis growth, promoting the thermal anisotropy. The PLD method was used for the growth of LCCO thin films, a method widely used for oxide thin films.

Hetero – epitaxial growth can be promoted, by using favourable lattice matched substrates. Substrates were also selected based on their transport and chemical parameters. Good adhesion and mechanical properties of the thin films narrowed the selection of substrates to oxides. Within Table 5.1 the ratios of LCCO lattice parameters *a* and *b*, over specified orientations of commercial substrates lattice parameters (Table 2.2) are presented. The values closer to integer values, suggest that these substrates are more suitable for *c* – axis LCCO growth.

Table 5.1: *Theoretical calculations for identifying suitable substrates for c – axis LCCO growth. The ratios of a and b LCCO lattice parameters over the lattice parameters of specifically oriented substrates at room temperature.*

Substrate (orientation)	***Structure***	$a_{LCCO}/a_{sub.}$	$a_{LCCO}/b_{sub.}$	$b_{LCCO}/a_{sub.}$	$b_{LCCO}/b_{sub.}$	***Suitable***
$SrLaAlO_4$ (010)	Tetragonal	3.010	0.895	3.358	0.998	Y
$Gd_3Ga_5O_{12}$	Cubic	0.913	0.913	1.019	1.019	Y
Al_2O_3 (0001)	Hexagonal	–	–	–	–	N
$\alpha - SiO_2$	Amorphous	–	–	–	–	N
$SrTiO_3$ (100)	Cubic	2.895	2.895	3.230	3.230	N

5.7 Growth on $SrLaAlO_4$ (100)

$SrLaAlO_4$ (010) (SLAO) was selected due to good domain lattice matching with LCCO. The *a* – axis of LCCO is expected to be parallel to the [100] of SLAO with a lattice mismatch of 0.33% by taking into account the three lattice parameters of SLAO. The *b* – axis of LCCO has a mismatch of –0.19%, with the lattice parameter along [001] of SLAO. A schematic representation of the expected epitaxial growth is presented in Fig. 5.5. Although

EFTHYMIOS CH. SVOUKIS

the lattice parameters are close, the oxygen sublattices of the two ceramic structures are quite different concerning their space arrangement.

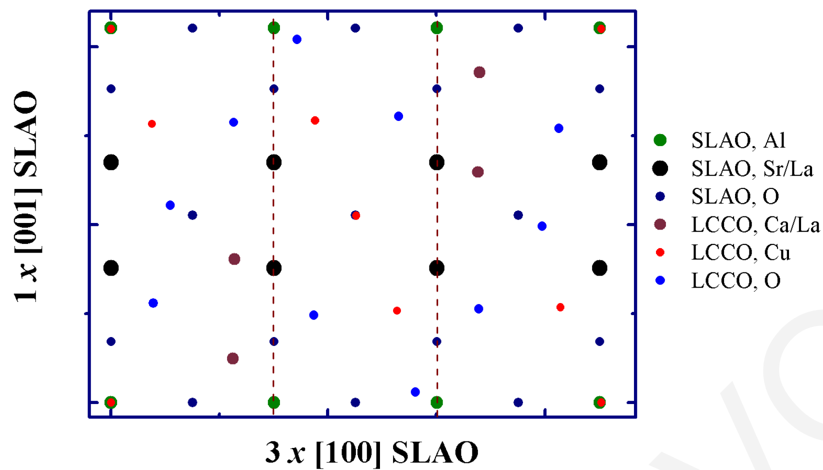

Figure 5.5: *The a – axis of LCCO has only 0.33% lattice mismatch with three lattice spacings of [100] SLAO. The b – axis has –0.19% mismatch with the [001] lattice parameter of SLAO. The position of oxygen atoms of LCCO and SLAO are different.*

All LCCO films were grown on SLAO by using the PLD method. As a background gas was used high purity (5.0) O_2 gas. The growth of thin films took place inside the commercial SURFACE deposition chamber using different deposition conditions. To obtain stoichiometric transfer, the pressure during deposition had to be adjusted in the range of 0.1–1.3*mbar* and this can be attributed to the high valence (+2) of copper (Cu) atoms within the LCCO structure. The initial ddeposition conditions we used were similar to those reported by Furubayashi *et al.* for the growth of $Ca_{14}Cu_{24}O_{41}$ on (0*k*0) $Sr_{14}Cu_{24}O_{41}$ single crystals [133]. The fluence ($\Phi = 1.3 Jcm^{-2}$) and distance target – substrate (d_{T-S}=41*mm*) were optimized, ensuring stoichiometric transfer. The influence of the deposition temperature on the growth of LCCO thin films was extensively studied. Series of LCCO films were grown with a small temperature step to investigate the crystallization processes during growth and determine the optimum temperature for the growth of crystalline thin films.

Structural characterization, using the Bragg – Brettano XRD configuration of LCCO films grown at different temperatures is presented in Fig. 5.6. The diffraction patterns revealed that the films grown at 650^oC or below exhibited amorphous behaviour. In contrary, within the XRD pattern of the films grown at 850^oC extra peaks appeared (marked with *) in addition to the (0*k*0) peaks. The appearance of the extra peaks can be attributed to randomly oriented crystallites resulting to textured polycrystalline LCCO thin films. Phase stability and

EFTHYMIOS CH. SVOUKIS

highly ordered(0*k*0) LCCO thin films are only obtained within a narrow temperature regime 700–800^oC.

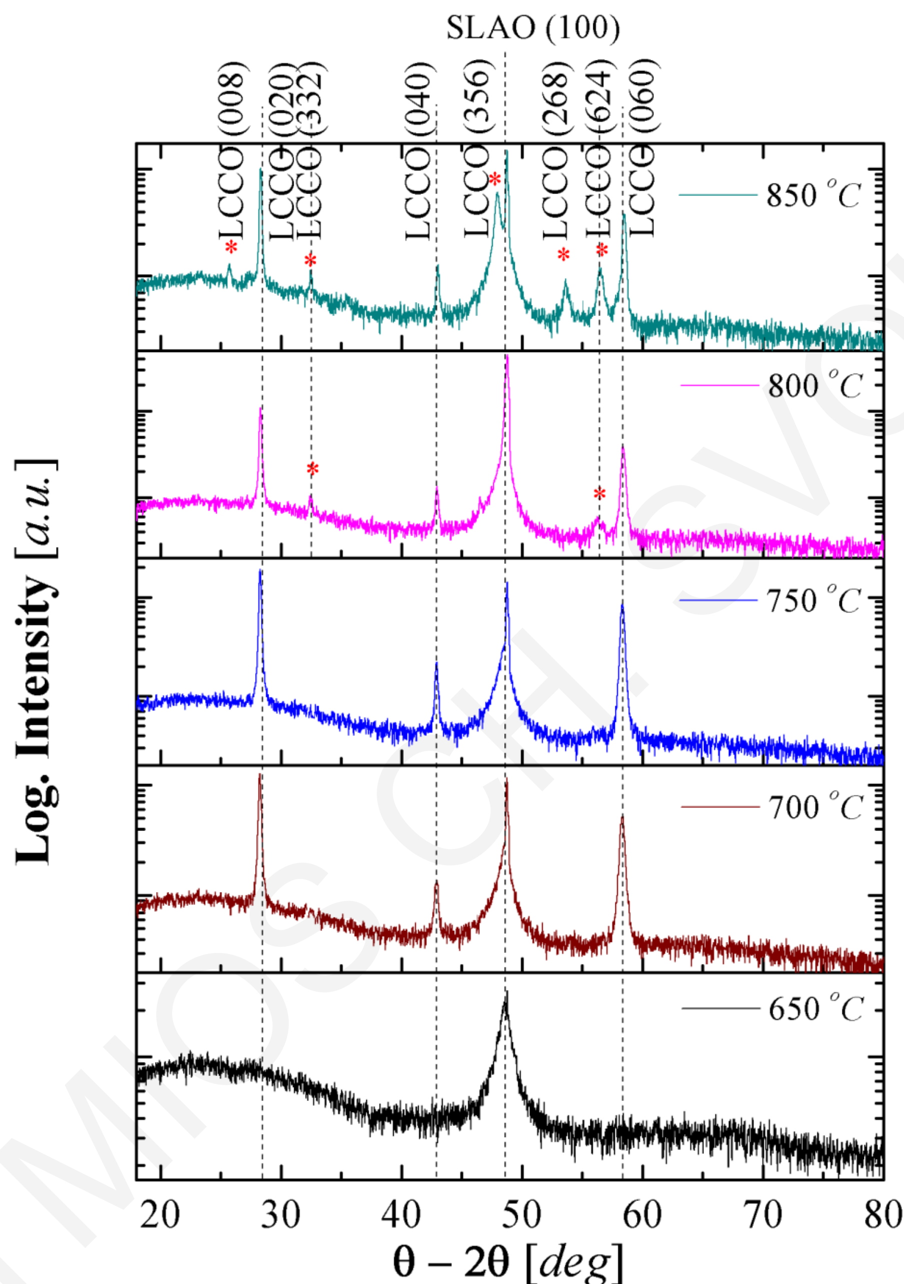

Figure 5.6: *XRD patterns of LCCO thin films grown on SLAO at different deposition temperatures. Only a small temperature regime (700–800^oC) exists where the LCCO thin films are crystalline, free of secondary phases and (0k0) oriented. With asterisks are marked additional peaks, appearing on the film grown at 850^oC. Films grown below 650^oC, showed no evidence of crystallinity.*

For all the films grown on SLAO at various deposition conditions, no evidence of (00*l*) peaks appeared on the XRD patterns, in contrast to other published work [134]. The

EFTHYMIOS CH. SVOUKIS

predictions for the expected *c* – axis growth on the specific substrate were not verified. Above the threshold deposition temperature, where crystallization appears, evidence of (0*k*0) reflections are evident within all XRD patterns.

All LCCO films grown on SLAO can be described as only / or highly *b* – axis oriented *i.e.*, chains and ladders are parallel to the SLAO initial free surface. This deviation from the prediction based on lattice mismatch calculations can be attributed to preferential growth of the films due to thermodynamic reasons, more specifically to minimization of the surface free energy.

Based on the structural study, the film grown at $750^o C$ showed the best crystallinity along the growth direction. The *b* – axis lattice parameter of the LCCO thin film, using the (040) peak, was calculated to be $12.670\,\overset{o}{A}$, exhibiting an ~0.4% expansion toward the growth direction.

The rocking curve of the (040) LCCO peak is presented in Fig. 5.7. The FWHM of the peak was calculated to 1.26^o, a value showing that there is small mosaicity, *i.e.,* divergence in the crystallites growth direction. This value can be decreased more by further tuning the deposition conditions and especially the deposition rate.

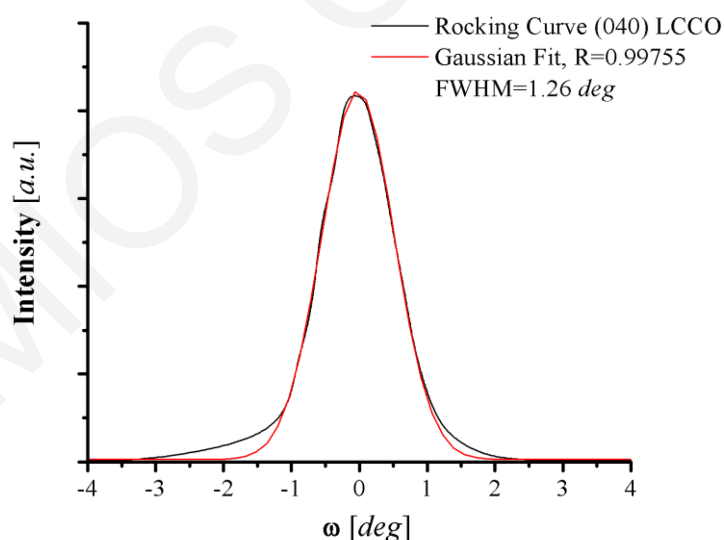

Figure 5.7: *Rocking curve of the (040) LCCO peak of a film grown at 750°C. The Gaussian Fit results in a FWHM of 1.26 deg.*

The determination of the *in* – plane growth orientation of the LCCO thin films was made using the asymmetric reflections (–260) and (3–10) for LCCO and SLAO, respectively. The *a* – axis lattice parameter of the LCCO thin film grown at $750^o C$, was calculated to be

EFTHYMIOS CH. SVOUKIS

11.235 Å, exhibiting an ~0.6% contraction. Azimuthal scans based on the previously reported reflections showed that LCCO crystallites have a predominant *in* – plane orientation.

In Fig. 5.8 the azimuthal scan of a film grown at 750^oC is presented. Two low intensity humps between the main peaks appear in the azimuthal scan of the LCCO pattern, revealing that a few LCCO crystallites are grown rotated *in* – plane 90° with respect to the predominant orientation. The epitaxial relationship of the predominant *in* – plane orientation is [001] LCCO parallel to [100] of SLAO.

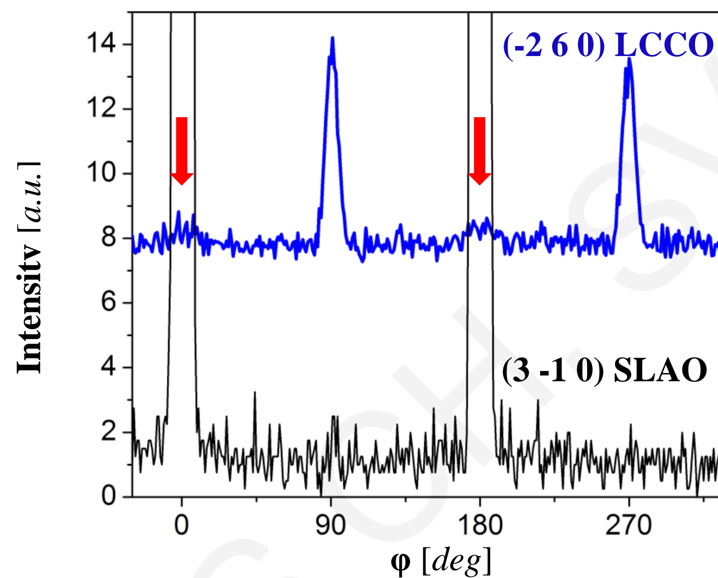

Figure 5.8: *Azimuthal scans of a LCCO thin film grown on SLAO (100). Low intensity peaks (marked with red arrows) appear between the main peaks of LCCO.*

The cross – plane thermal conductivity of a relatively thick LCCO thin film was investigated using the differential *3ω* method. To ensure reproducibility the growth of the thin film was performed using the optimum growth conditions, with an increased number of pulses (3000 *pulses*) to ensure an adequate thickness (≈350*nm*).

At room temperature, the *b* – axis thermal conductivity $\kappa \approx 2Wm^{-1}K^{-1}$ is ~70% of those one reported for the *b* – axis of LCCO single crystals [135]. At lower temperatures, the thermal conductivity decreases over temperature, a behavior that can be attributed to scattering processes within the thin film structure. The thermal conductivity of the LCCO film and the SLAO substrate are presented in Fig. 5.9.

EFTHYMIOS CH. SVOUKIS

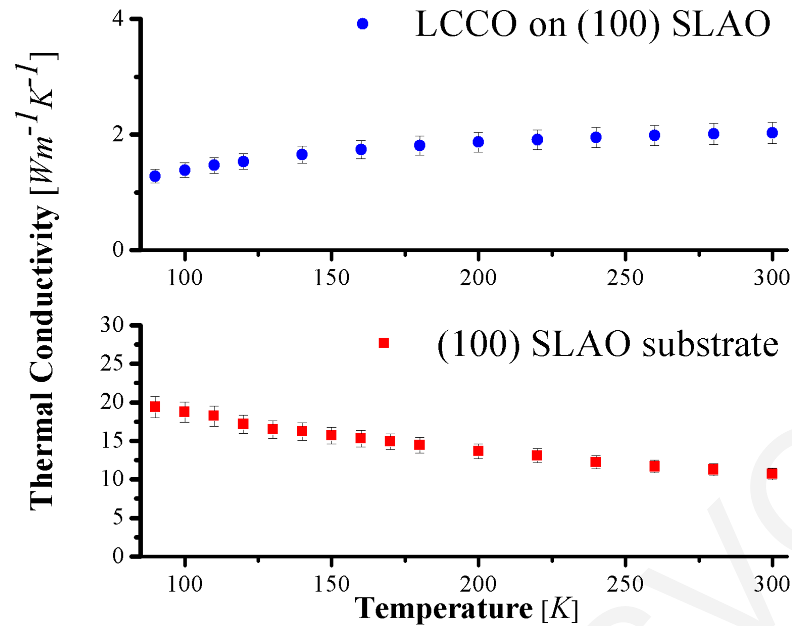

Figure 5.9: *Thermal conductivity as a function of temperature for a LCCO thin film grown on SLAO (top) and for a SLAO substrate (bottom). At room temperature the cross – plane thermal conductivity of the LCCO thin films is ~70% that of a LCCO single crystal* [135].

5.8 Growth on $Gd_3Ga_5O_{12}$ (100)

$Gd_3Ga_5O_{12}$ (100) (GGO) has a cubic garnet structure (Fig. 5.10) with a lattice parameter 12.376 Å close to those of *a* and *b* axis of LCCO. Specifically, at room temperature the lattice mismatch along the *a* – and *b* – axis of LCCO are –8.65% and 1.91%, respectively. As the lattice mismatch along the *a* – axis is of LCCO is higher than 7%, the structural properties of the grown films, will probably be affected.

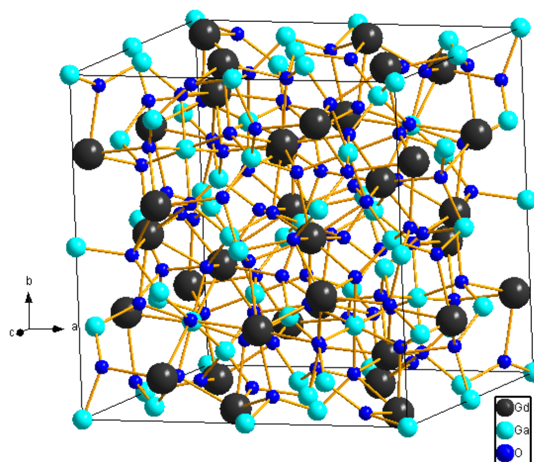

Figure 5.10: *The GGO cubic garnet crystal structure.*

EFTHYMIOS CH. SVOUKIS

The PLD method was used for the growth of LCCO thin films on GGO (100) substrates. The deposition conditions were similar to those used in the case of SLAO. The influence of deposition temperature on the structural properties of the films showed no difference from the case of SLAO. All LCCO thin films are only highly b – axis oriented. Within the temperature regime 700–800^oC only (0k0) LCCO peaks appear in the XRD patterns, evidence of a highly b – axis oriented thin film. A typical XRD pattern, using the Bragg – Brettano configuration, of a LCCO thin film grown at 700^oC is presented in Fig. 5.11.

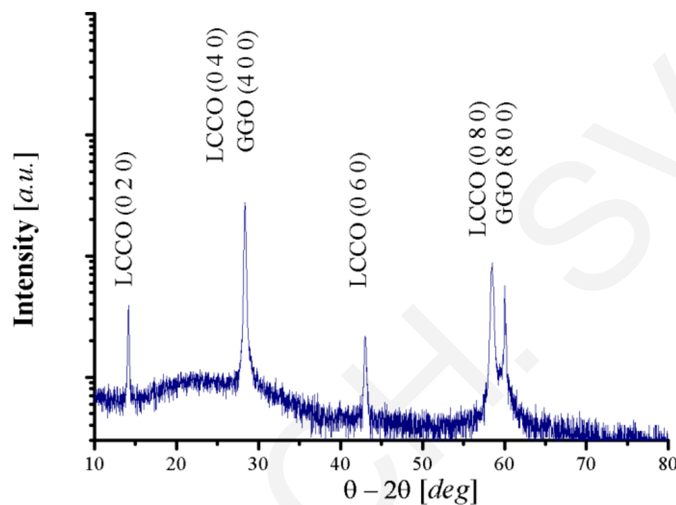

Figure 5.11: *XRD pattern of a LCCO film grown on GGO at 700°C. Only (0k0) reflections are present, evidence of a b – axis oriented thin film. All films grown on GGO (100) substrates within the temperature region 700–800°C showed similar XRD patterns.*

Post deposition LCCO films were studied using the RHEED method at various temperatures. A high electron voltage of 30kV was used for the acceleration of the electrons in a UHV environment for high contrast imaging. A RHEED pattern of a thin film grown at 700^oC is presented in Fig. 5.12. Island formation is the reason for the appearance of streaks, as a result of the broadening of the initial 1 – Dimensional reciprocal rods. Appearance of many spots (transmission like patters) can be attributed to scattering further inside the thin film, due to appearance of 3 – Dimensional structures. Within all LCOO thin films grown on GGO, similar RHEED patterns were observed, indicative of a Stranski – Krastanov growth type.

EFTHYMIOS CH. SVOUKIS

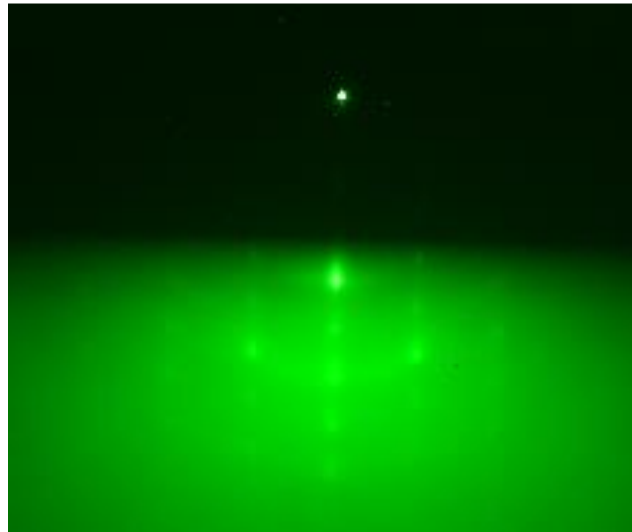

Figure 5.12: *RHEED pattern after the growth of LCCO on GGO at room temperature in a UHV environment. The incident electron beam is accelerated with 30kV. A spotty pattern appears along specific azimuthal angles, indicative of Stranski – Krastanov growth.*

The appearance of large particulates due to splashing is an intrinsic problem of PLD, which is correlated with the deposition parameters used. LCCO thin films grown on GGO, characterized by SEM over large areas, exhibited surfaces, which are mainly free of micron – size particles (Fig. 5.13). Further magnification showed the appearance of cracks. Because of their size the cracks cannot be attributed to strain relief but to thermal expansion coefficient differences (insert in Fig. 5.13.).

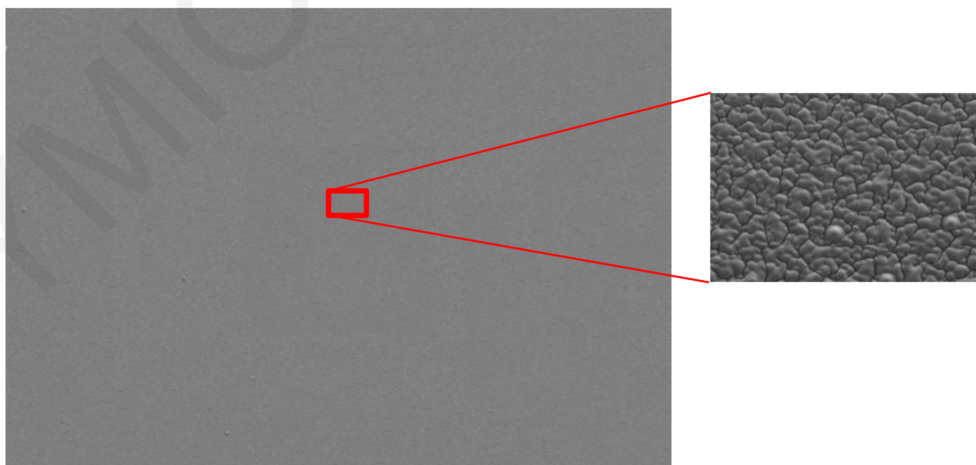

Figure 5.13: *SEM image of a LCCO thin film grown on GGO at 750°C. At large field of view, the surface is free of agglomeration particles. Magnified image of a small area revealed sub – micron cracks, attributed to thermal expansion coefficient difference (insert).*

EFTHYMIOS CH. SVOUKIS

5.9 Growth on α – SiO_2 and Al_2O_3 (0001)

As previously reported, regardless of the lattice mismatching or the deposition parameters used, the LCCO thin films are grown preferentially with the *b* – axis parallel to the growth direction. Compared to most compounds where temperature or substrate selection has a major impact on the growth of the thin films, LCCO shows an intrinsic tendency for *b* – axis growth. This can be attributed to thermodynamic reasons related to the LCCO system.

To validate the above assumption, LCCO films were grown on *a* – SiO_2 and Al_2O_3 (0001). Both of them are less suitable substrates for *c* – axis growth, allowing the emergence of the intrinsic tendency of the LCCO system. For both substrates, similar deposition conditions were used, resulting to *b* – axis oriented growth thin films. XRD patterns of LCCO thin films grown on *a* – SiO_2 and Al_2O_3 are presented in Fig. 5.14. Post deposition RHEED characterization of the films showed than in the case of *a* – SiO_2 the film is randomly oriented *in* – plane. In the case of Al_2O_3 Stranski – Krastanov growth type appears.

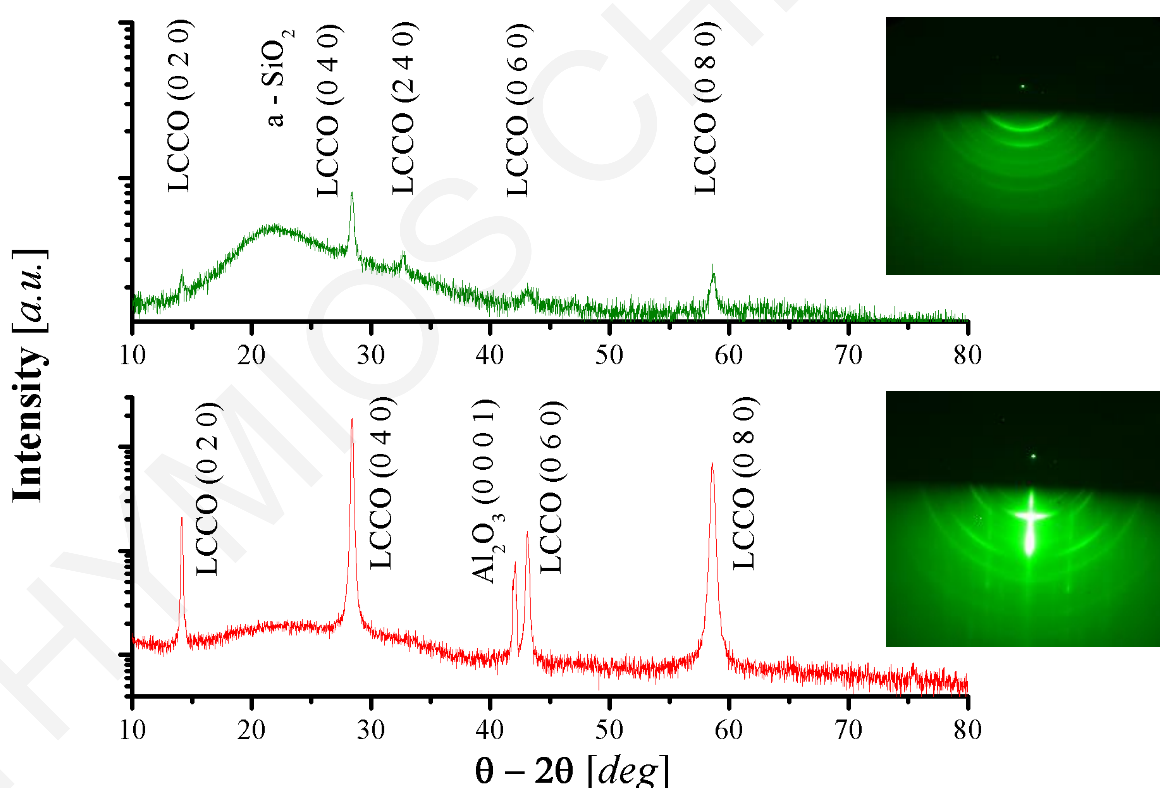

Figure 5.14: *XRD patterns of LCCO thin films grown at 700°C on "no lattice matching" substrates a – SiO_2 (top) and Al_2O_3 (0001) (bottom). Films in both cases are b – axis oriented due to thermodynamic reasons. Post deposition RHEED pattern is presented as insert for each thin film.*

EFTHYMIOS CH. SVOUKIS

5.10 Growth on LCCO (001) Single Crystal

Based on all the previous investigations using various substrates and deposition parameters, it is evident that *c* – axis LCCO thin films are not preferable for growth. A possible reason is that the ratio of lattice parameters $\left(c_{LCCO}/b_{LCCO}=2.19\right)$ is close to an integer number. Contrary to YBCO, deposited LCCO films exhibit preferential *b* – axis growth with no great influence by the substrate temperature on the growth direction [136].

The homo – epitaxial growth on a *a* – *b* plane oriented LCCO single crystal, would reveal the potential of *c* – axis LCCO growth. A LCCO thin film was deposited on a $22.8\pi\ mm^2$ ellipsoidal *a* – *b* plane LCCO single crystal at 700^oC, which was grown at the Laboratoire de Physico – Chimie de l 'Estat Solide in the Université Paris Sud, within the NOVMAG project using the travelling floating zone method [128]. Prior to deposition the surface of the crystal was carefully polished to RMS roughness down to only 20*nm* at the University of Groningen.

On the prior – and post – growth XRD patterns, only (00*l*) peaks are present. The intensity of the peaks is enhanced and no extra peaks appear on the post deposition pattern, which is evidence of the high crystallinity and purity of the thin film. The XRD patterns prior and post growth are presented in Fig. 5.15. Based on the results, *c* – axis LCCO growth is possible only in homo – epitaxy. This can be attributed to similarities of the substrate and film regarding the chemical potential and oxygen sub – lattice.

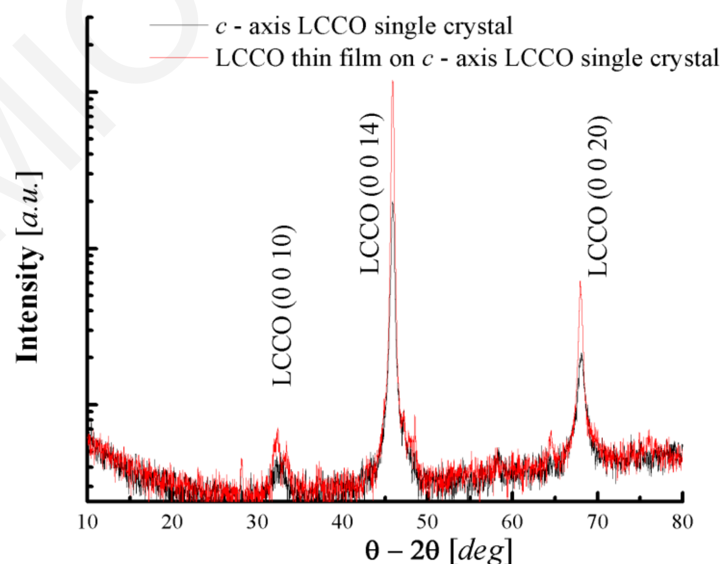

Figure 5.15: *XRD prior and post homoepitaxial growth of LCCO on a plane LCCO (001) single crystal. The (00l) peaks intensity is enhanced after the thin film growth.*

EFTHYMIOS CH. SVOUKIS

5.11 Growth on STO

Based on all the previous investigations, it is evident the intrinsic tendency of LCCO for preferential *b* – axis thin film growth. $SrTiO_3$ (STO) was selected as a possible substrate for the growth of epitaxial single – domain *b* – axis oriented films. Further STO has widely been used for the growth of YBCO and other high temperature superconductors [137].

5.11.1 Grown on $SrTiO_3$ (001)

STO (100) has a perovskite structure with cubic symmetry and lattice parameter $a_{STO} = 3.905\,\overset{o}{\mathrm{A}}$ at room temperature. The advantage of STO is the ability to control its surface termination through chemical and thermal methods.

5.11.1.1 Termination control

As a perovskite structure, STO can have two possible non – polar surface terminations, SrO and TiO_2 or a mixture of the two [138]. Initial surface termination and morphology of STO can dramatically alter the initial growth sequence of the thin film. By using chemical and thermal methods SrO can be eliminated [139]. Based on the literature, a methodology for TiO_2 termination and surface preparation of STO (100) single crystals was used. In Fig. 5.16 is shown an AFM image of an as received STO sample. The surface consists of terraces with disordered step heights. Furthermore, large impurities are present on the surface.

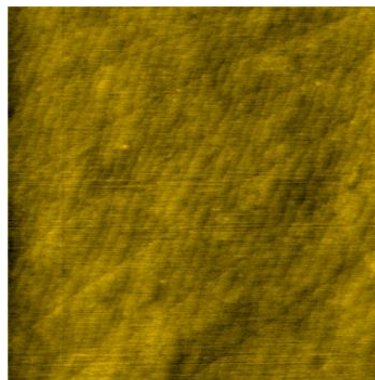

Figure 5.16: *8μm x 8μm AFM image of an as – received STO (001) substrate. Terraces, but not well defined, and impurities are present on the surface of the substrate.*

EFTHYMIOS CH. SVOUKIS

Mixed – terminated surface of STO substrates was modified by using the slightly modified Kawasaki *et al.* recipe, in order to obtain pure TiO_2 terminated surface [20]. The termination process and surface regrowth results from chemical and thermal treatment [140].

Initially STO substrates were placed in an ultrasonic bath with de – ionized water (R > 10$M\Omega$) for 20*min*. Different STO terminations have different chemical properties, therefore, selective chemical reactions can be used for surface transformations *e.g.* hydroxide complexes of specific cations can be selectively removed by etching. Commercial buffered hydrofluoric – acid (BHF, Merck, NH_4F : HF = 87.5:12.5) was selected for the removal of Sr – hydroxide complexes. TiO_2 surfaces are unaffected by water treatment, due to their enhanced chemical stability. STO samples were submerged for 5*sec*. in the acid solution. Finally, the neutralization of the acid, two di – ionized H_2O baths in a row were used.

Samples were thermally treated at different temperatures in vacuum or at presence of oxygen atmosphere for optimization of the treatment conditions [141]. The best heat treatment was found to be annealing at 900^oC in oxygen atmosphere.

AFM images of two samples, with different vicinal angles, annealed at 900^oC for 1hour in oxygen atmosphere are shown in Fig. 5.20a – b. A RHEED pattern of a STO (100) substrate after the chemical treatment is presented in Fig 5.20.c. Bright spots and Kikuchi lines are present in the RHEED pattern, revealing a smooth atomically flat surface.

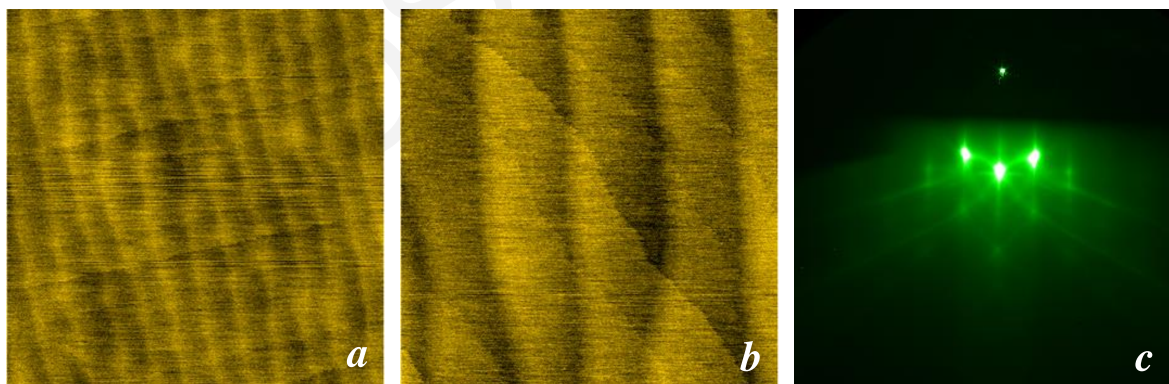

Figure 5.17: *2μm x 2μm AFM images of STO (001) samples after annealing at 900°C for 1 hour in oxygen atmosphere. The difference in the width of the terraces is due to difference in vicinal angles. The substrates surface morphology of large and small vicinal angle samples are presented in a and b, respectively. A RHEED pattern of a STO (001) substrate prior annealing is presented in image c.*

5.11.1.2 Thin film growth and characterization

LCCO films were deposited by PLD on STO (001) substrates heated to a range of temperatures. The KrF* excimer laser was used with a $\Phi = 1.3 Jcm^{-2}$ at a repetition rate of $1 Hz$. Oxygen partial pressure of $1.2 mbar$ and $d_{T\text{-}S} = 45 mm$, ensured stoichiometric transfer.

Phase purity and thin film growth orientation was initially investigated via XRD and EDX. Within the deposition temperature range of 700–800^oC LCCO thin films exhibit phase stability (within the resolution of the instrument) and only (0*k*0) peaks appear in their XRD patterns similarly to those deposited on other typical commercial oxide substrates. A $\theta - 2\theta$ XRD pattern of a thin film grown at 700^oC is presented in Fig. 5.18. EDX on selected thin films verified the absence of impurity atoms and stoichiometric transfer of the ceramic material from the target to the substrate. An EDX spectrum, with peaks only related to the atoms of the thin film and substrate, is presented as an insert in Fig. 5.18.

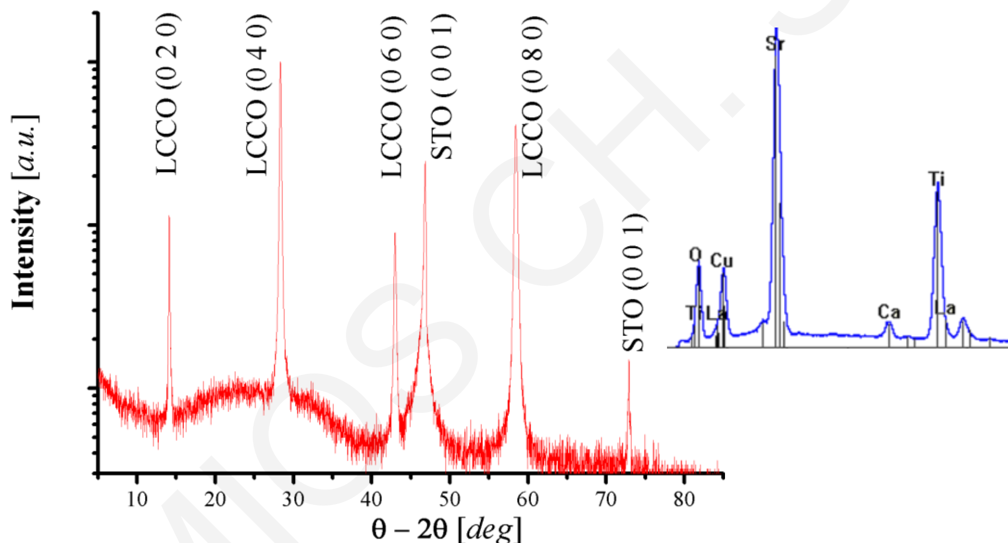

Figure 5.18: *XRD pattern of a LCCO thin film grown on a chemically and thermally treated STO (001) substrate at 700^oC. All peaks are related to the (0k0) peaks of LCCO. Insert of EDX spectrum, where peak positions are only related to the atoms of the substrate and the thin film.*

The structure of LCCO thin films was further investigated by TEM at Aristotle University of Thessaloniki. A JEOL 2011 TEM, operating at $200 kV$ and having a point resolution of $1.91\mathring{A}$, was used for the investigation of the structural features of the films. Specimens suitable for cross – sectional and planar view TEM observations, were prepared

EFTHYMIOS CH. SVOUKIS

using the traditional techniques, including mechanical polishing followed by ion thinning with Ar ions of energy of 4*keV*.

Diffraction patterns revealed the growth of a polycrystalline LCCO thin film on a STO (001) substrate, Fig. 5.19.a. The growth direction of the film [010] LCCO is parallel to [001] of STO. The appearance of small spots, close to the [001] spot of STO, can be attributed to the existence of LCCO nano – crystallites with small deviation angles.

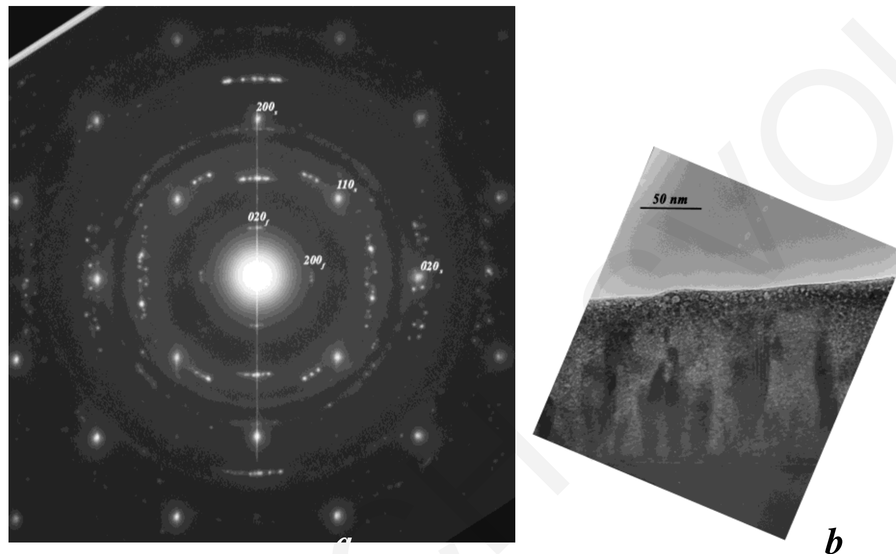

Figure 5.19: *Diffraction pattern of a LCCO film grown on a STO (001) substrate at 700°C. a) The existence of lighter intensity spots around the intensive spots in a diffraction image, is evidence of crystallites with small deviation angles. b) Conventional TEM of the same sample. Zone II type growth is present within the film structure, with average column width of 16.3nm. The thickness of the film was estimated to be 149 ± 8 nm.*

Conventional cross section imaging, was used to measure the thin film thickness and determine the growth characteristics in low magnification. Thin film growth can be described as Zone II with an average column diameter of 16.3*nm*. Conventional TEM image of the columnar growth is presented in Fig. 5.19.b. The thickness of the particular film was measured to be 149 ± 8 *nm* and good uniformity was verified. Based on the total number of pulses used for the growth of the thin film, the D_R is calculated to be $\sim 3\,\mathring{A}/pulse$.

Detailed investigation of the sample was achieved using high resolution analysis and conventional planar view TEM. The columnar microstructure within the thin film was verified. Fig.5.20, indicates that the columns are free of defects and adjacent columns have different growth directions. The poly – crystallinity of the film was confirmed through plannar view investigations, Fig. 5.21.

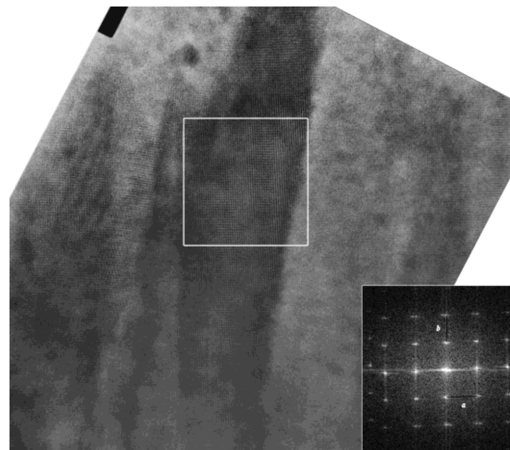

Figure 5.20: *Cross – section high resolution TEM image of a LCCO film grown on a STO (001) substrate at 700°C. The columns appear to be free of defects. A FFT transform of the selected area is presented as an inset.*

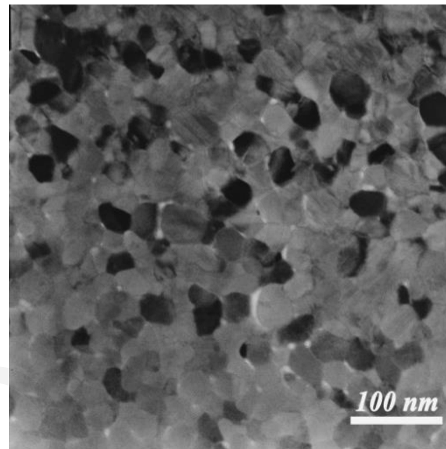

Figure 5.21: *Conventional planar view TEM image of the top surface of a LCCO thin film grown on a STO (001) substrate at 700°C.*

5.11.2 $SrTiO_3$ (110)

5.11.2.1 Preliminary experiments on STO (110)

STO (11x) surfaces, with *x* being and integer number are polar, therefore new phenomena are expected to emerge due to surface characteristics [142, 143]. STO (110) single crystals is a stack of alternating layers $SrTiO^{+4}$ and O_2^{-4}. The specific STO plane has an

EFTHYMIOS SVOUKIS

orthogonal like surface symmetry with parameters $3.905\,\mathring{A}$ and $5.523\,\mathring{A}$ along the directions [001] and [1–10], respectively [144]. A schematic representation of the STO (110) top surface is presented in Fig. 5.22.

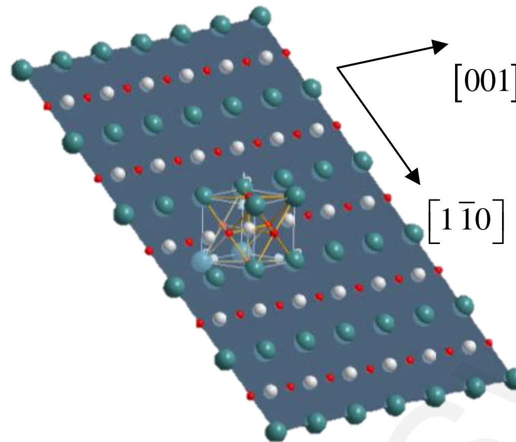

Figure 5.22: *Schematic representation of the non reconstructed surface of STO (110).*

Based on the lattice parameters of STO (110), LCCO can be grown with domain epitaxy. The *a* – axis of LCCO is expected to be parallel to the [001] of STO (110) with a lattice mismatch of –3.63% by taking into account three domains of STO (110). The *c* – axis of LCCO has a mismatch of –0.02%, by taking into account five domains along the [1–10] direction of STO (110). Good lattice matching makes this type of substrate a possible candidate for promoting the epitaxial single domain growth of *b* – axis oriented LCCO thin films.

LCCO films were deposited by PLD on STO (110) substrates. Substrates were heated over a range of temperatures to investigate the influence of the deposition temperature on the growth mode.

Out – of – plane structural characterization was performed using the Bragg – Brettano XRD configuration. XRD patterns of LCCO films grown at different temperatures is presented in Fig. 5.23. The diffraction patterns revealed that thin films grown at temperatures below 550^oC are amorphous. All films above 550^oC showed evidence of crystallinity. Phase stability and ordered (0*k*0) LCCO thin films are only present within a close temperature regime 650–700^oC. Thin films grown at temperatures above 750^oC showed the appearance of additional XRD peaks attributed to randomly oriented crystallites.

EFTHYMIOS CH. SVOUKIS

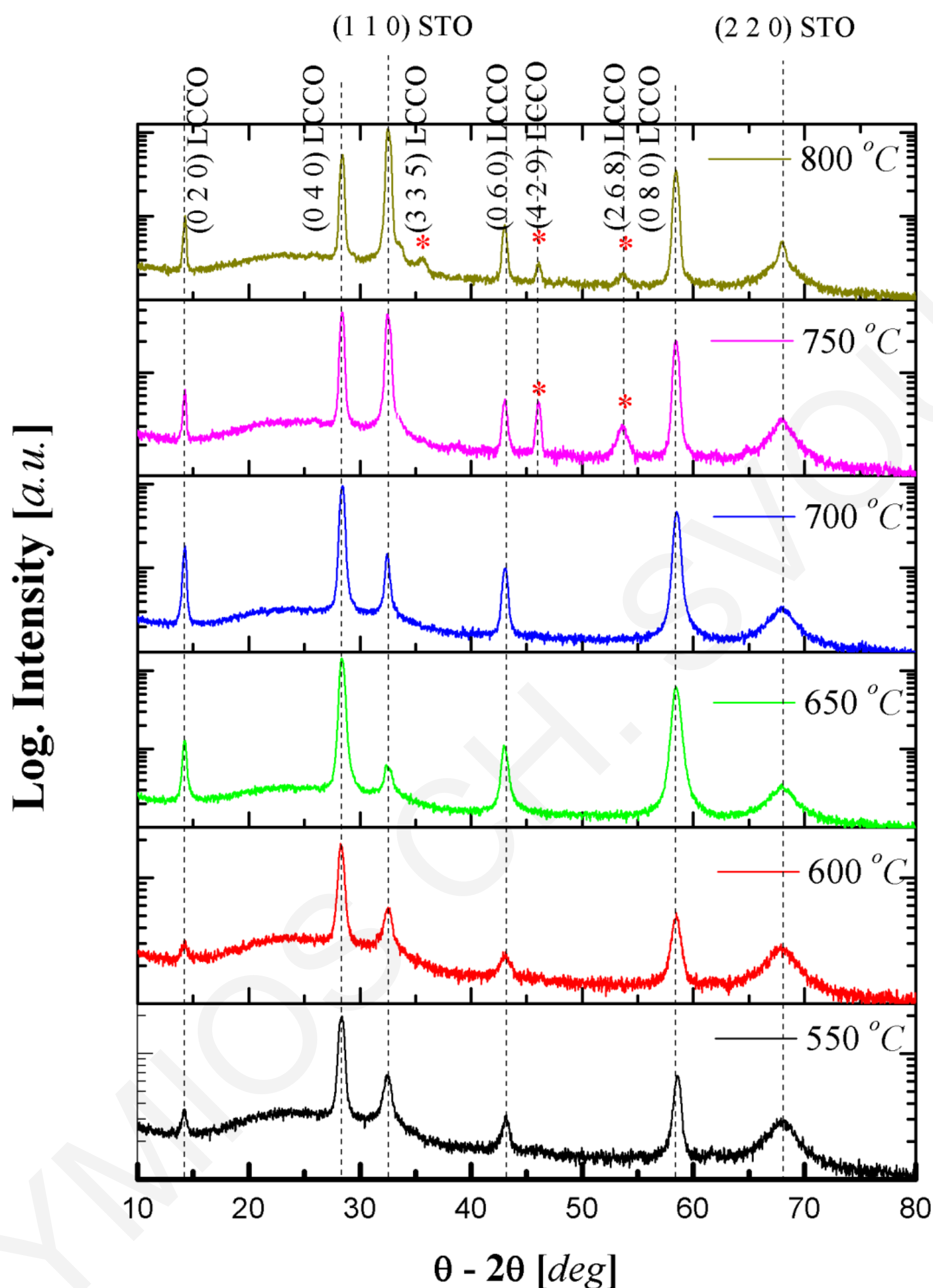

Figure 5.23: *XRD patterns of LCCO thin films grown on STO (110) substrates at different deposition temperatures. Only a small temperature regime (650–700°C) exists where the LCCO thin films are crystalline, free of secondary phases, and (0k0) oriented (with all the (0k0) peaks present).*

Based on the structural characterization, the deposition temperature of 700°*C* was selected for further investigation, due to the high intensities of the (0*k*0) appear in the XRD patterns. The influence of film thickness of the stoichiometry of the thin film was investigated

with the growth of thin films with different number of pulses 250, 500 and 1500 *pulses*. The EDX results for the LCCO target and the three LCCO thin films are shown in Table 5.2. The (La+Ca)/Cu ratio for all the films produced in the current study is very close to that of the target. The La/Ca ratio shows a La deficiency in all films which can be attributed to the higher vapour pressure of La compared to the other elements. Nearly perfect stoichiometric transfer is achieved, despite the complexity of the structure and the large number of atoms (316) in the unit cell of this incommensurable superstructure.

Table 5.2: *Results of EDX analysis for the LCCO target and the three LCCO thin films with different number of pulses. Nearly perfect stoichiometric transfer is achieved, despite the complexity of the structure.*

	Target	***Thin Films***		
		250 ***pulses***	**500** ***pulses***	**1500** ***pulses***
La/Ca	0.55 ± 0.01	0.48 ± 0.03	0.49 ± 0.03	0.45 ± 0.03
(La+Ca)/Cu	0.43 ± 0.01	0.44 ± 0.03	0.42 ± 0.03	0.40 ± 0.03
Thickness (*nm*)	N / A	90 ± 5	185 ± 10	550 ± 10

The microstructure of the 250 *pulses* thick LCCO thin film was investigated in detail with TEM. It was confirmed that the LCCO thin film was epitaxial. Fig. 5.24 demonstrates the overlap of the individual patterns of the substrate and the film; the open black circles indicate the positions of the diffracted beams coming from the substrate and the white rectangle stands for the reciprocal lattice unit cell.

The deduced interplanar spacings confirm that the structure of the substrate is cubic with a cell parameter $a_{STO} = 3.905\,\mathring{A}$. The second group of reflections corresponding to the dashed line frame originates from the film and the calculated interplanar spacings show an orthorhombic structure with cell parameters $a = 11.424\,\mathring{A}$, $b = 12.632\,\mathring{A}$ and $c = 27.598\,\mathring{A}$. The [010] direction of the film is perfectly parallel to the [110] direction of the substrate, revealing a very good epitaxial growth of the film.

EFTHYMIOS CH. SVOUKIS

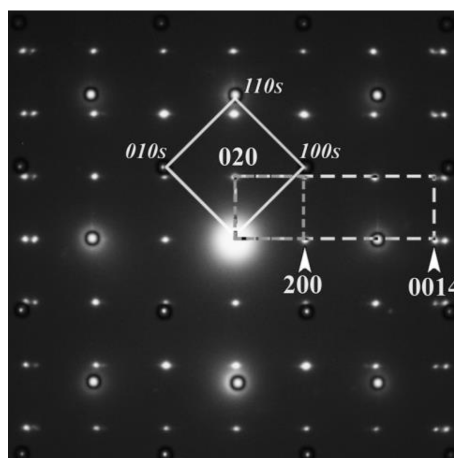

Figure 5.24: *Selected area electron diffraction pattern of a cross – section TEM sample demonstrating the overlap of the individual patterns of the substrate and the film.*

Fig. 5.25.a depicts a High Resolution TEM micrograph which reveals the columnar growth of the film, with thickness of 90±4*nm* and column width of up to 190*nm*. The white lines indicate the borders of the columns and the small white rectangle presents the unit cell of LCCO. The inset of Fig. 5.25.a shows a projection of the same structure overlapping with the magnified part of the micrograph is shown. The epitaxial relationship of the film in the columns "*a*", "*b*" and "*d*" is $[100]_{LCCO}//[1\text{-}10]_{STO}$ while in column "*c*" is [001]LCCO//[1-10]$_{STO}$.

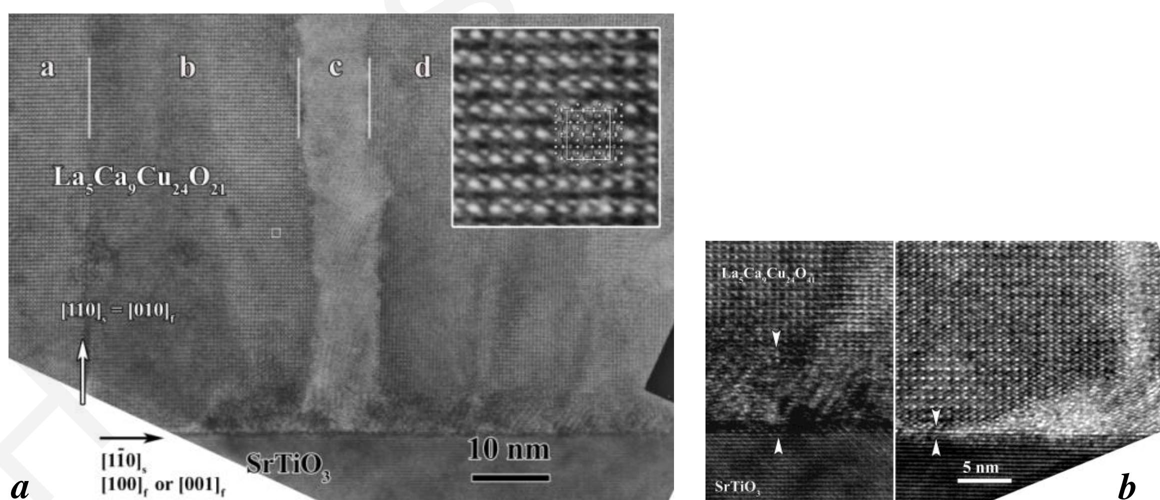

Figure 5.25: *a) High – Resolution TEM micrograph. b) Presence of a non – uniform extrinsic layer at early stages of growth.*

Careful examination of the inset of Fig. 5.25.b reveals the presence of a thin extrinsic layer, suggesting the growth of a different structure at the early stages of the growth. Moreover, it is obvious that the thickness of this layer is non – uniform. It is very interesting

that despite the minor no uniformity in the early stages of the film growth, the films grow epitaxially with the $[010]_{LCCO}$ direction of the film aligned perfectly parallel to the $[110]_{STO}$ direction of the substrate. Planar – view TEM imaging indicates that the majority of the columnar grains exhibit the epitaxial relationship $[100]_{LCCO}//[1\text{-}10]_{STO}$ (Fig. 5.26).

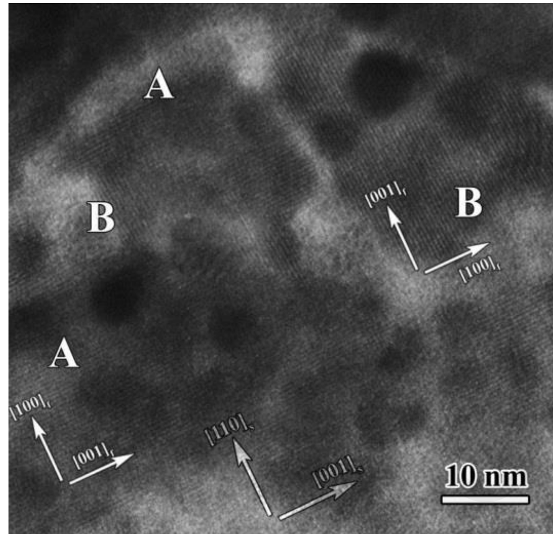

Figure 5.26: *A planar – view TEM demonstrating that the majority of the grains are oriented along a preferential orientation ($[100]_{LCCO}//[1\text{-}10]_{STO}$).*

The influence of thin film thickness on the thermal conductivity was investigated by using two samples grown with different number of pulses, 1500 and 500 *pulses*. The investigation was performed in the temperature range 90–300K using the *3ω* method. As shown in Fig. 5.27, the film thickness affects the measured thermal conductivity, *i.e.*, the thicker LCCO thin film exhibits higher thermal conductivity than the thinner in the entire temperature range.

This size effect is attributed to enhanced surface boundary scattering with decreasing thickness [99]. In addition as the temperature decreases we observe a significant reduction in the magnitude of the thermal conductivity. This is a characteristic glass – like temperature dependence. The room – temperature thermal conductivity values of the investigated thin films and the glass – like behaviour in the temperature range considered is similar to those reported for other substrates [101]. The origin of glass – like behaviour can be attributed to strong disorder related to partial mixing of specific cations on their respective sites [145], to atomic – scale defects such as interstitials and vacancies or to grain boundaries [146].

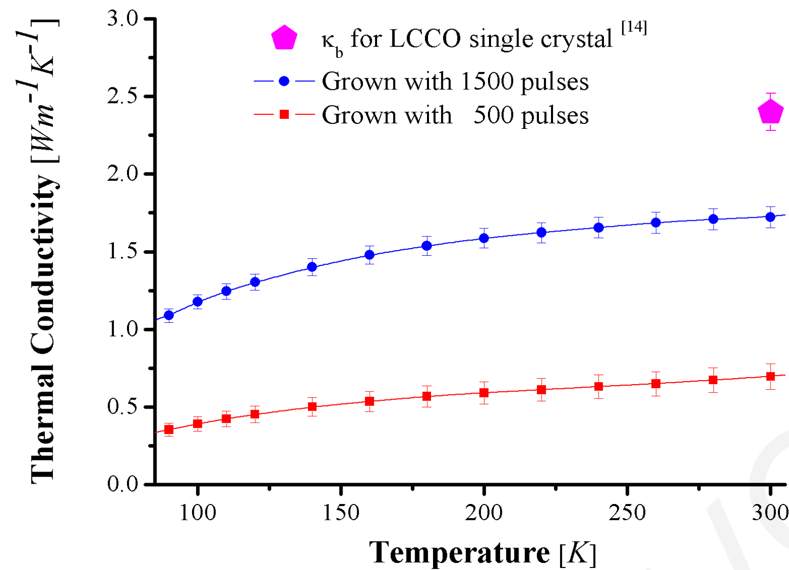

Figure 5.27: *Thermal conductivity as a function of temperature of two LCCO thin films grown on STO (110) substrates with 1500 and 500 pulses and keeping all the other deposition conditions the same. Film thickness affects the measured thermal conductivity. At room temperature the thermal conductivity of the thicker film is ~73% of the one reported for LCCO single crystals.*

The thermal conductivity of a rectangular shape LCCO pellet, synthesized by solid state reaction method, was measured using the conventional steady – state method. The sample was measured after sintering at 950^oC for 72*hours*. The thermal conductivity of the pellet as a function of temperature for both sintering temperatures is presented in Fig. 5.28.

The increase of the thermal conductivity after sintering can be attributed to *"necking"* of the adjacent grains within the pellet. In both sintering temperatures, the behaviour of the thermal conductivity was similar to that of the produced films. Therefore, the glass – like behaviour of the films of this study is related primarily to atomic – scale defects (*e.g.*, related to La deficiency), the grain boundaries and the interfacial layer identified by high resolution – TEM studies.

EFTHYMIOS CH. SVOUKIS

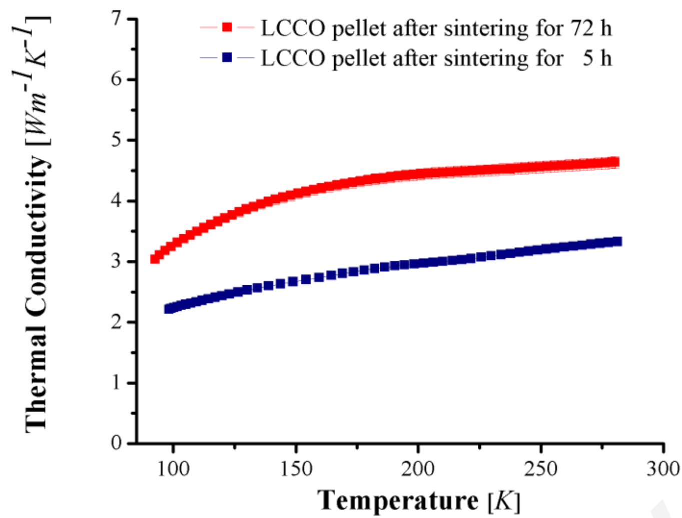

Figure 5.28: *Thermal conductivity as a function of temperature of a rectangular shape LCCO pellet, following sintering at 950°C for 5 and 72hours. The pellet was synthesized by solid state reaction method and measured using the conventional steady – state method. Sintering time affects the value of the measured thermal conductivity but doesn't change the qualitative behavior of the thermal conductivity over temperature.*

5.11.2.2 Single crystal LCCO thin film

STO (110) is a substrate suitable for the growth of a LCCO single crystal films. Deposition conditions used in the previous section resulted in the production of Zone III thin films. Fine tuning of the conditions was expected to result in hetero – epitaxial single crystal growth. The presence of the thin non – uniform extrinsic layer at the interface had also to be eliminated.

Preliminary deposition experiments were performed with $\Phi = 1.3Jcm^{-2}$. The D_R of the preliminary thin films were high compared to literature values for the PLD method in order to grow high quality films. Reduction of D_R during growth can be achieved by reduction of Φ used with a possible simultaneous increase of d_{T-S}.

$\Phi_{thres.} = 0.6Jcm^{-2}$ was experimentally found to be the minimum fluence for the stoichiometric transfer. Values above $\Phi_{thres.}$ resulted in crystalline b – axis oriented thin films. In Fig. 5.29, XRD patterns of a thin film grown using the modified Furubayashi *et al.* conditions and a film grown with reduced Φ are presented.

EFTHYMIOS CH. SVOUKIS

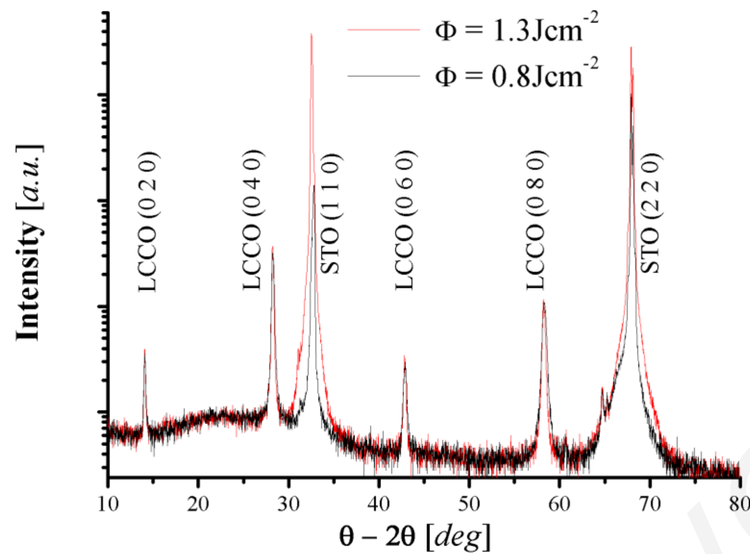

Figure 5.29: *XRD patterns of thin films grown with different Φ above $\Phi_{thres.}$. The $\Phi_{thres.}$, necessary for stoichiometric transfer and growth of crystalline thin films, was experimentally found to be 0.6Jcm^{-2}.*

The d_{T-S} plays a key role among the involved parameters for the epitaxial growth of LCCO thin films. Further optimization can enhance the crystallinity of the grown films. d_{T-S} is correlated to other PLD deposition parameters such as Φ, pressure of chamber, *etc.* Very long d_{T-S} can result in a non – stoichiometric thin film growth. Using a constant $\Phi = 0.8Jcm^{-2}$, the influence of d_{T-S} was systematically investigated. For d_{T-S} greater than 50*nm* no stoichiometric transfer was possible.

The appearance of the extrinsic layer at the interface was attributed to a non – stoichiometric plume at the early stages of growth. Based on the TEM investigations, the extrinsic layer was found to be non – uniform, reinforcing the above statement. A good pre – ablation process was used prior each deposition. This process was used for the removal of contamination or previously ablated material from the surface of the target. The first train pulses were also discarded to ensure constant Φ over the deposition.

A LCCO thin film was grown on STO (110) by taking account all the above considerations: $\Phi = 1.1Jcm^{-2}$, $d_{T-S} = 4.2mm$, pre – ablation = 300*pulses*, RR = 1*Hz*, P_{O2} =1.01*mbar* and total number of pulses = 250. Sample was initially investigated with XRR. Based on the model used for the simulation of the XRR data and the resolution of the instrument, no extrinsic layer at the interface was found. The same sample was further investigated with cross section TEM. The investigation revealed a *b* – axis single crystal LCCO thin film, free of columns and interface layer. A cross section TEM image of this film

EFTHYMIOS CH. SVOUKIS

is presented in Fig. 5.30. Based on XRR and TEM investigations, the D_R was calculated $\sim 0.5\,\mathring{A}/pulse$.

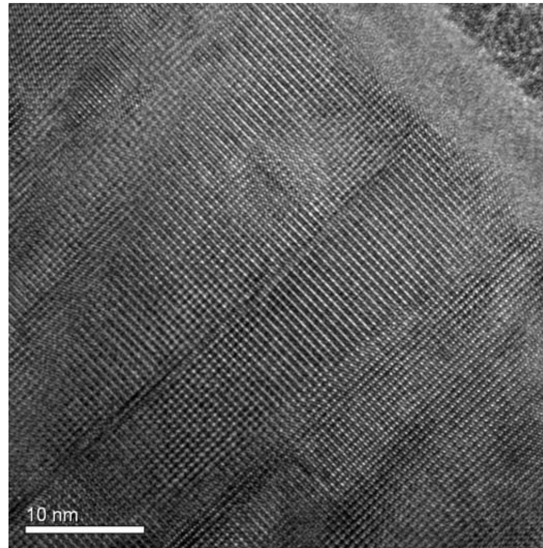

Figure 5.30: *Cross section HR – TEM image of a b – axis LCCO single – crystal thin film grown on STO (110).*

The thermal conductance of a LCCO single – crystal thin film was investigated via a thermal imaging technique at the University of Groningen. The sample was imaged while a small spot on the surface was heated. The investigation of the heat spreading over the surface can provide information for in – plane thermal conductivity. Heating was performed with a continuous wave Ar ion laser (λ=488*nm*). For this λ the absorption coefficient of the $SrTiO_3$ substrate is (nearly) zero, while it is 17–50μm^{-1} for the LCCO thin film (depending on the polarization of the light). This corresponds to a penetration depth of 20–60*nm*. Therefore, the largest part of the light is absorbed by the film. Imaging was possible by using a thick layer of *EuTTA*[9] on the surface. When *EuTTA* is excited with UV light the *Eu* – ion emits photons with λ=612*nm*, whose intensity is temperature dependent and therefore can be used as a temperature probe [130].

A small anisotropy of the heat distribution is present at the surface of the thin film. In bulk LCCO single crystals the effect is enhanced. The result is presented in Fig. 5.31.

[9] β – diketonate chelate europium (III) thenoyltrifluoroacetonate.

EFTHYMIOS CH. SVOUKIS

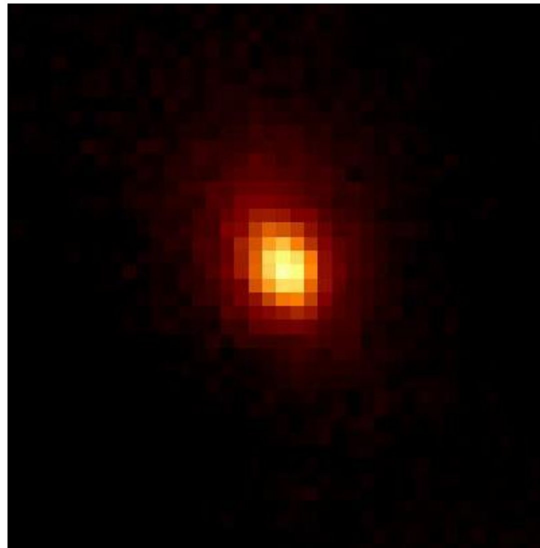

Figure 5.31: *Optical probing of heat spreading over the surface of a LCCO single – crystal thin film. A spot size of 0.5μm² with heating power 250μW was used. A small anisotropic spread, comparable to LCCO single crystal, is evident.*

5.12 Conclusions

In this chapter, growth and thermal characterization of LCCO thin films grown on various substrates along with deposition conditions were extensively investigated and the main aspects were presented.

It is found that LCCO has a tendency for *b* – axis oriented growth independent of the substrate and deposition conditions used. This tendency of LCCO is driven by internal thermodynamic reasons. Fine tuning of the deposition conditions can result on a *b* – axis LCCO thin film with the nano – crystallites oriented along the growth direction. *b* – axis single – crystal thin films were grown on STO(110) substrates, in a narrow window of deposition conditions.

The thermal conductivity of all LCCO thin films is affected by their structural characteristics. All LCCO thin films exhibit amorphous like behaviour thermal conductivity behaviour over a wide temperature range.

On the other hand, homo – epitaxial growth on an LCCO (001) single crystal shows the possibility of *c* – axis growth of the material.

EFTHYMIOS CH. SVOUKIS

Lithium Cobalt Oxide – $LiCoO_2$

6.1 Introduction

In the era of information, more and more memory is required for business and personal usage [147]. Conventional magnetic materials, used in the last decades can be described as obsolete. New materials can further enhance data storage capacity and archival speed.

Materials which belong to the layered cobalt oxide family, exhibit interesting physical properties. Na_xCoO_2 was initially proposed as a possible candidate for rewritable medium [148]. CP – AFM investigations on $NaCoO_2$ single crystals revealed controllable reversed local surface modifications, which are electrochemically driven [149].

Thin films of LCO have attracted a lot of interest due to possible use in micro – batteries for integration in chips and in medical electronics [150]. LCO structure and physical properties are very similar to those of $NaCoO_2$. LCO has widely been used as a cathode material, for lithium ion rechargeable batteries due to its high energy storage capacity and good cycling performance [151].

In 2011, LCO was reported to be a suitable material for non – volatile memory applications [152]. $NaCoO_2$ thin films are scarcely reported, in contrary to LCO for which high epitaxial thin films can be grown [153]. By applying a proper bias on the top surface of LCO thin films, electrochemically driven electrical resistance modifications occur due to intercalation / deintercalation processes [154, 155,156].

EFTHYMIOS CH. SVOUKIS

6.2 Data storage challenges

In conventional magnetic recording, magnetic fields are used to write or read locally on localized magnetic surfaces. The effectiveness of magnetic recording was greatly enhanced via the discovery of giant magnetoresistance in 1988 [157]; nevertheless the super – paramagnetic limit still exists restricting further miniaturization.

Optical storage (CD and DVD) is widely used in the market, due to its low production cost. However, the optical diffraction limit restricts further improvement [158].

Flash memory is compatible with the current IC processes and a suitable solution for embedded memory applications. However, flash memory requires high voltages for writing / erasing procedures. Cycling performance of flash memories needs also to be improved. The scaling factor is far behind the CMOS logic device scaling [159]. Further in the case of flash memory failure data recovery is not possible, in contrast to scanning probe based data storage technologies where data can be almost fully recovered.

IC industry is looking for a new candidate suitable for data recording – archival – recovery and back up. The new candidate characteristics have to be:

- Low power consumption during procedures.
- Low cost for mass production.
- Good cycling performance and re – writability.
- Compatible with current IC technology.

Scanning probe mediated approaches have been investigated for nanoscale patterning and for potential data storage applications. In polymers and ferroelectric materials, thermomechanical writing [160] and polarization switching [161] were examined, respectively by using AFM for reversible surface modifications.

Surface reversible patterning via AFM was initially reported on $NaCoO_2$ single crystals. Electrochemical reactions occur based on sodium intercalation / de – intercalation processes. However, $NaCoO_2$ structure is degradable when exposed to air. Sodium replaced by Li results to LCO, a structure exhibiting reversible electrochemical surface modifications, and thus a candidate for nano scale rewritable media [155].

EFTHYMIOS CH. SVOUKIS

6.3 $LiCoO_2$ structure and properties

6.3.1 Structure of HT – LCO

LCO has attracted a lot of attention after Mizushima *et al.* reported the possibility of its application for rechargeable batteries [151]. Stoichiometric LCO, which is used as a cathode material, has a rhombohedral structure, with space group $\left(R\overline{3}m\right)$ known as high temperature (HT). It consists of CoO_6 octahedra and Li^+ forming planes perpendicular to the [111] direction of the cubic rock salt structure [162]. Transformation of the structure to hexagonal symmetry results to lattice parameters of $a_{hex.} = 2.8138\,\overset{o}{A}$ and $c_{hex.} = 14.0516\,\overset{o}{A}$. The structure of LCO with hexagonal symmetry is presented in Fig. 6.1. Within hexagonal representation, it consists of two kinds of alternating layers stacked perpendicular to the *c* – axis:

- A CoO_2 layer.
- A layer of Li^+ ions, allowing free Li^+ ion 2D movement inside the planes.

A low temperature (LT) stoichiometric structure also exists, having the same oxygen sublattice and is distinguished by the arrangement of the Li and Co. In LT – LCO, 6% of Li^+ ions randomly occupy Co sites of and *vice versa*, resulting in cubic spinel symmetry with space group *Fd3m* [163].

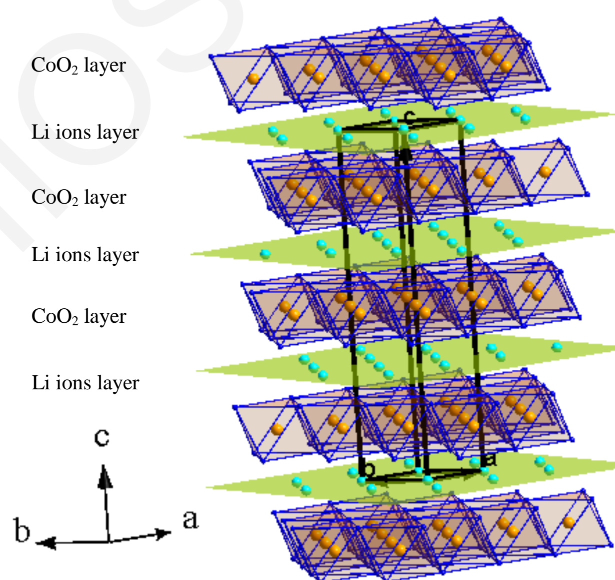

Figure 6.1: *Crystal structure representation of LCO for hexagonal lattice structure. Consists of alternating CoO_2 and Li^+ ions layers stacked along the c – axis.*

EFTHYMIOS CH. SVOUKIS

6.3.2 Lithium intercalation / de – intercalation

Compared to other intercalation $LiMO_2$ (M=Ni, Cu, Mn *etc.*) compounds, LCO is air stable and exhibits large intercalation energy ~4*eV*. In the case of a battery cell, the energy stored in a intercalation electrode is proportional to the intercalation potential and its capacity, normalized to the amount of "*active material*" [164].

The interesting electrical and thermoelectric properties of this compound can be attributed to the Li+ ion intercalation / de – intercalation, linked to the redox reactions of the cobalt oxide substructure, which modifies the interaction between the CoO_2 sheets. In bulk form (powder and single crystals) Li_xCoO_2 (LxCO), a complicated phase transition occurs when Li intercalation processes take place.

In the case of stoichiometric LCO (x=1), a hexagonal symmetry phase, known as (HEX I) exists. A second LxCO hexagonal phase (HEX II), with different $c_{hex.}$ lattice parameter can be found for $x \leq 0.93$. Both hexagonal phases are possible in the range $0.75 \leq x \leq 0.93$. For $0.51 \leq x \leq 0.75$, only HEX II is present. Further reduction of Li ($0.45 \leq x \leq 0.51$) results in a transformation of HEX II to a monoclinic structure M. Amatucci *et al.* also reported phases for $x \leq 0.45$ [165] verified via *ab initio* calculations by Van der Ven *et al.* [166]. Clearly lattice distortion due to change in the lattice parameters of the unit cell, destroys the super – lattice structure of HEX I. The phase diagram and c – axis lattice parameter of LxCO based on literature values for $0.3 \leq x \leq 1$ are presented in Fig. 6.2.

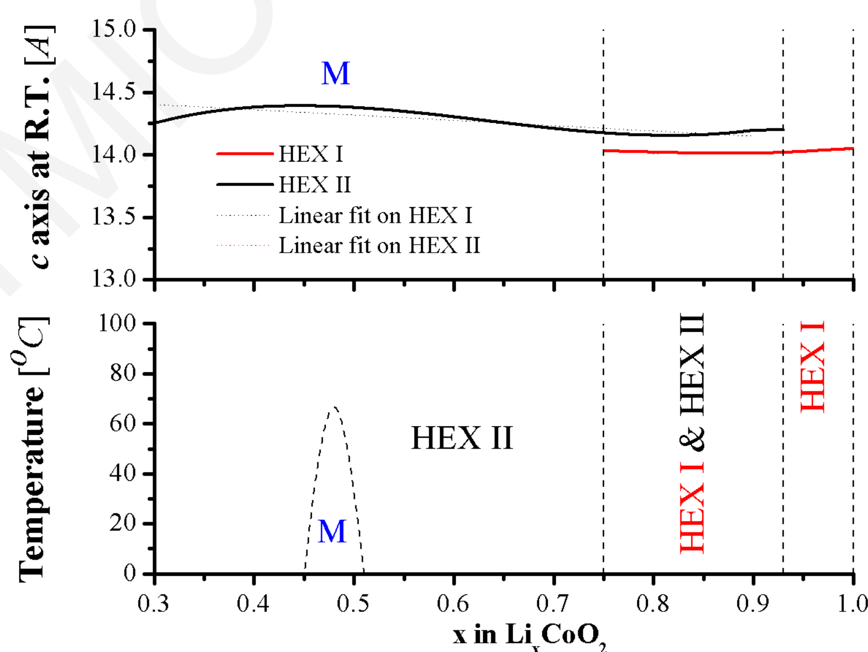

Figure 6.2: *Phase diagram and c – axis lattice parameter distortion, at room temperature for LxCO, based on literature reports* [165,167].

6.3.3 Electronic transport properties of LxCO

Structural changes based on intercalation / de – intercalation processes within the LxCO structure, are accompanied by electrical and transport changes. Na_xCoO_2, has a very similar structure and electronic properties with LxCO [168].

It has been reported that the resistivity of LxCO polycrystalline thin films is affected by the crystal mode growth. A metal – non – metal transition, affecting both the resistivity and *S* takes place at *x*~0.8, in the range were both hexagonal phases HEX I and HEX II are present [169]. A schematic diagram of the transition in the electronic and transport properties is presented in Fig. 6.3. For *x* values close to 0.80 ± 0.05, a peak performance in thermoelectric properties highlights LxCO in the family of oxide thermoelectric materials [170]. At high values of *x*, the electronic transport is strongly affected by disorder and electron correlations.

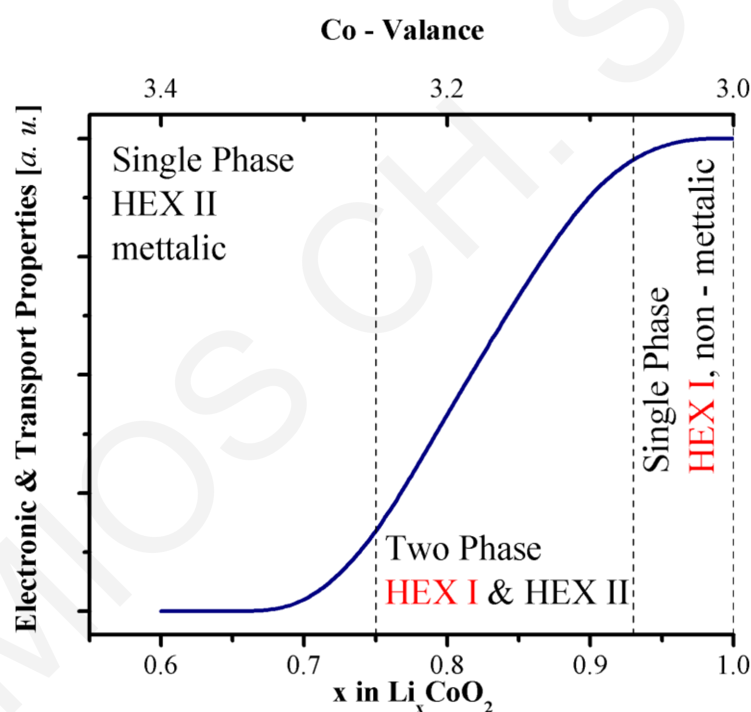

Figure 6.3: *Variation of electronic and transport properties related to the x value within the LxCO structure.*

The anisotropic structure of LCO, as in all layer structures, creates anisotropy in the transport properties. Based on the crystallographic orientation under investigation, properties may vary up to 3 orders of magnitude in LCO single crystals [171]. In order to fully understand the intrinsic transport mechanism in LxCO thin films, with ultimate goal its integration in the IC industry, single crystalline specimens with preferred growth orientation are highly desirable.

EFTHYMIOS CH. SVOUKIS

6.4 Synthesis of LxCO and target preparation

Fine crystalline LxCO powders were prepared by solid – state reaction of slightly non – stoichiometric amounts of Li_2CO_3 (99%) and Co_3O_4 (99.7%)). A small excess (3 – 5%*wt*) of Li_2CO_3 was added in the initial step to compensate for the slight volatilisation of lithium oxide during the reaction. Weighing was carried out in a glove box under Ar atmosphere and was followed by a first reaction of the well ground powders at 750^oC for 12*h*.

Resulting fine powders were characterized via high resolution XRD and patterns were refined via Rietveld Refinement using PowderCell. All reflections were indexed according to hexagonal symmetry and the lattice parameters of structure based on Rietveld analysis were found to be $a_{hex.} = 2.8149\,\overset{o}{A}$ and $c_{hex.} = 14.0590\,\overset{o}{A}$. Based on Figure 6.2, the phase of the LxCO powder is HEX I and $x = 0.99$.

The fine powder was cold pressed into a target with a 0.45*GPa* pressure for 10*min*. The produced 15*mm* target was sintered at 900^oC in air for 16*h*. For all annealing procedures, a heating / cooling rate of $5^oC / min$ was used to ensure a structurally perfect target.

6.5 Low pressure growth

Growth of single crystalline HT LCO thin films has been scarcely reported [171]. LCO contains volatile elements with high vapour pressures and hence stoichiometric transfer with PVD methods is a challenge [172]. Tsurahama *et al.* deposited HT – LCO by PLD using a two – step process. LT – LCO precursor films are grown in a narrow temperature range 250–300^oC, which are then transformed to HT by further annealing [173].

Initially LCO thin films on (0001) Al_2O_3 were grown by using PLD based and the Tsurahama *et al.* conditions. For the precursor LT phase the (0003*k*) peaks with $k \in I$, were absent. Post annealing at 650^oC in air for 5*h*, resulted in *c* – axis oriented HT – LCO. XRD patterns prior and post annealing are presented in Fig. 6.4.

EFTHYMIOS CH. SVOUKIS

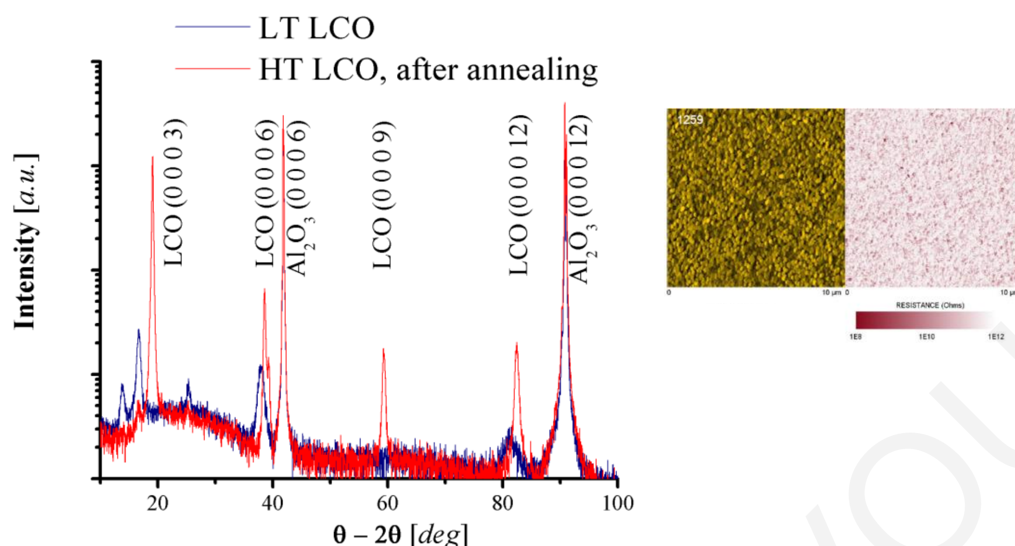

Figure 6.4: *XRD patterns of a LCO thin film grown at 275°C in low pressure conditions, prior and post annealing at 650°C for 5h in air. CP – AFM investigation of the same film after annealing (inset) revealed a granular highly resistive structure.*

CP – AFM investigations showed that the produced thin film was granular, with an average R_q=13.8*nm*, and very insulating (the value of *x* in the LxCO was close to 1) with no possibility of surface resistance modification ability (inset in Fig 6.4).

New deposition conditions, such as increase of the deposition pressure, were needed for the growth of epitaxial, low roughness thin films with the ability to modify their surface resistance.

6.6 Growth on c – cut Sapphire

The selection of *c* – cut sapphire as a possible substrate for epitaxial growth of LCO films was made due to the hexagonal symmetry of the top surface plane [0001]. The adhesion with the grown thin film is highly promoted because the substrate is also an oxide. Micron size cracks due to difference in the thermal expansion coefficients are not expected. Furthermore, sapphire surfaces can be modified and improved by heating procedures.

EFTHYMIOS CH. SVOUKIS

6.6.1 Substrate preparation

The top surfaces of the *c* – cut sapphire single crystals (obtained by CrysTek), used in the study were modified by using a thermal process similar to that proposed by M. Yoshimoto *et al.* [174]. All *c* – cut sapphire substrate, were initially placed in an ultrasonic bath with de – ionized water (R > 10$M\Omega$) for 20*min*. Samples were thermally treated at different temperatures in vacuum or in the presence of oxygen atmosphere to optimize the initial deposition surface. The best heat treatment was found to be annealing at 1200^oC in air for 5*h*, in agreement with Yoshimoto *et al.*

By using AFM in tapping mode, atomic steps were observed on the top surface of the substrates following the heating treatment. RHEED patterns of the same substrates showed bright spots and Kikuchi lines, evidence of nearly perfect initial substrate surface. In Fig. 6.5, an AFM image and a RHEED pattern of a thermally treated *c* – cut sapphire substrate surface is presented. In the RHEED pattern of the same sample, splitting of the spots due to terraces scattering is present.

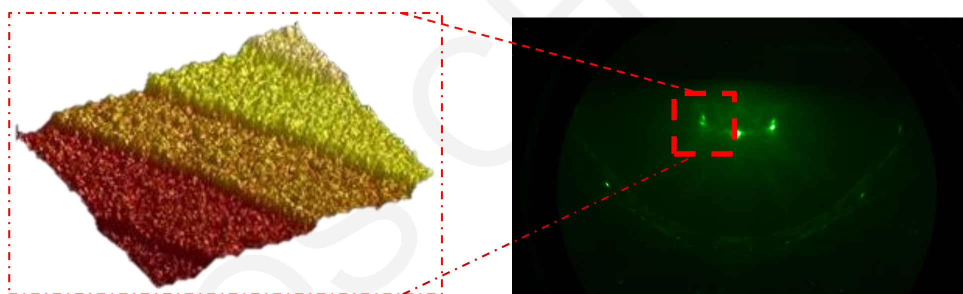

Figure 6.5: *$0.1\mu m^2$ AFM image and RHEED pattern of the same c – cut sapphire sample after annealing at 1200^oC for 5h. in air. Terraces are present in both cases.*

6.6.2 Thin film deposition

LCO films were grown by PLD on thermally treated *c* – cut sapphires heated to a range of temperatures. The KrF^* focused in an area S=10mm^2 on the target resulted at a $\Phi = 1.1 Jcm^{-2}$. The target was placed d_{T-S}=37*mm* away from the substrate and was toggled and rotated around its center at 20*rpm* during the deposition to keep the ablated target surface fresh. Prior each deposition the chamber was evacuated to a base pressure $P < 5 \cdot 10^{-6} mbar$. During the deposition process the oxygen pressure in the chamber was kept constant at 1*mbar*. Films were grown at different substrate deposition temperatures in the range of 200 to 800^oC, using heating and cooling rate of $10^oC / min$.

EFTHYMIOS CH. SVOUKIS

6.6.3 X – ray diffraction characterization

The phase purity and growth characteristics of the thin films were studied by XRD using out – of – plane and in – plane configurations.

6.6.3.1 Out – of – plane configuration

Figure 6.6 shows the XRD patterns of the deposited thin films grown at different temperatures on annealed *c* – cut sapphire substrates.

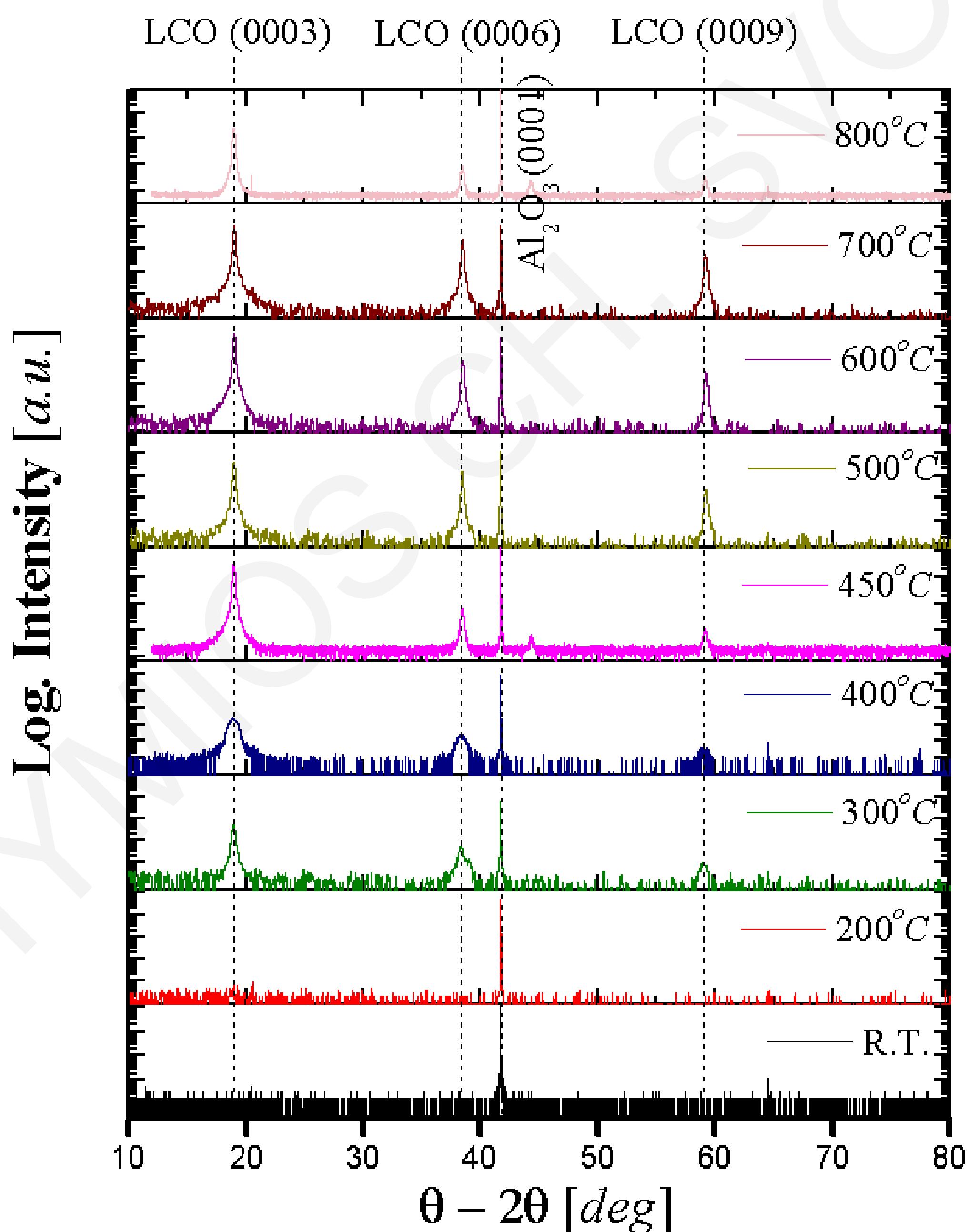

Figure 6.6: *XRD patterns of LCO thin films deposited on annealed c – cut sapphire substrates in the temperature range from room temperature to 800°C.*

EFTHYMIOS CH. SVOUKIS

The diffraction patterns revealed that the films grown at 200^oC or below exhibit amorphous behaviour. In XRD pattern of the films grown at 800^oC extra peaks appeared, which can be attributed to the decomposition of the LCO structure [175]. Phase stability and oriented c – axis LCO thin films are obtained on the temperature regime of 300–800^oC.

The appearance in the XRD patterns of all and only the (000l) reflections of the LCO structure is a clear evidence for the HT phase formation. The strong orientation of the films along the c – axis could be attributed to the lowest surface energy of the (000l) crystallographic planes [173].

Rocking curve scans were performed in all LCO thin films for the (0003) peak of LCO. The (0003) peak has the highest intensity compared to the other (000l) reflections of the LCO structure. All thin films investigated showed a FWHM <0.1*deg*. These values indicate that all crystallites are perfectly aligned along the growth direction. Also the values are one order of magnitude higher than the one measured on the (0006) of the c – cut sapphire.

HR XRD investigations close to (0003) peak of a thin film grown at 600^oC, revealed layered fringes, evidence of epitaxial growth. The pattern is presented in Fig. 6.7. Based on the HR XRD patterns, the c – axis lattice parameter of the LxCO thin films was calculated for all deposition temperatures and are presented in Fig. 6.8.

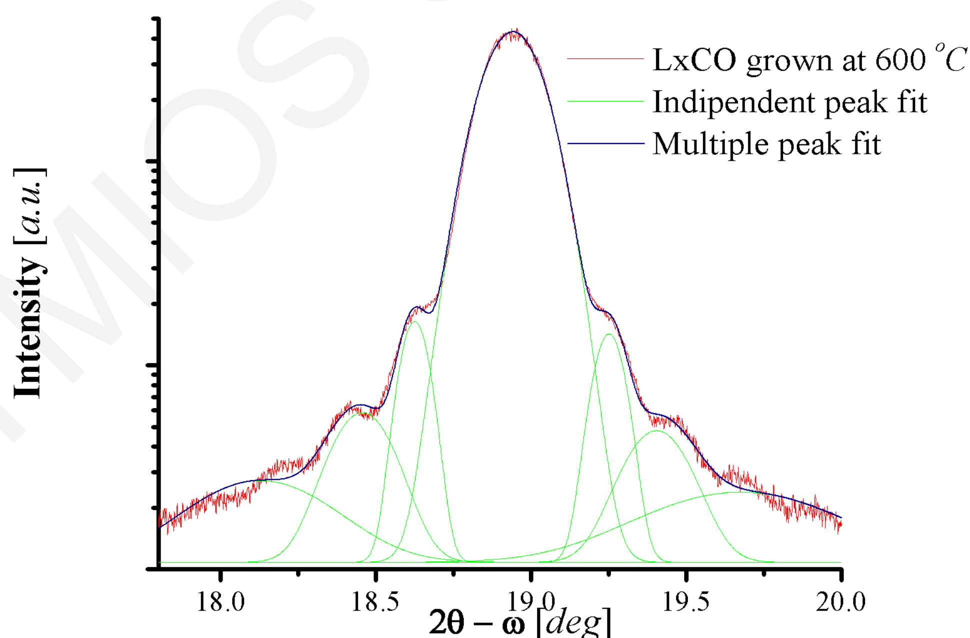

Figure 6.7: *HR XRD of the (0003) peak of a LCO thin film grown at 600°C. Layer fringes appear, evidence of epitaxial growth.*

EFTHYMIOS CH. SVOUKIS

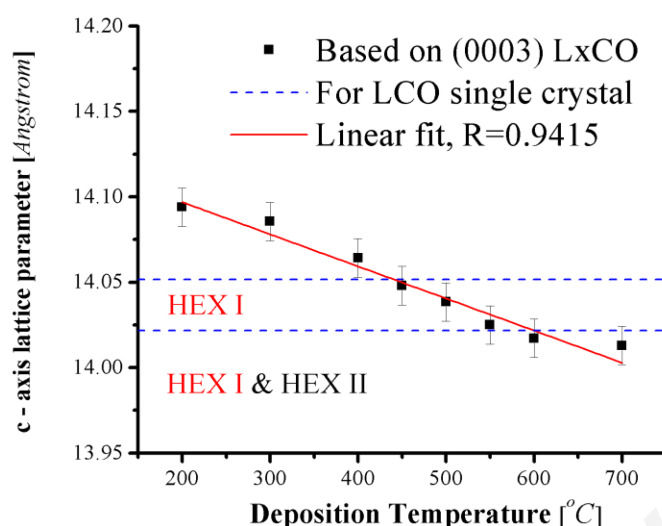

Figure 6.8: *The c – axis lattice parameter of the LCO thin films grown on c – cut sapphire, as a function of their deposition temperature.*

The *c* – axis lattice parameter of the thin films decreases monotonically as the deposition temperature increases with a rate $-1.9\cdot10^{-4}\ \overset{o}{A}/^{o}C$ .At low deposition temperatures, the measured lattice parameters are larger than the one reported in the literature for LCO single crystals or powders, and can be attributed to strain effects induced by the substrate. At temperatures close to $700^{o}C$, the lattice parameter is in the low – region of the HEX I phase. The impact of the deposition temperature on the *c* – axis lattice parameter will affect the electronic – transport properties of the LxCO thin films.

6.6.3.2 In – plane configuration

The determination of the *in* – plane growth orientation of the LCO thin films deposited on *c* – cut sapphire was made using the asymmetric reflections $(11\bar{2}3)$ and $(20\bar{2}0)$ for LCO and sapphire, respectively.

Azimuthal scans based on the aforementioned reflections showed that LCO is epitaxially grown *in* – plane. In Fig. 6.9 an azimuthal scan of a film grown at $600^{o}C$ is presented. Six low intensity peaks correspond to the six fold symmetry of the $(11\bar{2}3)$ reflections. The three high intensity peaks are attributed to $(20\bar{2}0)$ reflections of the substrate.

EFTHYMIOS CH. SVOUKIS

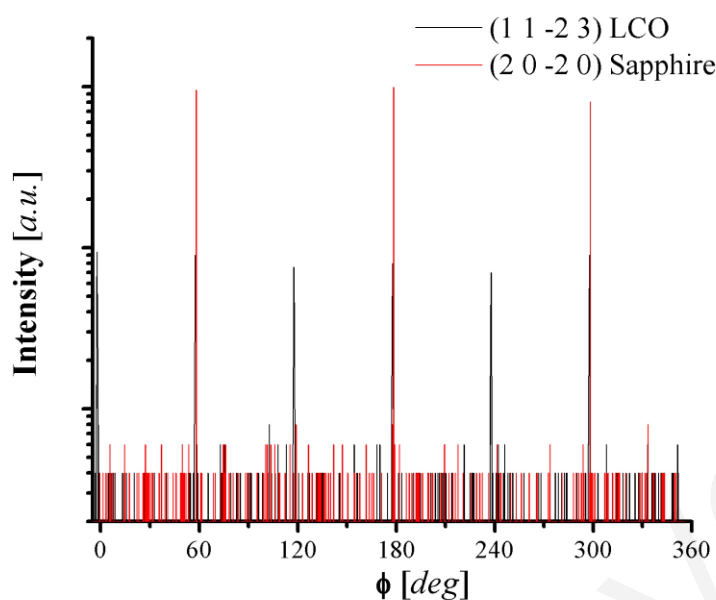

Figure 6.9: *Azimuthal scans of a LCO thin film grown on c – cut sapphire at 600°C. The in – plane epitaxy is verified from the symmetry of both the peaks of the substrate and the thin film.*

6.6.4 TEM growth investigation

The structure of LCO thin films as a function of the deposition temperature was further investigated by TEM, Figs. 6.10. Specimens suitable for cross – sectional view TEM observations, were prepared using conventional preparation techniques.

TEM investigations revealed the impact of the deposition temperature on the growth mode of the LCO thin films. For deposition temperatures below 200°*C*, LCO thin films can be described as amorphous (Fig. 6.10.a.). The diffraction pattern of the thin film grown at 200°*C*, has circles evidence of Zone I (Fig. 6.10.inset(f)) By increasing the deposition temperature, columnar growth is observed indication of Zone II (Fig. 6.10.b – c). At deposition temperature of 600°*C* (Fig. 6.10.d.), the thin film is epitaxially grown on the substrate. The diffraction pattern of the same sample showed aligned spots (Fig. 6.10.inset(h)), and the thin film is free of defects, has a perfect top surface and a sharp interface, suggesting that the Zone III has been reached.

Further increase of the deposition temperature to 700°*C* (Fig. 6.10.e.), dramatically changes the structure of the LCO thin films. Grain boundaries, dislocations and stress fields appear. Thermodynamic reasons and inter – diffusion phenomena drive the system far from epitaxial growth.

EFTHYMIOS CH. SVOUKIS

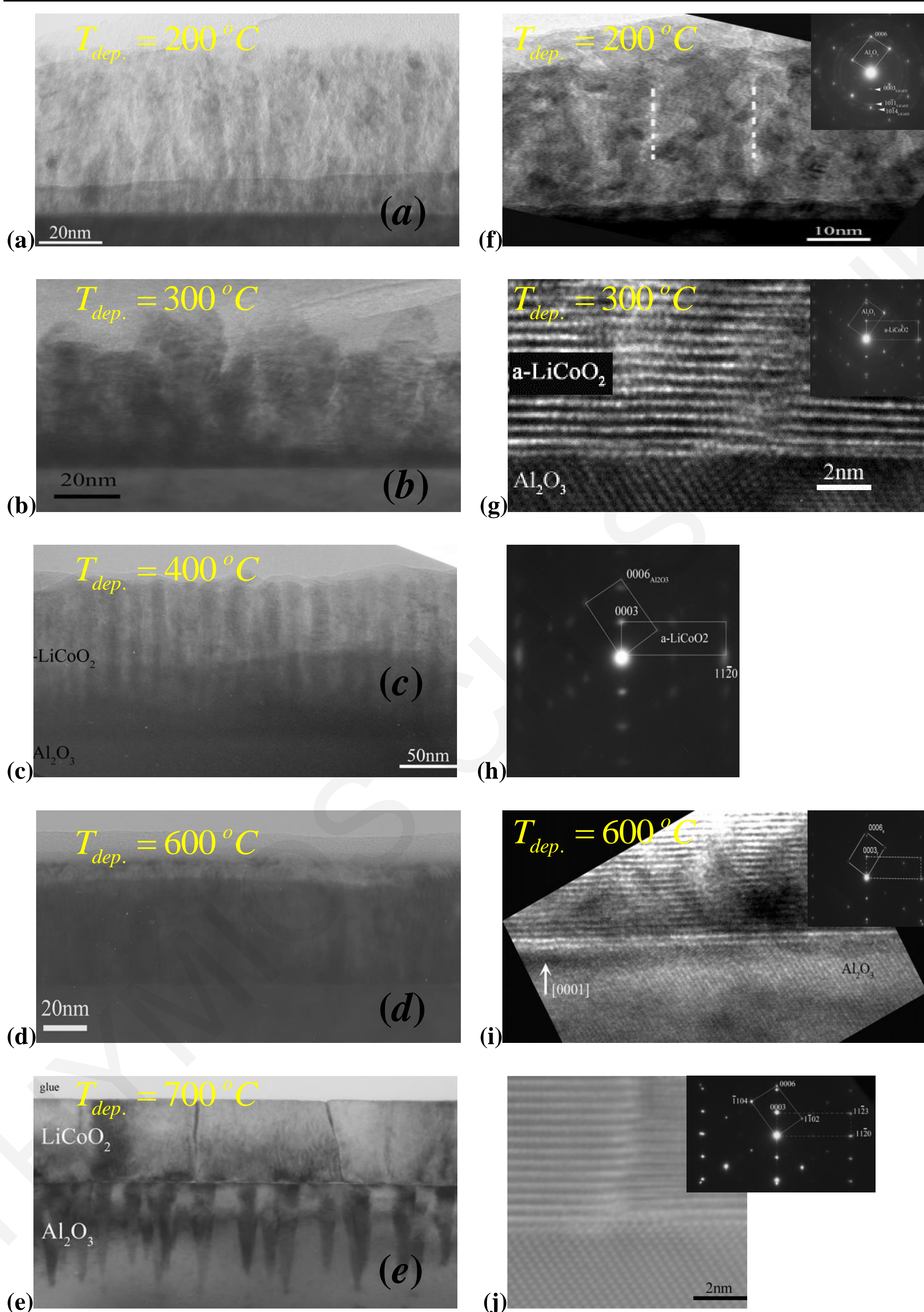

Figure 6.10: *Conventional TEM images (a – e), high resolution TEM images (g, i and j) and diffraction patterns (h and insets in: f, g, i and j) of LCO thin films grown on c – cut sapphire at various deposition temperatures 200, 300, 400, 600 and 700°C.*

6.6.5 Surface morphology investigation

The surface roughness of the films was evaluated over an area of 10 *x* 10 μm^2 using an AFM in contact mode. In Figs. 6.11, AFM images of the LCO thin film deposited on *c* – cut sapphires at various temperatures are presented.

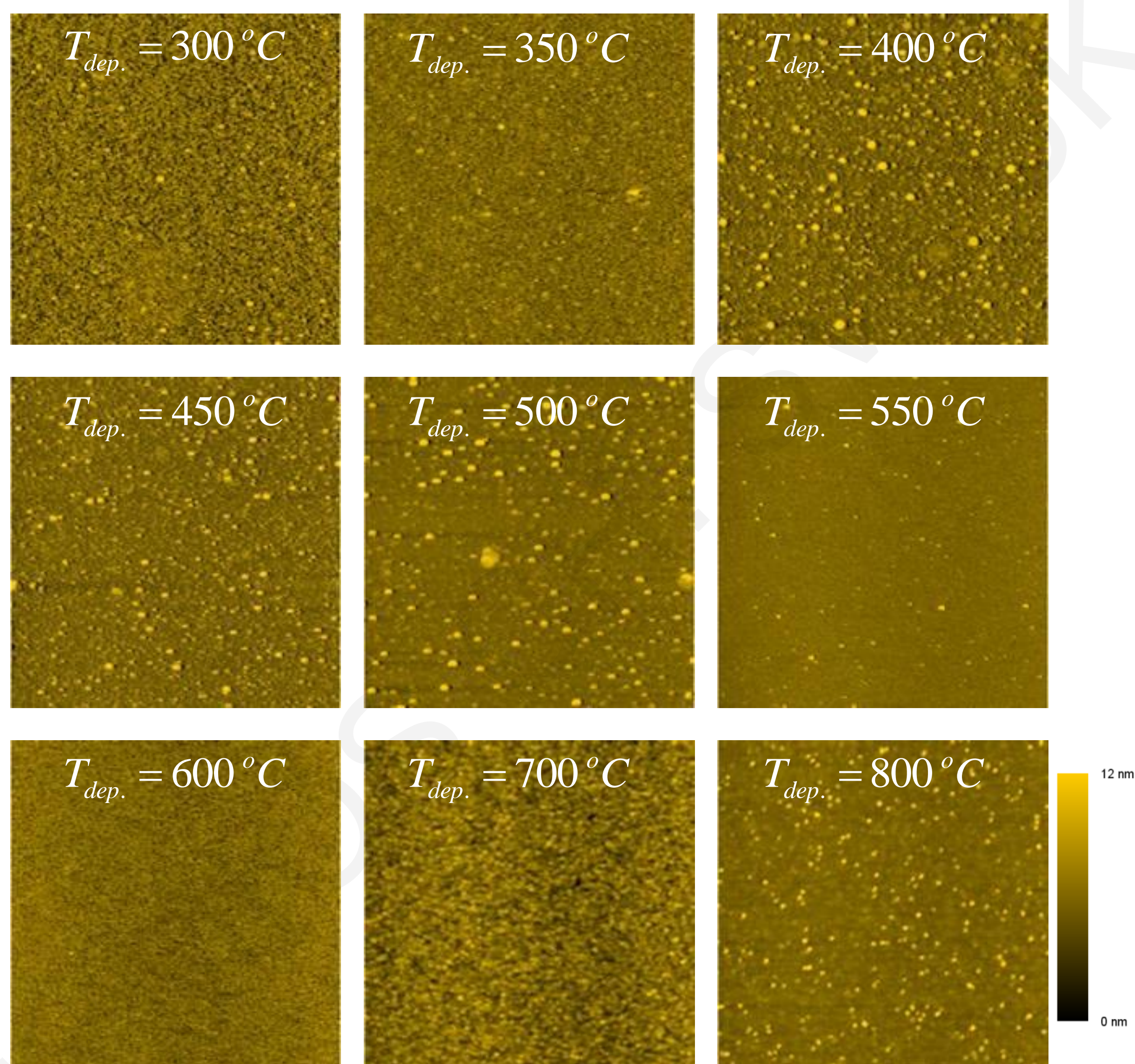

Figures 6.11: *AFM images (10 x 10* μm^2*) of LCO thin films deposited on c – cut sapphire at various deposition temperatures. The scale is the same for all images.*

The surface roughness of the thin films is dramatically affected by the deposition temperature. Surface roughness decrease, by increasing the deposition temperature of the thin film and it can be attributed to an enhanced surface diffusion. In Fig. 6.12, the surface roughness (R_q) is presented as a function of the deposition temperature.

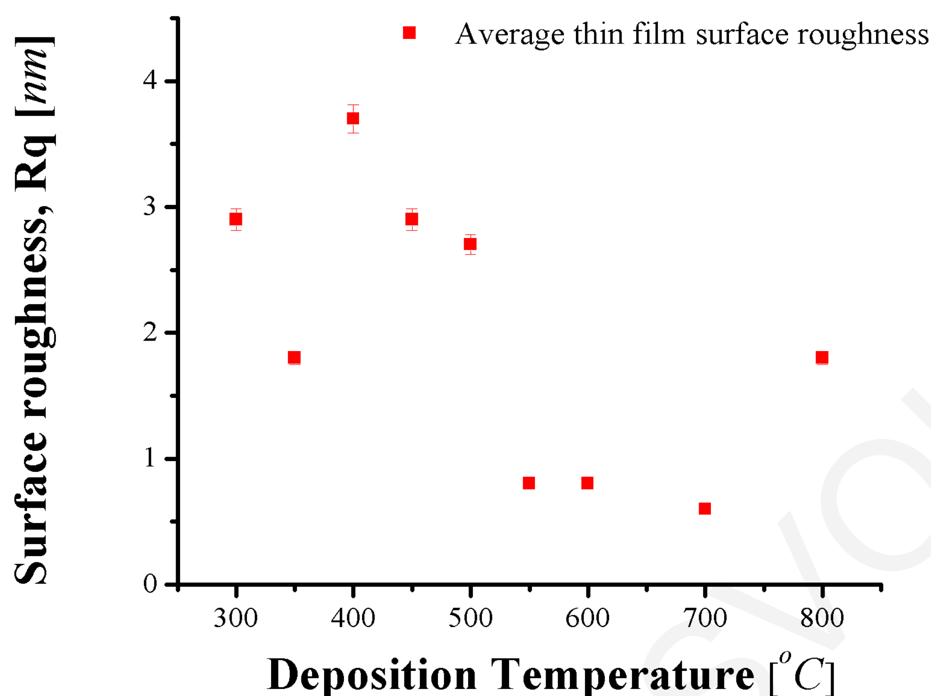

Figure 6.12: *The average surface roughness of LCO thin films on c – cut sapphire as a function of the deposition temperature. The roughness of the films can be reduced by performing growth at higher temperatures.*

The AFM results on the modification of the morphology with the deposition temperature are in good agreement with SEM imaging that was performed on large surface areas. SEM investigations showed that LCO thin films were free of cracks, holes and particulates. In Fig. 6.13, a secondary electron SEM image of a film deposited at 600^oC over a large area, with a field of view of $500\mu m$, is presented.

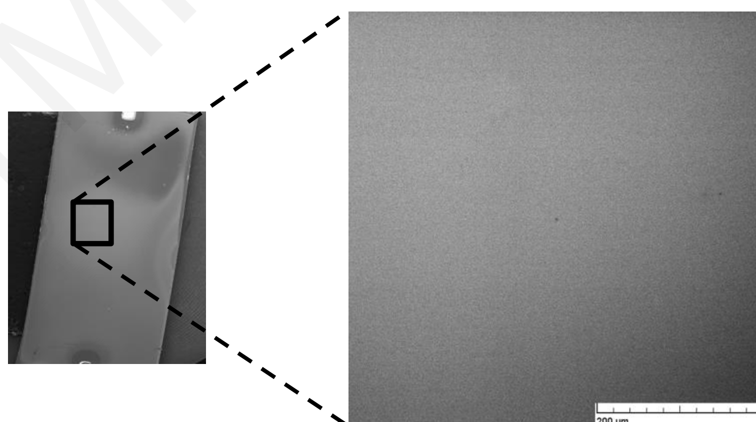

Figure 6.13: *SEM images of a LxCO thin film deposited on c – cut sapphire at 600^oC with a large field of view. The film is free of cracks, holes and particulates.*

6.6.6 CP – AFM surface resistive maps

CP – AFM provides simultaneously surface topography and surface resistance maps of the under investigation LCO thin film. In Figs. 6.14, surface resistance maps of the LCO thin films deposited on *c* – cut sapphire substrates at various temperatures are presented.

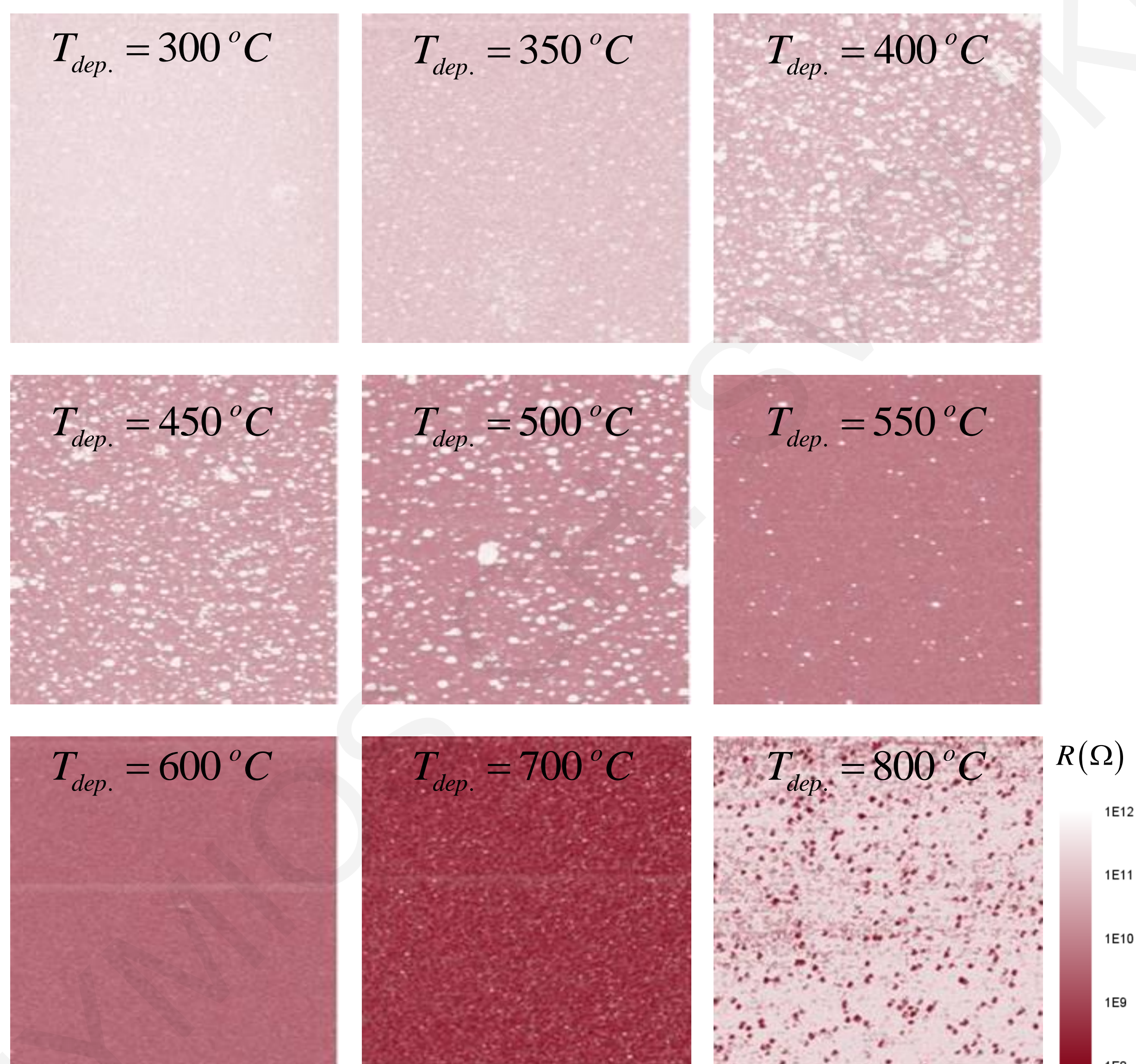

Figure 6.14: *CP – AFM surface resistance maps (10 x 10 μm^2) of LCO thin films deposited on c – cut sapphires at various deposition temperatures. The resistance scale is the same for all images.*

The surface resistance mappings shown in Figs. 6.14 were obtained from the same locations where the surface roughness had also been obtained (Figs 6.11) in order to correlate the surface roughness with the surface resistance. It is evident that the rough areas of the film

surfaces exhibit higher resistance and also the surface resistance is more uniform over the entire area of the smoother films.

By increasing the deposition temperature the average surface roughness is being reduced. In addition, the average surface resistance of the LCO thin films, is reduced by 4 orders of magnitude with a rate $\frac{d}{dT}\log(R) = -6.5\cdot10^{-3}\,{}^{\log(\Omega)}\!/_{{}^{o}C}$. In Fig. 6.15, the average resistance of the LCO thin films is presented as a function of the deposition temperature. The LCO film grown at $800^{o}C$, showed high values of surface roughness and resistance. This can be correlated to the appearance of extra peaks in Fig. 6.6, due to possible decomposition of LCO and formation of conductive Co nano – clusters within an insulating LCO matrix.

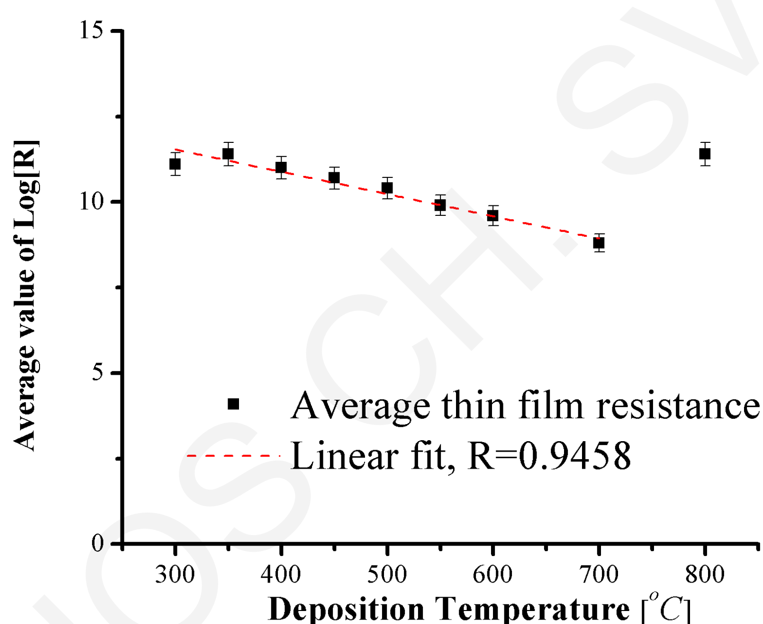

Figure 6.15: *The average logarithm of the surface resistance of the LCO thin films on c – cut sapphire as a function of the deposition temperature. The deposition temperature affects the surface electric properties of the thin films.*

The strong modification of the surface resistance as a function of the deposition temperature could be attributed to a change in Li – concentration and / or modification in the crystallinity of the thin films. Surface resistance mapping results are in agreement with the structural investigation of the *c* – axis lattice parameter presented in Fig. 6.9. By increasing the deposition temperature the *x* value in the LxCO structure decreases and the thin films become more conductive.

EFTHYMIOS CH. SVOUKIS

6.6.7 CP – AFM surface resistance modifications

The ability of surface resistance modification in LxCO thin films, by applying an external voltage bias, was examined using CP – AFM. In Figs. 6.16, are shown the maps of surface resistance modifications made on LCO thin films deposited at various *T* on *c* – cut sapphire substrates.

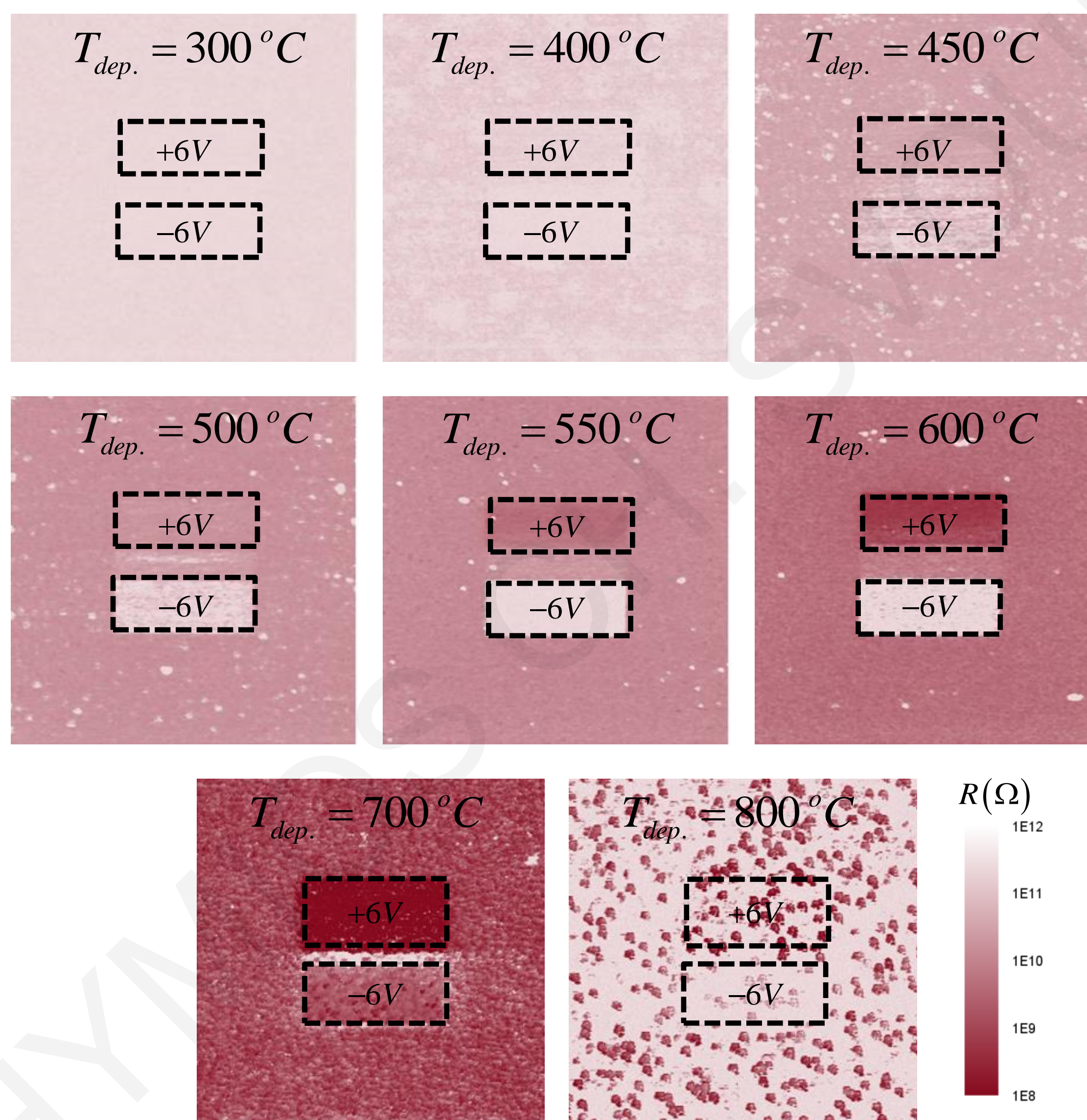

Figure 6.16: *Surface resistance modifications in LCO thin films grown on c – cut sapphire substrates at various deposition temperatures, by applying a +/– 6V bias. The resistance scale is the same for all images. The reading bias was +1V.*

Thin films grown at and 400^oC showed no possibility of surface resistance modification, unlike those grown at higher temperatures (up to 600^oC). By applying a positive – oxidative modification bias (+6*V*) on a selected area, a more conductive area was observed

EFTHYMIOS SVOUKIS

compared to the initial surface resistance state. In contrary, a negative bias (–6V) resulted in a more insulating region compared to the initial state. In Fig. 6.17, the average resistance of the LCO thin films prior and post positive and negative bias application is presented as a function of the deposition temperature.

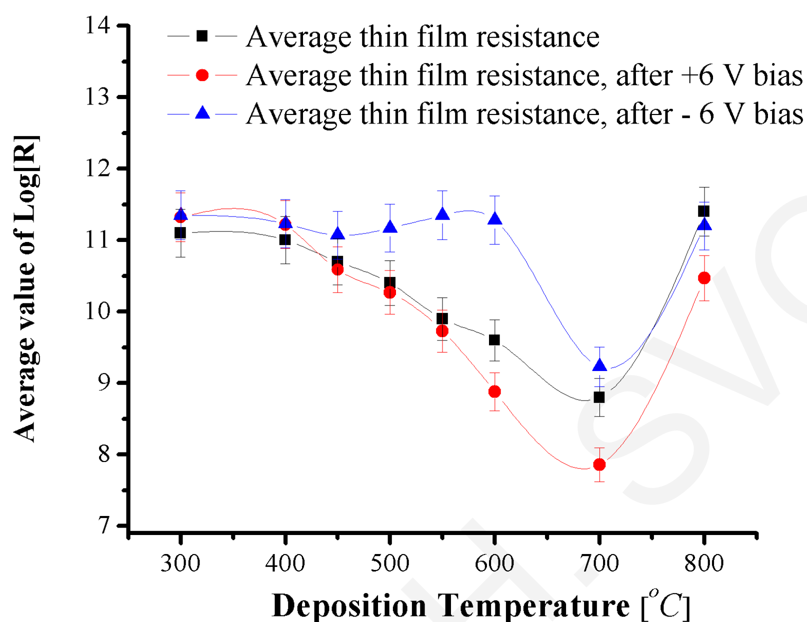

Figure 6.17: *Average logarithm of the surface resistance of the LCO films on c – cut sapphire as a function of the deposition temperature prior and post bias applications.*

LCO thin film grown at 600^oC, showed the best ability for surface modifications. A line scan of a film, with 1V reading bias, is presented in Fig. 6.18. A 2.5 order of magnitude difference in the areas biased with low to high voltage appears.

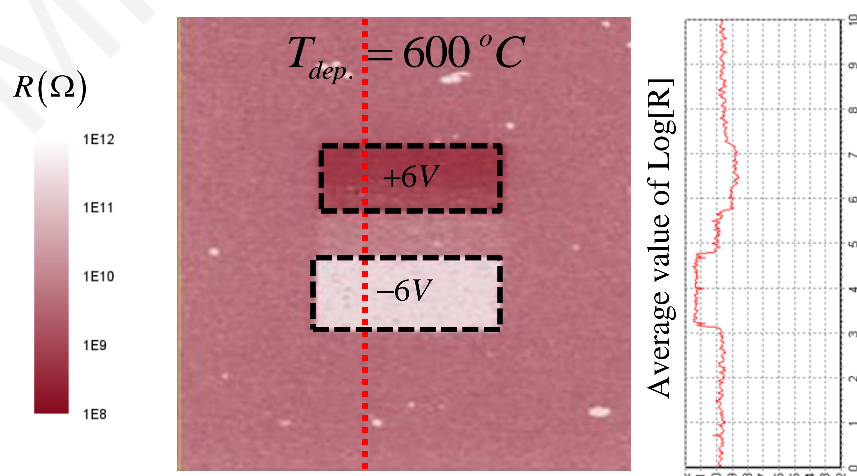

Figure 6.18: *Line scan on a surface – resistance modified LCO thin film. 2.5 orders of magnitude difference exist between the areas modified with low (–6V) and high (+6V) bias.*

EFTHYMIOS CH. SVOUKIS

6.7 Growth on n++ Si (111)

Current IC technology is Si – based and materials for novel applications have to be compatible with it. (111) – oriented Si substrates have been chosen due to the hexagonal like structure that Si has on the specific plane, Fig. 6.19. Commercial n++ doped Si wafers were used. Doped Si wafers were used, for the ability of using the substrate as conductive electrode in further investigations.

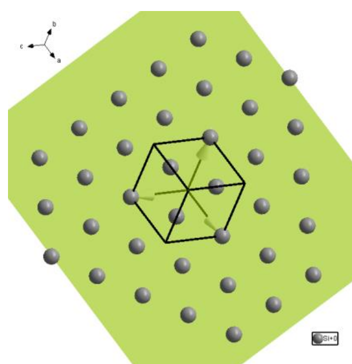

Figure 6.19: *Hexagonal – like symmetry of Si in plane (111).*

6.7.1 Substrate preparation

Using a mechanical wafer cutter, rectangular shape substrates with dimensions $5x10mm^2$ were obtained. These Si substrates were ultrasonically cleaned in de – ionized water (R > $10M\Omega$) for $5min$, in acetone for $10min$, and finally in isopropanol for $5min$. Then, the substrates were placed on Whatman cleaning tissue and were blown with high purity N_2 gas (5.0). This procedure ensures the removal of Si micron size pieces due to cutting and production of mirror like surface on the substrate.

The native SiO_2 layer on Si (111) was etched by submerging the substrates in commercial buffered hydrofluoric – acid (BHF, Merck, NH_4F : HF = 87.5:12.5) for $5sec$. For the neutralization of the acid, two di – ionized water baths in a raw were used. This procedure was performed minutes prior placement of the substrate in the deposition chamber to eliminate the growth of native SiO_2.

6.7.2 Thin film deposition

LCO films were grown by PLD on etched n++ Si (111) employing conditions similar to those used for the growth on *c* – cut sapphires. Laser beam focused on an area of $S=10mm^2$

EFTHYMIOS CH. SVOUKIS

resulted in a $\Phi = 1.1 Jcm^{-2}$. The target was placed d_{T-S}=42*mm* away from the substrate. The Si substrate was mounted on the sample carrier with silver paint, permitting good thermal contact with the heater. Prior each deposition the chamber was evacuated to a base pressure $P < 5 \cdot 10^{-6} mbar$. During the deposition process the oxygen pressure in the chamber was kept constant at 1*mbar*. The films were grown at different substrate deposition temperatures in the range of 300–600^oC, using a heating and cooling rate of $10^oC/min$.

6.7.3 Out of plane X – ray diffraction characterization

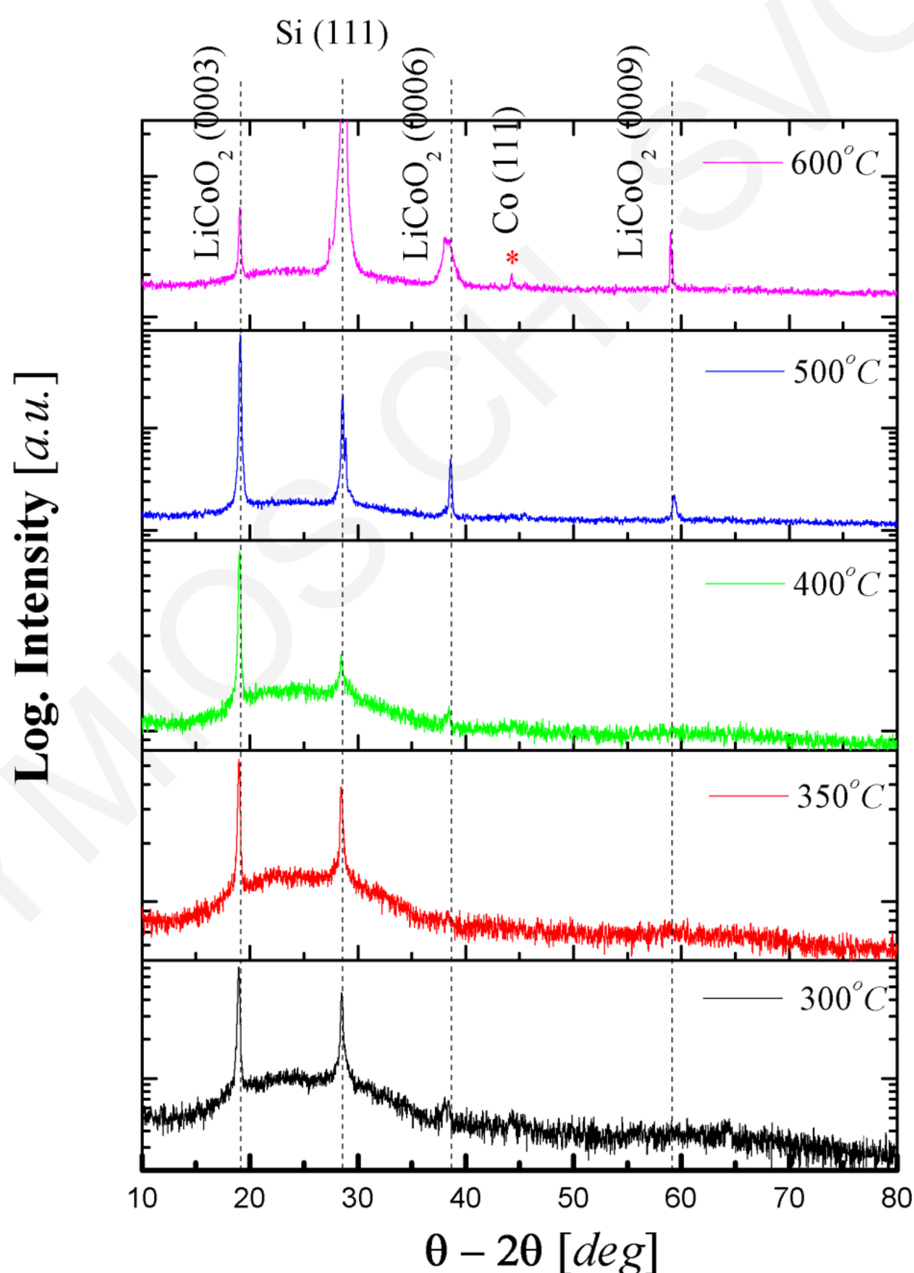

Figure 6.20: *XRD patterns of LCO thin films deposited on etched n++ Si (111) substrates in the temperature range of 300 to 600^oC.*

EFTHYMIOS CH. SVOUKIS

Out – of – plane XRD patterns of LCO thin films grown on etched n++ Si (111) are presented in Fig. 6.20. Phase stability and oriented *c* – axis HT – LCO thin films are obtained present within the temperature range of 300–500^oC. The appearance of all and only (000*l*) reflections of the LCO structure is a clear evidence of a strong orientation of the films along the *c* – axis. An extra peak appears only in the XRD spectrum of the film deposited at 600^oC denoted with an asterisk. The appearance of the extra peak can be attributed to Co clustering due to decomposition of the LCO structure [175]. The same behavior has been observed on LCO thin films grown on *c* – cut sapphires, but on higher deposition temperatures, such as 800^oC.

6.7.4 CP – AFM surface resistance mapping and modifications

The surface topology and the electrochemical properties of the thin films were examined in detail with CP – AFM, in contact mode operation, over areas of 10 *x* 10 μm^2. In each measurement, the probe was brought in contact with the sample, and the explored surface was scanned line by line in the selected area.

During the line scan measurement, the probe – surface applied force was held constant (typically a few 10^{-9} to a few $10^{-8}N$) and a bias voltage was applied between the probe and the sample (up to few *V*). The topographical and electrical maps of the studied area were simultaneously investigated, by recording synchronously height values and resistance of the specific area, respectively.

Despite the fact that similar deposition conditions were used as for the growth on *c* – cut sapphires, LCO thin films grown on n++ Si (111) have different topology and surface electrical properties. In Figs. 6.21 CP – AFM images of surface topology and resistance mapping are presented for LCO thin films grown at various deposition temperatures. For thin films grown above *i.e.* 600^oC granular structures appear, which is evidence of columnar growth.

EFTHYMIOS CH. SVOUKIS

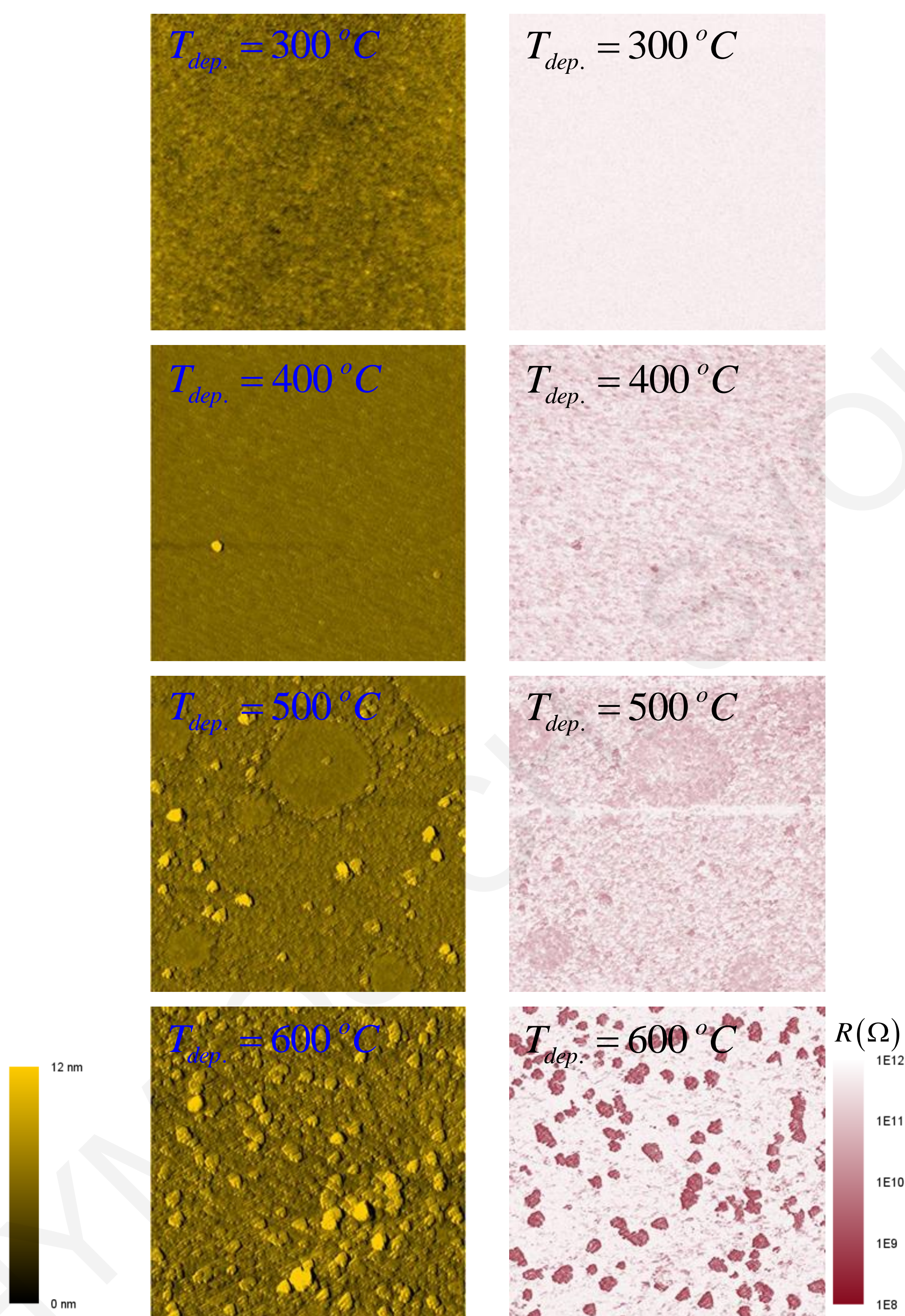

Figures 6.21: *CP – AFM images (10 x 10 μm²) of LCO thin films deposited on n++ Si (111) at various deposition temperatures. Roughness and resistance were investigated on each sample simultaneously.*

Surprisingly, in contrast to theoretical models of growth, the surface roughness of the LCO thin films increases as the deposition temperature increase. This is also in contrast to the previous investigation presented, of LCO thin films grown on *c* – cut sapphires. In Fig. 6.22,

the surface roughness (R_q) is presented as a function of the deposition temperature for LxCO thin films grown on n++ Si (111). LxCO thin films produced in the range of 300–400^oC, are smooth with average roughness similar to those produced on c – cut sapphires. For deposition temperatures above 400^oC, the average surface roughness increases linearly with a rate of $+5.7\cdot10^{-3}\ {nm}/{^oC}$. The thin film grown at 600^oC exhibits average surface roughness above one standard deviation from the mean of the whole series of the samples. Increase of the deposition temperature has a major impact on the surface roughness. This change in the roughness is in agreement with the XRD and the appearance of extra peaks at high temperatures (Fig. 6.20).

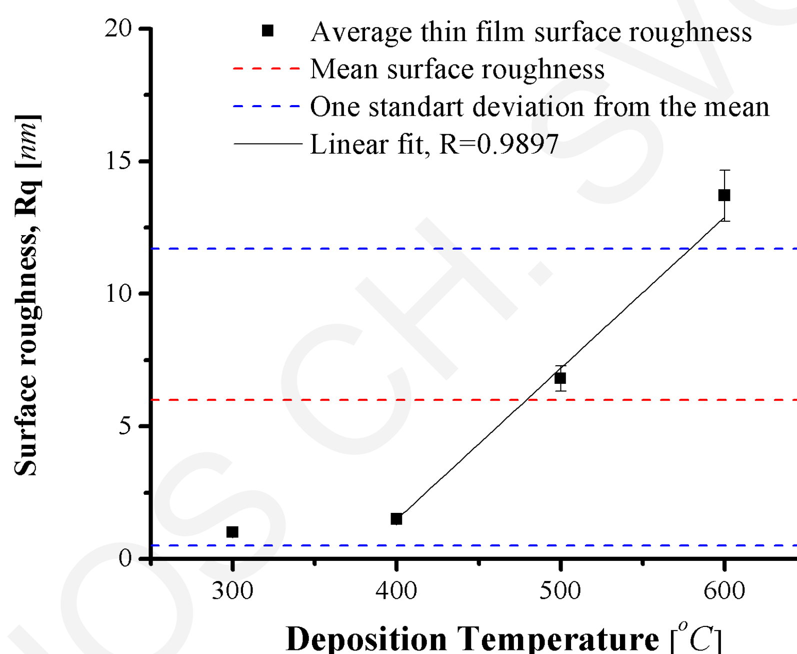

Figure 6.22: *The average surface roughness of the LCO thin films on n++ Si (111) as a function of the deposition temperature. At deposition temperatures above 400^oC, rough films are grown*

Surface resistance modifications were not possible on the as – deposited L_xCO thin films. Further annealing of the samples at 550^oC for 1h in air, completely changed their surface electrical behavior. In Figs 6.23, prior and post annealing surface modifications are presented. The average surface resistance of the thin film grown at 400^oC, decreased by 2.5 orders of magnitude. Films grown at 400^oC followed by annealing exhibit the best ability for surface resistance modification.

EFTHYMIOS CH. SVOUKIS

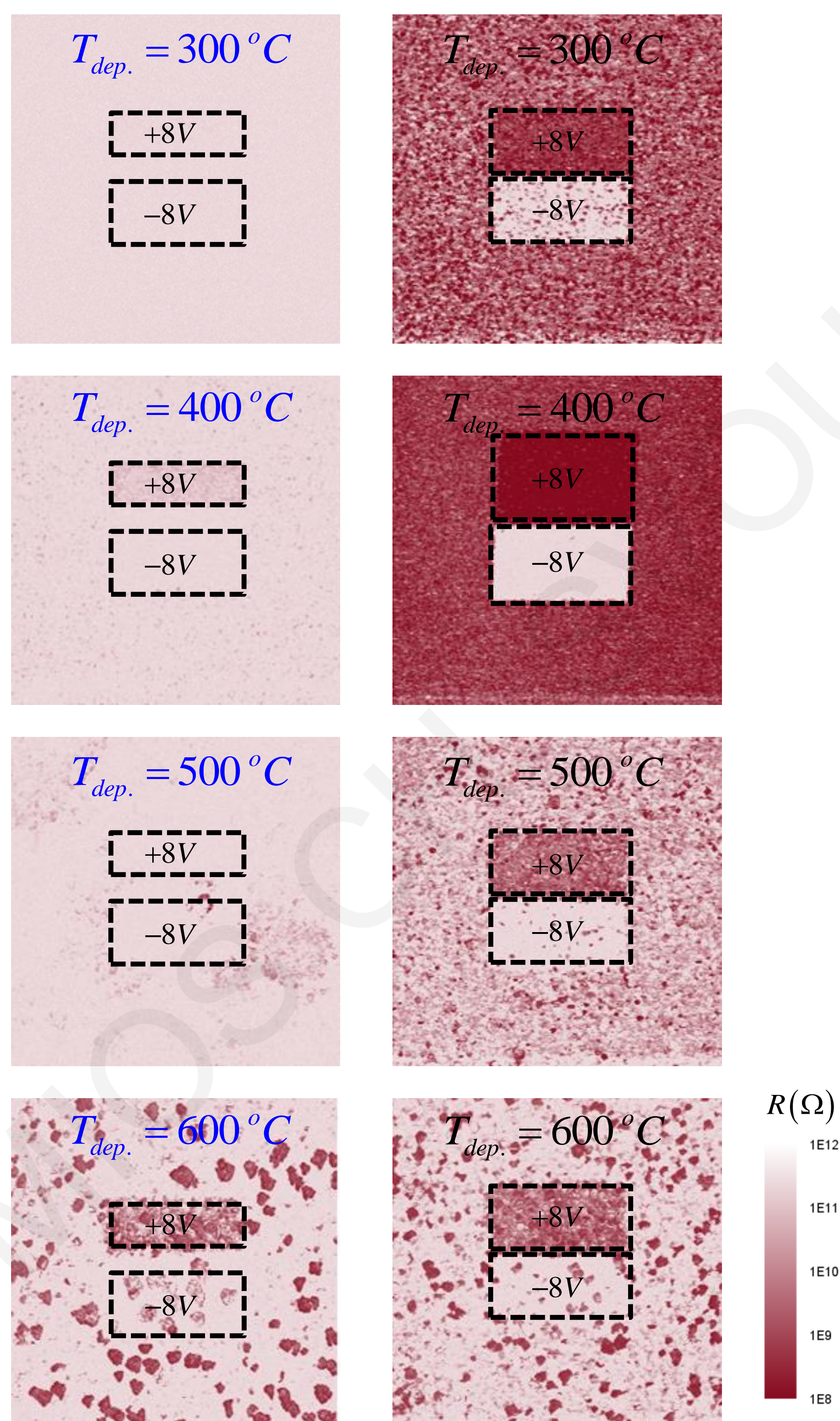

Figure 6.23: *Surface resistance modifications in the LCO thin films grown on n++Si (111) at various deposition temperatures, by applying a +/– 8V bias. On the left and right are shown the surface resistance modifications prior and post annealing at 550°C for 1h in air, respectively.*

By applying a positive – oxidative modification bias (+8*V*) and negative – reductive bias (–8*V*) resulted in a more conductive and more insulating area respectively compared to the initial surface resistance state. In Fig. 6.24 the prior and post annealing average resistance of the LCO thin films and also the average resistance following positive (+8*V*) / negative (–8*V*) bias application are presented as a function of the deposition temperature. A thin film grown at 400^oC was further tested for reversibility of the surface resistance modification process and results are presented in Fig. 6.25.

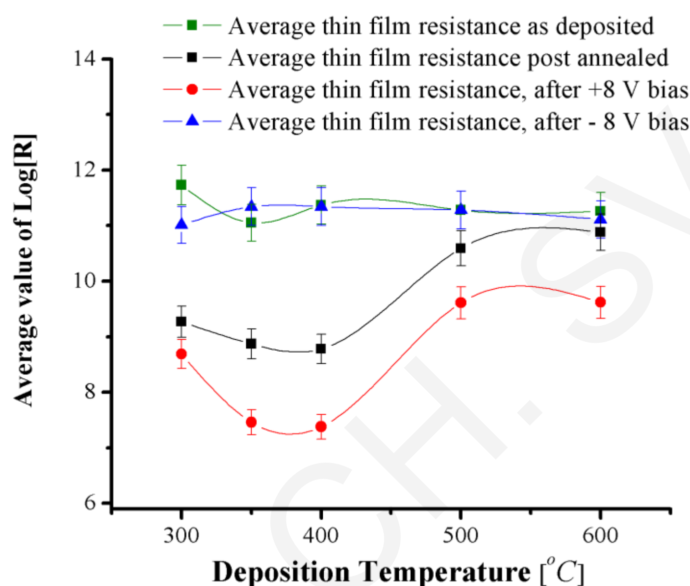

Figure 6.24: *Average logarithm of the surface resistance of L_xCO films on n++ Si (111) as a function of the deposition temperature prior and post bias application.*

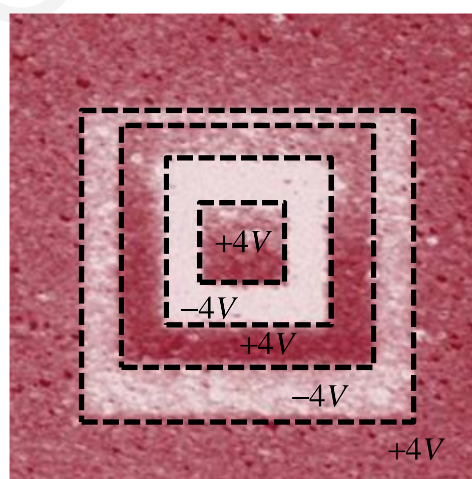

Figure 6.25: *Formation of conducting and insulating regions, using opposite probe voltage polarities in concentric squares. The experiment was performed on a post annealed LxCO sample grown at 400^oC on n++Si (111), using positive (+4V) and negative (-4V) bias and reading bias of +1V.*

EFTHYMIOS CH. SVOUKIS

6.7.5 TEM growth investigation on sample grown at 400^oC

Based on the previous investigations, LCO thin films grown at 400^oC, followed by a post annealing process at 550^oC for $1h$ in air showed reversibility of the surface resistance. Understanding of the mechanisms involved in the annealing process could be used for engineering and optimization of the thin film properties.

Two LxCO films were grown at the optimum conditions based on the previous investigations. Only one of the produced films was annealed at 550^oC for $1h$ in air using heating and cooling rate of $10^oC\ /\ min$. Both films were investigated with cross sectional TEM. Results are presented in Figs. 6.26.

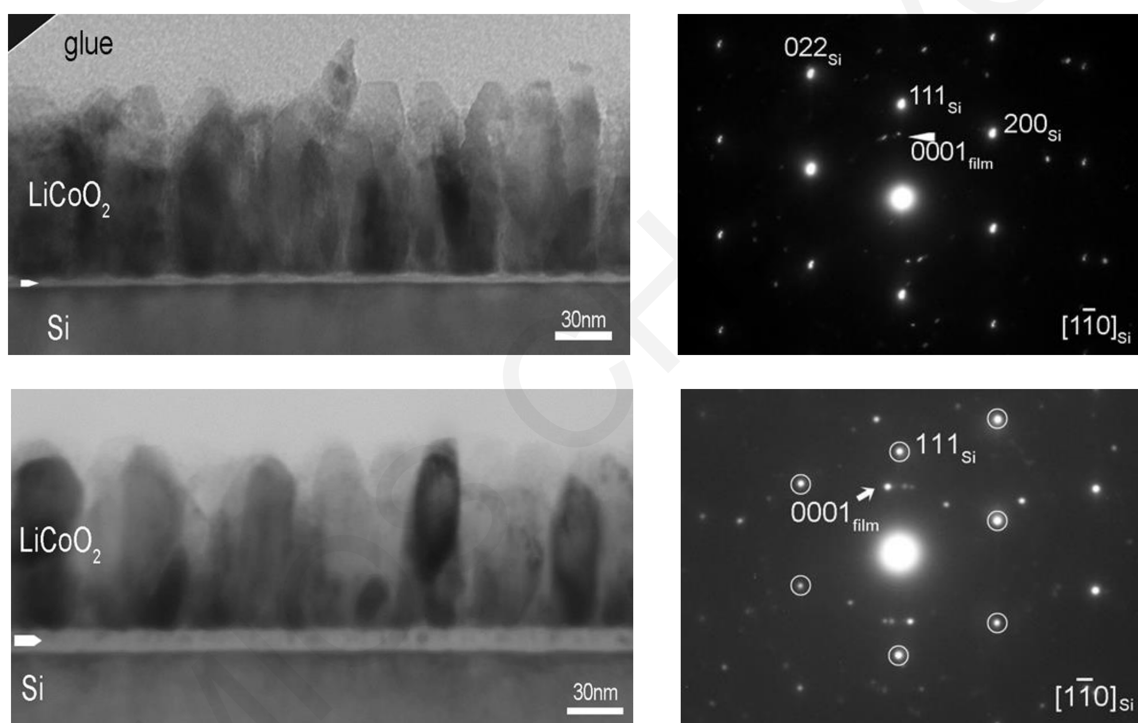

Figure 6.26: *Conventional TEM images and diffraction patters of LxCO thin films grown on n++ Si (111) at 400^oC prior and post annealing, top and bottom respectively.*

TEM investigation revealed the existence of a thin layer of SiO_2 on the as – deposited sample. Annealing process increases the thickness of the SiO_2 layer from ~3 – 9nm. Based on the diffraction pattern of the annealed thin film, the crystallinity has also been improved.

6.8 Mechanism of surface modification in LxCO thin films

In the case of Na_xCoO_2, surface conductivity modifications were attributed to the electrochemical reactions due to a water capillary meniscus formed at the probe – sample contact and possible involvement of redox reactions of Co [148].

We believe that the mechanism for modifications of the surface resistance, involves electrochemical reactions which occur within the condensation water capillary meniscus nanocell formed at the tip / film contact due to the humidity present in the air [152]. A schematic representation of the mechanism is presented in Fig. 6.27.

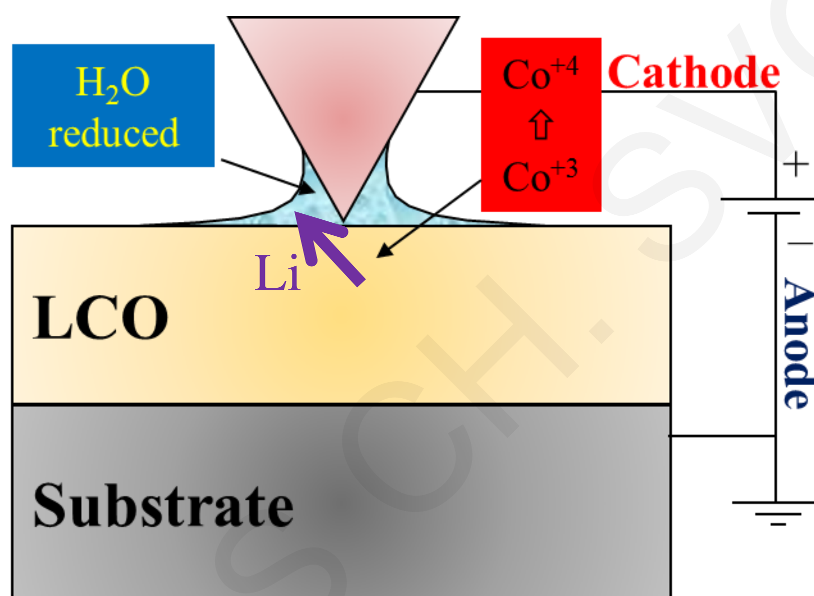

Figure 6.27: *Schematic diagram of the mechanism of electrochemical reactions occuring within the condensation H_2O capillary meniscus nanocell at the tip / film contact.*

In the case of a negative applied bias, Co ions are reduced and water at the tip / film contact meniscus oxidizes. Based on Fig. 6.3, reduction of Co is related to increase of the resistance, attributed to de – intercalation of Li and other cations in the volume of the thin film. Instead, application of positive bias oxidizes Co ions and result in local decrease of the resistance.

This reversible electrochemically – induced mechanism, with the compatibility of the material to current IC characteristics, strengthens the potential use of LCO films as nanoscale rewritable media.

EFTHYMIOS CH. SVOUKIS

6.9 Conclusions

In conclusion, a new possible material for data storage has been presented. The ability for surface resistance modifications in LCO thin films with the usage of a conventional CP – AFM was demonstrated.

The growth of high – quality and low – roughness thin films is desirable for the incorporation of novel materials in the IC industry. LCO thin film suitable for the IC industry have been grown on Al_2O_3 (0001) and Si (111), by using the PLD method.

By applying electric bias on the surface of the LCO thin films, resistive and conductive areas were created. The difference in the surface resistance post modifications via electric bias is typically 3 – 4 orders of magnitude. The phenomenon of surface resistance modification is reversible. Spatial resolution is only limited from the experimental procedures and instrumentation used.

EFTHYMIOS CH. SVOUKIS

Vanadium Dioxide – VO_2

7.1 Introduction

Transition metal oxides have attracted a lot of interest due their multifunctionalities, providing concepts for novel oxide – based electronic devices. The interest in these materials is further increased, due to new possibilities arising in nanoscale form or by creating artificial HSTs.

Vanadium dioxide (VO_2) is a strong correlated oxide that exhibits a first – order phase transition very close to room temperature. This "*smart material*" was initially proposed for daily application such as smart window coatings [176,177].

The nature of the electronic – structural transition is still unknown and has been under investigation for more than three decades. Recent *state – of – the – art* experiments started revealing the hidden aspects of this issue [178]. During the phase transition VO_2 changes from a high – temperature metallic rutile phase to a low – temperature semiconductor monoclinic phase. This phenomenon has widely been described as a metal – semiconductor transition. In this thesis, due to the relatively small charge gap of the low temperature phase (~0.6*eV*), it will be described as semiconductor – metal transition (SMT) [179].

In 2009, V. Pardo and W. E. Picket theoretically investigated the electronic structure of multilayer nanostructures $(TiO_2)_n/(VO_2)_m$ and predicted the appearance of quantum phenomena similar to those observed in graphene [180]. VO_2 could open a new world of opportunities in spintronic technology. The theoretically predicted exotic phenomena require a sharp interface between the VO_2 film and the substrate as well as a high quality thin film.

EFTHYMIOS CH. SVOUKIS

7.2 VO_2 structure and properties

In the complex oxygen (O) – vanadium (V) phase diagram, numerous phases appear. Several V_xO_{2x-1} stable phases (called Magnelli series), with SMT transitions, are also present in the phase diagram and shown in Fig. 7.1.

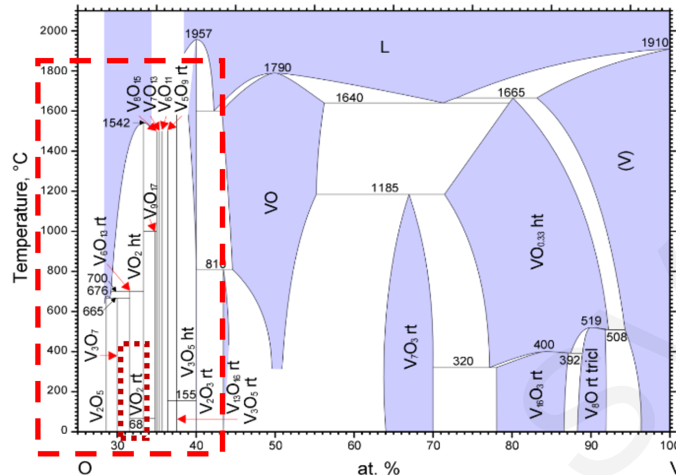

Figure 7.1: *The oxygen – vanadium phase diagram. Within the dashed rectangle, stable V_xO_{2x-1} phases are present* [181].

V_xO_{2x-1} stable phases exhibit SMT at various critical temperatures. Morin first reported a SMT transition in VO_2 single crystal at T_{SM} ~$341K$ [182]. An SMT close to room temperature could be used in various daily applications. Correlation of the VO_2 first order structural change with the electronic properties was experimentally and theoretically investigated. In Table 7.1 stable V_xO_{2x-1} structures for $x \geq 2$ accompanied with their SMT are shown.

Table 7.1: *V_xO_{2x-1} chemically stable phases exhibiting a SMT accompanied with the transition temperatures* [182,183].

V_xO_{2x-1}		*SMT Temp. (K)*	V_xO_{2x-1}		*SMT Temp. (K)*
x=2	V_2O_3	*155*	x=6	V_6O_{11}	*170*
x=3	V_3O_5	*430*	x=7	V_7O_{13}	-
x=4	V_4O_7	*238*	x=8	V_8O_{15}	*68*
x=5	V_5O_9	*135*	x=9	V_9O_{17}	*79*

EFTHYMIOS CH. SVOUKIS

7.2.1 Crystal structures of VO_2

VO_2 single crystals above T_{SM} stabilize in a tetragonal (rutile – R) phase. This high – temperature phase is based on a tetragonal body – centred unit cell with space group $P4_2/mnm$ and lattice parameters: $a_R = 4.554\,\overset{o}{A}$ and $c_R = 2.8557\,\overset{o}{A}$ [184,185]. V atoms form the unit cell and are surrounded by orthorombically distorted O octahedra formed by six O atoms [186]. V atoms form coupled chains along the c – axis, by sharing corner O atoms of the octahedral, in distances of c_R . A schematic diagram of the R structure is presented in Fig. 7.2.a.

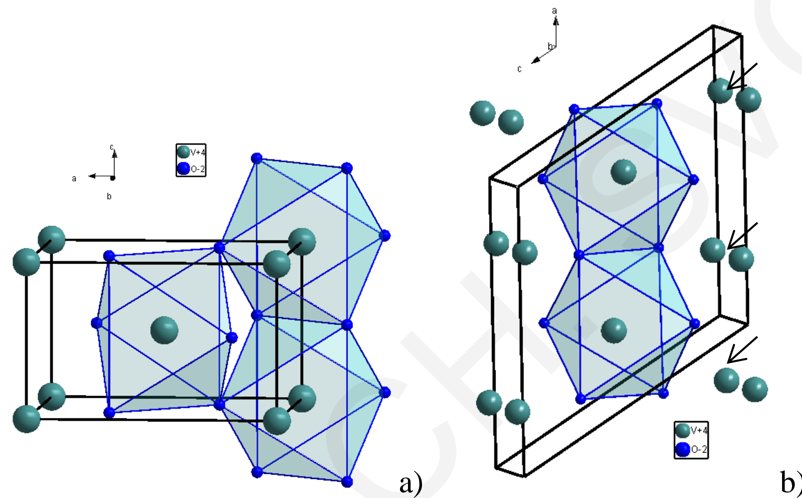

Figure 7.2: *Crystallographic structures of main VO_2 phases. a) R phase above T_{SM} and b) M_1 below T_{SM}. In the M_1 phase there is a pairing and tilting of the vanadium atoms along the a – axis. M_1 has double the volume of the R phase.*

Upon cooling below T_{SM}, at room temperature, VO_2 single crystals stabilize in a less symmetric monoclinic structure (M_1, shown in Fig. 7.2.b). M_1 belongs to space group $P2_1/c$, with reported lattice constants: $a_{M_1} = 5.7517\,\overset{o}{A}$, $b_{M_1} = 4.5378\,\overset{o}{A}$, $c_{M_1} = 5.3825\,\overset{o}{A}$ and $\hat{\beta} = 122.65^o$ [187]. M_1 structure can be described as double of the R phase with $a_{M_1} \approx 2c_R$. V atoms pair along the a – axis in a zig – zag way (arrows in Fig. 7.2.b), distorting and twisting the O octahedra in distances $2.619\,\overset{o}{A}$ and $3.164\,\overset{o}{A}$ instead of c_R [185].

EFTHYMIOS CHASOUKIS

7.2.2 Electronic properties of VO_2 phases

The electronic properties of VO_2 phases can qualitatively be explained based on energy band diagrams first proposed by Goodenough [188]. VO_2 electronic structure can be described as $3d^1$ compound, due to the remaining electron per V^{+4} cation.

The V d – states subjected to an anisotropic crystal field, degenerate into lower t_{2g} and higher e_g states, presented in Fig. 7.3.a. The overlapping of the t_{2g} states depends on the relative ratio of c/a in the VO_2 structure. In an ideal tetragonal structure $c/a = 0.66$ and the t_{2g} states are discrete [189].

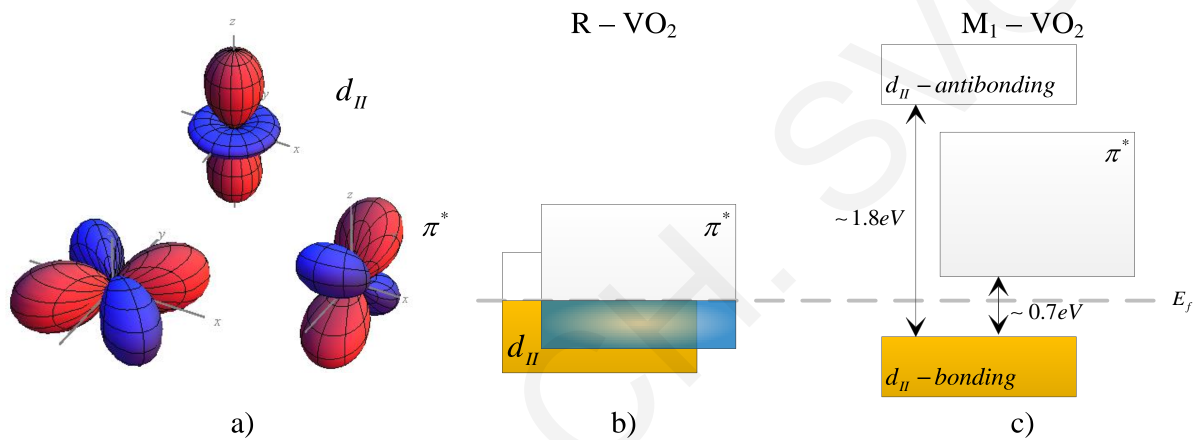

Figure 7.3: *a) The d_{II} and π^* states, top and bottom respectively. The schematic electronic band diagrams of VO_2 for R and M_1 phases close to the Fermi level are presented in b) and c) respectively.*

In the R phase, the t_{2g} states overlap, with $c_R/a_R \approx 0.627$, and the Fermi level is located near the t_{2g} states. In the presence of an octahedral crystal field from the six O atoms in the structure (Fig.7.2.a), t_{2g} states degenerate into a π^* double and a d_{II} state. The d_{II} is parallel to the c – axis of the R phase, resulting to a strong metallic V bonding. In the R phase, the single electron of a V atom resides in the lowest d_{II} state and that is the reason R is described as metallic [190].

Crystallization of VO_2 in a less symmetric structure (M_1), at temperatures below T_{SM}, results in dimerization of V pairs and also pertrubates the octahedral crystal field. The d_{II} states split in bonding and antibonding states, with lower and higher energy states, respectively, and a gap of ~1.8eV. Further, the tilting of the V pairs, which increases the overlapping of the O states, results in the shift of the π^* doublet to higher energies. A bandgap

EFTHYMIOS CH. SVOUKIS

(Peierls like) of ~0.7eV opens between the bonding d_{II} and the π^* doublet [191]. Schematic diagrams of R and M_1 phases are present in Fig. 7.3.b and c).

7.2.3 Phase transition mechanism

Since 1971 when Goodenough firstly proposed the simplified energy band diagrams of the VO_2, controversial mechanisms have been proposed for the explanation of the transition mechanism from R to M_1 phase. The point of debate concerning the transition is whether it can be described with the Peirels or the Mott – Hubbard mechanism [192].

In the Peirels mechanism, lattice distortion changes the Fermi surface and opens an energy gap [193]. The splitting of the d_{II} states, the pairing of the V atoms and the unit cell doubling can be interpreted with the Peirels mechanism. Based on this mechanism, the electronic band structure based on density functional theory calculations failed to yield the experimentally found bandgap of ~0.7eV [194].

A second mechanism based on strong electron correlations in the d_{II} states was proposed by Zylbersztejn and Mott [195]. According to this mechanism, the transition degenerates the band and the correlation energy becomes comparable with the bandwidth. The Mott – Hubbard mechanism is, however, inconsistent with the structural change and V atom pairing.

Pauget and Hugon attempted to put an end to the controversy by suggesting that VO_2 is close to a Mott – Hubbard insulator, with the lattice distortion playing a crucial role for the transition [196]. However their consideration is overoptimistic and the transition mechanism is under investigation.

7.3 Selection of TiO_2 (001) for a substrate

Growth of high quality VO_2 thin films is crucial for its incorporation in IC industry for technological applications. Compared to bulk samples where cracking effects occur due to SMT, thin films can withstand distortion effects.

EFTHYMIOS CH. SVOUKIS

Last years, a lot of experimental work has been performed on the growth of high quality VO_2 thin films. Growth is challenging due to the multi – valence states of V and the narrow pressure – temperature window available for the growth of stoichiometric VO_2.

Substrate plays a key role in the growth of epitaxial thin films, and as described in Ch. 4 selection of suitable substrate for promotion of epitaxy is crucial. By applying various PVD techniques, VO_2 thin films have been grown on oxide substrates or by applying an ultrathin oxide buffer layer as in the case of T.H. Yang *et al.* [197]. Correlation of structural and transport properties of VO_2 thin films have also been lately reported.

TiO_2 was selected as a substrate for detailed investigation by Muraoka *et al.* due to chemical and similarities with VO_2 [198]. Lattice parameter matching of substrate – thin film and the R structure of TiO_2 can promote epitaxial growth and eliminate the formation of defects or cracks during growth. In Table 7.2, lattice constants of the R structures of VO_2 and TiO_2 are summarized accompanied by the lattice mismatch [184,185,187].

Table 7.2: *Lattice constant and mismatches of R structures of VO_2 and TiO_2 at room temperature* [184,185,187].

Film / Substrate	**Lattice constant (Å)**	
	a	***c***
R – VO_2	4.554(6)	2.855(7)
R – TiO_2	4.593(3)	2.958(7)
Lattice Mismatch %	0.86	3.62

7.3.1 TiO_2 (001) termination control

TiO_2 has widely been used for the epitaxial growth of a variety of oxide thin films [199]. It has been scarcely reported the relation of bulk defects (*e.g.* oxygen vacancies after UHV or oxygen annealing) with the morphology of the substrates.

Commercial low – miscut (<0.5*deg*) TiO_2(001) single crystals were chemically treated for reduction of resins or particulates from the polished surface. Initially, they were ultrasonically cleaned in acetone for 20*min*, followed by isopropanol for 10*min*. For both

EFTHYMIOS CH. SVOUKIS

ultrasonic baths, high purity organic chemicals were used. Then, the substrates were placed on Whatman cleaning tissue and blown with N_2 high purity gas (5.0).

A modified Kawasaki *et al.* recipe, was used for the termination process and surface regrowth [200]. Chemical and thermal treatments were systematically investigated. TiO_2 substrates were placed for etching in a commercial buffered hydrofluoric – acid (BHF, Merck, NH_4F : HF = 87.5:12.5) for 5*sec*. For the neutralization of the acid, two di – ionized water baths (R > 10$M\Omega$) in a row were used. In Fig. 7.4.a, an AFM image of an as – received TiO_2 substrate is presented. The surface has very low roughness $R_q = 1.7\,\mathring{A}$ and is free of particulates. Surface crystallinity of the same TiO_2 (001) substrate was investigated by RHEED (electron energy of 28*keV*, and beam current of 33μA) in UHV conditions at room temperature. In the RHEED pattern spots and Kikuchi lines appear evidence of high quality surface and is presented in Fig.7.4.b.

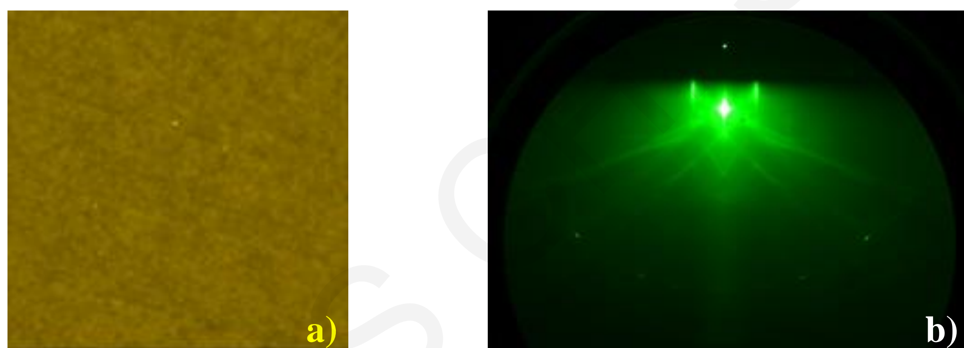

Figure 7.4: *16 μm^2 AFM image (a) and RHEED pattern (b) of an as – received TiO_2 (001) substrate at room temperature.*

The influence of post – annealing treatment in vacuum or in the presence of oxygen atmosphere for optimization of the treatment conditions was investigated. The optimum thermal treatment was found to be annealing of the substrates at 800^oC in oxygen atmosphere. AFM investigations revealed the appearance of a smooth surface with a low roughness of $R_q \sim 1.0\,\mathring{A}$, shown in Fig. 7.5.a. Investigation of the sample by RHEED under in the same conditions (electron energy of 28*keV*, and beam current of 33μA) in UHV at room temperature, revealed brighter spots compared to Fig.7.4.b, evidence of higher surface crystallinity and smoothness.

EFTHYMIOS SVOUKIS

The influence of oxygen atmosphere in the thermal treatment was investigated by annealing a substrate at 800^oC in UHV conditions. AFM investigation showed 3 – Dimensional surface reconstruction with $R_q = 10.3\overset{o}{A}$ (Fig.7.4.c.).

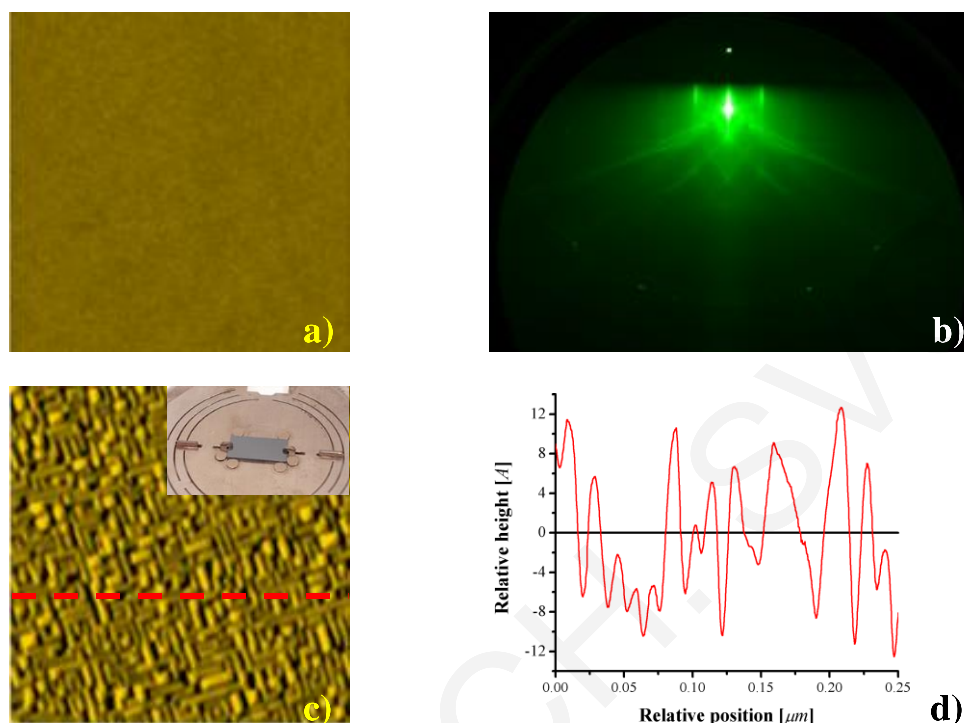

Figure 7.5: *16 μm² AFM image and RHEED pattern of a chemically and thermally treated at 800°C TiO_2 (001) substrate are presented in a) and b) respectively. Reconstruction of TiO_2 (001) surface observed after annealing in UHV conditions at 800°C, is shown in the 0.06 μm² AFM image in c). Inset in c): a real image showing color change of the substrate. A line scan of the reconstructed surface is presented in d).*

7.3.2 Growth of VO_2 thin films

A KrF* laser operated at 5*Hz* was used to ablate a metallic vanadium target (99.9% purity) at an incident angle of 45°. The focused spot size was S=50mm^2 on the target and an average $\Phi = 1.3 Jcm^{-2}$ was used in all the depositions.

The 2 – inch target was placed d_{T-S}=52*mm* away from the substrate and was rotated (20*rpm*) and toggled during the deposition to keep the ablated target surface fresh. Prior each deposition the chamber was evacuated to a base pressure $P < 5 \cdot 10^{-6} mbar$.

During the deposition process pure oxygen was introduced in the chamber and the pressure was kept constant at 0.017*mbar* using a mass flow controller. Films were grown at various substrate temperatures in the range of 200–600^oC, using heating and cooling rates of 10^oC / *min*. In Fig. 7.6 a schematic diagram of temperature and pressure conditions during a typical deposition are presented.

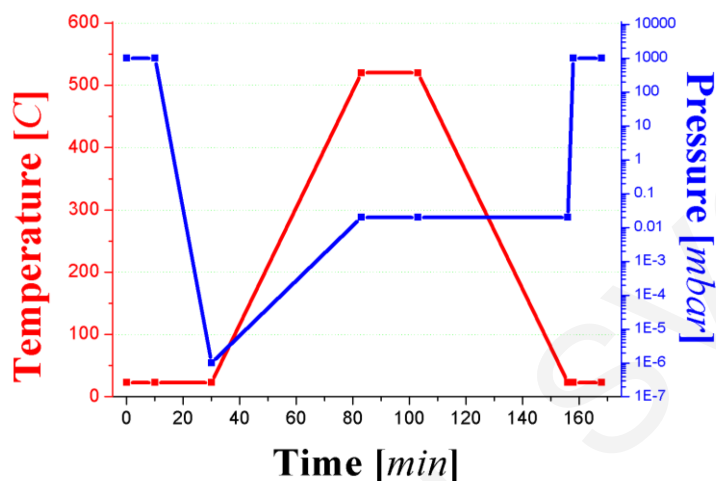

Figure 7.6: *Schematic diagram of the deposition conditions (temperature and pressure) over a typical deposition.*

7.3.1 RHEED in situ investigation

VO_2 thin film growth has been monitored *in situ* via RHEED (electron energy of 28*keV*, and beam current of 33μA). Initial surface morphology and crystallinity were examined in UHV conditions at room temperature, verifying the effectiveness of the chemical and thermal treatments.

Spots and Kikuchi lines were observed for the substrate prior deposition, indicative of an atomically flat substrate. Such a pattern of a TiO_2 (001) substrate is presented as an inset in Fig. 7.7.

During deposition, the intensity of the specular spot was recorded over time. Intensity oscillations have been recorded for thin films, a manifestation of layer – by – layer (Frank – van der Merwe) growth. This kind of growth is promoted via high substrate – thin film bonding. Fig. 7.7 displays a typical RHEED oscillation obtained during the growth of VO_2 thin films.

EFTHYMIOS CHRISTOUKIS

Typically ~12*sec* (60*pulses*) are needed for the growth of a single monolayer, resulting to a $D_R \sim 0.06\,\mathring{A}/pulse$. Based on the *c* – axis lattice parameter of VO_2 single crystal, ~48*pulses* are needed for the full coverage of an atomic plane. Similar growth investigation via *in situ* RHEED have only be presented for the growth of VO_2 / TiO_2 supper – lattices with MBE [201].

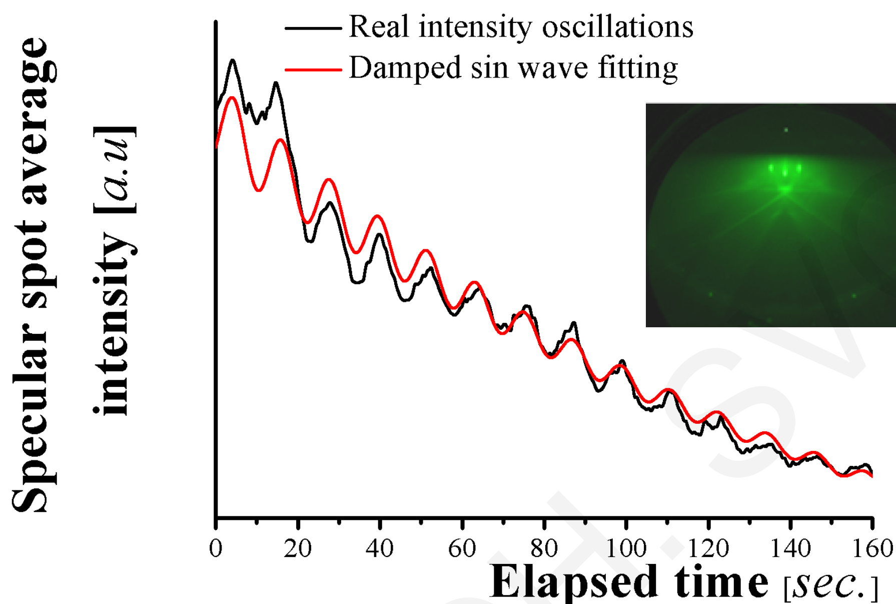

Figure 7.7: *Specular spot intensity oscillations of a VO_2 thin film grown on TiO_2 (001), at 400°C in 0.017mbar, which are evidence of a layer – by – layer growth. A RHEED pattern of the bare substrate prior deposition is presented as an inset.*

7.4 X – ray diffraction characterization

7.4.1 Out – of – plane configuration

Fig. 7.8 shows the XRD patterns of the deposited thin films on annealed TiO_2 (001) grown at different deposition temperatures. Diffraction patterns revealed that thin films grown at room temperature exhibited week crystallinity. Above 200°*C*, intensive peaks corresponding to VO_2 appear.

EFTHYMIOS CH. SVOUKIS

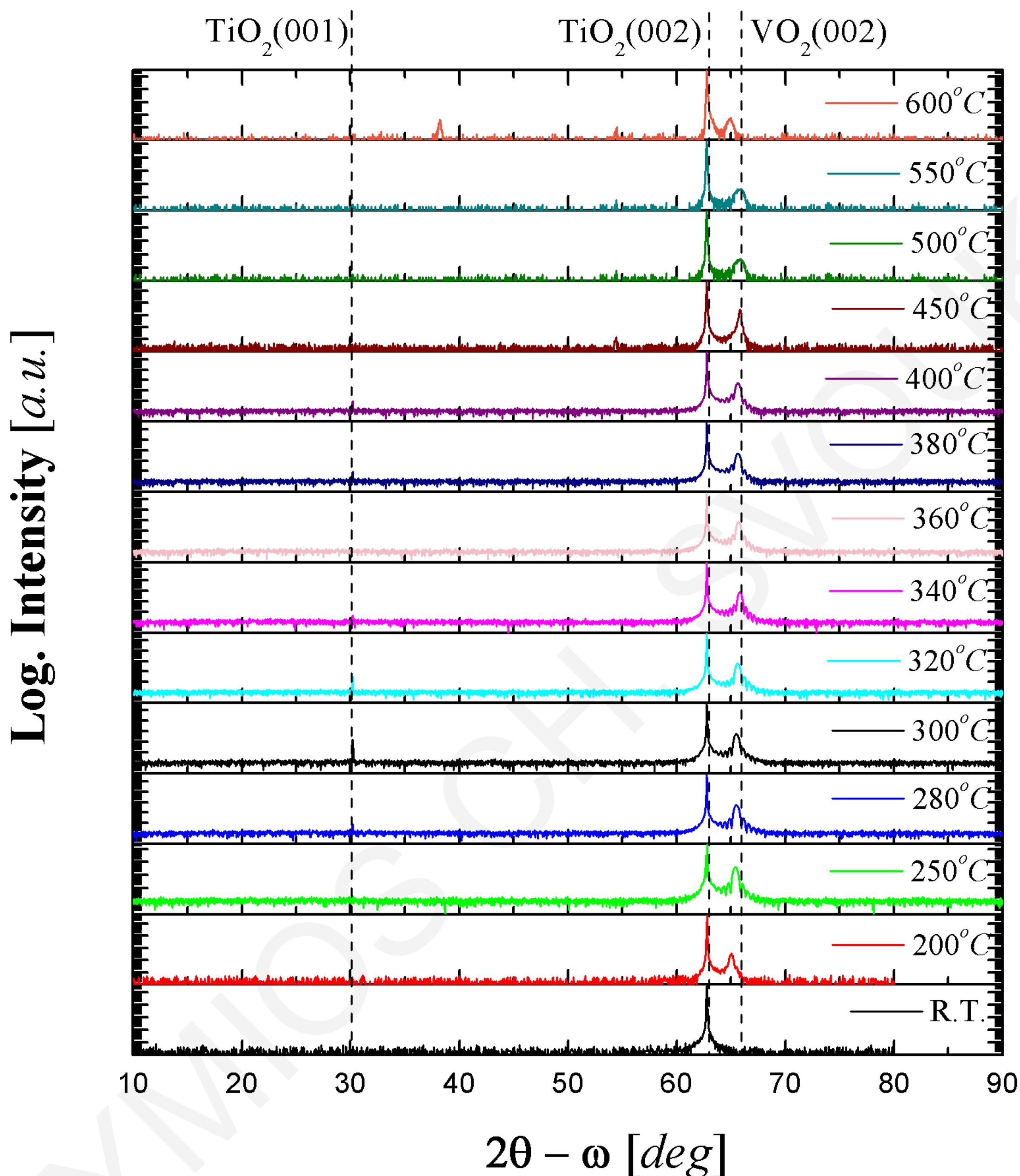

Figure 7.8: *$2\theta - \omega$ XRD patterns of VO_2 thin films produced in various deposition temperatures.*

For accurate lattice parameter calculation, HR XRD $2\theta/\omega$ scans were performed in the produced thin films. The XRD patterns close the (002) peak of VO_2 are presented in Fig. 7.9. Measurement conditions were selected to ensure the adequate statistics.

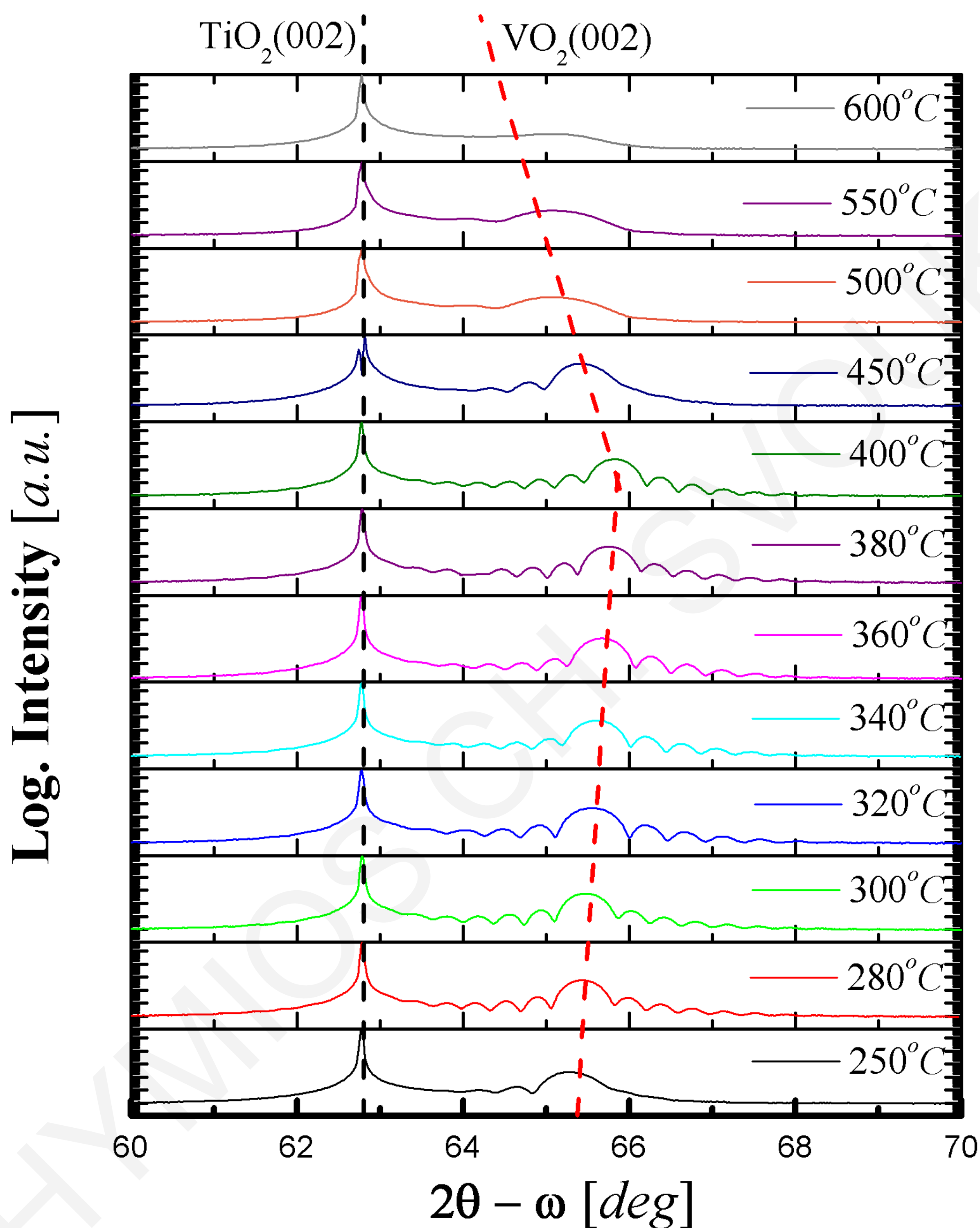

Figure 7.9: *High resolution 2θ – ω patterns of VO_2 thin films in small step scans close to (002) peaks of TiO_2 substrate and VO_2 thin film.*

EFTHYMIOS CHRISOVALANTIS

HR XRD investigations showed the appearance of lattice fringes, in thin films grown at 280–400^oC, evidence of epitaxial growth. The average thickness of the produced thin films based on the lattice fringes was calculated to be 24.1 ± 4.3*nm*. The position center of the VO_2

(002) peak monotonically shifts to higher 2θ–ω values as the deposition temperature increases in the range of 200–400^oC. Further increase of the deposition temperature eliminates the appearance of lattice fringes and also shifts the position of the VO_2 (002) peak to lower values.

Based on the HR XRD patterns, the c – axis lattice parameter of the VO_2 thin films was calculated for all deposition temperatures and is presented in Fig. 7.10. At low deposition temperatures 200–250^oC, the measured lattice parameters are comparable to the value reported in the literature for VO_2 single crystals in room temperature. Within the range of 200–400^oC, the c – axis lattice parameter decreases monotonically as the deposition temperature increases with a rate $-1.2\cdot10^{-4}\ \overset{o}{A}/{}^oC$. For deposition temperatures above 400^oC the lattice parameter of VO_2 seem to increase again. These results are in agreement with those published by Muraoka and Hiroi and were attributed to *in* – plane epitaxial strain [198].

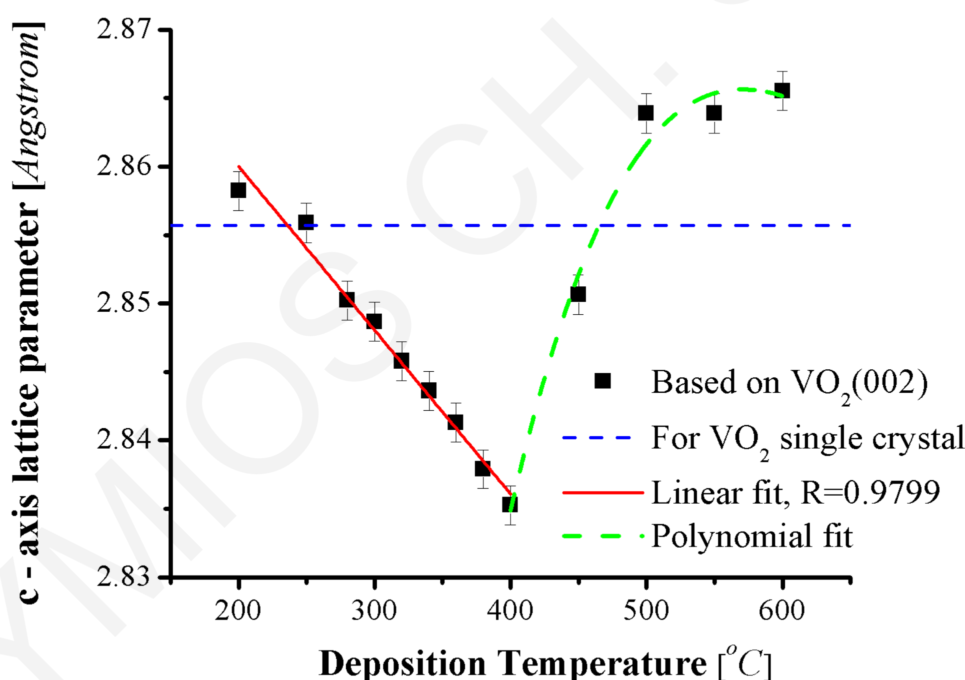

Figure 7.10: *The c – axis lattice parameter of the VO_2 thin films grown on TiO_2 (001), as a function of their deposition temperature.*

Rocking curve scans on the (002) diffraction peak were performed for all VO_2 thin films. In Fig. 7.11.a, a rocking curve of a thin film grown at 400^oC is presented, whereas in part (b) at the same figure the FWHM of the produced thin films is presented as a function of the deposition temperature. All thin films investigated with rocking curve showed an average FWHM of 0.066 ± 0.004*deg*. These values indicate that all thin films are almost perfectly

EFTHYMIOS CH. SVOUKIS

aligned along the growth direction. For thin films grown above 450^oC, the FHWM values increase as the deposition temperate increases.

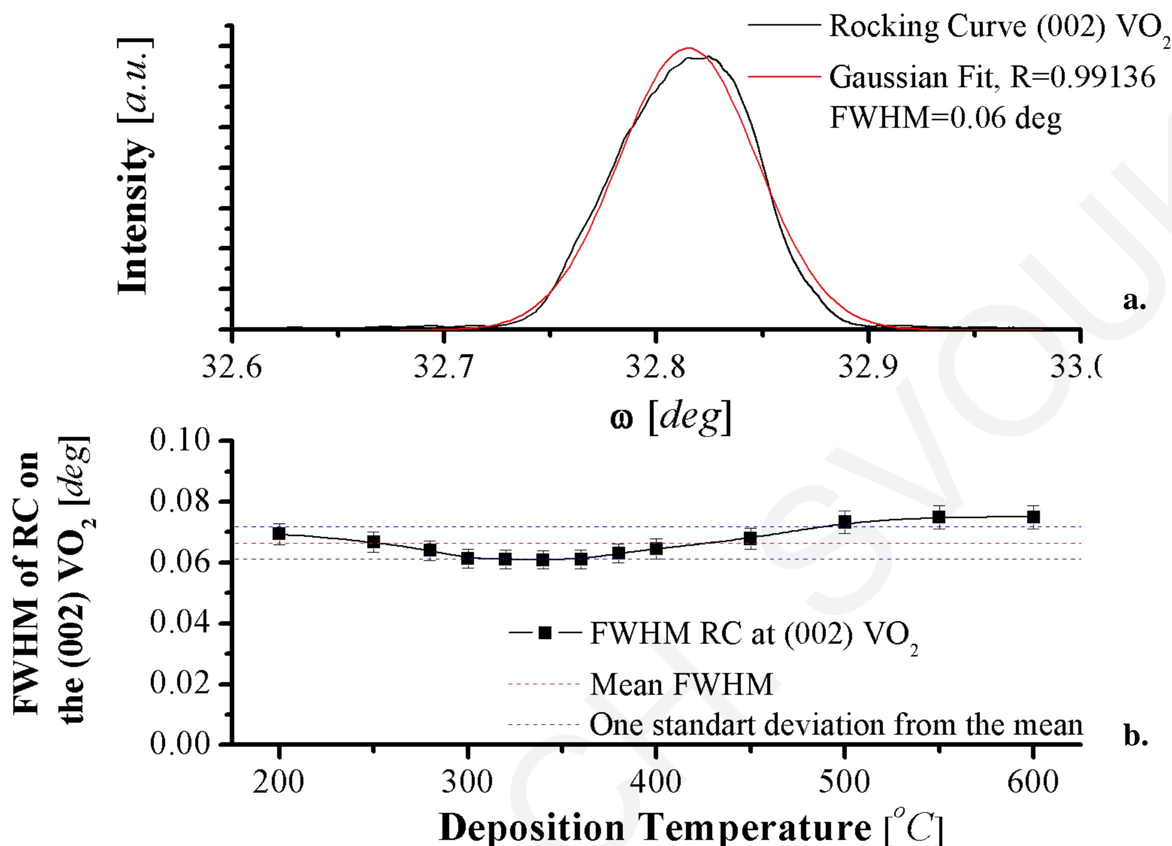

Figure 7.11: *a) Rocking curve on the (002) VO_2 peak for a thin film grown at 400^oC. b) FWHM of the rocking curve of VO_2 thin films as a function of their deposition temperature.*

7.4.2 In – plane configuration

To assess the *in* – plane orientation of the film with respect to the substrate, azimuthal – scans were carried out on skew planes of VO_2 and TiO_2 in a symmetric geometry measurement. The (220) plane family has been chosen both for film and substrate. The azimuth scan shows four maxima, in accordance with the fourfold symmetry of the normal to the (001) planes of the tetragonal structures.

In Fig. 7.12, azimuthal scans of a VO_2 thin films grown at 200, 400 and 600^oC is presented. In all azimuthal – scans the peaks corresponding to the substrate were on top of those of the film, showing a possible cube – on – cube epitaxy.

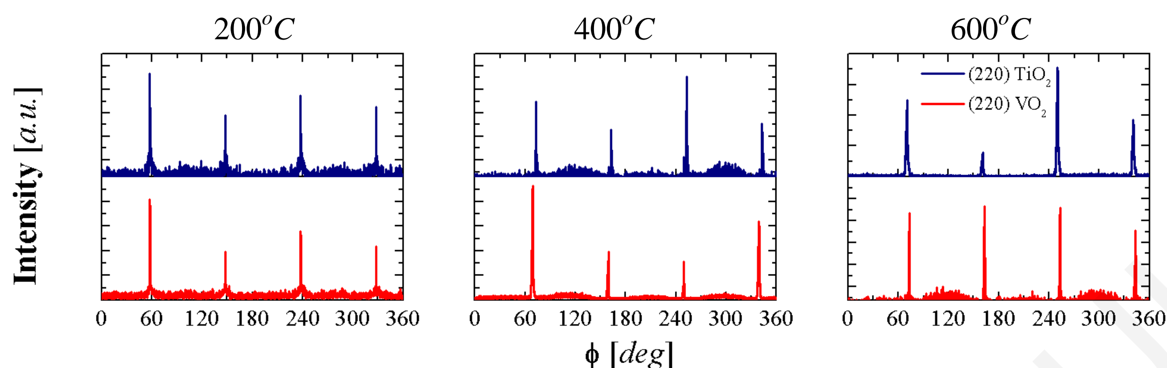

Figure 7.12: *Azimuthal scan of a VO_2 thin films grown on TiO_2 at 200, 400 and 600°C. Film and substrate azimuths are in the same direction, showing a possible cube – on – cube epitaxy.*

Space mapping investigations of the $(\bar{1}\bar{1}2)$ node of TiO_2 and VO_2 verified the cube – on – cube epitaxy. The position of the peaks of film and substrate, indicate that the *in* – plane parameters of the film and substrate are the same $a = b = 4.593\,\overset{o}{A}$, therefore, the films are fully strained. This can be attributed to the substrate clamping effect [202]. A 3D image of the reciprocal space mapping for a film grown at 400°*C* is presented in Fig. 7.13. Investigations on samples grown above 400°*C* revealed multiple peaks related to the film, Fig 7.13.b.

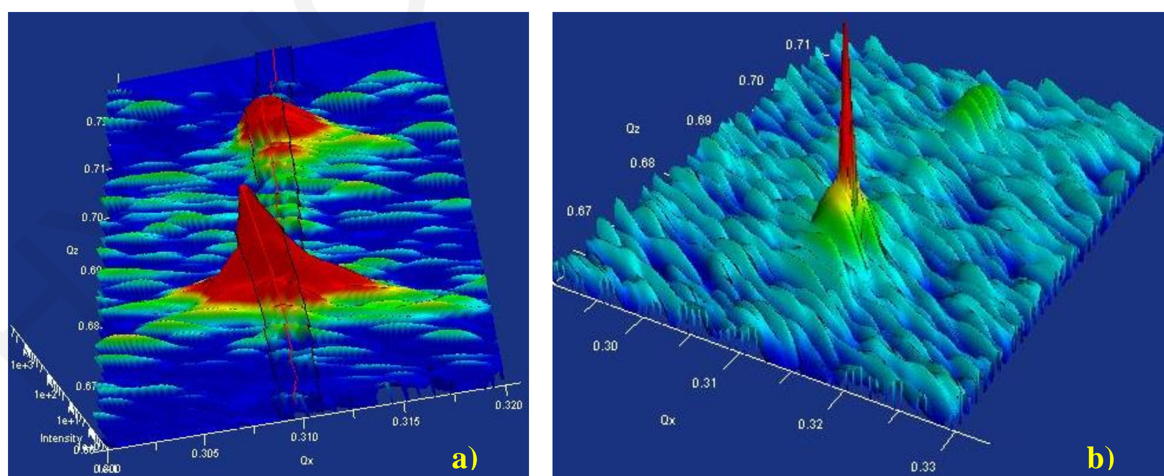

Figure 7.13: *3D images of the reciprocal space mapping for VO_2 thin film grown at 400°C and 500°C, in a) and b), respectively.*

7.4.3 XRR

Investigation of the film quality and evaluation of the thickness was performed using XRR measurements. In Fig. 7.14 XRR curves for VO_2 thin films grown at various temperatures are presented.

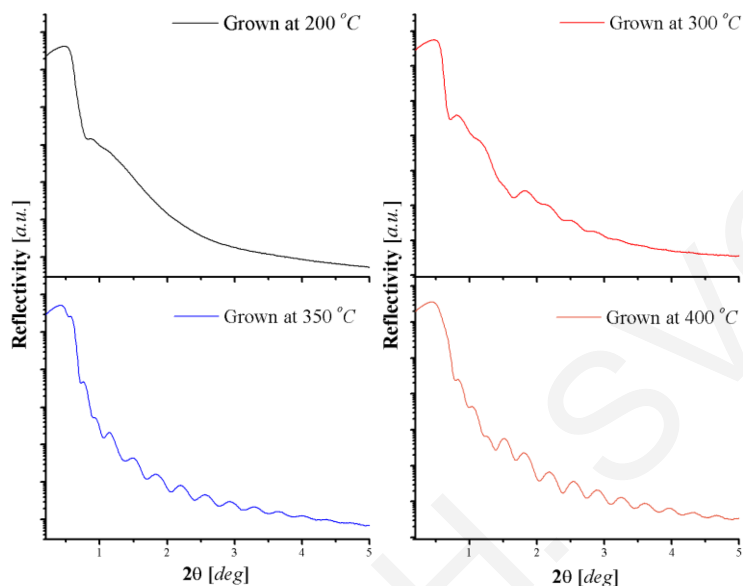

Figure 7.14: *XRR measurements on thin films grown at 200, 300, 350 and 400°C.*

The determination of the thickness was possible by fitting the acquired data with simulation models. In Fig 7.15.a a simulation of the XRR data is presented and in Fig 7.15.b the thickness of the films is presented as a function of the deposition temperature. The average thickness is close to the one predicted via lattice fringes and RHEED.

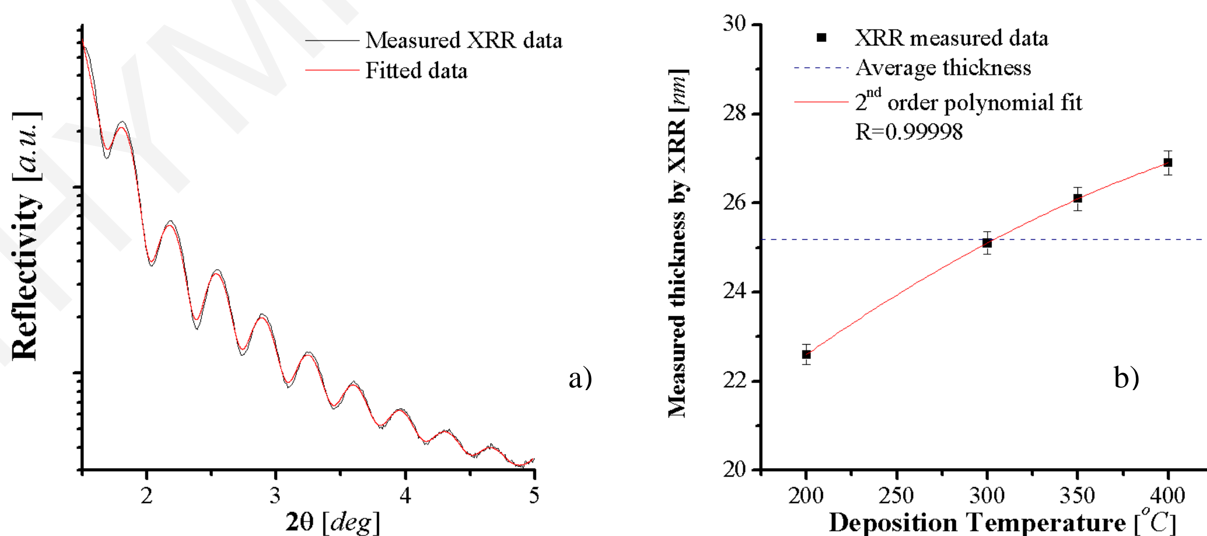

Figure 7.15: *a) Simulation of XRR data. b) Thickness of films as a function of the deposition temperature for specified number of pulses.*

EFTHYMIOS CH. SVOUKIS

7.5 Surface morphology investigation and elemental analysis

The surface roughness of the films was evaluated using an AFM in contact mode. In Fig. 7.16, AFM images of VO_2 thin films grown at various deposition temperatures are presented.

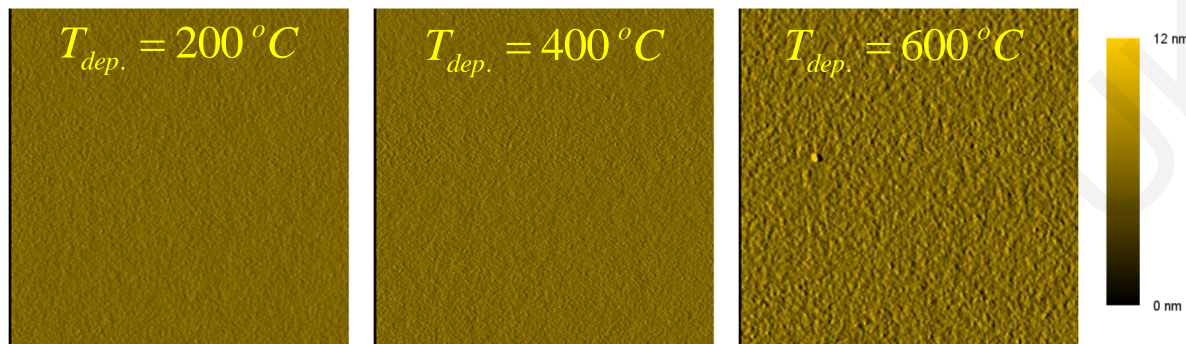

Figure 7.16: *AFM images (10 x 10 μm^2) of VO_2 thin films deposited on TiO_2 (001) substrate at various temperatures. The scale is the same for all images.*

The AFM results on the change of the surface morphology are in good agreement with SEM imaging that was performed on large surface areas. SEM investigations verified that VO_2 thin films were free of cracks, holes and particulates. In Fig. 7.17.b, a secondary electron SEM image of a film grown on TiO_2 at $400^{o}C$ is presented. In addition, EDX investigations were also performed for elemental analysis of the films. In the EDX patterns peaks corresponding to Ti, V and O were only present. A typical EDX spectrum is presented in Fig. 5.5.a.

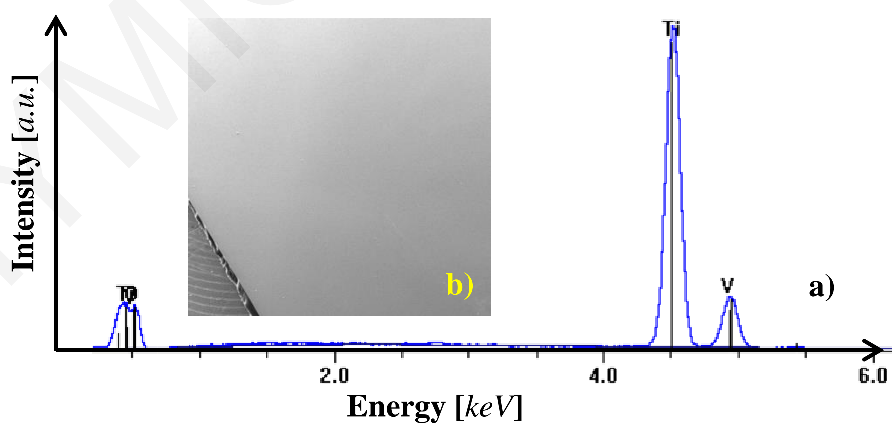

Figure 7.17: *EDX analysis spectrum (a) and a secondary electron SEM image (b) are shown, for a sample grown at $400^{o}C$.*

EFTHYMIOS CH. SVOUKIS

7.6 TEM growth investigation

VO_2 thin films grown at 280, 300, 400, 500 and 600^oC were investigated via TEM. The cross – section specimens for TEM observations have been prepared by mechanical polishing followed by ion milling at low angle. In Fig 7.18, TEM images, SAED patterns and HR TEM images of films grown at 280–400^oC are presented.

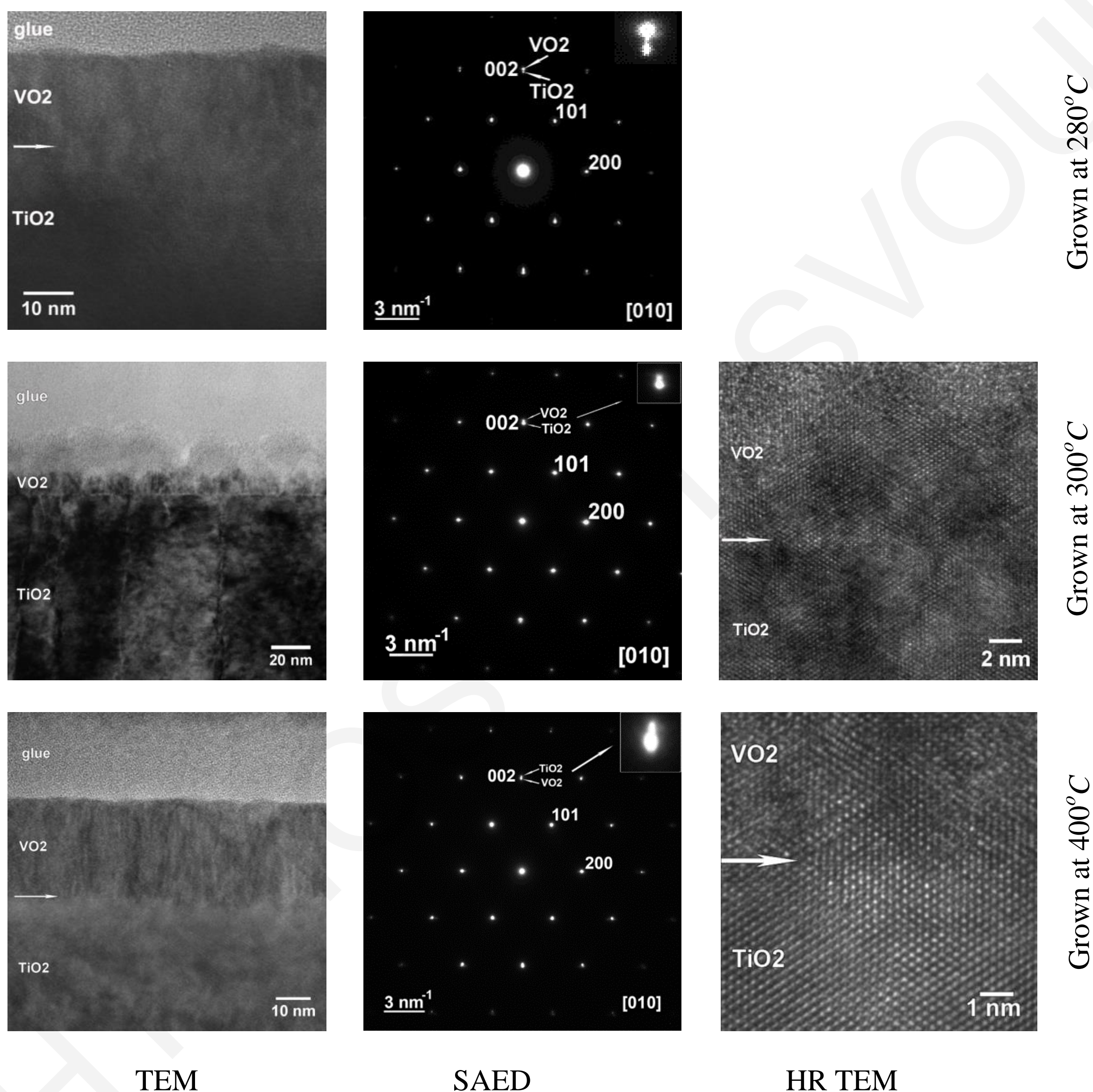

Figures 7.18: *TEM images, SAED patterns and HR TEM images of VO_2 thin films grown on TiO_2 at 280, 300 and 400^oC. The deposition temperature affects the type of growth. At 400^oC the film is epitaxially grown, whereas below 400^oC, a columnar growth has been observed.*

TEM images in Fig. 7.18 reveal the columnar growth for thin films grown at 280 and 300^oC (Zone I & II). For thin films grown at 400^oC, no columns were observed through the investigated volume indicating that Zone III has been reached and also a sharp interface is

EFTHIMIOS SVOUKIS

present. Deposition temperature plays a key role as explained in Ch. 4.4.2. SAED patterns revealed the epitaxial growth of the VO_2 thin films on the TiO_2 substrates. The SAED patterns (Fig. 7.18) indicate the presence of two structures: the TiO_2 rutile structure and the VO_2 rutile structure. The presence of these two structures is indicated by the 002 splitted spot in the diffraction pattern shown by arrows and zoomed into the inset in SAED patterns. The orientation relationship between the crystallographic axis of the VO_2 thin film with respect to the TiO_2 substrate is $[002]_{R-VO2}//[002]_{R-TiO2}$ and $[101]_{R-VO2}//[101]_{R-TiO2}$. Based on the SAED patterns, the lattice misfit between the TiO_2 substrate and VO_2 thin film is –2.9% out – of – plane (lower compared to the one theoretically predicted, Table 7.2) and 0.8% in plane. Similar investigations were also performed on VO_2 thin films grown at 500 and 600^oC and the results are presented in Fig 7.19.

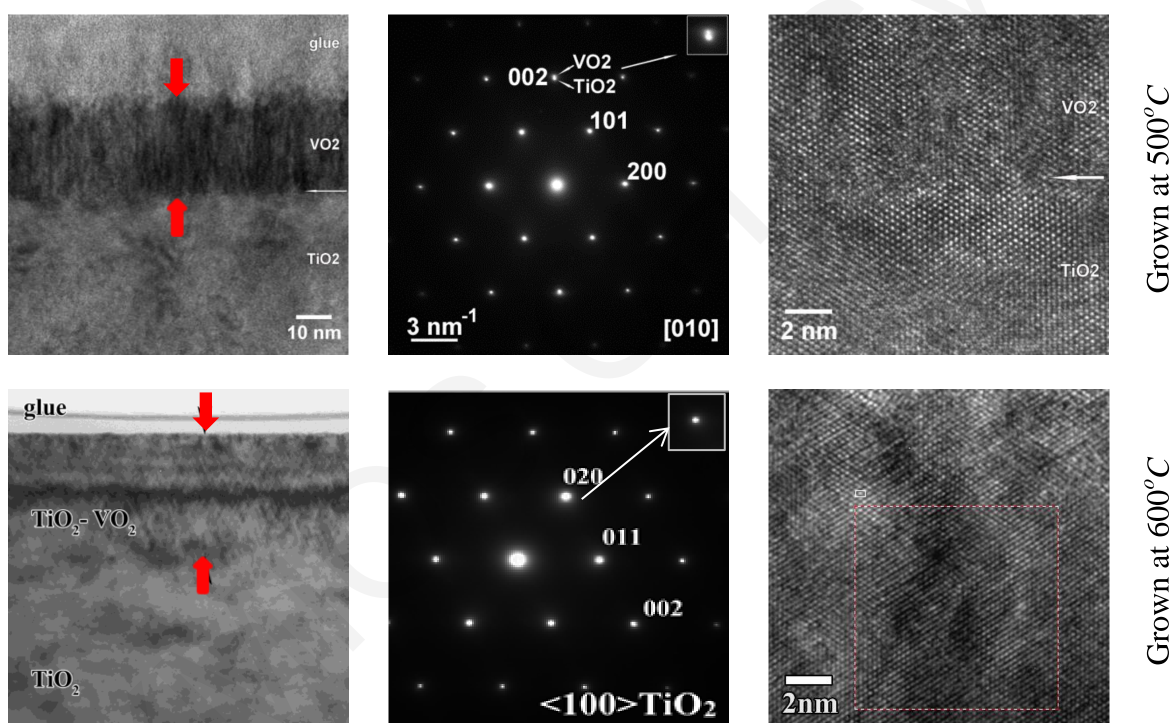

Figures 7.19: *TEM images, SAED patterns and HR TEM images of VO_2 films grown at 500 and 600^oC.*

TEM images in Figs. 7.19 of thin films grown at 500 and 600^oC reveal a characteristic area, indicated by the two red arrows on the images. This area is not exactly uniform along the surface of the films. Within the SAED patterns of the same films no splitting of the two structures based in the 002 or 020 spot on diffraction the patterns was observed. The features of this region indicate an interdiffusion process during the film's deposition leading to the formation of $V_xTi_{1-x}O_2$ solid solution. The possible formation of a solid solution has also been proposed in 2011 by Y. Muraoka *et. al.* [203].

Elemental analysis and distribution was performed with the use of electron energy loss spectroscopy on samples investigated via TEM with nano scale resolution. Spectrum imaging maps revealed the elemental distribution of V, Ti and O specimens. Based on the V and Ti maps, atomic interdiffusion at the interface between TiO_2 substrate and VO_2 thin film grown at 400^oC was not observed and is presented in Fig 7.20. Based on the elemental analysis close to the interface, the deposition temperature of 400^oC was found to be the highest temperature, where single crystal VO_2 are grown free of interdiffusion processes, exhibiting a sharp interface between the TiO_2 substrate and the thin film.

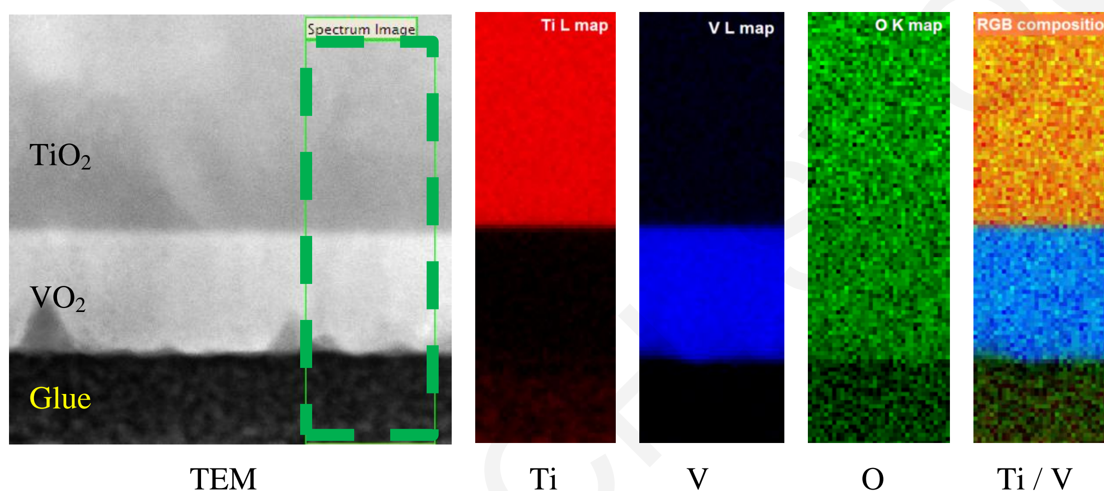

Figures 7.20: *TEM image of a VO_2 thin film grown at 400°C. Elemental distribution maps of Ti, V and O for the same specimen. No interdiffusion and a sharp interface between substrate and thin film was detected.*

7.7 Electrical characterization

The produced thin films were electrically characterized via the standard four – probe method for both heating and cooling cycles. In Fig. 7.21 a systematic investigation of the resistance of thin films grown at various temperatures between room temperature and 600^oC is presented. All thin films exhibit a SMT transition; therefore, its relation with the deposition temperature is obvious. A large change in the resistance is observed in all the thin films. All thin films exhibit an SMT below than the literature value reported T_{SM} for a VO_2 single crystal. This is in correlation to the structural results by XRD presented in previous section. Due to strain effects, the T_{SM}, is below the reported value for single crystals. Similar behaviour of the T_{SM} has also been reported in the literature [198,204,205,206].

EFTHYMIOS CHRISTOUKIS

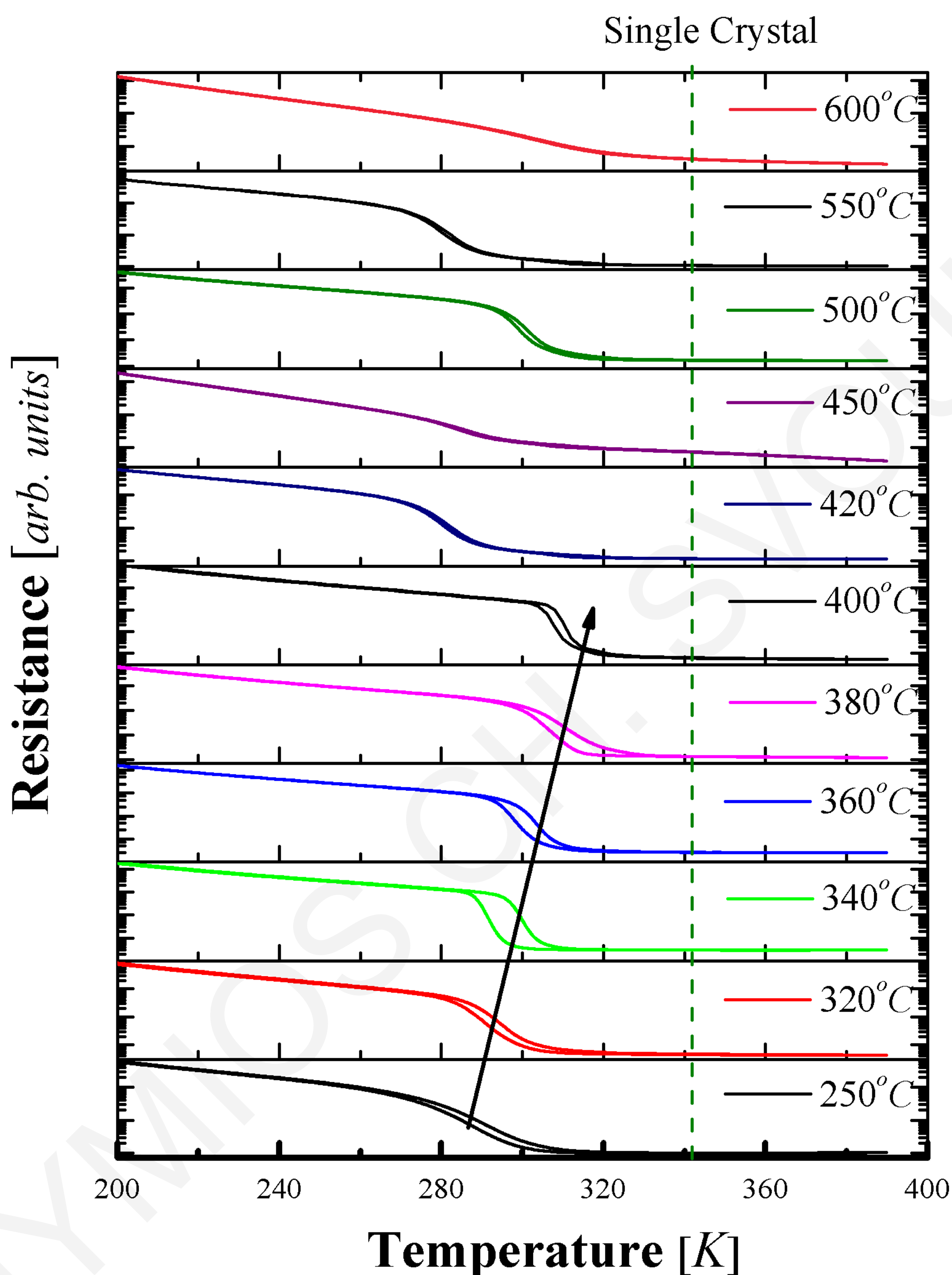

Figure 7.21: *Resistance of VO_2 thin films grown at various deposition temperatures upon heating and cooling. An SMT is present in all samples, below the reported value for a VO_2 single crystal.*

Based on the thickness of the films that had been measured via XRR, the resistivity of each sample was calculated, for all grown samples. Below 400^oC, the T_{MS} where the SMT

EFTHYMIOS CH. SVOUKIS

takes place increases as the deposition temperatures increases. Despite that the T_{SM} of the grown thin films is below the one reported for VO_2 single crystals

In Fig. 7.22, the resistivity of a thin film grown at 400^oC is presented. A large sharp SMT is observed, evidence of a high quality thin film. The exponential fitting below $280K$ (R=0.9997), verified the semiconductor behavior below the T_{SM}. In the same image as an inset is presented the resistivity close to the SMT transition. The change in the resistivity is ~ 4 orders of magnitude. SMT transition for both cycles follows the same behavior. Within the cooling cycle, SMT appears in lower temperatures compared to the heating as it is expected from the literature.

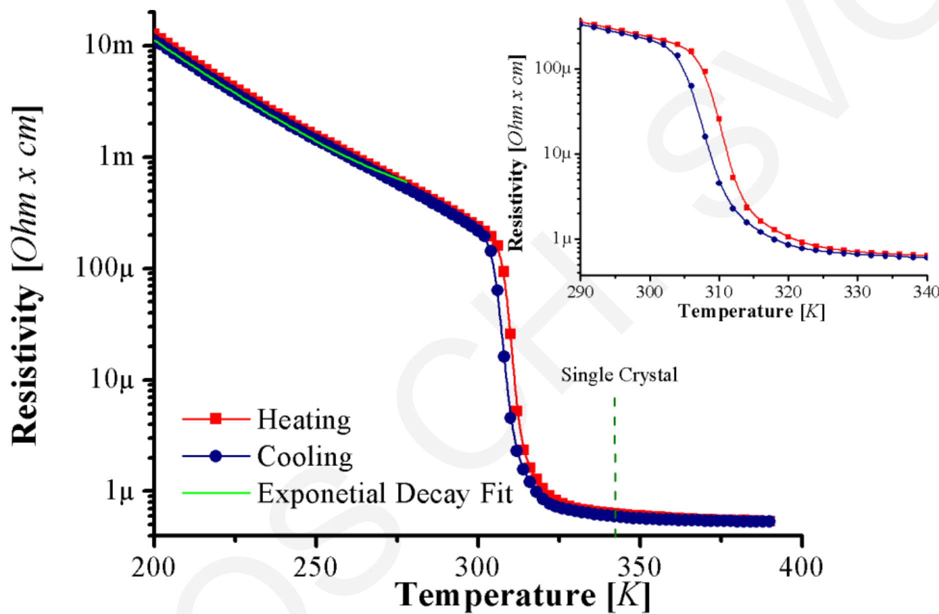

Figure 7.22: *Electrical resistivity of the VO_2 thin film grown at 400^oC. With red and blue are shown the heating and cooling cycles, respectively. The SMT close to T_{SM} is presented as an inset.*

Based in the Gaussian fit model, the $T_{SM,}$ during the heating and cooling cycle was estimated to be ~ $310.5K$ and ~ $307.9K$. It has to be noted that T_{SM} of the transition is below the temperature reported for VO_2 single crystals or other thin films. The hysteresis related to SMT reversibility was determined $\Delta H = T_{SMT.heating} - T_{SMT.cooling} =\sim 2.6K$. The transition width, evidence of the sharpness of the SMT (based on the FWHM of Gaussian fitting) was calculated $\Delta T \sim 6.3K$. Both ΔH and ΔT values are comparable with other reported values for VO_2 thin films grown on other substrates (*e.g.* Al_2O_3, yttria – stabilized zirconia, Si) [207,208,209]. In Fig. 7.23, the Gaussian fittings on the derivate of the resistivity in heating and cooling cycles are presented.

EFTHYMIOS CH. SVOUKIS

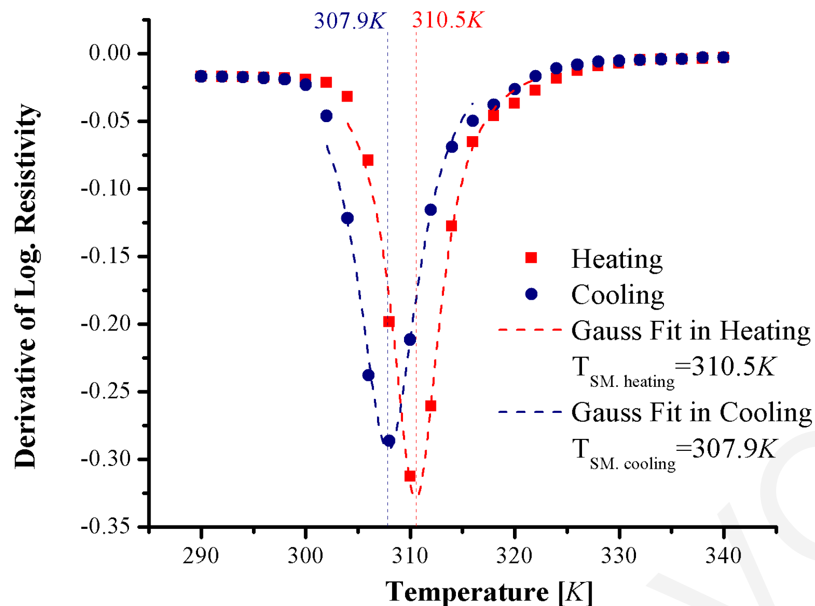

Figure 7.23: *Derivative of the electrical resistivity of a VO_2 thin film grown at 400^oC. With red and blue are shown the heating and cooling cycles, respectively. The transition temperatures for both cycles was calculated based on the Gaussian model.*

7.8 Conclusions

VO_2 thin films have been proposed for the appearance of quantum phenomena in HSTs form. The growth of high quality VO_2 films, free of defects and inter diffusion effects is a prerequisite for the use in quantum phenomena investigations.

In this chapter, the growth of VO_2 thin films on TiO_2 was systematically investigated. Based on our results, the deposition temperature has a major impact on the structure of the films; at low temperature columnar growth appears, whereas at high temperatures a solid solution is formed in a part of the film near the interface. A small window at 400^oC exists, where single – crystal VO_2 thin films are grown.

All thin films produced exhibit a SMT, with a T_{SM} below the reported values for VO_2 single crystals. This behaviour has been attributed to the strain generated by substrate / film mismatch. As the thickness of the deposited layer increases, the critical thickness is reached. Dislocations and defect are formed during growth resulting in the relaxation of the induced strain.

EFTHYMIOS CH. SVOUKIS

Conclusions & Main Results

This thesis work is the first work performed at UCY in the field of growth and characterization of epitaxial oxide thin films. New paths and challenges appeared after the completion of the current work. Science never stops, undiscovered areas in all three topics presented in this thesis still exist for new explorers…

8.1 LCCO

LCCO is a possible candidate for potential usage in ICs for thermal management. It exhibits a new highly efficient magnetic mode of thermal conduction based on magnetic excitations. Compared to conventional materials with high thermal conductivity, LCCO offers significant advantages: a) it is electrically insulating, b) heat is conducted primarily along one crystal axis and c) heat is carried by localised spins, thus potentially allowing for tunable heat dissipation control.

By applying the PLD method stoichiometric, single phase LCCO thin films were grown on a variety of substrates. It is found that LCCO has a tendency for *b* – axis growth independent of the substrate and deposition conditions used. Systematic investigations on lattice matching and mis – matching substrates proved that this tendency of LCCO is driven by internal thermodynamic reasons.

Fine tuning of the deposition conditions for all crystalline substrates, resulted in *b* – axis LCCO thin film with all the nano – crystallites oriented along the growth direction. Homo – epitaxial growth on an LCCO (001) single crystal demonstrated the possibility of *c* – axis growth of the material.

EFTHYMIOS CH. SVOUKIS

On STO (110) substrates, single crystal *b* – axis thin films were grown over a narrow window of deposition conditions. Based on an imaging technique, co – workers verified the anisotropic heat spreading on the top surface.

Growth of LCCO thin films with their *c* – axis parallel to their growth axis is possible to be achieved by fine tuning of the lattice matching between the candidate substrate and LCCO. The arrangement of the oxygen atoms in the top surface of the substrate can enhance the desired growth.

Incorporation of LCCO in ICs for thermal management applications could be possible by using the above ideal substrate material as an ultrathin buffer layer for the growth of epitaxial *c* – axis LCCO.

8.2 LCO

LCO has been proven to be a new possible material for data storage applications. LCO has many similarities with $NaCoO_2$, in which resistive switching phenomena were reported previously. LCO, compared to NaCoO2; a) can be grown in thin films, b) it is highly stable, and c) is mechanically suitable for scanning probe mediated approaches in nanoscale patterning.

The growth of high – quality and low – roughness thin films is desirable for the incorporation of novel materials in the IC industry. LCO thin films suitable for the IC industry have been grown on Al_2O_3 (0001) and Si (111), by using the PLD method. The effect of the growth condition on the structural properties was systematically investigated and optimum conditions for each substrate were found. The compatibility with Si has also been proven and the material is closer to enter the manufacturing stage.

By applying electric bias of opposite polarity on the surface of the LCO thin films, resistive and conductive areas were created. The difference in the surface resistance post modifications via electric bias is typically 3 – 4 orders of magnitude. The ability of modification is related to the structural properties of the thin films. The phenomenon of surface resistance modification is reversible by applying an inverted bias. The spatial

EFTHYMIOS CH. SVOUKIS

resolution of resistance modification has been proven to be limited only by the experimental procedures and instrumentation used in the CP – AFM apparatus.

Based on the crystal anisotropy of the LCO structure, the speed of electrochemical reactions can be increased by growing films along the *b* – axis. Preliminary experiments (not presented in this thesis) verified the possibility of changing the growth direction of the LCO thin films by using different planes of $SrTiO_3$ as substrates.

8.3 VO_2

VO_2 exhibits a first – order structural / electronic transition very close to room temperature. The nature of the transition has been investigated for more than three decades; however, it is not resolved.

Recently VO_2 thin films have been proposed for the appearance of quantum phenomena in HSTs form. These *exotic* predicted phenomena, require thin films with: a) a sharp interface, b) high quality (free of defects) and c) without interdiffusion effects at the interface.

VO_2 thin films grown on TiO_2 were systematically grown and investigated. Based on our results, the deposition temperature has a major impact on the structure of the films. A small window for the deposition conditions exists, where single crystal VO_2 thin films are grown. All thin films produced exhibit a SMT, with a T_{SM} below the reported values for VO_2 single crystals. This behaviour was attributed to the strain generated by substrate / film mismatch.

Based on the ability for epitaxial growth of VO_2 thin films, the possibility of experimental investigation of V. Pardo and W. E. Picket predictions comes one step closer. Further understanding of the mechanism of strain relief can expand the usage of VO_2 to daily applications.

EFTHYMIOS CH. SVOUKIS

Appendix – A

Transport properties are crucial in the research of novel materials. In non – isolated systems, particle currents or / and entropy currents emerge. Generally in the presence of external disturbances, such as thermal gradients (∇T) or electric fields (E)[10], a system will approach a steady state. Within the linear response theory the particle $(\Im_e)$ and thermal $(\Im_{th})$ currents can be expressed as:

$$\left(\frac{\Im_e}{\Im_{th}}\right) = \begin{pmatrix} L_{11} & L_{12} \\ L_{21} & L_{22} \end{pmatrix} \cdot \left(\frac{E}{\nabla T}\right), \tag{9.1}$$

where $L_{i,j}$ denote the transport coefficients of the system, related to measurable quantities. In the simplified case, where the (∇T) is zero, the electric current within the sample is proportional to the electric field (E):

$$\Im_e = L_{11} E \cdot \tag{9.2}$$

and the thermal current:

$$\Im_{th} = L_{21} E \tag{9.3}$$

Eq. (9.2) is also known as Ohm's law $(\Im_e = \sigma E)$ and the coefficient L_{11} is identified as the electrical conductivity $([\sigma] = \Omega^{-1} m^{-1})$ of the material.

By dividing Eq. (9.2) and (9.3) the Peltier equation emerges:

$$\Im_{th} = \Pi\, \Im_e\ , \tag{9.4}$$

---

[10] In the most general case, $\vec{E} = \vec{\nabla} V + \frac{1}{e} \vec{\nabla} \mu$, where $\vec{\nabla} V$ is the external voltage gradient and $\vec{\nabla} \mu$ the electrochemical potential gradient of the many body system, with e the electron charge.

EFTHYMIOS CH. SVOUKIS

where, $\Pi = \dfrac{L_{21}}{L_{11}}$ is known as the Peltier coefficient [210].

By assuming that no particle currents appear $\left(\Im_e = 0\right)$ and that there is a small thermal gradient, Eq. (9.1) can be expressed as:

$$E = S\,\nabla T, \quad \Im_{th} = L_{21}E + L_{22}\nabla T\,, \tag{9.5}$$

where the parameter $S = -\dfrac{L_{12}}{L_{11}}$ is known as the Seebeck coefficient. By simplifying the above equation the thermal gradient can be expressed as:

$$\Im_{th} = -\underbrace{\left(L_{12}\frac{L_{21}}{L_{11}} - L_{22}\right)}_{\kappa}\nabla T\,. \tag{9.6}$$

The thermal conductivity $\left([\kappa] = Wm^{-1}K^{-1}\right)$, can be expressed as $\kappa = L_{21}\dfrac{L_{12}}{L_{11}} - L_{22}$. By using the Kelvin – Onsager relation $\left(\Pi = S\,T = -\dfrac{L_{21}}{L_{11}}T\right)$, Eq. (9.6) is transformed to:

$$\Im_{th} = -\underbrace{\left(-TS^2\sigma - L_{22}\right)}_{\kappa}\nabla T \;\; [211]. \tag{9.7}$$

In the case of insulator materials, the term $-TS^2\sigma$ is relatively low, due to the minute values of σ, therefore $\kappa \approx -L_{22}$ [104,210]. This simplification is valid in the general case, of multi quasi - particles (magnons and / or phonons) of heat within the material and becomes exact only in the case that phonons act as quasi – particles.

In real materials due to their anisotropic structure, the thermal conductivity has to be expressed as a tensor:

$$\hat{\kappa} = \begin{pmatrix} \kappa_{xx} & \kappa_{xy} & \kappa_{xz} \\ \kappa_{yz} & \kappa_{yy} & \kappa_{yz} \\ \kappa_{zx} & \kappa_{zy} & \kappa_{zz} \end{pmatrix} \tag{9.8}$$

In general the tensor is non diagonal. Within materials with symmetries (*e.g.*, tetragonal), the tensor can be diagonalized and so be treated as scalar along the crystallographic axis [126].

EFTHYMIOS CH. SVOUKIS

Within solid samples, heat is transported via quasi – particles with finite velocities. The total conduction is composed by a summation of the quasi components. In solids, heat is mainly conducted via phonons and electrons. Within this part of the thesis, an insulating material is studied, therefore electronic heat and charge conduction can be neglected.

According to the Callaway approximation, thermal conductivity at low temperatures compared to the Debye temperature ($T \leq T_D$) can be expressed as:

$$\kappa(T) = \frac{k_B}{2\pi^2 \upsilon}\left(\frac{k_B T}{h}\right)^3 \int_0^{T_D/T} \tau_{rel}(T) \cdot \frac{x^4 e^x}{\left(e^x - 1\right)^2} dx \quad [212,213], \tag{9.9}$$

Where k_B and h are the Boltzman and Planck constant respectively. Within the Callaway approximation an isotropic Debye – like phonon spectrum is assumed, with a velocity υ for all branches (longitudinal and transverse). Scattering mechanisms are also considered via the parameter of relaxation time $\tau_{rel}(T)$. In Eq. (9.10), a summation of all the possible contributions (Matthiessen's rule) is shown.

$$\tau_{rel}^{-1}(T) = \underbrace{\tau_N^{-1}(T) + \tau_U^{-1}(T)}_{\tau_p^{-1}(T)} + \tau_d^{-1}(T) + \tau_S^{-1}(T) + \ldots \,, \tag{9.10}$$

with $\tau_p(T)$ represents the contributions due to phonon – phonon scattering (Normal (N) and Umklapp (U)), $\tau_d(T)$ the phonon – structural defects scattering and $\tau_s(T)$ the scattering of the phonons with the sample boundary.

In the temperature region above the Debye temperature, the thermal conductivity can be described by the Drude model:

$$\kappa(T) = \frac{1}{3} C_v(T) \upsilon_m^2(T) \tau_{rel}(T) \,. \tag{9.11}$$

In Eq.(9.11), $C_v(T)$ is the specific heat and $\upsilon_m(T)$ is the mean velocity of phonons. At high temperatures, the specific heat has a constant value and $\tau_{rel}(T) \sim T^{-1}$, therefore:

$$\kappa(T) \sim T^{-1} \quad [193]. \tag{9.12}$$

Within low – dimensional systems (*e.g.* cupates), short range order exists only in finite temperature. Thermal and quantum fluctuations drive the system from the low energy state, which is ordered and can exist only at a finite temperature [214].

EFTHYMIOS CH. SVOUKIS

In principle, heat can also be carried out in solids by magnetic / spin waves so called *magnons* and *spinons*, that have been theoretically predicted decades ago [215]. Magnons and spinons are propagating oscillations of the spin orientation within a magnetically ordered material[11]. In Fig. 9.1 an antiferromagnetic magnon is graphically presented [193].

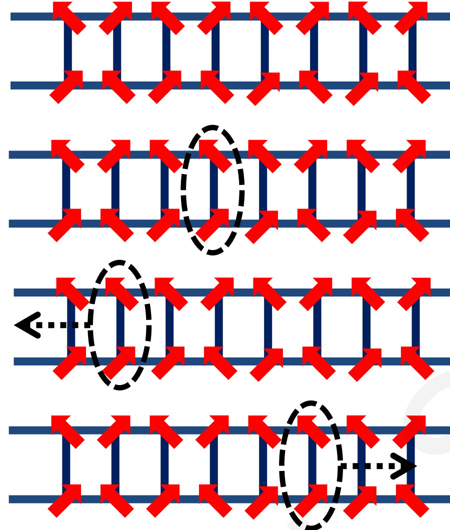

Figure 9.1: *A magnon in a perfectly ordered antiferromagnetic ladder, created from a flip of a single spin. The excitation can move along the ladder in two possible directions.*

Thermal conductivity as expressed in Eq. (9.11), in the case of magnons is still valid. An extra term $\tau_m^{-1}(T)$ has to be added in the relaxation time of Eq. (9.10). This term is attributed to the scattering processes of magnons with defects, magnons, phonons and holes $\left(\tau_m^{-1}(T)=\tau_d^{-1}(T)+\tau_m^{-1}(T)+\tau_p^{-1}(T)+\tau_h^{-1}(T)\right)$ [217]. For novel applications, tuneable thermal conductivity could be achieved by doping the magnetic structure with magnetic impurities (*e.g.* Co, Fe); therefore, external control of thermal conductivity is possible via a magnetic field or light [22].

[11] For one – dimensional systems, thermal and quantum fluctuations result in the absence of short range order even at zero temperature. In two – dimensional system, short range is present, therefore, these systems magnetically are closer to liquids than solid and are called quantum spin liquids [216].

Appendix – B

The thermal conductivity of the LCCO (001) single crystal was investigated using the *3ω* method. The sample was placed on a sample holder and mounted via silver paint and $50\mu m$ gold wires (insert in Fig. 10.1). By applying the methodology of an anisotropic thick sample, the thermal conductivity was measured in a wide temperature range. At every temperature the third harmonic voltage was measured for a frequency range of the driving current. The experimental results are presented in Fig. 10.1. Thermal conductivity values along the *c* – axis were found to be close to those reported in large samples [129,130] and are presented in Fig. 10.2.

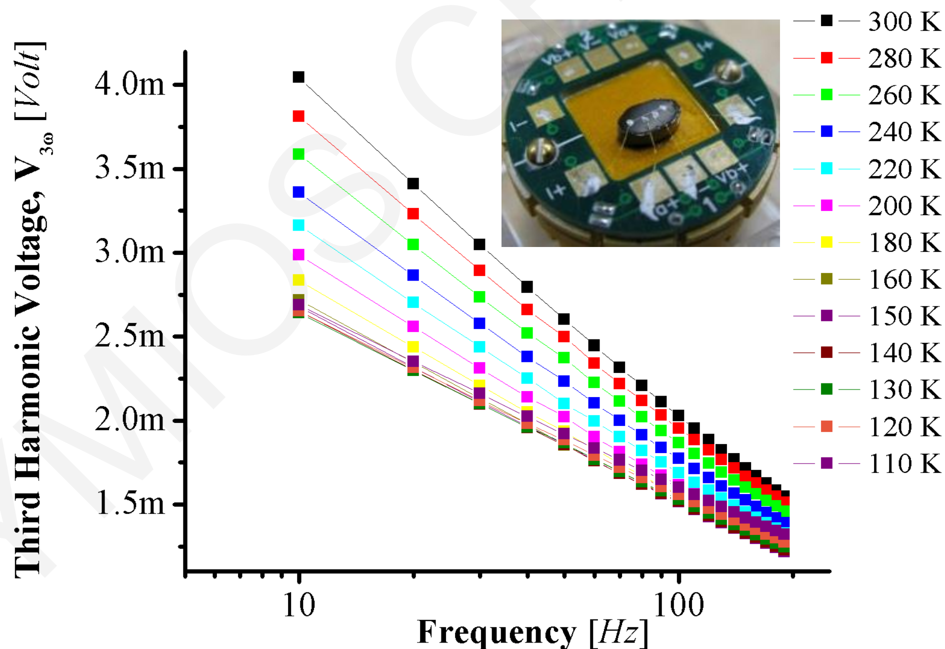

Figure 10.1: *Third harmonic voltage as a function of frequency for a range of temperatures for a LCCO(001) single crystal. Inset: the sample placed on the sample holder.*

The discrepancy between the values obtained using the *3ω* and those reported on micron – size samples can be attributed to structural defects within the volume of the single crystal. Investigations by using micro – tomography revealed micron – cracks within the

LCCO single crystal (insert in Fig. 10.2). Defects within the volume destroy the ladders and chain sub – shell structures and, therefore, diminish the magnon contribution to thermal conductivity.

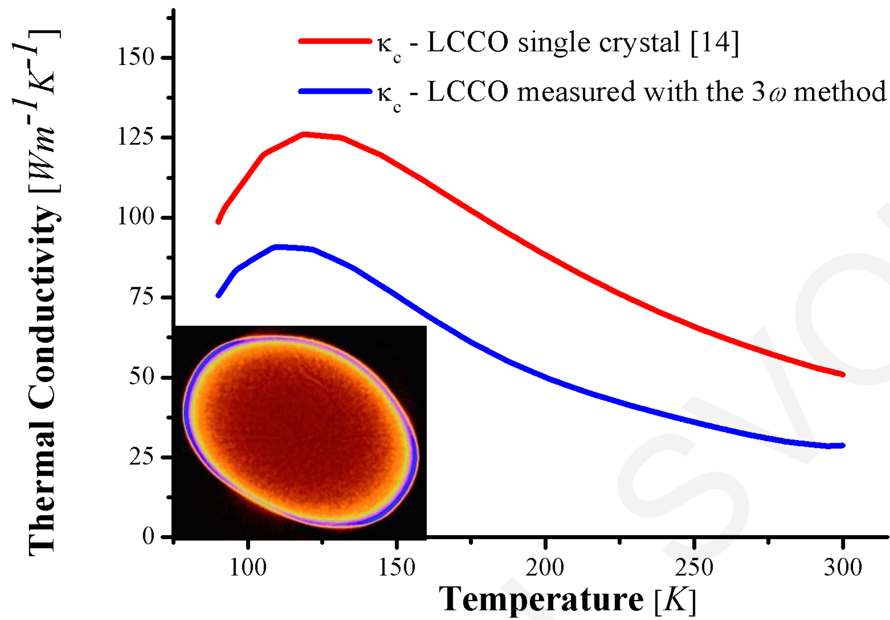

Figure 10.2: *Thermal conductivity of the LCCO single crystal as a function of temperature and comparison with typical literature values for micron – size crystals.*

EFTHYMIOS CH. SVOUKIS

References

1. Moore, G. Cramming More Components onto Integrated Circuits. *Electronics* **38,** 114–117 (1965).

2. Eerenstein, W., Mathur, N. D. & Scott, J. F. Multiferroic and magnetoelectric materials. *Nature* **442,** 759–765 (2006).

3. Jonker, G. H. & Van Santen, J. H. Ferromagnetic compounds of manganese with perovskite structure. *Physica* **16,** 337–349 (1950).

4. Rao, C. N. R. & Cheetham, A. K. Giant Magnetoresistance in Transition Metal Oxides. *Science* **272,** 369–370 (1996).

5. Wu, M. K. *et al.* Superconductivity at 93 K in a new mixed-phase Y-Ba-Cu-O compound system at ambient pressure. *Phys. Rev. Lett.* **58,** 908–910 (1987).

6. Jeon, N. J. *et al.* Compositional engineering of perovskite materials for high-performance solar cells. *Nature* **517,** 476–480 (2015).

7. Callister. *Materials Science and Engineering: An Introduction and Software (Intellipro) IMS to Accompany Materials Science and Engineering*. (John Wiley & Sons Incorporated, 1999).

8. Ohtomo, A., Muller, D. A., Grazul, J. L. & Hwang, H. Y. Artificial charge-modulationin atomic-scale perovskite titanate superlattices. *Nature* **419,** 378–380 (2002).

9. Nazir, S. & Schwingenschlögl, U. High charge carrier density at the NaTaO3/SrTiO3 hetero-interface. *Appl. Phys. Lett.* **99,** 073102–073102–3 (2011).

10. Ohtomo, A. & Hwang, H. Y. A high-mobility electron gas at the LaAlO3/SrTiO3 heterointerface. *Nature* **427,** 423–426 (2004).

11. Yu, L. & Zunger, A. A polarity-induced defect mechanism for conductivity and magnetism at polar–nonpolar oxide interfaces. *Nat. Commun.* **5,** (2014).

12. George, S. M. Atomic Layer Deposition: An Overview. *Chem. Rev.* **110,** 111–131 (2010).

EFTHYMIOS CH. SVOUKIS

13. Kelly, P. J. & Arnell, R. D. Magnetron sputtering: a review of recent developments and applications. *Vacuum* **56,** 159–172 (2000).

14. Ploog, K. Molecular Beam Epitaxy of III-V Compounds: Technology and Growth Process. *Annu. Rev. Mater. Sci.* **11,** 171–210 (1981).

15. Manfra, M. J. Molecular Beam Epitaxy of Ultra-High-Quality AlGaAs/GaAs Heterostructures: Enabling Physics in Low-Dimensional Electronic Systems. *Annu. Rev. Condens. Matter Phys.* **5,** 347–373 (2014).

16. Koster, G., Kropman, B. L., Rijnders, G. J. H. M., Blank, D. H. A. & Rogalla, H. Quasi-ideal strontium titanate crystal surfaces through formation of strontium hydroxide. *Appl. Phys. Lett.* **73,** 2920–2922 (1998).

17. Choi, J., Eom, C. B., Rijnders, G., Rogalla, H. & Blank, D. H. A. Growth mode transition from layer by layer to step flow during the growth of heteroepitaxial SrRuO3 on (001) SrTiO3. *Appl. Phys. Lett.* **79,** 1447–1449 (2001).

18. Nie, Y. F. *et al.* Atomically precise interfaces from non-stoichiometric deposition. *Nat. Commun.* **5,** (2014).

19. Rijnders, G. J. H. M., Koster, G., Blank, D. H. A. & Rogalla, H. In situ monitoring during pulsed laser deposition of complex oxides using reflection high energy electron diffraction under high oxygen pressure. *Appl. Phys. Lett.* **70,** 1888–1890 (1997).

20. Kawasaki, M. *et al.* Atomic Control of the SrTiO3 Crystal Surface. *Science* **266,** 1540–1542 (1994).

21. Park, J. W. *et al.* Creation of a two-dimensional electron gas at an oxide interface on silicon. *Nat. Commun.* **1,** 94 (2010).

22. NOVMAG. at <http://www.novmag.eu/>

23. Grove, W. R. On the Electro-Chemical Polarity of Gases. *Philos. Trans. R. Soc. Lond.* **142,** 87–101 (1852).

24. Ohring, M. *Materials science of thin films deposition and structure*. (Academic Press, 2002).

25. Mattox, D. M. *The Foundations of Vacuum Coating Technology*. (Springer, 2003).

26. Rijnders, A. J. H. M. The Initial Growth of Complex Oxides: Study and Minipulation. (Twente, 2001).

EFTHYMIOS CH. SVOUKIS

27. Ohring, M. in *Materials Science of Thin Films (Second Edition)* 95–144 (Academic Press, 2002).

28. Prusseit, W. in *Second-Generation HTS Conductors* (ed. Goyal, A.) 81–96 (Springer US, 2005).

29. Hayakawa, S. *Handbook of Sputter Deposition Technology: Principles, Technology, and Applications*. (Noyes Publications, 1992).

30. Mattox, D. M. *Handbook of Physical Vapor Deposition (PVD) Processing*. (Elsevier Science, 2007).

31. Maiman, T. H. Stimulated Optical Radiation in Ruby. *Nature* **187,** 493–494 (1960).

32. Smith, H. M. & Turner, A. F. Vacuum Deposited Thin Films Using a Ruby Laser. *Appl. Opt.* **4,** 147–148 (1965).

33. Ready, J. F. Development of plume of material vaporized by giant pulse laser. *Appl. Phys. Lett.* **3,** 11–13 (1963).

34. Brown, M. S. & Arnold, C. B. in *Laser Precision Microfabrication* (eds. Sugioka, K., Meunier, M. & Piqué, A.) 91–120 (Springer Berlin Heidelberg, 2010).

35. Venkatesan, T. & Green, S. M. Pulsed Laser Deposition: Thin Films in a Flash. (Cover story). *Ind. Phys.* **2,** 22 (1996).

36. Eason, R. *Pulsed Laser Deposition of Thin Films: Applications-Led Growth of Functional Materials*. (John Wiley & Sons, 2007).

37. Dijkkamp, D. *et al.* Preparation of Y-Ba-Cu oxide superconductor thin films using pulsed laser evaporation from high Tc bulk material. *Appl. Phys. Lett.* **51,** 619–621 (1987).

38. History of laser intensity. *Wikipedia, the free encyclopedia* at <http://en.wikipedia.org/wiki/File:History_of_laser_intensity.svg>

39. Krebs, H.-U. *et al.* in *Advances in Solid State Physics* (ed. Kramer, B.) 505–518 (Springer Berlin Heidelberg, 2003).

40. Willmott, P. R. & Huber, J. R. Pulsed laser vaporization and deposition. *Rev. Mod. Phys.* **72,** 315–328 (2000).

41. Silfvast, W. T. *Laser Fundamentals*. (Cambridge University Press, 2004).

42. Basting, D. & Marowsky, G. *Excimer Laser Technology*. (Springer, 2005).

EFTHYMIOS CH. SVOUKIS

43. Gallagher, A. in *Excimer Lasers* (ed. Rhodes, D. C. K.) 139–179 (Springer Berlin Heidelberg, 1984).

44. Prof, O. S. *et al.* in *Springer Handbook of Lasers and Optics* (ed. Prof, F. T.) 583–936 (Springer New York, 2007).

45. Lorusso, A., Nassisi, V., Velardi, L. & Sicilano, M. V. Velocity distribution of ions in UV laser induced plasma plumes. *J. Phys. Conf. Ser.* **227,** 012037 (2010).

46. Geohegan, D. B. *et al.* in *Laser-Surface Interactions for New Materials Production* (eds. Miotello, A. & Ossi, P. M.) 1–17 (Springer Berlin Heidelberg, 2010).

47. Coso, R. del *et al.* Critical parameters influencing the material distribution produced by pulsed laser deposition. *Appl. Phys. A* **69,** S553–S556 (1999).

48. Singh, R. K. Spatial thickness variations in laser-deposited thin films. *Mater. Sci. Eng. B* **45,** 180–185 (1997).

49. Geohegan, D. B. & Puretzky, A. A. Dynamics of laser ablation plume penetration through low pressure background gases. *Appl. Phys. Lett.* **67,** 197–199 (1995).

50. Leca, V. Heteroepitaxial growth of copper oxide superconductors by Pulsed Laser Deposition. (Twente, 2003).

51. Laser Tools, Lasers, Applications, Laser System Products, Solutions. at <http://www.coherent.com/>

52. Eksma Optics. at <http://eksmaoptics.com/>

53. US Department of Commerce, N. National Institute of Standards and Technology. at <http://www.nist.gov/index.html>

54. SURFACE ...always one step ahead. at <http://www.surface-tec.com/>

55. Koster, G. Artificially Layered Oxides by Pulsed Laser Deposition. (Twente, 1999).

56. Hegde, M. S. Epitaxial oxide thin films by pulsed laser deposition: Retrospect and prospect. *J. Chem. Sci.* **113,** 445–458 (2001).

57. Nagar, S. Multifunctional magnetic materials prepared by Pulsed Laser Deposition. (Royal Institute of Technology, 2012).

58. Vasantgadkar, N. A., Bhandarkar, U. V. & Joshi, S. S. A finite element model to predict the ablation depth in pulsed laser ablation. *Thin Solid Films* **519,** 1421–1430 (2010).

EFTHYMIOS CH. SVOUKIS

59. Farkas, B. & Geretovszky, Z. On determining the spot size for laser fluence measurements. *Appl. Surf. Sci.* **252,** 4728–4732 (2006).

60. Kim, J.-H., Lee, S. & Im, H.-S. The effect of target density and its morphology on TiO2 thin films grown on Si(100) by PLD. *Appl. Surf. Sci.* **151,** 6–16 (1999).

61. Bäuerle, P. D. D. in *Laser Processing and Chemistry* 221–257 (Springer Berlin Heidelberg, 2000).

62. Norton, D. P. Synthesis and properties of epitaxial electronic oxide thin-film materials. *Mater. Sci. Eng. R Rep.* **43,** 139–247 (2004).

63. Heitz, J., Wang, X. Z., Schwab, P., Bäuerle, D. & Schultz, L. KrF laser-induced ablation and patterning of Y–Ba–Cu–O films. *J. Appl. Phys.* **68,** 2512–2514 (1990).

64. Schou, J. Physical aspects of the pulsed laser deposition technique: The stoichiometric transfer of material from target to film. *Appl. Surf. Sci.* **255,** 5191–5198 (2009).

65. Aruta, C. *et al.* Critical influence of target-to-substrate distance on conductive properties of LaGaO3/SrTiO3 interfaces deposited at 10−1 mbar oxygen pressure. *Appl. Phys. Lett.* **101,** 031602–031602–5 (2012).

66. Phillips, J. M. Substrate selection for high-temperature superconducting thin films. *J. Appl. Phys.* **79,** 1829–1848 (1996).

67. Rethfeld, B. Free-electron generation in laser-irradiated dielectrics. *Phys. Rev. B* **73,** 035101 (2006).

68. Schneider, C. W. & Lippert, T. in *Laser Processing of Materials* (ed. Schaaf, P.) 89–112 (Springer Berlin Heidelberg, 2010).

69. Willmott, P. R. & Huber, J. R. Pulsed laser vaporization and deposition. *Rev. Mod. Phys.* **72,** 315–328 (2000).

70. Singh, R. K. & Narayan, J. Pulsed-laser evaporation technique for deposition of thin films: Physics and theoretical model. *Phys. Rev. B* **41,** 8843–8859 (1990).

71. Anisimov, S. I., Bäuerle, D. & Luk'yanchuk, B. S. Gas dynamics and film profiles in pulsed-laser deposition of materials. *Phys. Rev. B* **48,** 12076–12081 (1993).

72. Zel′dovich, I. B., Zel'dovich, Y. B. & Raizer, Y. P. *Physics of Shock Waves and High-temperature Hydrodynamic Phenomena*. (Courier Dover Publications, 2002).

EFTHYMIOS CH. SVOUKIS

73. Strikovski, M. & Jr, J. H. M. Pulsed laser deposition of oxides: Why the optimum rate is about 1 Å per pulse. *Appl. Phys. Lett.* **73,** 1733–1735 (1998).

74. Warrender, J. M. & Aziz, M. J. Kinetic energy effects on morphology evolution during pulsed laser deposition of metal-on-insulator films. *Phys. Rev. B* **75,** 085433 (2007).

75. Canulescu, S. *et al.* Mechanisms of the laser plume expansion during the ablation of LiMn2O4. *J. Appl. Phys.* **105,** 063107 (2009).

76. Dinnebier, R. E. & Billinge, S. J. L. in *Powder Diffraction* (eds. Dinnebier, R. E. & Billinge, S. J. L.) 1–19 (Royal Society of Chemistry).

77. Warren, B. E. *X-ray diffraction*. (Dover Publications, 1990).

78. X-ray Diffraction : SHIMADZU (Shimadzu Corporation). at <http://www.shimadzu.com/an/elemental/xrd/>

79. Intelligent X-ray diffraction system | Rigaku - X-ray analytical instrumentation. at <http://www.rigaku.com/products/xrd/smartlab>

80. Birkholz, M. *Thin Film Analysis by X-Ray Scattering*. (John Wiley & Sons, 2006).

81. Rigaku Smartlab Training Text.

82. Bowen, D. K., Tanner, B. K. *High resolution X-ray diffractometry and topography*. (Taylor & Francis, 1998).

83. Bowen, D. K., Tanner, Brian Keith. *X-ray metrology in semiconductor manufacturing*. (CRC/Taylor & Francis, 2006).

84. Williams, D. B. & Carter, C. B. *Transmission Electron Microscopy: A Textbook for Materials Science. Diffraction. II*. (Springer, 1996).

85. Fultz, B. & Howe, J. M. *Transmission electron microscopy and diffractometry of materials*. (Springer, 2013).

86. Braun, W. *Applied RHEED: Reflection High-energy Electron Diffraction During Crystal Growth /Wolfgang Braun*. (Springer, 1999).

87. Droopad, R., Williams, R. L. & Parker, S. D. RHEED intensity oscillations observed during the MBE growth of InSb (100). *Semicond. Sci. Technol.* **4,** 111 (1989).

88. Ichimiya, A. *Reflection High-Energy Electron Diffraction*. (Cambridge University Press, 2004).

EFTHYMIOS CH. SVOUKIS

89. Wang, K. & Smith, A. R. Efficient kinematical simulation of reflection high-energy electron diffraction streak patterns for crystal surfaces. *Comput. Phys. Commun.* **182,** 2208–2212 (2011).

90. Wang, Z. L. *Reflection electron microscopy and spectroscopy for surface analysis*. (Cambridge University Press, 1996).

91. Thiel, S. P. Study of Interface Properties in LaAlO3/SrTiO3 Heterostructures. (Augsburg, 2009).

92. Braun, W., Däweritz, L. & Ploog, K. H. Origin of Electron Diffraction Oscillations during Crystal Growth. *Phys. Rev. Lett.* **80,** 4935–4938 (1998).

93. Stoyanov, S. Layer growth of epitaxial films and superlattices. *Surf. Sci.* **199,** 226–242 (1988).

94. Cahill, D. G. Heat Transport in Dielectric Thin Films and at Solid-Solid Interfaces. *Microscale Thermophys. Eng.* **1,** 85–109 (1997).

95. Cahill, D. G. & Pohl, R. O. Thermal conductivity of amorphous solids above the plateau. *Phys. Rev. B* **35,** 4067–4073 (1987).

96. Cahill, D. G., Katiyar, M. & Abelson, J. R. Thermal conductivity of a-Si:H thin films. *Phys. Rev. B* **50,** 6077–6081 (1994).

97. Gustafsson, S. E. & Karawacki, E. Transient hot-strip probe for measuring thermal properties of insulating solids and liquids. *Rev. Sci. Instrum.* **54,** 744–747 (1983).

98. Nordling, C. & Österman, J. *Physics handbook for science and engineering*. (Studentlitteratur, 2006).

99. Borca-Tasciuc, T., Kumar, A. R. & Chen, G. Data reduction in 3ω method for thin-film thermal conductivity determination. *Rev. Sci. Instrum.* **72,** 2139–2147 (2001).

100. Svoukis, E. Development of the 3ω method for thermal conductivity characterization of bulk samples. (University of Cyprus).

101. Athanasopoulos, G. I. *et al.* Thermal conductivity of Ni, Co, and Fe-doped La5Ca9Cu24O41 thin films measured by the 3ω method. *Thin Solid Films* **518,** 4684–4687 (2010).

102. Kim, K. S., Song, J. Y., Chung, E. K., Park, J. K. & Hong, S. H. Relationship between mechanical properties and microstructure of ultra-fine gold bonding wires. *Mech. Mater.* **38,** 119–127 (2006).

EFTHYMIOS CH. SVOUKIS

103. Wilson, M., 1947 Jan. 7-. *Nanotechnology: basic science and engineering technologies*. (Chapman & Hall/CRA, 2002).

104. Papageorgiou, C. Nanocomposite materials with enhanced Thermoelectric Properties. (Cyprus, 2013).

105. Markov, I. V. & EbSCOhost. *Crystal Growth for Beginners Fundamentals of Nucleation, Crystal Growth and Epitaxy.* (World Scientific Publishing Company, Incorporated, 2003).

106. Yang, T.-H. Integration of VO2 films on Al2O3 and Si (100) substrates: structure - property correlations and applications. (North Carolina State University, 2011).

107. Narayan, J. & Larson, B. C. Domain epitaxy: A unified paradigm for thin film growth. *J. Appl. Phys.* **93,** 278–285 (2002).

108. Adam, N. K. *The physics and chemistry of surfaces*. (Oxford University Press, 1952).

109. Frank, F. C. & Merwe, J. H. van der. One-Dimensional Dislocations. I. Static Theory. *Proc. R. Soc. Lond. Ser. Math. Phys. Sci.* **198,** 205–216 (1949).

110. Volmer, M. & Weber, A. Nucleus formationin supersaturated systems. *Z Phys Chem* **119,** 277 (1926).

111. McMitchell, S. R. C. An investigation into controlling the growth mode of ferroelectric thin films using pulsed laser deposition. (Birmingham, 2008).

112. Saad, M. M. *et al.* Intrinsic dielectric response in ferroelectric nano-capacitors. *J. Phys. Condens. Matter* **16,** L451 (2004).

113. Thornton, J. A. High Rate Thick Film Growth. *Annu. Rev. Mater. Sci.* **7,** 239–260 (1977).

114. Freund, L. B. & Suresh, S. *Thin Film Materials: Stress, Defect Formation and Surface Evolution*. (Cambridge University Press, 2003).

115. Mazor, A., Srolovitz, D. J., Hagan, P. S. & Bukiet, and B. G. Columnar growth in thin films. *Phys. Rev. Lett.* **60,** 424–427 (1988).

116. Zhang, Z. W., Chen, G. & Chen, G. L. Dynamics and mechanism of columnar grain growth of pure iron under directional annealing. *Acta Mater.* **55,** 5988–5998 (2007).

117. Athanasopoulos, G. I. *et al.* Pulsed laser deposition and thermal characterization of Ni-doped La5Ca9Cu24O41 thin films. *Appl. Surf. Sci.* **257,** 5200–5203 (2011).

EFTHYMIOS CH. SVOUKIS

118. Svoukis, E. *et al.* Structural and thermal characterization of La5Ca9Cu24O41 thin films grown by pulsed laser deposition on (1 1 0) SrTiO3 substrates. *Thin Solid Films* **520,** 4613–4616 (2012).

119. Lee, S. How to select a heat sink. *Electronics Cooling* (1995).

120. Zotos, X., Naef, F. & Prelovsek, P. Transport and conservation laws. *Phys. Rev. B* **55,** 11029–11032 (1997).

121. Sologubenko, A. V., Giannò, K., Ott, H. R., Vietkine, A. & Revcolevschi, A. Heat transport by lattice and spin excitations in the spin-chain compounds SrCuO2 and Sr2CuO3. *Phys. Rev. B* **64,** 054412 (2001).

122. Hess, C. *et al.* Magnon heat transport in (Sr,Ca,La)14Cu24O41. *Phys. Rev. B* **64,** 184305 (2001).

123. McCarron III, E. M., Subramanian, M. A., Calabrese, J. C. & Harlow, R. L. The incommensurate structure of (Sr14−xCax)Cu24O41 (0 < x ∼ 8) a superconductor byproduct. *Mater. Res. Bull.* **23,** 1355–1365 (1988).

124. Matsuda, M., Katsumata, K., Eccleston, R. S., Brehmer, S. & Mikeska, H.-J. Magnetic excitations and exchange interactions in the spin-12 two-leg ladder compound La6Ca8Cu24O41. *Phys. Rev. B* **62,** 8903–8908 (2000).

125. Windt, M. *et al.* Observation of Two-Magnon Bound States in the Two-Leg Ladders of (Ca,La)14Cu24O41. *Phys. Rev. Lett.* **87,** 127002 (2001).

126. M. R. Ribeiro, P. One-Dimensional Quantum Magnets in Cuprates: Single Crystal Growth and Magnetic Heat Transport Studies. (der Fakultat Mathematik und Naturwissenschaften der Technischen Universitat Dresden).

127. Ammerahl, U., Büchner, B., Colonescu, L., Gross, R. & Revcolevschi, A. Interplay between magnetism, charge localization, and structure in Sr14-xCaxCu24O41. *Phys. Rev. B* **62,** 8630–8633 (2000).

128. Ammerahl, U. & Revcolevschi, A. Crystal growth of the spin-ladder compound (Ca,La)14Cu24O41 and observation of one-dimensional disorder. *J. Cryst. Growth* **197,** 825–832 (1999).

129. Hohensee, G. T., Wilson, R. B., Feser, J. P. & Cahill, D. G. Magnon-phonon coupling in the spin-ladder compound Ca9La5Cu24O41 measured by time-domain thermoreflectance. *Phys. Rev. B* **89,** 024422 (2014).

EFTHYMIOS CH. SVOUKIS

130. Otter, M. *et al.* Optical probing of anisotropic heat transport in the quantum spin ladder Ca9La5Cu24O41. *Int. J. Heat Mass Transf.* **55,** 2531–2538 (2012).

131. 2010, -October 6. in *Thermal Conductivity 30/Thermal Expansion 18* 823–833 (DEStech Publications, Inc., 2010).

132. Intel® Core™ i7 Processor. *Intel* at <http://www.intel.com/content/www/us/en/processors/core/core-i7-processor.html>

133. Furubayashi, Y. *et al.* Epitaxial growth of single-crystalline thin film of Ca14Cu24O41: A heavily hole-doped two-legged spin ladder. *Phys. Rev. B* **60,** R3720–R3723 (1999).

134. Pervolaraki, M., Pasuk, I., Stan, G. E. & Giapintzakis, J. Pulsed laser deposition of highly textured La5Ca9Cu24O41 films on SrLaAlO4 (1 0 0) and Gd3Ga5O12 (1 0 0) substrates. *Appl. Surf. Sci.* **258,** 9475–9479 (2012).

135. Hess, C. Heat conduction in low-dimensional quantum magnets. *Eur. Phys. J. Spec. Top.* **151,** 73–83 (2007).

136. Liu, L., Zhao, Z., Liu, H. & Li, Y. Effect of Deposition Temperature on the Epitaxial Growth of YBCO Thin Films on RABiTS Substrates by Pulsed Laser Deposition Method. *IEEE Trans. Appl. Supercond.* **20,** 1553–1556 (2010).

137. Wen, J. G., Traeholt, C. & Zandbergen, H. W. Stacking sequence of YBa2Cu3O7 thin film on SrTiO3 substrate. *Phys. C Supercond.* **205,** 354–362 (1993).

138. Padilla, J. & Vanderbilt, D. Ab initio study of SrTiO3 surfaces. *Surf. Sci.* **418,** 64–70 (1998).

139. Ohnishi, T. *et al.* Preparation of thermally stable TiO2-terminated SrTiO3(100) substrate surfaces. *Appl. Phys. Lett.* **85,** 272–274 (2004).

140. Rijnders, G., Blank, D. H. A., Choi, J. & Eom, C.-B. Enhanced surface diffusion through termination conversion during epitaxial SrRuO3 growth. *Appl. Phys. Lett.* **84,** 505–507 (2004).

141. Bachelet, R., Sánchez, F., Palomares, F. J., Ocal, C. & Fontcuberta, J. Atomically flat SrO-terminated SrTiO3(001) substrate. *Appl. Phys. Lett.* **95,** 141915 (2009).

142. Diebold, U. Oxide surfaces: Surface science goes inorganic. *Nat. Mater.* **9,** 185–187 (2010).

EFTHYMIOS CH. SVOUKIS

143. Enterkin, J. A. *et al.* A homologous series of structures on the surface of SrTiO3(110). *Nat. Mater.* **9,** 245–248 (2010).

144. Biswas, A. *et al.* Universal Ti-rich termination of atomically flat SrTiO3 (001), (110), and (111) surfaces. *Appl. Phys. Lett.* **98,** 051904 (2011).

145. Boffoué, M. O. *et al.* Thermal conductivity of SrBi2Nb2O9 ferroelectric thin films. *Appl. Phys. Lett.* **89,** 092904 (2006).

146. Lee, S.-M., Cahill, D. G. & Allen, T. H. Thermal conductivity of sputtered oxide films. *Phys. Rev. B* **52,** 253–257 (1995).

147. Western Digital Hard Drives, Network Drives, Media Players. at <http://www.wdc.com/en/>

148. Schneegans, O. *et al.* NaxCoO2: A New Opportunity for Rewritable Media? *J. Am. Chem. Soc.* **129,** 7482–7483 (2007).

149. Delmas, C., Braconnier, J.-J., Fouassier, C. & Hagenmuller, P. Electrochemical intercalation of sodium in NaxCoO2 bronzes. *Solid State Ion.* **3–4,** 165–169 (1981).

150. Bates, J. B., Dudney, N. J., Neudecker, B., Ueda, A. & Evans, C. D. Thin-film lithium and lithium-ion batteries. *Solid State Ion.* **135,** 33–45 (2000).

151. Mizushima, K., Jones, P. C., Wiseman, P. J. & Goodenough, J. B. LixCoO2 (0<x<-1): A new cathode material for batteries of high energy density. *Mater. Res. Bull.* **15,** 783–789 (1980).

152. Moradpour, A. *et al.* Resistive Switching Phenomena in LixCoO2 Thin Films. *Adv. Mater.* **23,** 4141–4145 (2011).

153. Svoukis, E. *et al.* Growth and transport properties of HT–LixCoO2 thin films deposited by pulsed laser deposition. *Appl. Surf. Sci.* **258,** 9366–9369 (2012).

154. Strukov, D. B., Snider, G. S., Stewart, D. R. & Williams, R. S. The missing memristor found. *Nature* **453,** 80–83 (2008).

155. Ielmini, D. *et al.* in *Frontiers in Electronic Materials* (eds. Heber, J., Schlom, D., Tokura, Y., Waser, -Ing Rainer & Wuttig, tthias) 219–231 (Wiley-VCH Verlag GmbH & Co. KGaA, 2012). at <http://onlinelibrary.wiley.com/doi/10.1002/9783527667703.ch43/summary>

156. Mai, V. H. *et al.* Memristive and neuromorphic behavior in a LixCoO2 nanobattery. *Sci. Rep.* **5,** (2015).

EFTHYMIOS CH. SVOUKIS

157. Chappert, C., Fert, A. & Van Dau, F. N. The emergence of spin electronics in data storage. *Nat. Mater.* **6,** 813–823 (2007).

158. Kim, H.-S. *et al.* Diffraction limit of the focusing waveguide grating coupler for optical probe information storage. *Nanotechnology* **14,** 684 (2003).

159. Min, S. Semiconductor Flash Memory Scaling. (University of California, 2003).

160. Gotsmann, B., Duerig, U., Frommer, J. & Hawker, C. J. Exploiting Chemical Switching in a Diels–Alder Polymer for Nanoscale Probe Lithography and Data Storage. *Adv. Funct. Mater.* **16,** 1499–1505 (2006).

161. Ahn, C. H., Rabe, K. M. & Triscone, J.-M. Ferroelectricity at the Nanoscale: Local Polarization in Oxide Thin Films and Heterostructures. *Science* **303,** 488–491 (2004).

162. Nakamura, K. *et al.* 7Li NMR study on Li+ ionic diffusion and phase transition in LixCoO2. *Solid State Ion.* **177,** 821–826 (2006).

163. Santiago, E. I., Bueno, P. R., Andrade, A. V. C., Paiva-Santos, C. O. & Bulhões, L. O. S. Quantitative structural analysis of the transition from LT-LixCoO2 to HT-LixCoO2 using the rietveld method: correlation between structure and electrochemical performance. *J. Power Sources* **125,** 103–113 (2004).

164. Bouwman, P. Lithium Intercalation in preferentially oriented submicron LiCoO2 films. (University of Twente, 2002).

165. Amatucci, G. G., Tarascon, J. M. & Klein, L. C. CoO2, The End Member of the Li x CoO2 Solid Solution. *J. Electrochem. Soc.* **143,** 1114–1123 (1996).

166. Van der Ven, A., Aydinol, M. K., Ceder, G., Kresse, G. & Hafner, J. First-principles investigation of phase stability in LixCoO2. *Phys. Rev. B* **58,** 2975–2987 (1998).

167. Reimers, J. N. & Dahn, J. R. Electrochemical and In Situ X-Ray Diffraction Studies of Lithium Intercalation in Li x CoO2. *J. Electrochem. Soc.* **139,** 2091–2097 (1992).

168. Ménétrier, M., Saadoune, I., Levasseur, S. & Delmas, C. The insulator-metal transition upon lithium deintercalation from LiCoO2: electronic properties and 7Li NMR study. *J. Mater. Chem.* **9,** 1135–1140 (1999).

169. Miyoshi, K. *et al.* Magnetic and electronic properties of LixCoO2 single crystals. *Phys. Rev. B* **82,** 075113 (2010).

EFTHYMIOS CH. SVOUKIS

170. Ishida, Y., Mizutani, A., Sugiura, K., Ohta, H. & Koumoto, K. Metal-nonmetal transition in LixCoO2 thin films and thermopower enhancement at high Li concentration. *Phys. Rev. B* **82,** 075325 (2010).

171. Takahashi, Y. *et al.* Anisotropic Electrical Conductivity in LiCoO2 Single Crystal. *J. Solid State Chem.* **164,** 1–4 (2002).

172. Iriyama, Y., Inaba, M., Abe, T. & Ogumi, Z. Preparation of c-axis oriented thin films of LiCoO2 by pulsed laser deposition and their electrochemical properties. *J. Power Sources* **94,** 175–182 (2001).

173. Tsuruhama, T., Hitosugi, T., Oki, H., Hirose, Y. & Hasegawa, T. Preparation of Layered-Rhombohedral LiCoO2 Epitaxial Thin Films Using Pulsed Laser Deposition. *Appl. Phys. Express* **2,** 085502 (2009).

174. Yoshimoto, M. *et al.* Atomic-scale formation of ultrasmooth surfaces on sapphire substrates for high-quality thin-film fabrication. *Appl. Phys. Lett.* **67,** 2615–2617 (1995).

175. Antolini, E. Preparation and properties of Li-Co-O compounds. *J. Eur. Ceram. Soc.* **18,** 1405–1411 (1998).

176. Batista, C., Ribeiro, R. M. & Teixeira, V. Synthesis and characterization of VO2-based thermochromic thin films for energy-efficient windows. *Nanoscale Res. Lett.* **6,** 301 (2011).

177. Zhou, J. *et al.* VO2 thermochromic smart window for energy savings and generation. *Sci. Rep.* **3,** (2013).

178. Qazilbash, M. M. *et al.* Mott Transition in VO2 Revealed by Infrared Spectroscopy and Nano-Imaging. *Science* **318,** 1750–1753 (2007).

179. Lazarovits, B., Kim, K., Haule, K. & Kotliar, G. Effects of strain on the electronic structure of VO2. *Phys. Rev. B* **81,** 115117 (2010).

180. Pardo, V. & Pickett, W. E. Half-Metallic Semi-Dirac-Point Generated by Quantum Confinement in TiO2/VO2 Nanostructures. *Phys. Rev. Lett.* **102,** 166803 (2009).

181. ASM Alloy Phase Diagrams Database. at <http://www1.asminternational.org/asmenterprise/apd/default.aspx>

182. Morin, F. J. Oxides Which Show a Metal-to-Insulator Transition at the Neel Temperature. *Phys. Rev. Lett.* **3,** 34–36 (1959).

EFTHYMIOS CH. SVOUKIS

183. Griffiths, C. H. & Eastwood, H. K. Influence of stoichiometry on the metal-semiconductor transition in vanadium dioxide. *J. Appl. Phys.* **45,** 2201–2206 (1974).

184. Kawada, I., Kimizuka, N. & Nakahira, M. Crystallographic investigations of the phase transition of VO_2. *J. Appl. Crystallogr.* **4,** 343–347 (1971).

185. Rogers, K. D. An X-ray diffraction study of semiconductor and metallic vanadium dioxide. *Powder Diffr.* **8,** 240–244 (1993).

186. Donev, E. Metal semiconductor transitions in nanoscale vanadium dioxide thin films, subwavelength holes and nanoparticles. (University of Nashville, 2008).

187. Narayan, J. & Bhosle, V. M. Phase transition and critical issues in structure-property correlations of vanadium oxide. *J. Appl. Phys.* **100,** 103524 (2006).

188. Goodenough, J. B. The two components of the crystallographic transition in VO2. *J. Solid State Chem.* **3,** 490–500 (1971).

189. Israelsson, M. & Kihlborg, L. The phase relations in the VO2|WO2 system. *Mater. Res. Bull.* **5,** 19–29 (1970).

190. Aetukuri, N. B. *et al.* Control of the metal-insulator transition in vanadium dioxide by modifying orbital occupancy. *Nat. Phys.* **9,** 661–666 (2013).

191. Shin, S. *et al.* Vacuum-ultraviolet reflectance and photoemission study of the metal-insulator phase transitions in VO2, V6O13, and V2O3. *Phys. Rev. B* **41,** 4993–5009 (1990).

192. Liu, G.-H., Deng, X.-Y. & Wen, R. Electronic and optical properties of monoclinic and rutile vanadium dioxide. *J. Mater. Sci.* **45,** 3270–3275 (2010).

193. Kittel, C. *Introduction to solid state physics*. (Wiley & Sons, Inc., 2005).

194. Wentzcovitch, R. M., Schulz, W. W. & Allen, P. B. VO2: Peierls or Mott-Hubbard? A view from band theory. *Phys. Rev. Lett.* **72,** 3389–3392 (1994).

195. Zylbersztejn, A. & Mott, N. F. Metal-insulator transition in vanadium dioxide. *Phys. Rev. B* **11,** 4383–4395 (1975).

196. Paquet, D. & Leroux-Hugon, P. Electron correlations and electron-lattice interactions in the metal-insulator, ferroelastic transition in VO2: A thermodynamical study. *Phys. Rev. B* **22,** 5284–5301 (1980).

EFTHYMIOS CH. SVOUKIS

197. Yang, T.-H., Mal, S., Jin, C., Narayan, R. J. & Narayan, J. Epitaxial VO2/Cr2O3/sapphire heterostructure for multifunctional applications. *Appl. Phys. Lett.* **98,** 022105 (2011).

198. Muraoka, Y. & Hiroi, Z. Metal–insulator transition of VO2 thin films grown on TiO2 (001) and (110) substrates. *Appl. Phys. Lett.* **80,** 583–585 (2002).

199. Diebold, U. The surface science of titanium dioxide. *Surf. Sci. Rep.* **48,** 53–229 (2003).

200. Yamamoto, Y., Nakajima, K., Ohsawa, T., Matsumoto, Y. & Koinuma, H. Preparation of Atomically Smooth TiO2 Single Crystal Surfaces and Their Photochemical Property. *Jpn. J. Appl. Phys.* **44,** L511 (2005).

201. Tashman, J. W. *et al.* Epitaxial growth of VO2 by periodic annealing. *Appl. Phys. Lett.* **104,** 063104 (2014).

202. Kittiwatanakul, S., Lu, J. & Wolf, S. A. Transport Anisotropy of Epitaxial VO2 Films near the Metal–Semiconductor Transition. *Appl. Phys. Express* **4,** 091104 (2011).

203. Muraoka, Y. *et al.* Spectroscopic evidence of the formation of (V,Ti)O2 solid solution in VO2 thinner films grown on TiO2(001) substrates. *J. Appl. Phys.* **109,** 043702–043702–6 (2011).

204. Chen, C. *et al.* Influence of defects on structural and electrical properties of VO2 thin films. *J. Appl. Phys.* **110,** 023707 (2011).

205. Shibuya, K., Kawasaki, M. & Tokura, Y. Metal-insulator transitions in TiO2/VO2 superlattices. *Phys. Rev. B* **82,** 205118 (2010).

206. Fan, L. L. *et al.* Strain dynamics of ultrathin VO_2 film grown on TiO_2 (001) and the associated phase transition modulation. *Nano Lett.* **14,** 4036–4043 (2014).

207. Pei-ran, Z., Yamamoto, S., Miyashita, A. & Naramoto, H. Pulsed Laser Deposition of VO 2 Single Crystal Thin Films on Sapphire Substrates. *Chin. Phys. Lett.* **15,** 904 (1998).

208. Gupta, A. *et al.* Semiconductor to metal transition characteristics of VO2 thin films grown epitaxially on Si (001). *Appl. Phys. Lett.* **95,** 111915 (2009).

209. Ruzmetov, D., Heiman, D., Claflin, B. B., Narayanamurti, V. & Ramanathan, S. Hall carrier density and magnetoresistance measurements in thin-film vanadium dioxide across the metal-insulator transition. *Phys. Rev. B* **79,** 153107 (2009).

EFTHYMIOS CH. SVOUKIS

210. Ashcroft, N. W. & Mermin, N. D. *Solid state physics*. (Holt, Rinehart and Winston, 1976).

211. Ziman, J. M. *Electrons and phonons: the theory of transport phenomena in solids*. (Clarendon Press ; Oxford University Press, 2001).

212. Callaway, J. Model for Lattice Thermal Conductivity at Low Temperatures. *Phys. Rev.* **113,** 1046–1051 (1959).

213. Callaway, J. Low-Temperature Lattice Thermal Conductivity. *Phys. Rev.* **122,** 787–790 (1961).

214. Blumberg, G. *et al.* Sliding Density Wave in Sr14Cu24O41 Ladder Compounds. *Science* **297,** 584–587 (2002).

215. Sato, H. On the Thermal Conductivity of Ferromagnetics. *Prog. Theor. Phys.* **13,** 119–120 (1955).

216. Balents, L. Spin liquids in frustrated magnets. *Nature* **464,** 199–208 (2010).

217. Hess, C., Baumann, C. & Büchner, B. Scattering processes and magnon thermal conductivity in. *J. Magn. Magn. Mater.* **290–291, Part 1,** 322–325 (2005).

EFTHYMIOS CH. SVOUKIS